Title
Measurement and Control of Nanoscale Interactions and Assemblies

Author
Schwartz, Jeffrey James

Publication Date
2016

Peer reviewed|Thesis/dissertation

UNIVERSITY OF CALIFORNIA

Los Angeles

Measurement and Control of Nanoscale Interactions and Assemblies

A dissertation submitted in partial satisfaction of the

requirements for the degree Doctor of Philosophy

in Physics

by

Jeffrey James Schwartz

2016

ABSTRACT OF THE DISSERTATION

Measurement and Control of Nanoscale Interactions and Assemblies

by

Jeffrey James Schwartz

Doctor of Philosophy in Physics

University of California, Los Angeles, 2016

Professor Jianwei Miao, Co-Chair

Professor Paul S. Weiss, Co-Chair

Detailed understanding and control of the intermolecular forces that govern molecular assembly are necessary to engineer structure and function at the nanoscale. Liquid crystal (LC) assembly is exceptionally sensitive to surface properties, capable of transducing nanoscale intermolecular interactions into a macroscopic optical readout. Self-assembled monolayers (SAMs) modify surface interactions and are known to influence LC alignment. Here, we exploit the different dipole magnitudes and orientations of carboranethiol and -dithiol positional isomers to deconvolve the influence of SAM-LC dipolar coupling from variations in molecular geometry, tilt, and order. Director orientations and anchoring energies are measured for LC cells employing various carboranethiol and -dithiol isomer alignment layers. Using LC alignment as a probe of interaction strength, we elucidate the role of dipolar coupling of molecular monolayers to their environment in determining molecular orientations.

Determining the three-dimensional, atomic-scale structures of complex or buried structures will transform our understanding of chemical and biological processes at the nanoscale. We outline the development of a technique to elucidate single-molecule structure using a scanning tunneling microscope to detect, to localize, and to resolve nuclear spin signals. Inhomogeneous magnetic field will add another dimension to the spin resolution, enabling three-dimensional mapping of spin species. Targeted systems include: cobalt nanoparticles, organic molecules possessing a nuclear spin center, and linear, 'chain-like' molecules containing biologically relevant nuclei.

We address the importance of the dynamic molecular ink concentration at a polymer stamp/substrate interface during microcontact displacement or insertion printing. We demonstrate that by controlling molecular flux, we can influence both the molecular-scale order and the rate of molecular exchange of SAMs on gold surfaces. Surface depletion of molecular ink at a polymer stamp/substrate interface is driven predominantly by diffusion into the stamp interior, which we model numerically. Controlling interfacial concentration improves printed film reproducibility and the fractional coverage of multicomponent films can be controlled to within a few percent. We describe two experiments that illustrate control over ink transfer during experiments: the role of contact time on monolayer reproducibility and molecular order, and the fine control of fractional monolayer coverage in SAMs modified using displacement printing.

This dissertation of Jeffrey James Schwartz is approved.

Thomas G. Mason

Jianwei Miao, Committee Co-Chair

Paul S. Weiss, Committee Co-Chair

University of California, Los Angeles

2016

TABLE OF CONTENTS

LIST OF FIGURES

prepared with matching self-assembled monolayers of *m*-9-carboranethiol (M9), *m*-1-carboranethiol (M1), *o*-9-carboranethiol (O9), *o*-1-carboranethiol (O1), *o*-9,12-carboranedithiol (9O12), and *o*-1,2-carboranedithiol (1O2), as indicated. At these surfaces, uniaxial, planar alignment was manifest in 4-cyano-4′-pentylbiphenyl (5BC) LCs, as evidenced by the variations in optical transmittance possessing four-fold rotational symmetry. Cells were constructed with angles of either 0° or 90° between the alignment layers' gold deposition axes, inducing untwisted (red) or twisted (blue) nematic structures, respectively. Initially, one or both of a cell's gold deposition axes were aligned with the polarizer axis, defined to be at 0°. Rotation angles were measured with respect to this reference orientation, incremented in 5° steps. Reported spectra are averages of analyses performed on n separate LC cells, each consisting of three measured regions, where the radial line widths indicate the data's standard deviation. Spectra are scaled such that their respective transmittance maxima are equal; in actuality, the maximum transmittance of an untwisted nematic cell nearly equals the minimum transmittance of a cell with a 90° twist in its director.....32

Figure 2.4: Normalized optical transmittances of electrically modulated liquid crystal (LC) cells viewed between crossed polarizers. Alignment layers were prepared with matching self-assembled monolayers of *m*-9-carboranethiol (M9), *m*-1-carboranethiol (M1), *o*-9-carboranethiol (O9), *o*-1-carboranethiol (O1), *o*-9,12-carboranedithiol (9O12), and *o*-1,2-carboranedithiol (1O2), as indicated. These surfaces induced uniaxial planar alignment in 4-cyano-4′-pentylbiphenyl (5CB) LCs. Cells were constructed with perpendicular gold deposition axes, producing twisted nematic structures, and were positioned between crossed polarizers such that their zero-voltage optical transmittance was maximized. Subsequently, a sinusoidally varying (1 kHz) voltage was applied between the alignment layers in order to distort the LC director away from the surface. Root-mean-

Figure 2.8: Normalized optical transmittances of electrically modulated liquid crystal (LC) cells viewed between crossed polarizers. Alignment layers were prepared with matching self-assembled monolayers of *m*-1-carboranethiol (M1), which induced uniaxial planar alignment in *N*-(4-methoxybenzylidene)-4-butylaniline (MBBA) LCs. Cells were constructed with 0° or 90° angles between their alignment layers' gold deposition axes, producing untwisted (red) or twisted (blue) nematic structures, respectively. Cells were positioned between crossed polarizers such that their zero-voltage optical transmittance was maximized (minimized) for twisted (untwisted) nematic structures. Subsequently, a sinusoidally varying (1 kHz) voltage was applied between the alignment layers. Root-mean-square voltages, varied in 0.1 V steps, are indicated along the horizontal axes. Reported spectra are averages (black lines) of analyses performed on $n = 3$ separate LC cells, of each type, where the vertical widths of the surrounding blue outlines indicate the data's standard deviation. No changes in the transmittance spectra were observed with increasing voltage, indicating that the MBBA mesogens did not reorient as a result of the applied electric field. 57

Figure 2.9: Transmission fringes observed in liquid crystal (LC) wedge cells viewed between crossed polarizers while illuminated with monochromatic light (wavelength $\lambda = 531$ nm). Alignment layers prepared with matching self-assembled monolayers of *m*-1-carboranethiol (M1), *m*-9-carboranethiol (M9), *o*-1-carboranethiol (O1), *o*-9-carboranethiol (O9), and *o*-9,12-carboranedithiol (9O12), as indicated, induced uniaxial planar alignment of *N*-(4-methoxybenzylidene)-4-butylaniline (MBBA) LCs. Wave plates inserted between the polarizers modified the optical retardation of light transmitted through the cells by fixed amounts (Γ_{WP}). Here, positive (negative) values of Γ_{WP} signify that a wave plate's optically slow axis was aligned parallel (perpendicular) to a cell's gold evaporation direction ($\overrightarrow{\mathbf{Au}}$). Arrows and dashed

LIST OF TABLES

LIST OF ABBREVIATIONS AND SYMBOLS

1AD	1-adamantanethiol
1ATC9	3-mercapto-*N*-nonylpropionamide
Å	ångström
AC	time-varying
AFM	atomic force microscopy
Au	gold
B	magnetic induction
BPDT	biphenyl-4,4′-dithiol
C6	hexanethiol
C8	octanethiol
C8DT	octanedithiol
C10	decanethiol
C10DT	decanedithiol
C11OH	11-mercapto-1-undecanol
C12	1-dodecanethiol
C18	1-octadecanethiol
Co	cobalt

Co-NP cobalt nanoparticle

dBm decibel-milliwatts

DC constant, time independent

eV electron volt

ESN-STM electron spin noise STM

fcc face-centered cubic

G gauss

h Planck's constant, approximately 6.626×10^{-34} J s

ħ reduced Planck's constant, $\left(h/2\pi\right)$

hcp hexagonal close-packed

H magnetic field

HOPG highly ordered pyrolytic graphite

I current

k_B Boltzmann constant, approximately 1.381×10^{-23} m^2 kg s^{-2} K^{-1}

MRFM magnetic resonance force microscopy

MRI magnetic resonance imaging

μ magnetic moment

μCP microcontact printing

μDP	microdisplacement printing
μ_N	nuclear magneton
mM	millimolar
m_s	projection of the quantum mechanical spin onto the *z*-axis
M	magnetization
M_s	saturation magnetization
NMR	nuclear magnetic resonance
NPPB	4-(2′-nitro-4′-phenylethynyl-phenylethynyl)-benzenethiol
NV	nitrogen-vacancy
Φ_B	magnetic flux
P	pressure
Pc	phthalocyanine
PDMS	polydimethylsiloxane
RF	radio frequency
S	sulfur
SAM	self-assembled monolayer
SEM	scanning electron microscopy
SNR	signal-to-noise ratio

STM	scanning tunneling microscope
T	temperature
T_C	Curie temperature
TEM	transmission electron microscopy
TPDT	*p*-terphenyl-4,4″-dithiol
V	volt
XRD	X-ray diffraction

ACKNOWLEDGMENTS

Now, at the culmination of my graduate training, I am fortunate to have the opportunity to express publically, in writing, my deep gratitude to the people who have assisted me in reaching this milestone in my life. Although I may never be able to acknowledge properly all those who have contributed to my personal and professional development, here I attempt to provide a satisfactory summary, recognizing that there are likely unintentional and undeserved omissions.

I begin by thanking my family, who have shown me unwavering support for over 28 years. My grandparents provided a wonderfully nurturing environment in which to grow up, with my grandmother (Phyllis) acting as a second mother to me. My other grandmother (Leona), herself a former science teacher, continuously spurred my curiosity, giving me my first microscope to examine pond water and, later, professional-grade laboratory equipment to assist in my experiments. For her part, my mother (Nancy) always tried to provide the education and opportunities that would enable me to pursue my dreams. One of those opportunities afforded me was to take over our kitchen and backyard in the pursuit of my personal science experiments. Most families would not tolerate the sights, sounds, and smells of mysterious liquids boiling on the stove, powders baking in the oven, or crystals growing in the refrigerator, but mine did…and so much more. My brother (Michael) was there by my side during many of these experiments in the backyard and around our neighborhood, together with our oldest friend, Andrew Conroy. I cannot overemphasize the importance of these experiences (and therefore the people who enabled them) in shaping me into the scientist, and person, I am today.

In the course of my formal education, I had many excellent teachers, most auspiciously Dr. Robert Scheer (physics), Mr. Bryan McMahon (chemistry), and Mr. Jack King (computer science). It is hardly a coincidence that the subjects they taught are not only still my favorites but also are

the ones I apply now on a daily basis. I cannot fail to acknowledge, specifically, the support and encouragement shown by Dr. Scheer and Mr. McMahon of my home science experiments, even when they did not turn out as expected. More than 10 years later, Dr. Scheer still saves the shattered bits and pieces of the force sensor I destroyed in one of my more memorable accidents; he considers it far more valuable as a memento and illustration of his student's exploits than any replacement I could provide. I am incredibly grateful to these teachers who emboldened and empowered me to put into practice what I learned inside, and outside, their classrooms.

I am indebted to Profs. Jose Perez, Anvar Zakhidov, and Lloyd Bumm for giving me my first tastes of "real" scientific research. These three professors, at three different universities, served as early role models and showed me what a career in science was like. Despite my inexperience, Prof. Perez treated me as a valued colleague and demonstrated an infectious drive to overcome challenges in the lab, instilling in me some of the confidence and creativity I display today. Prof. Zakhidov allowed me (what I now know to be) an almost unbelievable amount of independence in my undergraduate research, while simultaneously providing incredible career support and guidance that continues to this day. Prof. Bumm helped me fulfil a lifelong dream of 'seeing' at the molecular scale when he introduced me to my first, but certainly not last, scanning tunneling microscope and undeniably influenced the course of my professional development.

My advisor, Prof. Paul Weiss, has served as a scientific role model for me over the years. More than anyone else, Paul has shown me the 'behind-the-scenes' aspects of scientific research, publishing, and academic life. He fosters and reinforces admirable qualities in all his students, myself included. Additionally, despite his many obligations and other draws on his time, Paul has never failed to provide for my best interests and professional development. I am extremely grateful to him for his years of mentorship and the wonderful opportunities he made possible.

I will always feel a special connection to all of my labmates (my academic siblings) who worked alongside me in the Weiss Group. After more than 6 years, this amounts to several dozen scientists and engineers from all around the world. But that bond feels especially strong within a particular subset: Dr. Nate Hohman, Dr. Moonhee Kim, Prof. Shelley Claridge, and David McMillan. The five of us were the first wave of people to move to UCLA from Penn State in August, 2009. At the time, I was a brand new ("0^{th} year") student in the Group, having barely unpacked my belongings in State College, before being told the news (*on my first day in the lab*) of our move to Los Angeles. Nevertheless, Nate, Moonhee, Shelley, and David (all of whom were significantly more senior than myself) immediately befriended and included me as their equal as we adjusted to our new lives and settled the western frontier of the Weiss Empire. Beyond these experiences, I am especially grateful to Shelley for the years of unassuming mentoring that she provided to me as we worked side-by-side developing new instrumentation and writing scientific articles together.

As time progressed, additional waves of students and postdocs joined us from Penn State, as well as new members originating from UCLA, who brought with them the diverse set of skills and personalities that made our lab such an enjoyable environment in which to work. The 6^{th} floor of CNSI would just not have been the same without my friends Prof. Sarawut Cheunkar, Prof. Heidi Bednar, Dr. Amit Vaish, Dr. Huan Cao, Dr. Yuxi Zhao, and Prof. Wei-Ssu Liao. I cannot imagine the lab without the valuable contributions and delightful mix of personalities of Dr. John Thomas, Dr. Liane Slaughter, Andrew Guttentag, Garrett Wadsworth, Andrew Serino, Miles Silverman, Harsharn Auluck, Mya LeThai, John Abendroth, Nako Nakatsuka, Diana Yugay, Kris Barr, and especially my former roommate and companion while working late nights in the lab, Dr.

Bala Krishna Pathem. I am immensely thankful for all these people who made my time in the Weiss Group so congenial.

Over the years, I had the privilege mentoring other students as we collaborated on shared research projects. As a consequence of this special relationship, these colleagues (Alexandra Mendoza, Natcha Wattanatorn, Chunru Fan, Olivia Irving, and Hua Zheng) made a particularly strong contribution to all that I accomplished in graduate school, for which I am tremendously grateful.

I also wish to recognize the contributions of others, outside the Weiss Group, that have helped me during my time at UCLA, including Dr. Adam Stieg (Nano and Pico Characterization Lab), Shylo Stiteler (physical sciences student machine shop), and Jenny Lee (Department of Physics & Astronomy).

Additionally, I thank Profs. Kai Wu and Tomohide Takami for giving me the opportunities to visit and to work in their Beijing and Seoul laboratories, respectively, even if only for a brief time. I will never forget those experiences, which immeasurable broadened my perspective on ways in which science is conducted in other parts of the world.

Finally, I extend special thanks to Michael Policarpio, who has been an unfailing and selflessly supportive friend to me since elementary school. What a pleasant surprise it was to be ‘classmates’ again at UCLA, even if only for a short time. I cherish our shared memories and look forward to more to come.

This work was generously supported by the U.S. Department of Energy through grants DE-SC-0005025 and DE-SC-1037004.

Co-author Contributions to Published Work Included in This Dissertation:

Chapters 1 and 3 contains sections adapted from a published review:

> Claridge, S. A.; Schwartz, J. J.; Weiss, P. S. "Electrons, Photons, and Force: Quantitative Single-Molecule Measurements from Physics to Biology." *ACS Nano* **2011**, *5*, 693–729. DOI: 10.1021/nn103298x

All authors contributed to the researching and writing of this review. This work received financial support from the U.S. Department of Energy (DE-SC00-05161), U.S. National Science Foundation (NSF-CHE-1041943), U.S. National Institutes of Health, and the Kavli Foundation. This is an unofficial adaptation of an article that appeared in an ACS publication. ACS has not endorsed the content of this adaptation or the context of its use.

Chapter 2 is adapted from a manuscript submitted for publication:

> Schwartz, J. J.; Mendoza, A. M.; Wattanatorn, N.; Zhao, Y.; Nguyen, V. T.; Spokoyny, A. M.; Mirkin, C. A.; Baše, T.; Weiss, P. S. "Surface Dipole Control of Liquid Crystal Alignment." *J. Am. Chem. Soc.* (submitted).

J. J. Schwartz initiated the project and developed it in collaboration with A. M. Mendoza, N. Wattanatorn, Y. Zhao, and P. S. Weiss. Experiments were performed by J. J. Schwartz, A. M. Mendoza, N. Wattanatorn, and Y. Zhao. V. T. Nguyen, A. M. Spokoyny, C. A. Mirkin, and T. Baše synthesized chemicals used in the experiments. The manuscript was written by J. J. Schwartz with contributions from all co-authors. This work received financial support from the U.S. Department of Energy (DE-SC-0005025), the National Science Foundation (DGE-1144087), and the Royal Thai Government.

Chapter 4 is adapted with permission from:

> Schwartz, J. J.; Hohman, J. N.; Morin, E. I.; Weiss, P. S. "Molecular Flux Dependence of Chemical Patterning by Microcontact Printing." *ACS Appl. Mater. Interfaces* **2013**, *5*, 10310–10316. DOI: 10.1021/am403259q
>
>

J. N. Hohman initiated the project and developed it in collaboration with all co-authors. J. J. Schwartz preformed numerical modeling and analysis. The manuscript was written by J. N. Hohman and J. J. Schwartz with contributions from all co-authors. This work received financial support from the U.S. National Science Foundation (CHE-1013042) and the Kavli Foundation.

VITA

Jeffrey Schwartz received an Academic Distinction Scholarship to attended The University of Texas at Dallas (UTD) from 2005 to 2009, where he earned a Bachelor of Science degree in physics, *magna cum laude*. While at UTD, Jeffrey researched topics related to polymer and dye-sensitized solar cells in the Alan G. MacDiarmid NanoTech Institute, under the mentorship of Prof. Anvar Zakhidov. Jeffrey continued his academic training with Prof. Paul S. Weiss, initially entering the physics Ph.D. program at The Pennsylvania State University, and subsequently leading the Weiss Group's move to the University of California, Los Angeles (UCLA) in 2009. During his time at UCLA, Jeffrey received the Rudnick-Abelmann Scholarship in 2013, which recognizes outstanding students in the Department of Physics and Astronomy. Jeffrey also trained abroad, working in the laboratory of Prof. Kai Wu in Beijing, China, during the summer of 2012, supported by a fellowship from the Joint Research Institute in Science and Engineering, between Peking University and UCLA. Later, in 2014, Jeffrey taught physics at Stanford University as part of the Stanford Pre-Collegiate Institutes' summer program for gifted youth.

PUBLICATIONS

Defect-Tolerant Aligned Dipoles within Two-Dimensional Plastic Lattices. John C. Thomas, **Jeffrey J. Schwartz**, J. Nathan Hohman, Shelley A. Claridge, Harsharn S. Auluck, Andrew C. Serino, Alexander M. Spokoyny, Giang Tran, Kevin F. Kelly, Chad A. Mirkin, Jerome Gilles, Stanley J. Osher, and Paul S. Weiss, *ACS Nano* **9**, 4734 (2015). DOI: 10.1021/acsnano.5b01329

Differentiating Amino Acid Residues and Side Chain Orientations in Peptides Using Scanning Tunneling Microscopy. Shelley A. Claridge, John C. Thomas, Miles A. Silverman, **Jeffrey J. Schwartz**, Yanlian Yang, Chen Wang, and Paul S. Weiss, *J. Am. Chem. Soc.* **135**, 18528 (2013). DOI: 10.1021/ja408550a

Molecular Flux Dependence of Chemical Patterning by Microcontact Printing. **Jeffrey J. Schwartz**, J. Nathan Hohman, Elizabeth I. Morin, and Paul S. Weiss, *ACS Appl. Mater. Interfaces* **5**, 10310 (2013). DOI: 10.1021/am403259q

Electrons, Photons, and Force: Quantitative Single-Molecule Measurements from Physics to Biology. Shelley A. Claridge, **Jeffrey J. Schwartz**, and Paul S. Weiss, *ACS Nano* **5**, 693 (2011). DOI: 10.1021/nn103298x

Field Emission Properties of ZnO, ZnS and GaN Nanostructures. Y. Mo, **J. J. Schwartz**, M. H. Lynch, P. A. Ecton, A. Neogi, J. M. Perez, Y. Fujita, H. W. Seo, Q. Y. Chen, L. W. Tu, and N. J. Ho, in *Nanoscale Photonics and Optoelectronics*, edited by Z. M. Wang and A. Neogi (Springer, New York, 2010), pp. 131-156. DOI: 10.1007/978-1-4419-7587-4 7

CONFERENCE PRESENTATIONS

Surface Dipole Control of Liquid Crystal Alignment. **Jeffrey Schwartz**, Yuxi Zhao, Alexandra Mendoza, Natcha Wattanatorn, Paul Weiss. Oral presentation at the March 2015 meeting of the American Physical Society, San Antonio, TX.

Hydrogen-Bonding Networks in Self-Assembled Monolayers. **Jeffrey J. Schwartz**, Jian Shang (尚鉴), Jing Liu (刘婧), Xin Jin (金鑫), Paul S. Weiss, Kai Wu (吴凯). Poster presented at the 2013 Seaborg Symposium, Los Angeles, CA.

Self-Assembly of CdSe and PbS/PbSe Quantum Dots on Gold and other Surfaces Using Dithiol Functionalization. **Jeffrey Schwartz**, Miaoxin Zhou, Anvar Zakhidov. Poster presented at the March 2009 meeting of the American Physical Society, Pittsburgh, PA.

Growth and Characterization of Wide Band Gap Semiconductors (Zinc Oxide, Zinc Sulfide). **Jeffrey Schwartz**, Jose Perez, Yudong Mo. Poster presented at 2007 Joint Fall Meeting of the Texas Sections of the APS and AAPT, College Station, TX.

CHAPTER 1

Introduction to Nanoscale Assembly and Measurement

1.1 Motivation

Understanding the structure of mater at the atomic and molecular scales represents an increasingly important challenge spanning a myriad of disciplines, including physics, chemistry, engineering, and medicine. The precise arrangement and composition of a material's atomic constituents determines many of its physical and chemical properties. For example, a material's electronic band structure and catalytic activity not only are influenced by the periodic arrangement of its atoms, but also by the specific crystal facets exposed to the environment.[1–4] Additionally, the functions of numerous biological systems, ranging from peptides to entire cells, are determined by a hierarchy of molecular structures.[5–9] Our growing ability to measure and control the organization of materials at these smallest practical scales (~10^{-10}–10^{-9} m) drives advances in electronics, energy production and storage, pharmaceuticals, as well as in basic research.[10–15]

1.2 Self-Assembled Monolayers

Self-assembled monolayers (SAMs) are single-molecule thick layers that form spontaneously on an underlying substrate.[16] These layers assemble through a combination of

chemical and physical interactions between the adsorbate and the substrate surface as well as between neighboring adsorbates. The concerted effects of these interactions results in a variety of structures and surface features,[17] characteristic of the molecular assemblies and low-dimensionality materials, which can be exploited to control nanoscale properties.[15,18,19]

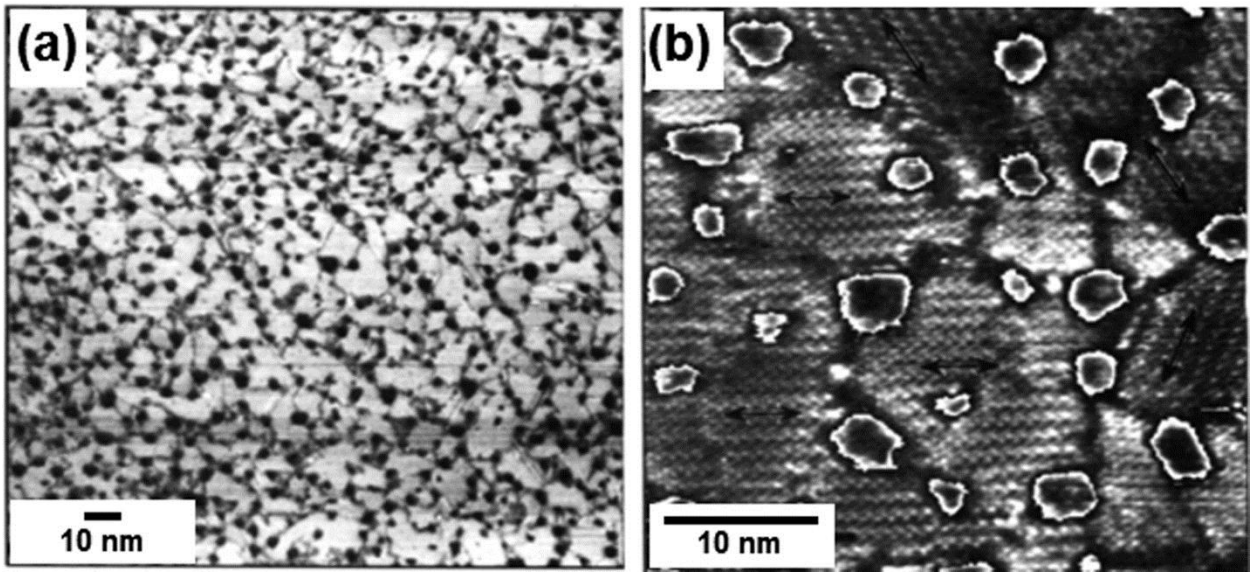

Figure 1.1: Scanning tunneling microscopy used to measure heterogeneity in self-assembled monolayers of alkanethiols on Au{111}. Addition of thiols to an atomically flat gold surface causes reconstruction of the gold surface under ordered molecular domains and creates irregular one-atom deep pits where thiols have removed gold atoms. The etch pits act to trap tilt domain defects (lines running between pits in both images). Adapted with permission from References 20 and 21. Copyright 1994 American Chemical Society.

Alkanethiolate and, more generally, molecules possessing thiol functionalities assembled on gold surfaces represent an archetypal system of study.[16] Both inorganic surfaces and self-assembled 2D lattices of alkanethiols bound to Au{111} surfaces via their thiol headgroups have been studied extensively.[22] For example, Poirier and Tarlov observed that adding alkanethiols to

an atomically flat gold surface has a number of important effects in addition to forming a SAM (Figure 1.1).[20] The gold structure distorts under the 5−15 nm ordered domains in the monolayer, forming a $c(4 \times 2)$ lattice, and irregular one-atom deep pits form in the gold surface as atoms are removed by thiols in solution. Domain boundaries, the largest and most reactive defects in the SAM, are found to run between pairs of vacancy islands, an example of resolving complex inter-related processes on surfaces at the single-molecule level.

Numerous other molecular attachment chemistries[23–27] and surface types[28–33] have also been studied. The expansive parameter space of molecules and surfaces, as well as their exposed and buried moieties, enable a rich variety of molecular assemblies. Assembled structures are largely mediated by intermolecular (intra-SAM) forces between molecular functionalities. As a result, these interactions influence the surface structure of the molecular lattice[34–37] and can induce phase separation between dissimilar adsorbed species.[38–41] Hydrogen-bonding networks[42–44] represent a particularly strong form of molecular dipole-dipole interactions[45–48] within a SAM. These, and other, interactions have been used extensively to engineer structures at the nanoscale.[49,50,44,51,47,52] The ability to influence the long-range molecular order, as well as the type and density of defects, in these assemblies has been used to control the placement of molecules in prescribed environments for further study.[53,54]

1.3 Single-Molecule Measurements

Numerous techniques exist with which to make measurements with single-molecule sensitivity and/or resolution. Here, we classify these measurements broadly based on the probe type used,[21] either electron[55] or force-based measurements.[56,57] Each probe type has unique measurement advantages, which we discuss briefly in this section to provide context and to aid understanding of the capabilities and limits of these technique, as well how the physical properties

of the sample influences the choice of probes. Additionally, we discuss the operation of select techniques particularly relevant to this dissertation.

Although not discussed in depth, we briefly discuss photon-based measurements to determine the atomic structure of materials, most notably using X-ray diffraction (XRD).[58] This technique relies on the interference of scattered short wavelength electromagnetic radiation (X-rays) from the periodic arrangement of matter within a crystal lattice. The size and symmetry of the resulting diffraction pattern is characteristic of the arrangement and spacing of the crystal's constituent components and can be used to infer its internal structure. Analogous techniques using scattered electrons and neutrons also exist, which can reveal positional and magnetic ordering of a material with atomic resolution.[59–61] These techniques are limited, however, to materials that possess long-range, crystalline order.

Electrons: Scanning Tunneling Microscopy and Transmission Electron Microscopy

Electrons have a number of features that make them useful probes at the very short length scales relevant for single-molecule measurements. Their small mass means they exhibit substantial quantum mechanical tunneling behavior, which allows measurement of distances up to a few nanometers with sub-Ångström sensitivity. Coupling tunneling with inelastic processes enables measurement of vibrational and other energy levels.[62,63] The sub-Ångström wavelength of high-energy electrons means they are able to resolve atomic-scale features in diffraction experiments.[64] Since electrons are responsible for molecular bonding, measuring electronic conductance through a molecule can in some cases also probe single-molecule conformations.[65]

The excellent spatial resolution achieved in electron-based single-molecule measurements comes at a cost. Observed areas are typically quite small (often much less than 1 μm^2). Thus, while measuring the behavior of a single molecule relative to its immediate environment is

straightforward, relating it to micro- to macroscopic features can be more difficult. Electron-based measurements also place fairly stringent requirements on sample preparation: scanning tunneling microscopy generally requires samples no more than a few nanometers thick on conductive substrates, and transmission electron microscopy (TEM) requires samples to be electron-transparent (usually less than 100 nm thick and composed of low-atomic-number materials).

Scanning tunneling microscopy enables direct, real-space characterization of topographic and electronic features on a surface with atomic resolution.[66,67] The scanning tunneling microscope (STM) relies on its ability to measure minute changes in the quantum mechanical tunneling current flowing between an atomically sharp probe and a sample. The probe is rastered across the sample's surface while a bias (typically about 1 V) is applied and a tunneling current (picoamperes to nanoamperes) is measured. The tunneling current decreases exponentially with increasing tip−surface distance and is measurable up to distances of a few nanometers. Thus, the topography of surface features, including single molecules and atoms, can be measured with both vertical and lateral resolution better than 0.1 nm (sometimes 0.1 pm). The tunneling current also depends on the electronic structure of the molecule in the tunneling junction; thus, it is possible to quantify energy levels within the molecule using this technique.

Typically, a STM operates in a constant current mode. As the probe tip moves laterally over the surface, topographic or electronic features cause the tunneling current to vary. A feedback loop serves to maintain a constant tunneling current by extending or retracting the tip toward or away from the surface, respectively, to counteract these changes. The probe tip is controlled using a piezoelectric actuator, which enables precise (sub-Ångström) control over its three-dimensional position by exploiting the known, linear response of the actuator to applied electrical biases. Measuring the change in the tip-sample separation required to maintain a constant tunneling

current as a function of position enables one to infer the apparent topographic height of a sample's surface.

By contrast, TEM imaging relies on the transmission (and scattering) of a beam of electrons incident on a thin sample.[68,69] In TEM (Figure 1.2, top center), molecules are deposited on a thin, electron-transparent surface, and a beam of high-energy electrons (on the order of 100 keV) is directed through the sample. Unscattered electrons can be collected in a CCD, producing a negative image of the strong electron scatterers. Scattering intensity depends on both crystallographic order and the atomic number of the scatterer. For low-contrast samples such as proteins, salts containing high-atomic-number nuclei, such as uranyl acetate, can be used to enhance contrast. Diffraction patterns in scattered electrons can also be analyzed to measure crystallographic structure in ordered samples. Typical spatial resolutions are on the order of 1 nm, although there are recent examples of resolutions better than 0.1 nm.

Since each pixel in an STM image is collected sequentially, frame rates are relatively slow: a 256 × 256 pixel image, collected at 1 ms per pixel (about 6000 tunneling electrons in 1 ms at 1 pA), requires approximately 1 min to acquire. Such collection rates are a result of bandwidth limitations imposed by the STM feedback loop and transimpedance amplifier. In order to achieve high gains (typically 10^8–10^{10} V A^{-1}) with minimal added noise to the measured tunneling current, the STM amplifiers are designed to operate with slowly varying current inputs, typically $\leq 10^3$ Hz. As such, the signals probed using an STM typically are limited to those that vary lowly varying in time. However, this constraint is overcome in certain, specialized, STM operation modes that employ atypical hardware additions, some of which are discussed in Chapter 3.

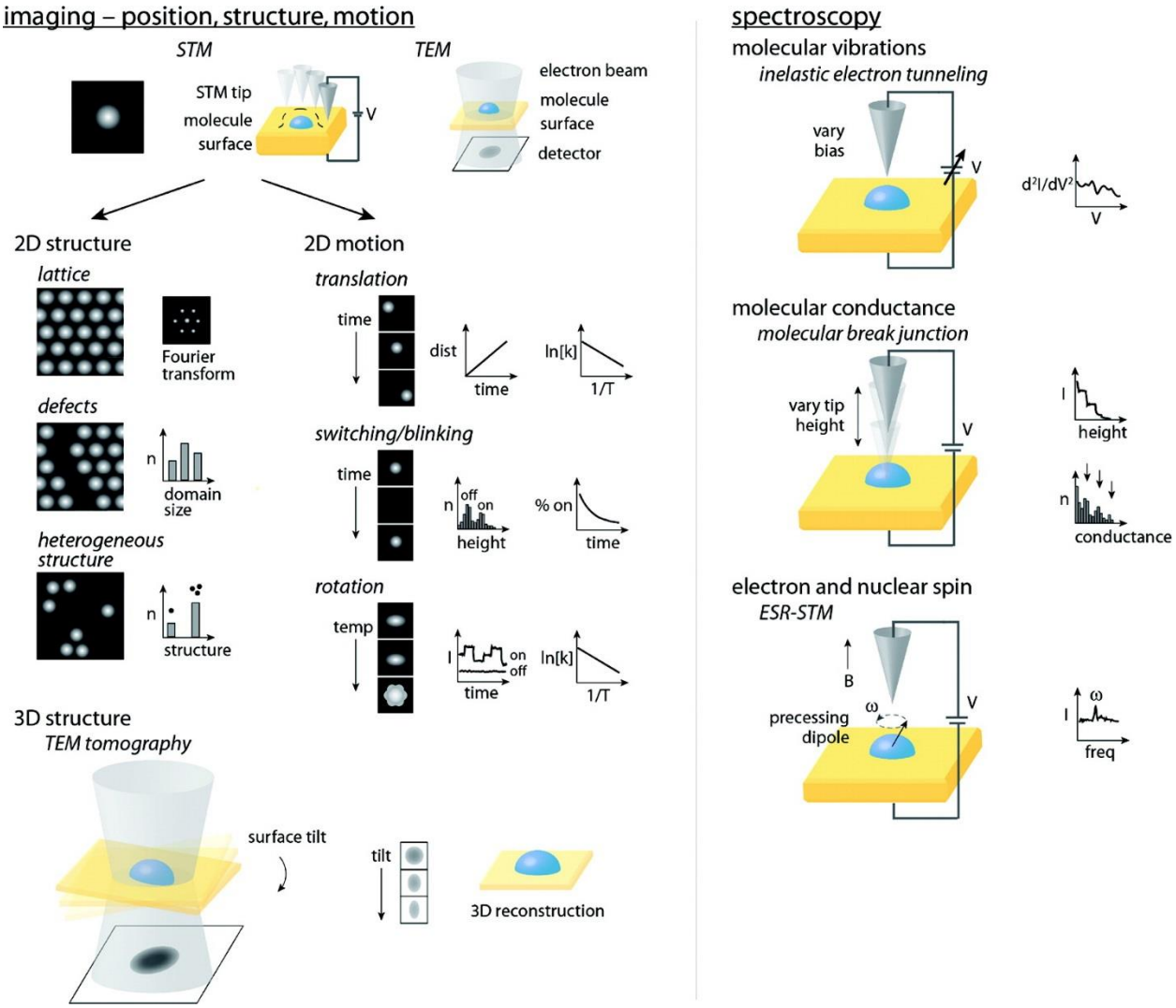

Figure 1.2: Overview of electron-based single-molecule measurements. Electrons can be used to perform label-free structural measurements of single atoms and molecules, including molecular lattices and their defects, heterogeneous structures, and motion including diffusion and switching. Single-molecule spectroscopy can also be performed using a scanning tunneling microscope by varying either bias or tip height or by applying a magnetic field to polarize spins. Figure adapted from Reference 21.

Faster native frame rates (on the order of milliseconds) make TEM better suited to the study of dynamic processes. A variety of in situ TEM designs enable measurements of nanoscale

responses to external stimuli such as mechanical force from an atomic force microscope or the application of an electric field. The requirement that samples be strong electron scatters has meant that most studies have examined dynamic processes in larger (>10 nm) nanoscale particles of inorganic materials.[70] However, some measurements are approaching the resolution and sensitivity necessary for single-molecule experiments. For instance, tumbling motions of individual La atoms confined within $La_2@C_{80}$−carbon nanotube peapod assemblies have been observed.[71] Importantly, the ability to observe the motion of high-contrast species may enable tagging experiments similar to many of the optical experiments discussed in later sections.

The high-energy electron beam requires that samples be measured under vacuum, which has limited studies in liquid, restricting many types of dynamic processes. The recent development of enclosed liquid TEM sample holders[72–74] has enabled the measurement of both diffusion of small (∼5 nm) inorganic nanocrystals[73] and the rate of growth of individual nanocrystals in solution, with particles becoming visible starting at about 2 nm in diameter.[74] Again, the ability to measure single particles directly in real space provides insights unavailable from bulk measurements. For instance, measurements of large numbers of diffusion events in anisotropic rod-shaped particles have quantified differences in diffusion rates along the long and short axes.[73]

Both scanning tunneling microscopy and TEM can be used to measure the structure and motion of molecules on surfaces;[64,75–78] a STM can also be used to perform spectroscopy on single molecules (Figure 1.2, right).[79] One of the powerful advantages to performing label-free real-space measurements at subnanometer length scales is that it allows the single-molecule measurement not only of ordered structures but also of defects and heterogeneous structures. This is important since nanoscale reactivity is often determined by the behavior of high-energy defects and other heterogeneous features.[80,81]

Molecular lattices have traditionally been measured using crystallographic techniques such as XRD, but in some cases, it is both possible and advantageous to measure lattices using single-molecule techniques.[22] In STM, the organization of the molecules on the surface is measured directly in real-space, and image-processing software is used to calculate lattice parameters based on the Fourier transformation of the image. A typical calculation might be made using a 20 nm × 20 nm image containing roughly 10^3 molecules in a single 2D layer. In relation, 3D single-crystal XRD measurements require a 50−500 μm^3 crystal containing on the order of 10^{15} molecules[82] and averages out heterogeneous features. Conversely, a 2D STM lattice measurement shows heterogeneous features but may or may not provide information about the locations of nuclei within the molecules, depending on molecular orientation.[22,83]

Molecular lattice structures based on STM image analysis have informed much of the understanding of the behavior of SAMs on surfaces.[22,84] Such measurements can be made under vacuum or atmospheric conditions or at liquid−solid interfaces. The properties of a monolayer depend strongly upon both its epitaxy with the underlying substrate and the strength of intermolecular interactions within the monolayer, also determined by lattice spacing. Substrate epitaxy is critical enough that SAM lattices are described in relation to the substrate lattice. For example, the $(\sqrt{3} \times \sqrt{3})R30°$ lattice formed by *n*-alkanethiolates on Au{111} has a lattice constant of 4.995 Å = $\sqrt{3}$ × 2.884 Å (the Au lattice constant) and is rotated 30° relative to the Au lattice.[85] A wide variety of SAM lattices have been measured,[86] including alkanethiols, alkaneselenols, functional cage molecules, amino acids, sugars, and DNA bases. Even complex structures such as lattices formed by different stereochemical binding patterns of modified oligo(phenylene ethynylene) molecules can be measured.[87] In cases where binding is more promiscuous, such as

n-alkaneselenolates on Au{111}, Moiré patterns can still form, resulting in large unit cells comprising many molecules.[27]

Lattice structures measured by TEM complement the length scales of those measured using an STM. While it is difficult to measure lattices for small-molecule organic species due to their low electron scattering cross sections, TEM has been used to measure both atomic lattices in higher-atomic-number inorganic nanocrystals with sizes comparable to single proteins and structures of superlattices composed of nanocrystals.[88] In certain cases, it is also possible to achieve even higher resolution using aberration-corrected lenses and for structures with inherently high contrast or low background. For instance, fullerene peapod structures can be observed inside carbon nanotubes,[89] and when the structures are assembled using endohedral lanthanide fullerenes, the positions of individual lanthanide atoms can be measured within the assembly.[71]

Recently, it has also become possible to determine 3D structures for large, high-symmetry organic molecules such as virus capsids by compiling thousands of real-space images taken from individual capsids at a range of angles.[90–92] This technique has been used to derive crystal structures of aqueoviruses[91] and the holoenzyme of propionyl-coenzyme A carboxylase[92] with resolutions as good as 3.3 and 3.2 Å, providing important insights into the biological functions of each. Although computationally intensive, such analyses are valuable for a broad range of biologically important molecules that have not yet been successfully crystallized and therefore cannot be analyzed by standard bulk structural techniques such as XRD.

While the ability to measure regular structures at the nanoscale has proved important in understanding the properties of nanostructured surfaces and materials, the ability to probe structural heterogeneities is equally vital. Defects and disordered areas are often the most reactive sites in molecular and atomic lattices, and heterogeneous, noncrystalline structures can be the most

important to probe at the single-molecule level since they are difficult or impossible to characterize using bulk or ensemble measurements. Scanning tunneling microscopy resolves surface structure and defects with molecular detail and has been used to quantify changes in SAM structure, including nanometer-scale increases in domain size[93,94] and changes in lattice structure[95,96] due to thermal annealing, as well as nanometer-scale phase segregation in multicomponent SAMs.[42,97]

Force: Atomic Force Microscopy

Atomic force microscopy (AFM),[98] and its various modalities (Figure 1.3), measures the forces between a sharp cantilever and a surface and can be used to measure the topography of adsorbed single molecules. Typical lateral resolution is 1−10 nm (depending on the radius of curvature of the cantilever tip), with vertical resolution better than 1 nm. However, careful instrumental design (often including ultrahigh vacuum and cryogenic temperatures) and noncontact imaging based on frequency shifts can provide subnanometer lateral resolution. As in the case of scanning tunneling microscopy, atomic force microscopy relies on a feedback mechanism to maintain a constant scanning parameter as the tip moves over the surface. The particular parameter that is held constant varies depending on the precise AFM modality employed and can include the amplitude, phase, or oscillation frequency of the scanning probe, or more specialized combinations of these. Typically, the motion of the scanning probe normal to the surface is monitored using a photodiode to sense the position of a laser beam reflected off the cantilever, the position of which depends on the tip–surface forces under investigation. In this way, nanoscale forces are amplified and transduced by the known, linear response of the cantilever material. Cantilevers and probes of a wide variety of materials are used that have desirable physical and chemical properties, depending on the targeted system and may include stiff/flexible cantilevers and cantilevers with specialized coatings.[99]

Force-based methods are also useful for understanding force-induced conformational changes in single molecules. Such measurements typically involve a molecule tethered to a surface and to a probe (such as the tip of an atomic force microscope, magnetic bead, or nanoparticle suitable for optical trapping). Forces on the order of 0.1−1000 pN are applied to the probe, resulting in measured displacements on the order of nanometers, usually corresponding to protein unfolding or motion of a molecular motor.[100]

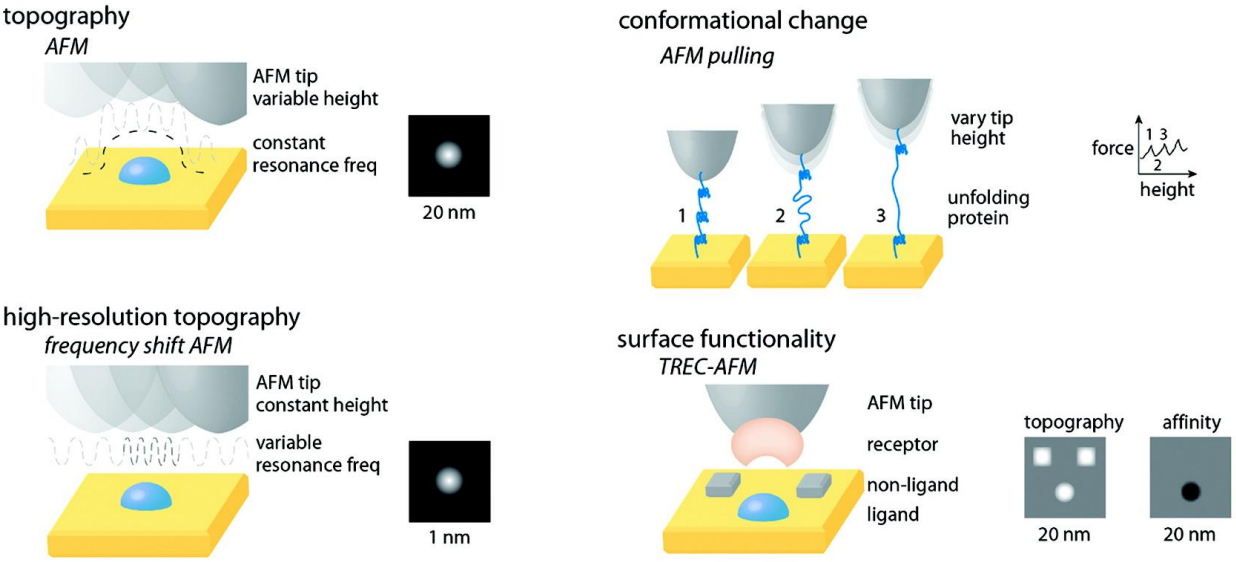

Figure 1.3: Force-based measurements of single molecules. In atomic force microscopy (AFM), a scanning probe can be used to image surface topography, motion of single molecules, and surface functionality. Figure adapted from Reference 21.

Atomic force microscopy is often used to measure the topography of surfaces. In standard AFM measurements, a cantilever ending in a pointed tip with a radius of curvature on the order of 10 nm is rastered across a surface. In contact mode, the cantilever touches the surface, while in noncontact mode, the tip is vibrated near the surface, and changes in the resonance amplitude are used to detect the proximity of the surface. The relatively blunt tip restricts the applications of

standard-usage AFMs in single-molecule imaging: although vertical resolutions on the order of 0.1 nm are common, lateral resolutions are generally on the order of a few nanometers.

However, much higher resolution can be achieved by performing measurements in noncontact mode and quantifying frequency shifts in the resonance damping signal of the oscillating cantilever due to repulsive or attractive forces between the tip and the surface. This property has been exploited in a number of contexts.

For instance, Sugimoto and Custance were able to identify individual surface atoms of Sn, Pb, and Si in a thin layer of alloy with a complex structure.[101] Spectroscopic information can also be derived: Wiesendanger and co-workers have measured molecular vibrations in single metallofullerenes inside carbon nanotubes,[102] similar to the inelastic tunneling spectroscopic measurements performed with an STM.

Combining frequency shift detection with tip modification techniques enables even higher resolution. Using a tip modified with a CO molecule, Gross and co-workers have resolved the placement of each atom in a single planar aromatic pentacene molecule on a surface (Figure 1.4) in ultrahigh vacuum at 5 K.[103]

Other tip modification and nonstandard data acquisition strategies have been used at room temperature in solution to map biomolecular recognition at the single-molecule level. Tip modification has been used to measure recognition events including DNA hybridization, antibody−antigen, ligand−receptor, and lectin−carbohydrate interactions.[104,105] Dynamic recognition imaging creates simultaneous topography and recognition images based on the minima and maxima of an oscillating low-Q (~1) cantilever functionalized with ligands.[106] Interactions

between ligands on the cantilever and receptors on the surface restrict the maximum deflection, creating an apparent depression at the recognition site.

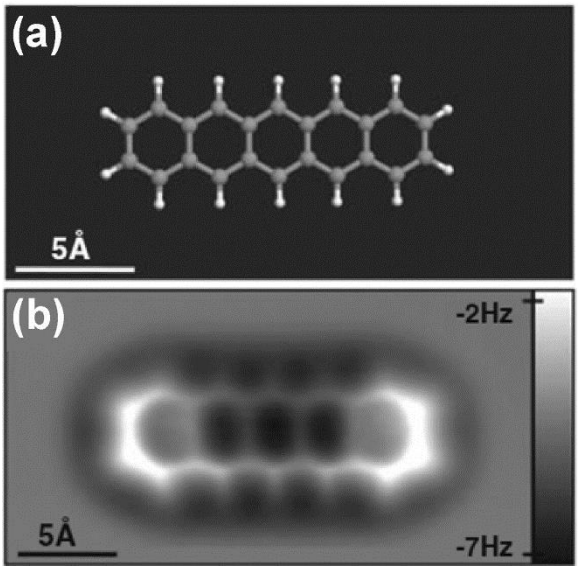

Figure 1.4: (a) Ball-and-stick model of pentacene molecule. (b) Frequency-shift AFM measurement of pentacene on Cu{111} with a single CO molecule adsorbed to the tip. Adapted with permission from Reference 103.

Measurements of conformational changes in biomolecules typically require that the molecule be tethered to two different objects, at least one of which can be moved controllably. Examples of mobile probes include AFM tips, microscopic beads that can be engaged in optical traps, and microscopic magnetic beads that can be controlled by external magnetic fields. Such mechanical measurements provide important insights for a variety of biomolecular machines and structural proteins, which must either pull or resist pulling. Early demonstrations included AFM-based measurements of forces required to unfold subunits of titin muscular proteins (unfolding begins at 20−30 pN and finishes at 150−300 pN for each subunit)[107] and cytoskeletal spectrin proteins (completing at ~25−35 pN).[108]

A number of factors are critical in measuring such forces correctly.[104] The chemistry (nonspecific vs thiol or other covalent attachment) used to tether the biomolecule to the probe and the surface can be key to ensuring reproducible measurements. Nonspecific adsorption is more straightforward in terms of sample preparation but may require screening of measured force curves to reject curves with unsuitable binding. The rate at which the pulling force is varied also impacts measurements; for example, in the titin measurements above, measured unfolding forces varied from 130 pN at 0.01 μm s^{-1} to 190 pN at 1 μm s^{-1}.[107]

1.4 Organization

This dissertation is organized into five main chapters describing research elucidating the roles of intermolecular interactions on the assembly and structures of materials at the nanoscale. To this end, Chapter 1 serves as an introduction to nanoscale assembly as well as some of the tools and techniques used to probe structures at the atomic and molecular level. Chapters 2–4 present the results of experiments utilizing these techniques to understand related aspects of SAM adsorbate interactions with their environment. Chapter 2 studies the role of intermolecular dipole-dipole interactions of carboranethiol adsorbates on the alignment of subsequent molecular adsorbates (liquid crystals). Chapter 3 outlines the development of a new STM measurement modality to measure nuclear spins within adsorbates in an effort determine submolecular structure, as well as progress towards optimized sample preparation. Chapter 4 describes a series of experiments studying optimized surface patterning via microcontact and microdisplacement printing, which is used in the sample preparation discussed in Chapter 3. Chapter 5 summarizes some of the important results of these experiments and briefly discusses future prospects for this work. Finally, we include an appendix containing some of the code used in the numerical modeling and automated data processing used in Chapter 4.

1.5 References

(1) Franceschetti, A.; Zunger, A. The Inverse Band-Structure Problem of Finding an Atomic Configuration with given Electronic Properties. *Nature* **1999**, *402*, 60–63.

(2) Castro Neto, A. H.; Guinea, F.; Peres, N. M. R.; Novoselov, K. S.; Geim, A. K. The Electronic Properties of Graphene. *Rev. Mod. Phys.* **2009**, *81*, 109–162.

(3) Yang, P. Surface Chemistry: Crystal Cuts on the Nanoscale. *Nature* **2012**, *482*, 41–42.

(4) Zhang, B.; Wang, D.; Hou, Y.; Yang, S.; Yang, X. H.; Zhong, J. H.; Liu, J.; Wang, H. F.; Hu, P.; Zhao, H. J.; Yang, H. G. Facet-Dependent Catalytic Activity of Platinum Nanocrystals for Triiodide Reduction in Dye-Sensitized Solar Cells. *Sci. Rep.* **2013**, *3*.

(5) National Research Council (US) Committee on Research Opportunities in Biology. Molecular Structure and Function. In *Opportunities in Biology*; National Academies Press: Washington, D.C., 1989; pp. 33–76.

(6) Groll, M.; Ditzel, L.; Löwe, J.; Stock, D.; Bochtler, M.; Bartunik, H. D.; Huber, R. Structure of 20S Proteasome from Yeast at 2.4 Å Resolution. *Nature* **1997**, *386*, 463–471.

(7) Nissen, P.; Hansen, J.; Ban, N.; Moore, P. B.; Steitz, T. A. The Structural Basis of Ribosome Activity in Peptide Bond Synthesis. *Science* **2000**, *289*, 920–930.

(8) Alberts, B.; Johnson, A.; Lewis, J.; Raff, M.; Roberts, K.; Walter, P. Analyzing Protein Structure and Function. In *Molecular Biology of the Cell*; Garland Science: New York, 2002.

(9) Ferreira, K. N.; Iverson, T. M.; Maghlaoui, K.; Barber, J.; Iwata, S. Architecture of the Photosynthetic Oxygen-Evolving Center. *Science* **2004**, *303*, 1831–1838.

(10) Castell, M. R.; Muller, D. A.; Voyles, P. M. Dopant Mapping for the Nanotechnology Age. *Nat. Mater.* **2003**, *2*, 129–131.

(11) Hoelder, S.; Clarke, P. A.; Workman, P. Discovery of Small Molecule Cancer Drugs: Successes, Challenges and Opportunities. *Mol. Oncol.* **2012**, *6*, 155–176.

(12) Lounnas, V.; Ritschel, T.; Kelder, J.; McGuire, R.; Bywater, R. P.; Foloppe, N. Current Progress in Structure-Based Rational Drug Design Marks a New Mindset in Drug Discovery. *Comput. Struct. Biotechnol. J.* **2013**, *5*, 1–14.

(13) Bassett, L. C.; Heremans, F. J.; Christle, D. J.; Yale, C. G.; Burkard, G.; Buckley, B. B.; Awschalom, D. D. Ultrafast Optical Control of Orbital and Spin Dynamics in a Solid-State Defect. *Science* **2014**, *345*, 1333–1337.

(14) Anasori, B.; Xie, Y.; Beidaghi, M.; Lu, J.; Hosler, B. C.; Hultman, L.; Kent, P. R. C.; Gogotsi, Y.; Barsoum, M. W. Two-Dimensional, Ordered, Double Transition Metals Carbides (MXenes). *ACS Nano* **2015**, *9*, 9507–9516.

(15) Hong, J.; Hu, Z.; Probert, M.; Li, K.; Lv, D.; Yang, X.; Gu, L.; Mao, N.; Feng, Q.; Xie, L.; Zhang, J.; Wu, D.; Zhang, Z.; Jin, C.; Ji, W.; Zhang, X.; Yuan, J.; Zhang, Z. Exploring Atomic Defects in Molybdenum Disulphide Monolayers. *Nat. Commun.* **2015**, *6*, 6293.

(16) Love, J. C.; Estroff, L. A.; Kriebel, J. K.; Nuzzo, R. G.; Whitesides, G. M. Self-Assembled Monolayers of Thiolates on Metals as a Form of Nanotechnology. *Chem. Rev.* **2005**, *105*, 1103–1170.

(17) Zharnikov, M.; Frey, S.; Rong, H.; Yang, Y.-J.; Heister, K.; Buck, M.; Grunze, M. The Effect of Sulfur–Metal Bonding on the Structure of Self-Assembled Monolayers. *Phys. Chem. Chem. Phys.* **2000**, *2*, 3359–3362.

(18) Bumm, L. A.; Arnold, J. J.; Cygan, M. T.; Dunbar, T. D.; Burgin, T. P.; Jones, L.; Allara, D. L.; Tour, J. M.; Weiss, P. S. Are Single Molecular Wires Conducting? *Science* **1996**, *271*, 1705–1707.

(19) Li, W.; Müller, M. Defects in the Self-Assembly of Block Copolymers and Their Relevance for Directed Self-Assembly. *Annu. Rev. Chem. Biomol. Eng.* **2015**, *6*, 187–216.

(20) Poirier, G. E.; Tarlov, M. J. The c(4×2) Superlattice of *n*-Alkanethiol Monolayers Self-Assembled on Au(111). *Langmuir* **1994**, *10*, 2853–2856.

(21) Claridge, S. A.; Schwartz, J. J.; Weiss, P. S. Electrons, Photons, and Force: Quantitative Single-Molecule Measurements from Physics to Biology. *ACS Nano* **2011**, *5*, 693–729.

(22) Poirier, G. E. Characterization of Organosulfur Molecular Monolayers on Au(111) Using Scanning Tunneling Microscopy. *Chem. Rev.* **1997**, *97*, 1117–1128.

(23) Lio, A.; Charych, D. H.; Salmeron, M. Comparative Atomic Force Microscopy Study of the Chain Length Dependence of Frictional Properties of Alkanethiols on Gold and Alkylsilanes on Mica. *J. Phys. Chem. B* **1997**, *101*, 3800–3805.

(24) Murphy, K. L.; Tysoe, W. T.; Bennett, D. W. A Comparative Investigation of Aryl Isocyanides Chemisorbed to Palladium and Gold: An ATR-IR Spectroscopic Study. *Langmuir* **2004**, *20*, 1732–1738.

(25) Gouzman, I.; Dubey, M.; Carolus, M. D.; Schwartz, J.; Bernasek, S. L. Monolayer vs. Multilayer Self-Assembled Alkylphosphonate Films: X-Ray Photoelectron Spectroscopy Studies. *Surf. Sci.* **2006**, *600*, 773–781.

(26) Taylor, C. E.; Schwartz, D. K. Octadecanoic Acid Self-Assembled Monolayer Growth at Sapphire Surfaces. *Langmuir* **2003**, *19*, 2665–2672.

(27) Monnell, J. D.; Stapleton, J. J.; Jackiw, J. J.; Dunbar, T.; Reinerth, W. A.; Dirk, S. M.; Tour, J. M.; Allara, D. L.; Weiss, P. S. Ordered Local Domain Structures of Decaneselenolate and Dodecaneselenolate Monolayers on Au{111}. *J. Phys. Chem. B* **2004**, *108*, 9834–9841.

(28) Mekhalif, Z.; Riga, J.; Pireaux, J.-J.; Delhalle, J. Self-Assembled Monolayers of N-Dodecanethiol on Electrochemically Modified Polycrystalline Nickel Surfaces. *Langmuir* **1997**, *13*, 2285–2290.

(29) Lee, J. P.; Kim, H. K.; Park, C. R.; Park, G.; Kwak, H. T.; Koo, S. M.; Sung, M. M. Photocatalytic Decomposition of Alkylsiloxane Self-Assembled Monolayers on Titanium Oxide Surfaces. *J. Phys. Chem. B* **2003**, *107*, 8997–9002.

(30) Chitre, K.; Yang, Q.; Salami, T. O.; Oliver, S. R.; Cho, J. Microstructure and Mechanical Properties of Ceramic/self-Assembled Monolayer Bilayer Coatings. *J. Electron. Mater.* **2005**, *34*, 528–533.

(31) Kühnle, A. Self-Assembly of Organic Molecules at Metal Surfaces. *Curr. Opin. Colloid Interface Sci.* **2009**, *14*, 157–168.

(32) Caprioli, F.; Decker, F.; Marrani, A. G.; Beccari, M.; Castro, V. D. Copper Protection by Self-Assembled Monolayers of Aromatic Thiols in Alkaline Solutions. *Phys. Chem. Chem. Phys.* **2010**, *12*, 9230–9238.

(33) Gooding, J. J.; Ciampi, S. The Molecular Level Modification of Surfaces: From Self-Assembled Monolayers to Complex Molecular Assemblies. *Chem. Soc. Rev.* **2011**, *40*, 2704–2718.

(34) Tao, Y.-T.; Wu, C.-C.; Eu, J.-Y.; Lin, W.-L.; Wu, K.-C.; Chen, C. Structure Evolution of Aromatic-Derivatized Thiol Monolayers on Evaporated Gold. *Langmuir* **1997**, *13*, 4018–4023.

(35) Yang, Y.; Wang, C. Hierarchical Construction of Self-Assembled Low-Dimensional Molecular Architectures Observed by Using Scanning Tunneling Microscopy. *Chem. Soc. Rev.* **2009**, *38*, 2576–2589.

(36) Rosei, F.; Schunack, M.; Naitoh, Y.; Jiang, P.; Gourdon, A.; Laegsgaard, E.; Stensgaard, I.; Joachim, C.; Besenbacher, F. Properties of Large Organic Molecules on Metal Surfaces. *Prog. Surf. Sci.* **2003**, *71*, 95–146.

(37) van der Lit, J.; Marsman, J. L.; Koster, R. S.; Jacobse, P. H.; den Hartog, S. A.; Vanmaekelbergh, D.; Klein Gebbink, R. J. M.; Filion, L.; Swart, I. Modeling the Self-Assembly of Organic Molecules in 2D Molecular Layers with Different Structures. *J. Phys. Chem. C* **2016**, *120*, 318–323.

(38) Folkers, J. P.; Laibinis, P. E.; Whitesides, G. M.; Deutch, J. Phase Behavior of Two-Component Self-Assembled Monolayers of Alkanethiolates on Gold. *J. Phys. Chem.* **1994**, *98*, 563–571.

(39) Stranick, S. J.; Parikh, A. N.; Tao, Y.-T.; Allara, D. L.; Weiss, P. S. Phase Separation of Mixed-Composition Self-Assembled Monolayers into Nanometer Scale Molecular Domains. *J. Phys. Chem.* **1994**, *98*, 7636–7646.

(40) Smith, R. K.; Reed, S. M.; Lewis, P. A.; Monnell, J. D.; Clegg, R. S.; Kelly, K. F.; Bumm, L. A.; Hutchison, J. E.; Weiss, P. S. Phase Separation within a Binary Self-Assembled Monolayer on Au{111} Driven by an Amide-Containing Alkanethiol. *J. Phys. Chem. B* **2001**, *105*, 1119–1122.

(41) Farrell, R. A.; Fitzgerald, T. G.; Borah, D.; Holmes, J. D.; Morris, M. A. Chemical Interactions and Their Role in the Microphase Separation of Block Copolymer Thin Films. *Int. J. Mol. Sci.* **2009**, *10*, 3671–3712.

(42) Lewis, P. A.; Smith, R. K.; Kelly, K. F.; Bumm, L. A.; Reed, S. M.; Clegg, R. S.; Gunderson, J. D.; Hutchison, J. E.; Weiss, P. S. The Role of Buried Hydrogen Bonds in Self-Assembled Mixed Composition Thiols on Au{111}. *J. Phys. Chem. B* **2001**, *105*, 10630–10636.

(43) Gutzler, R.; Lappe, S.; Mahata, K.; Schmittel, M.; Heckl, W. M.; Lackinger, M. Aromatic Interaction vs. Hydrogen Bonding in Self-Assembly at the Liquid–Solid Interface. *Chem. Commun.* **2009**, 680–682.

(44) Liang, H.; Sun, W.; Jin, X.; Li, H.; Li, J.; Hu, X.; Teo, B. K.; Wu, K. Two-Dimensional Molecular Porous Networks Formed by Trimesic Acid and 4,4′-Bis(4-Pyridyl)biphenyl on Au(111) through Hierarchical Hydrogen Bonds: Structural Systematics and Control of Nanopore Size and Shape. *Angew. Chem. Int. Ed.* **2011**, *50*, 7562–7566.

(45) Sushko, M. L.; Shluger, A. L. Dipole−Dipole Interactions and the Structure of Self-Assembled Monolayers. *J. Phys. Chem. B* **2007**, *111*, 4019–4025.

(46) Hohman, J. N.; Zhang, P.; Morin, E. I.; Han, P.; Kim, M.; Kurland, A. R.; McClanahan, P. D.; Balema, V. P.; Weiss, P. S. Self-Assembly of Carboranethiol Isomers on Au{111}: Intermolecular Interactions Determined by Molecular Dipole Orientations. *ACS Nano* **2009**, *3*, 527–536.

(47) Thomas, J. C.; Schwartz, J. J.; Hohman, J. N.; Claridge, S. A.; Auluck, H. S.; Serino, A. C.; Spokoyny, A. M.; Tran, G.; Kelly, K. F.; Mirkin, C. A.; Gilles, J.; Osher, S. J.; Weiss, P. S. Defect-Tolerant Aligned Dipoles within Two-Dimensional Plastic Lattices. *ACS Nano* **2015**, *9*, 4734–4742.

(48) Zenasni, O.; Marquez, M. D.; Jamison, A. C.; Lee, H. J.; Czader, A.; Lee, T. R. Inverted Surface Dipoles in Fluorinated Self-Assembled Monolayers. *Chem. Mater.* **2015**, *27*, 7433–7446.

(49) Paniagua, S. A.; Hotchkiss, P. J.; Jones, S. C.; Marder, S. R.; Mudalige, A.; Marrikar, F. S.; Pemberton, J. E.; Armstrong, N. R. Phosphonic Acid Modification of Indium−Tin Oxide Electrodes: Combined XPS/UPS/Contact Angle Studies. *J. Phys. Chem. C* **2008**, *112*, 7809–7817.

(50) Bishop, K. J. M.; Wilmer, C. E.; Soh, S.; Grzybowski, B. A. Nanoscale Forces and Their Uses in Self-Assembly. *Small* **2009**, *5*, 1600–1630.

(51) Kim, J.; Rim, Y. S.; Liu, Y.; Serino, A. C.; Thomas, J. C.; Chen, H.; Yang, Y.; Weiss, P. S. Interface Control in Organic Electronics Using Mixed Monolayers of Carboranethiol Isomers. *Nano Lett.* **2014**, *14*, 2946–2951.

(52) Kulkarni, C.; Bejagam, K. K.; Senanayak, S. P.; Narayan, K. S.; Balasubramanian, S.; George, S. J. Dipole-Moment-Driven Cooperative Supramolecular Polymerization. *J. Am. Chem. Soc.* **2015**, *137*, 3924–3932.

(53) Mullen, T. J.; Srinivasan, C.; Hohman, J. N.; Gillmor, S. D.; Shuster, M. J.; Horn, M. W.; Andrews, A. M.; Weiss, P. S. Microcontact Insertion Printing. *Appl. Phys. Lett.* **2007**, *90*, 063114.

(54) Lewis, P. A.; Donhauser, Z. J.; Mantooth, B. A.; Smith, R. K.; Bumm, L. A.; Kelly, K. F.; Weiss, P. S. Control and Placement of Molecules via Self-Assembly. *Nanotechnology* **2001**, *12*, 231–237.

(55) Gimzewski, J. K.; Joachim, C. Nanoscale Science of Single Molecules Using Local Probes. *Science* **1999**, *283*, 1683–1688.

(56) Greenleaf, W. J.; Woodside, M. T.; Block, S. M. High-Resolution, Single-Molecule Measurements of Biomolecular Motion. *Annu. Rev. Anal. Chem.* **2007**, *36*, 171–190.

(57) Bustamante, C.; Bryant, Z.; Smith, S. B. Ten Years of Tension: Single-Molecule DNA Mechanics. *Nature* **2003**, *421*, 423–427.

(58) Eckert, M. Max von Laue and the Discovery of X-Ray Diffraction in 1912. *Ann. Phys.* **2012**, *524*, A83–A85.

(59) Thomson, G. P. Experiments on the Diffraction of Cathode Rays. *Proc. R. Soc. London, Ser. A* **1928**, *117*, 600–609.

(60) Davisson, C.; Germer, L. H. Diffraction of Electrons by a Crystal of Nickel. *Phys. Rev.* **1927**, *30*, 705–740.

(61) Zinn, W. H. Diffraction of Neutrons by a Single Crystal. *Phys. Rev.* **1947**, *71*, 752–757.

(62) Jaklevic, R. C.; Lambe, J. Molecular Vibration Spectra by Electron Tunneling. *Phys. Rev. Lett.* **1966**, *17*, 1139–1140.

(63) Lambe, J.; Jaklevic, R. C. Molecular Vibration Spectra by Inelastic Electron Tunneling. *Phys. Rev.* **1968**, *165*, 821–832.

(64) Smith, D. J. The Realization of Atomic Resolution with the Electron Microscope. *Rep. Prog. Phys.* **1997**, *60*, 1513.

(65) Donhauser, Z. J.; Mantooth, B. A.; Kelly, K. F.; Bumm, L. A.; Monnell, J. D.; Stapleton, J. J.; Price, D. W.; Rawlett, A. M.; Allara, D. L.; Tour, J. M.; Weiss, P. S. Conductance Switching in Single Molecules through Conformational Changes. *Science* **2001**, *292*, 2303–2307.

(66) Binnig, G.; Rohrer, H.; Gerber, C.; Weibel, E. Surface Studies by Scanning Tunneling Microscopy. *Phys. Rev. Lett.* **1982**, *49*, 57–61.

(67) Binnig, G.; Rohrer, H. Scanning Tunneling Microscopy. *Surf. Sci.* **1983**, *126*, 236–244.

(68) Knoll, M.; Ruska, E. Das Elektronenmikroskop. *Z. Physik* **1932**, *78*, 318–339.

(69) Ruska, E. The Development of the Electron Microscope and of Electron Microscopy. *Rev. Mod. Phys.* **1987**, *59*, 627–638.

(70) Howe, J. M.; Mori, H.; Wang, Z. L. *In Situ* High-Resolution Transmission Electron Microscopy in the Study of Nanomaterials and Properties. *MRS Bull.* **2008**, *33*, 115–121.

(71) Smith, B. W.; Luzzi, D. E.; Achiba, Y. Tumbling Atoms and Evidence for Charge Transfer in $La_2@C_{80}$@SWNT. *Chem. Phys. Lett.* **2000**, *331*, 137–142.

(72) Williamson, M. J.; Tromp, R. M.; Vereecken, P. M.; Hull, R.; Ross, F. M. Dynamic Microscopy of Nanoscale Cluster Growth at the Solid–Liquid Interface. *Nat. Mater.* **2003**, *2*, 532–536.

(73) Zheng, H.; Claridge, S. A.; Minor, A. M.; Alivisatos, A. P.; Dahmen, U. Nanocrystal Diffusion in a Liquid Thin Film Observed by *in Situ* Transmission Electron Microscopy. *Nano Lett.* **2009**, *9*, 2460–2465.

(74) Zheng, H.; Smith, R. K.; Jun, Y.; Kisielowski, C.; Dahmen, U.; Alivisatos, A. P. Observation of Single Colloidal Platinum Nanocrystal Growth Trajectories. *Science* **2009**, *324*, 1309–1312.

(75) Weiss, P. S.; Eigler, D. M. Site Dependence of the Apparent Shape of a Molecule in Scanning Tunneling Micoscope Images: Benzene on Pt{111}. *Phys. Rev. Lett.* **1993**, *71*, 3139–3142.

(76) Hansma, P. K.; Tersoff, J. Scanning Tunneling Microscopy. *J. Appl. Phys.* **1987**, *61*, R1–R24.

(77) Urban, K. W. Studying Atomic Structures by Aberration-Corrected Transmission Electron Microscopy. *Science* **2008**, *321*, 506–510.

(78) Eigler, D. M.; Weiss, P. S.; Schweizer, E. K.; Lang, N. D. Imaging Xe with a Low-Temperature Scanning Tunneling Microscope. *Phys. Rev. Lett.* **1991**, *66*, 1189–1192.

(79) Moore, A. M.; Weiss, P. S. Functional and Spectroscopic Measurements with Scanning Tunneling Microscopy. *Annu. Rev. Anal. Chem.* **2008**, *1*, 857–882.

(80) Ertl, G. Reactions at Well-Defined Surfaces. *Surf. Sci.* **1994**, *299–300*, 742–754.

(81) Somorjai, G. A. Modern Surface Science and Surface Technologies: An Introduction. *Chem. Rev.* **1996**, *96*, 1223–1236.

(82) McKie, D.; McKie, C. *Essentials of Crystallography*; Blackwell Scientific Publications: Oxford, 1986.

(83) Wong, K.; Kwon, K.-Y.; Rao, B. V.; Liu, A.; Bartels, L. Effect of Halo Substitution on the Geometry of Arenethiol Films on Cu(111). *J. Am. Chem. Soc.* **2004**, *126*, 7762–7763.

(84) Schreiber, F. Structure and Growth of Self-Assembling Monolayers. *Prog. Surf. Sci.* **2000**, *65*, 151–257.

(85) Chidsey, C. E. D.; Loiacono, D. N. Chemical Functionality in Self-Assembled Monolayers: Structural and Electrochemical Properties. *Langmuir* **1990**, *6*, 682–691.

(86) De Feyter, S.; De Schryver, F. C. Two-Dimensional Supramolecular Self-Assembly Probed by Scanning Tunneling Microscopy. *Chem. Soc. Rev.* **2003**, *32*, 139–150.

(87) Weigelt, S.; Busse, C.; Petersen, L.; Rauls, E.; Hammer, B.; Gothelf, K. V.; Besenbacher, F.; Linderoth, T. R. Chiral Switching by Spontaneous Conformational Change in Adsorbed Organic Molecules. *Nat. Mater.* **2006**, *5*, 112–117.

(88) Shevchenko, E. V.; Talapin, D. V.; Murray, C. B.; O'Brien, S. Structural Characterization of Self-Assembled Multifunctional Binary Nanoparticle Superlattices. *J. Am. Chem. Soc.* **2006**, *128*, 3620–3637.

(89) Smith, B. W.; Monthioux, M.; Luzzi, D. E. Carbon Nanotube Encapsulated Fullerenes: A Unique Class of Hybrid Materials. *Chem. Phys. Lett.* **1999**, *315*, 31–36.

(90) Yu, X.; Jin, L.; Zhou, Z. H. 3.88 Å Structure of Cytoplasmic Polyhedrosis Virus by Cryo-Electron Microscopy. *Nature* **2008**, *453*, 415–419.

(91) Zhang, X.; Jin, L.; Fang, Q.; Hui, W. H.; Zhou, Z. H. 3.3 Å Cryo-EM Structure of a Nonenveloped Virus Reveals a Priming Mechanism for Cell Entry. *Cell* **2010**, *141*, 472–482.

(92) Huang, C. S.; Sadre-Bazzaz, K.; Shen, Y.; Deng, B.; Zhou, Z. H.; Tong, L. Crystal Structure of the $\alpha_6\beta_6$ Holoenzyme of Propionyl-Coenzyme A Carboxylase. *Nature* **2010**, *466*, 1001–1005.

(93) Poirier, G. E.; Tarlov, M. J. Molecular Ordering and Gold Migration Observed in Butanethiol Self-Assembled Monolayers Using Scanning Tunneling Microscopy. *J. Phys. Chem.* **1995**, *99*, 10966–10970.

(94) Xiao, X.; Wang, B.; Zhang, C.; Yang, Z.; Loy, M. M. T. Thermal Annealing Effect of Alkanethiol Monolayers on Au(111) in Air. *Surf. Sci.* **2001**, *472*, 41–50.

(95) Li, X.; Xu, B.; Xiao, X.; Yang, X.; Zang, L.; Tao, N. Controlling Charge Transport in Single Molecules Using Electrochemical Gate. *Faraday Discuss.* **2006**, *131*, 111–120.

(96) Cyganik, P.; Buck, M.; Strunskus, T.; Shaporenko, A.; Witte, G.; Zharnikov, M.; Wöll, C. Influence of Molecular Structure on Phase Transitions: A Study of Self-Assembled Monolayers of 2-(Aryl)-Ethane Thiols. *J. Phys. Chem. C* **2007**, *111*, 16909–16919.

(97) Lüssem, B.; Müller-Meskamp, L.; Karthäuser, S.; Waser, R.; Homberger, M.; Simon, U. STM Study of Mixed Alkanethiol/Biphenylthiol Self-Assembled Monolayers on Au(111). *Langmuir* **2006**, *22*, 3021–3027.

(98) Binnig, G.; Quate, C. F.; Gerber, C. Atomic Force Microscope. *Phys. Rev. Lett.* **1986**, *56*, 930–933.

(99) Carpick, R. W.; Salmeron, M. Scratching the Surface: Fundamental Investigations of Tribology with Atomic Force Microscopy. *Chem. Rev.* **1997**, *97*, 1163–1194.

(100) Neuman, K. C.; Nagy, A. Single-Molecule Force Spectroscopy: Optical Tweezers, Magnetic Tweezers and Atomic Force Microscopy. *Nat. Methods* **2008**, *5*, 491–505.

(101) Sugimoto, Y.; Pou, P.; Abe, M.; Jelinek, P.; Pérez, R.; Morita, S.; Custance, Ó. Chemical Identification of Individual Surface Atoms by Atomic Force Microscopy. *Nature* **2007**, *446*, 64–67.

(102) Ashino, M.; Wiesendanger, R.; Khlobystov, A. N.; Berber, S.; Tománek, D. Revealing Subsurface Vibrational Modes by Atom-Resolved Damping Force Spectroscopy. *Phys. Rev. Lett.* **2009**, *102*, 195503.

(103) Gross, L.; Mohn, F.; Moll, N.; Liljeroth, P.; Meyer, G. The Chemical Structure of a Molecule Resolved by Atomic Force Microscopy. *Science* **2009**, *325*, 1110–1114.

(104) Hinterdorfer, P.; Dufrêne, Y. F. Detection and Localization of Single Molecular Recognition Events Using Atomic Force Microscopy. *Nat. Methods* **2006**, *3*, 347–355.

(105) Francius, G.; Lebeer, S.; Alsteens, D.; Wildling, L.; Gruber, H. J.; Hols, P.; Keersmaecker, S. D.; Vanderleyden, J.; Dufrêne, Y. F. Detection, Localization, and Conformational Analysis of Single Polysaccharide Molecules on Live Bacteria. *ACS Nano* **2008**, *2*, 1921–1929.

(106) Ebner, A.; Kienberger, F.; Kada, G.; Stroh, C. M.; Geretschläger, M.; Kamruzzahan, A. S. M.; Wildling, L.; Johnson, W. T.; Ashcroft, B.; Nelson, J.; Lindsay, S. M.; Gruber, H. J.; Hinterdorfer, P. Localization of Single Avidin–Biotin Interactions Using Simultaneous Topography and Molecular Recognition Imaging. *ChemPhysChem* **2005**, *6*, 897–900.

(107) Rief, M.; Gautel, M.; Oesterhelt, F.; Fernandez, J. M.; Gaub, H. E. Reversible Unfolding of Individual Titin Immunoglobulin Domains by AFM. *Science* **1997**, *276*, 1109–1112.

(108) Rief, M.; Pascual, J.; Saraste, M.; Gaub, H. E. Single Molecule Force Spectroscopy of Spectrin Repeats: Low Unfolding Forces in Helix bundles1. *J. Mol. Biol.* **1999**, *286*, 553–561.

CHAPTER 2

Surface Dipole Control of Liquid Crystal Alignment

2.1 Introduction

Self-assembly plays critical roles in the development of materials with customized chemical and physical properties from the bottom up, and provides insights into molecular-scale phenomena.[1–4] Non-covalent interactions, including dipolar and dispersion forces, mediate molecular assembly and influence the properties and functions of pure and composite materials.[5–9] Understanding and controlling the types and strengths of these interactions, particularly at interfaces, enables engineering precisely tailored structures at the nanoscale.[10–15] Self-assembled monolayers (SAMs) not only exemplify these structures, but also serve as a powerful and versatile means of tuning the interactions of a surface with its surroundings and other molecular adsorbates.[16–19] A great deal of work has been done using SAMs to control the adsorption, position, orientation, and nucleation of crystalline and molecular assemblies.[20–26] Despite recent progress, however, predictive understanding of complex, extended assemblies across textured surfaces remains challenging.[27,28]

Liquid crystals (LCs) assemble with long-range orientational order due to anisotropic intermolecular interactions with their surroundings and are particularly sensitive to surface textures and coatings.[29–31] Industrially, LC alignment is controlled by unidirectional rubbing[32,33] or other techniques that break the rotational symmetry of the alignment surfaces.[34–36] One such alternative utilizes the dune-like surface texture of obliquely deposited, semi-transparent gold films[37,38] to direct LC alignment.[34,37,39–42] In this case, mesogens adopt in-plane orientations with their long axes perpendicular to the oblique deposition direction, minimizing elastic strain within the LC assembly.

Abbott and others have shown that SAMs also influence the alignment of LCs,[43–48] with the ability to control both azimuthal and polar orientations, which have found use in sensors.[49] However, a convolution of steric effects, surface topography, and intermolecular forces complicate our understanding of the mechanisms responsible for alignment.[46,47,50–52] Molecular adsorbates, in the form of either well-organized SAMs or adventitious surface contamination, can alter LC arrangement by changing the preferred in-plane alignment axis or inducing homeotropic alignment, normal to the surface.[43,45,53] In the case of alignment layers treated with SAMs, different LC orientations have been observed using polar and non-polar adsorbate molecules.[44,38,51] Additionally, chiral and 'odd-even'[54] effects have been observed, showing that LC alignment is sensitive to variations in the symmetry[55–57] and orientation[46,47] of the exposed moieties of the terminal functionality of the SAM. Self-assembled adsorbates used in previous studies typically varied in two or more of these factors *simultaneously* (e.g., comparing structural analogs with different exposed moieties: $–CH_3$, –OH, and –COOH). As such, the independent effects of molecular geometry, orientation, and dipole moment on LC alignment are difficult to determine.

We used positional isomers of carboranethiol and -dithiol molecules[58] to deconvolve the effects of SAM dipole magnitude and orientation on the alignment of LCs. The isomers chemisorb onto gold surfaces through the formation of Au–S bonds, thereby assembling into monolayers with exposed carborane moieties. Each isomer possesses an identical molecular geometry and assembles 'upright' with negligible tilt and a characteristic lattice spacing (7.2 and 7.6 Å for monothiol and dithiol species, respectively).[14,59–64] The primary attribute that distinguishes SAMs of each isomer is their different constituent dipole moments. Intermolecular forces between carboranethiol monolayers and mesogens resulted in uniaxial planar alignment of LCs along one of two distinct directions relative to the underlying, anisotropic, substrate: parallel or perpendicular to the oblique gold deposition direction ($\overrightarrow{\text{Au}}$). The effects of these short-range, nanoscale forces[14,65] were transduced and amplified by the LCs to a macroscopic scale, enabling optical readout via transmitted light. Azimuthal anchoring energies of LCs on carboranethiol and -dithiol monolayers were measured to quantify SAM-LC coupling. This work targets and elucidates the roles of surface dipoles, in the form of adsorbed molecular dipoles, on the alignment and orientation of subsequent adsorbates (LCs), which has applications in sensing, catalysis, photovoltaics, and templated growth of nanostructures.[66–69] Self-assembled carboranethiols are well-suited to this purpose as they enable direct comparison of the effects of different isomers' molecular dipoles, while holding constant other factors influencing LC alignment that have confounded previous studies.

2.2 Results and Discussion

Figure 2.1 illustrates the molecules used in these studies. Caboranethiol isomers *m*-9-carboranethiol (M9), *m*-1-carboranethiol (M1), *o*-9-carboranethiol (O9), *o*-1-carboranethiol (O1), and -dithiol isomers *o*-9,12-carboranedithiol (9O12) and *o*-1,2-carboranedithiol (1O2) possess dipole moments with various strengths and orientations.[70] The dipole moments of these

six carboranethiols were calculated using density functional theory.[14,60,71,72] Although the molecular dipoles will be altered upon chemisorption to a gold surface,[73] we use these values to make qualitative comparisons of their relative strengths, orientations, and the degree to which they modify the surface energy of a substrate through their dipolar fields.[60,72] We use two LCs, 4-cyano-4′-pentylbiphenyl (5CB) and *N*-(4-methoxybenzylidene)-4-butylaniline (MBBA), possessing oppositely signed dielectric anisotropies (Δε), to probe these fields. Mesogens with positive Δε (5CB) align parallel to an applied electric field, whereas the long axes of mesogens with negative Δε (MBBA) align perpendicular to an applied field. Comparison of the alignment of 5CB and MBBA on carboranethiol monolayers enables us to infer the role of the dipolar field on LC alignment.[43]

To monitor SAM-regulated mesogen alignment, LC cells were constructed as shown in Figure 2.2A. The outgoing polarization of light transmitted through a cell depends on the angle between the polarization of the incoming light and the orientation of the nematic director, which represents the average alignment direction of mesogens in a LC. If the mesogens align homeotropically, this angle is independent of cell rotations about axes normal to the alignment layers and the cells appear 'dark' (0% transmittance) when viewed between crossed polarizers. Variations in the intensity of transmitted light with rotations of the cell, however, indicate planar alignment of the nematic director. Figure 2.3 shows the modulation in the intensity of the light transmitted through 5CB cells as they were rotated between crossed polarizers (Figure 2.2B); corresponding MBBA data are provided in the Section 2.5.2. Alignment layers treated with M9, M1, O9, O1, 9O12, and 1O2 SAMs all induced uniaxial planar alignment in both 5CB and MBBA cells, as indicated by the four-fold symmetry of their transmittance spectra. Cells constructed without a twist in their nematic directors vary from nearly extinguishing all transmitted light to

transmitting ~50%. By contrast, cells that possess a 90° twist in their directors have transmittances varying from ~50% to nearly 100%, due to the rotation of the transmitted light's polarization as it traverses the cell.[74]

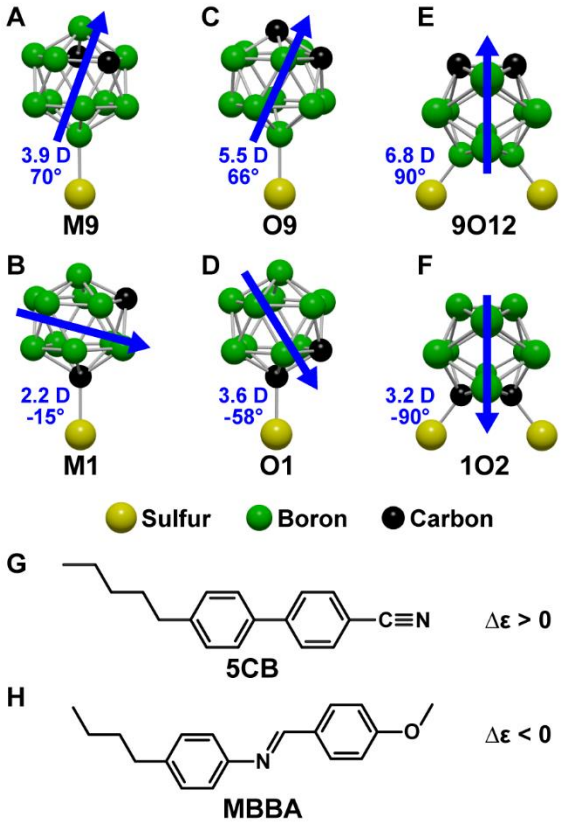

Figure 2.1: Molecular structures of carboranethiol and -dithiol isomers: (A) *m*-9-carboranethiol (M9), (B) *m*-1-carboranethiol (M1), (C) *o*-9-carboranethiol (O9), (D) *o*-1-carboranethiol (O1), (E) *o*-9,12-carboranedithiol (9O12), and (F) *o*-1,2-carboranedithiol (1O2). Dipole moment magnitudes and orientations, calculated for isolated molecules, are indicated in blue. Positive (negative) angles estimate dipole orientations above (below) the plane of the substrate when assembled onto gold surfaces. Mesogen molecular structures of (G) 4-cyano-4′-pentylbiphenyl (5CB) and (H) *N*-(4-methoxybenzylidene)-4-butylaniline (MBBA) with corresponding dielectric anisotropy (Δε) signs noted. Hydrogen atoms are omitted from all structures for clarity.

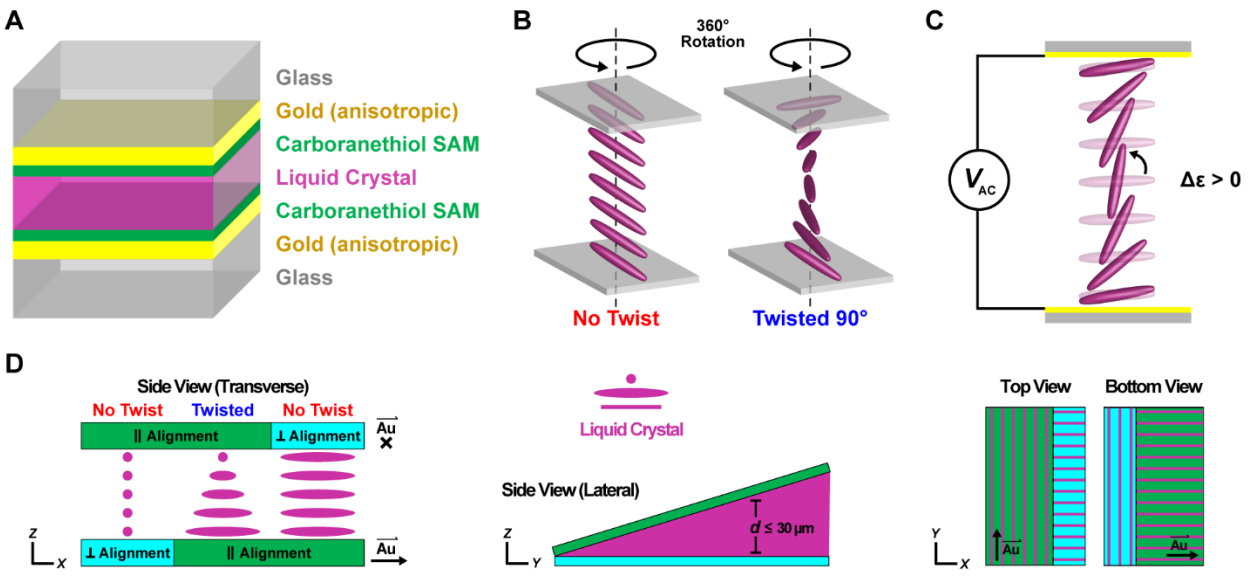

Figure 2.2: (A) Schematic of liquid crystal (LC) cells used in rotation and electrically modulated optical transmittance measurements ("transmittance cells"). Carboranethiol and -dithiol self-assembled monolayers (SAMs) adsorbed on semitransparent, anisotropic gold films induced uniaxial planar alignment of a LC at the interface. Schematics illustrating the rotation of LC cells 360° about axes normal to their alignment planes (B) and a Fréedericksz transition (C) in a LC with positive dielectric anisotropy ($\Delta\varepsilon > 0$) upon application of an alternating electric potential (V_{AC}). (D) Wedge cell geometry used to measure azimuthal anchoring energies, as viewed from multiple perspectives ("anchoring energy cells"). Each alignment layer was divided into two distinct sections defined by SAMs composed of complementary molecules. Here, a carboranethiol or -dithiol isomer SAM (green) is shown to induce LC alignment parallel to the gold deposition direction ($\overrightarrow{\mathbf{Au}}$), although other isomers may instead promote planar alignment perpendicular to $\overrightarrow{\mathbf{Au}}$. Alkanethiol SAMs (blue) were used to induce planar LC alignment orthogonal to that induced by the carboranethiol or -dithiol isomer. Once assembled, the cell was comprised of three nematic regions, one possessing a ~90° twist in the azimuthal director orientation, while the other two exhibited untwisted LC alignment (90° apart) through the bulk of the cell. The thickness (d) of the

gap between the alignment layers varied due to the presence of a spacer (not shown) at only one end of the cell.

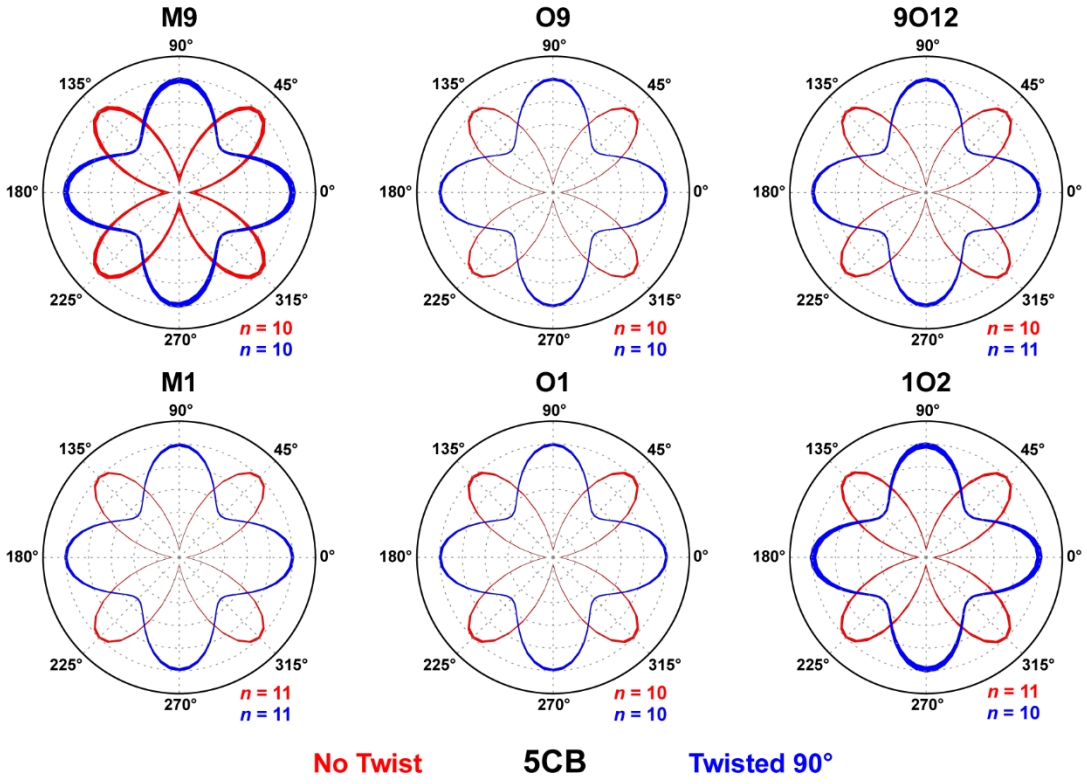

Figure 2.3: Optical transmittances (indicated by the radial distance from the origin, in arbitrary units) of liquid crystal (LC) cells rotated between crossed polarizers. Alignment layers were prepared with matching self-assembled monolayers of *m*-9-carboranethiol (M9), *m*-1-carboranethiol (M1), *o*-9-carboranethiol (O9), *o*-1-carboranethiol (O1), *o*-9,12-carboranedithiol (9O12), and *o*-1,2-carboranedithiol (1O2), as indicated. At these surfaces, uniaxial, planar alignment was manifest in 4-cyano-4′-pentylbiphenyl (5BC) LCs, as evidenced by the variations in optical transmittance possessing four-fold rotational symmetry. Cells were constructed with angles of either 0° or 90° between the alignment layers' gold deposition axes, inducing untwisted (red) or twisted (blue) nematic structures, respectively. Initially, one or both of a cell's gold deposition axes were aligned with the polarizer axis, defined to be at 0°. Rotation

angles were measured with respect to this reference orientation, incremented in 5° steps. Reported spectra are averages of analyses performed on $\boldsymbol{n}$ separate LC cells, each consisting of three measured regions, where the radial line widths indicate the data's standard deviation. Spectra are scaled such that their respective transmittance maxima are equal; in actuality, the maximum transmittance of an untwisted nematic cell nearly equals the minimum transmittance of a cell with a 90° twist in its director.

Applying a potential difference between the alignment layers generates an electric field that can distort the planar alignment of LCs with $\Delta\varepsilon > 0$, inducing them to adopt an orientation parallel to the field (normal to the surface), as illustrated in Figure 2.2C.[75] This reorientation of the mesogens alters the transmittances of LC cells viewed between crossed polarizers, as shown in Figure 2.4. Transmittances of twisted nematic cells containing 5CB ($\Delta\varepsilon > 0$) decrease to near 0% with increasing field strengths. By contrast, twisted nematic cells made using MBBA do not exhibit a change in their transmittance due to their $\Delta\varepsilon < 0$, maintaining planar alignments that are reinforced by the applied field (see Section 2.5.3). The applied potentials produce no lasting changes to the carboranethiol monolayers, as evidenced by the reproducibility of the voltage-modulated transmittance curves through repeated sweeping of the potential's amplitude between 0 and 7 V. The observed optical responses of the cells to applied electric fields is further indication of the planar alignment adopted by both 5CB and MBBA LCs on carboranethiol and -dithiol SAMs.

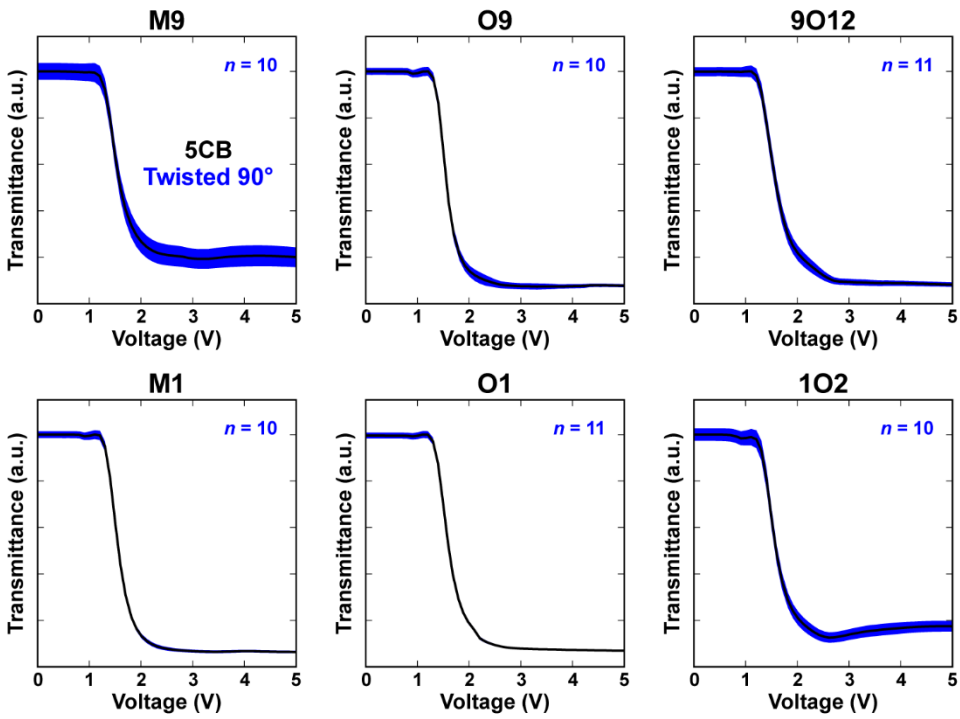

Figure 2.4: Normalized optical transmittances of electrically modulated liquid crystal (LC) cells viewed between crossed polarizers. Alignment layers were prepared with matching self-assembled monolayers of *m*-9-carboranethiol (M9), *m*-1-carboranethiol (M1), *o*-9-carboranethiol (O9), *o*-1-carboranethiol (O1), *o*-9,12-carboranedithiol (9O12), and *o*-1,2-carboranedithiol (1O2), as indicated. These surfaces induced uniaxial planar alignment in 4-cyano-4′-pentylbiphenyl (5CB) LCs. Cells were constructed with perpendicular gold deposition axes, producing twisted nematic structures, and were positioned between crossed polarizers such that their zero-voltage optical transmittance was maximized. Subsequently, a sinusoidally varying (1 kHz) voltage was applied between the alignment layers in order to distort the LC director away from the surface. Root-mean-square voltages, varied in 0.1 V steps, are indicated along the horizontal axes. Reported spectra are averages (black lines) of analyses performed on $\boldsymbol{n}$ separate LC cells, where the vertical widths of the surrounding blue outlines indicate the data's standard deviation.

The rotation- and field-induced variations in transmittance described above were observed uniformly over the entire area (~1 cm^2) of each cell measured. These results indicate uniaxial planar alignment of 5CB and MBBA on anisotropic gold surfaces treated with each of the six carboranethiols considered here. However, these observations, alone, do not uniquely determine the nematic director orientation on a surface. Transmittance minima of untwisted nematics are expected when the director aligns along either of the crossed polarizers' axes, while maxima are expected at these orientations for cells constructed with 90° twists in their directors. These expectations are realized in Figure 2.3; transmittance extrema coincide with cell rotations that align $\overrightarrow{\text{Au}}$ parallel to, and 45° from, the polarizers' axes. Two possible in-plane director orientations can produce this effect: director alignment parallel or perpendicular to $\overrightarrow{\text{Au}}$.

In order to determine, unambiguously, the LC orientation relative to the gold deposition axis (parallel or perpendicular), a wedge cell geometry was used, as illustrated in Figure 2.5. Illuminating a LC wedge with monochromatic light, polarized 45° from its optical axis, produced a series of bright and dark fringes visible within the cell when observed between crossed polarizers. These fringes result from changes in the transmitted light's polarization as it traverses the birefringent cell. The optical retardation (Γ) between ordinary and extraordinary waves causes transmitted light to vary continuously between linear and elliptical polarization states, dependent on the wedge thickness (d). In the two extremes, light exits the wedge linearly polarized parallel or perpendicular to its incoming polarization, producing transmittance minima and maxima, respectively. The conditions on the optical retardation (wedge thickness) required for a transmittance extreme are given by:

$$\Gamma = \Delta n \cdot d = \begin{cases} (m + ½)\lambda, \text{maxima} \\ \\ m\lambda, \text{minima} \end{cases} \qquad m = 0, 1, 2, 3, \ldots \qquad \textbf{Eq. 2.1}$$

where λ is the wavelength of light, Δn is the LC's birefringence, and m is an integer enumerating the fringe order. Wave plates, inserted in series with a wedge cell between crossed polarizers, modify the total retardation by fixed amounts and cause the apparent positions of the fringes to shift. When the optical axes of a wave plate and untwisted nematic align, the total retardation of the transmitted light increases, whereas when their optical axes are crossed, the retardation decreases. Increased (decreased) optical retardation results in shifts in the fringe position toward (away from) the vertex of the wedge, toward the thinner (thicker) end of the cell. In this way, one can infer the orientation of the nematic director from the known orientation of a wave plate's slow axis and the direction of the observed shift in fringe positions.

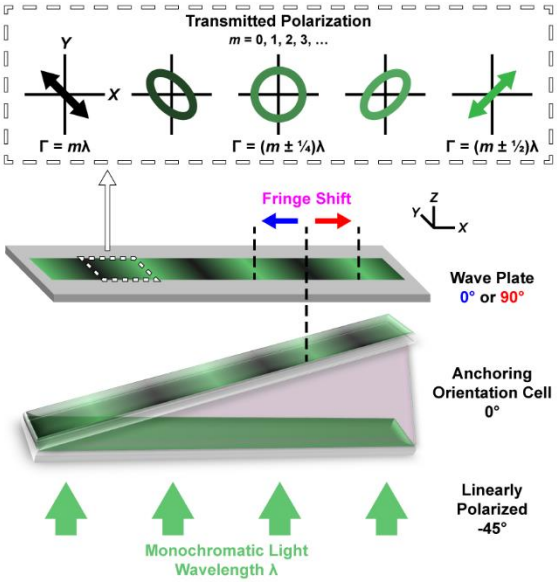

Figure 2.5: Wedge cell scheme used to determine the in-plane liquid crystal director orientation with respect to the alignment layers' gold deposition axes ("anchoring orientation cells"). Linearly polarized, monochromatic light (λ = 531 nm) traversing the cell accumulates an optical retardation

(Γ) dependent on the wedge thickness. As a result, the transmitted light varies between linear and elliptical polarization states, as indicated along the top of the figure. This retardation is modified by placing wave plates in series with the cell. When the optical axes of the cell and wave plate align, the overall retardation increases, whereas when the optical axis of the wave plate is perpendicular to that of the nematic, the total retardation is reduced. When viewed through an analyzer (not shown), oriented 90° from the incoming light's polarization, a series of bright and dark fringes are visible within the cell due to extinction of light polarized along the initial direction. As shown, the wave plate modifies the optical retardation of the transmitted light by $\lambda/2$, thereby causing the transmittance maxima to become minima, and vice versa. All angles indicate orientations in the *xy*-plane with respect to the +*x*-axis.

As shown in Figure 2.6, the fringes observed in cells made using M1, O1, and 1O2 SAMs shift toward the thinner ends of the cells with increased optical retardation along $\overrightarrow{\text{Au}}$. This result indicates that the 5CB director is aligned parallel to $\overrightarrow{\text{Au}}$ in these cells. By contrast, cells prepared with M9, O9, and 9O12 SAMs induced planar alignment of the 5CB director perpendicular to $\overrightarrow{\text{Au}}$, as the fringes were observed to move toward the thicker ends of the cells. We note that self-assembled carboranethiol and -dithiol isomers with dipole moments directed toward the gold surface induced 5CB alignment parallel to $\overrightarrow{\text{Au}}$, whereas isomers with dipoles directed away from the substrate induced planar alignment perpendicular to $\overrightarrow{\text{Au}}$. A similar tendency was also observed in the case of MBBA LCs (see Section 2.5.4), with the exceptions of M9 and 1O2 SAMs, *vide infra*. Comparing the in-plane alignment orientations of 5CB and MBBA directors enables us to examine the coupling mechanism between the mesogens and carboranethiol SAMs. If a dipolar electric field due to the SAM dominates the interaction, then orthogonal director orientations of

the two LCs (with oppositely signed values of Δε) are expected. However, this behavior is not observed, which is understandable due to the inversion symmetry of the nematic director ($\vec{\eta}$ and $-\vec{\eta}$ represent equivalent director orientations).[76] Therefore, the molecular dipole moments in the SAM must influence mesogen alignment by other means.

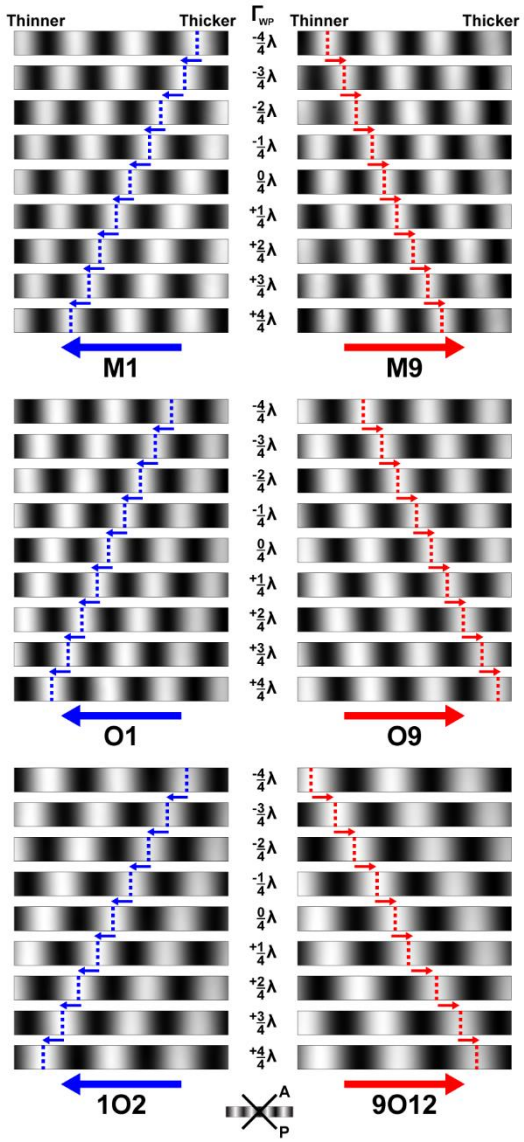

Figure 2.6: Transmission fringes observed in liquid crystal (LC) wedge cells viewed between crossed polarizers while illuminated with monochromatic light (wavelength λ = 531 nm). Alignment layers prepared with matching self-assembled monolayers of *m*-1-carboranethiol (M1),

m-9-carboranethiol (M9), *o*-1-carboranethiol (O1), *o*-9-carboranethiol (O9), *o*-1,2-carboranedithiol (1O2), and *o*-9,12-carboranedithiol (9O12), as indicated, induced uniaxial planar alignment of 4-cyano-4′-pentylbiphenyl (5CB) LCs. Wave plates inserted between the polarizers modified the optical retardation of light transmitted through the cells by fixed amounts (Γ_{WP}). Here, positive (negative) values of Γ_{WP} signify that a wave plate's optically slow axis was aligned parallel (perpendicular) to a cell's gold deposition direction ($\overrightarrow{\mathbf{Au}}$). Arrows and dashed lines track transmittance maxima of constant order within 4.8 mm × 0.5 mm fields of view. Fringes in cells containing M1, O1, and 1O2 monolayers were observed to shift toward the thinner ends of the wedges with increasing Γ_{WP} (blue), indicating that their nematic directors were oriented parallel to $\overrightarrow{\mathbf{Au}}$. By contrast, fringes shifted toward the thicker ends of cells containing M9, O9, and 9O12 monolayers (red), indicating director alignment perpendicular to $\overrightarrow{\mathbf{Au}}$.

Anchoring energy measures the work (per unit area) required to reorient a LC director perpendicular to its preferred, 'easy axis,' orientation on a surface. We compare azimuthal anchoring energies of 5CB aligned by M1, O9, O1, and 9O12 monolayers as a means of quantifying SAM-LC interactions. In doing so, we test for differences in anchoring strengths between isomers that align LCs in the same, and perpendicular, directions on anisotropic gold surfaces. A torque-balance measurement scheme[77,78] was adopted to estimate anchoring energies on patterned, hybrid, alignment layers assembled in a wedge configuration, as illustrated in Figure 2.2D. Twisted and untwisted nematic regions in a cell were created using bifunctional alignment layers, paring carboranethiol SAMs with alkanethiol monolayers known to induce planar LC alignment in orthogonal directions.[46] The untwisted nematic regions within the cells enable determination of the easy axes of both the top and bottom alignment layers, which coincide with the director orientation. In the twisted nematic regions, however, the director deviates from

the surfaces' easy axes due to an elastic restoring torque acting on the mesogens as a result of the twist deformation through the bulk of the cell. The angle (φ) by which the director deviates from the easy axes, and thus partially untwists itself, is related to the azimuthal anchoring energy (W_{az}):

$$W_{az} = \frac{2K_{22}\Psi}{d\sin(2\varphi)} \qquad \textbf{Eq. 2.2}$$

where K_{22} is the twist elastic constant of the mesogen and Ψ is the overall twist of the nematic director through a cell with thickness d (see Figure 2.11). In wedge cells, d varies continuously along their longitudinal axes and, as such, must be determined at each measurement location. Wedge thicknesses may be inferred from their apparent (transmitted) colors. When illuminated with white light and viewed between polarizers crossed at ±45° from the optical axis of an untwisted nematic with known birefringence, the color of transmitted light is related to a cell's thickness using a Michel-Lévy interference color chart.[79] However, this chart provides only a *qualitative* measure since it is based on a subjective judgment of color and is prone to misinterpretation. Monochromatic transmission fringes visible within a cell, like those seen in Figure 2.6, provided a *quantitative* means of estimating the wedge thickness using known values of Δn and λ in Eq. 2.1. In this way, we determined the 5CB azimuthal anchoring energies summarized in Table 2.1.

If LC alignment is modulated by the monolayer's constituent dipole moments, we expect to observe differences in the anchoring strengths of alignment layers treated with different carboranethiol and -dithiol isomers. We found a nearly bimodal distribution of anchoring energies from the four carboranethiol SAMs tested here, with the stronger (weaker) anchoring surfaces corresponding to those with normal dipoles oriented toward (away from) the substrate. Anisotropic gold surfaces functionalized with either O9 or 9O12 aligned 5CB with approximately half the

strength, perpendicular to $\overrightarrow{Au}$, as monolayers of M1 or O1, which induced alignment parallel to $\overrightarrow{Au}$. Although each of these molecules possess distinct dipole magnitudes and orientations, the anchoring strengths of M1 and O1 (both monothiol species) SAMs did not differ appreciably. By contrast, the anchoring energy measured on 9O12 (dithiol) SAMs was found to be ~10% less than the value measured on O9 (monothiol) SAMs. However, that decrease in anchoring energy coincides with a matching reduction in the areal density of 9O12 molecules within close-packed SAMs, compared with O9 monolayers, due to the larger nearest-neighbor spacing of carboranedithiol adsorbates.[14,60,64] These findings suggest that the polarity of the normal dipole moment, toward or away from the surface, and the molecular packing density are the dominant factors affecting LC anchoring in these systems. We note that the measured anchoring energies of 5CB LCs on carboranethiol monolayers (~7 and ~14 $\mu J \cdot m^{-2}$) exceed the values reported for oligo(ethylene glycol)-containing SAMs (<6 $\mu J \cdot m^{-2}$),[78,80] though both are almost 2 orders of magnitude weaker than the anchoring strengths of rubbed polyamide films.[81,82]

Uncertainty in the local gold deposition angle is expected to be a major contributor to variations in the measured azimuthal anchoring energies.[38,80,83,84] All of the gold films used in these studies were deposited at the same angle, normally 50° away from the surface normal. However, due to the finite sizes of the glass substrates and their positions relative to the evaporating metal source, departures of up to 6° from the intended angle are possible (see Section 2.5.7). Variations in the average grain size and surface roughness affect the substrate's contribution to LC alignment, resulting in stronger anchoring on gold films deposited at higher, more oblique, angles.[83] Additionally, uncertainty in the anchoring energy typically increases with deposition angle due, in part, to its sensitivity to uncertainties in the nematic director's twist and deviation from the easy axes.[80] This sensitivity becomes more pronounced with increasing anchoring strength (higher

deposition angles). The anchoring energies reported here reflect averages of measurements performed on multiple cells, inversely weighted by their estimated variances. Such averaging, however, biases the reported values in favor of lower anchoring energies that possess correspondingly smaller uncertainties. The complete data sets, as well as a discussion of the statistical methods used in our analysis, are provided in Section 2.5.6.

Table 2.1: Anchoring energy (W_{az}) of 5CB liquid crystals in cells prepared with various carboranethiol self-assembled monolayers (SAMs).

Anchoring SAM[a]	$p_{\perp}$[b]	W_{az} (μJ·m^{-2})	Sample Size, *n*
O9[c]	↑	7.5 ± 0.1	28
9O12[d]	↑	6.7 ± 0.1	29
M1[e]	↓	14.3 ± 0.4	36
O1[f]	↓	14.3 ± 0.4	37

[a]Carboranethiol or -dithiol isomer used to align 4-cyano-4′-pentylbiphenyl (5CB). [b]Normal dipole ($p_{\perp}$) orientation toward (↓) or away from (↑) the gold surface. [c]*o*-9-carboranethiol. [d]*o*-9,12-carboranedithiol. [e]*m*-1-carboranethiol. [f]*o*-1-carboranethiol.

As noted above, we observe a trend in the alignment of LCs by carboranethiol monolayers prepared on anisotropic gold surfaces that follows the polarity of the adsorbate's normal dipole moment. The constituent molecules of a SAM, in general, possess dipoles with components oriented parallel and normal to the functionalized surface. The cumulative effects of the in-plane molecular dipoles are diminished by their varying or disordered azimuthal orientations expected at room temperature.[14] Molecules may adsorb to the surface with random in-plane dipole orientations and, in the cases of M9, M1, O9, and O1, which possess only a single attachment to

the substrate, rotate about their Au–S bonds. If long-range orientation order is present, the formation of differently polarized domains (including closure domains) would compensate for a net in-plane dipole over macroscopic scales. Additionally, image dipoles, formed through the redistribution of charge on the underlying gold substrate, would further attenuate the effects of in-plane molecular dipoles. Normal dipole moments, however, are not subject to these mitigating factors. Each carboranethiol in a single-species SAM adsorbs to the surface with the same polar orientation and, as such, enhances the net dipole moment normal to the surface. Carboranedithiol isomers (9O12 and 1O2) were included in these experiments due to their expected dipole orientations normal to the surface as a result of their bilateral molecular symmetry. Since these isomers bind to the substrate via two Au–S bonds, they are not free to rotate azimuthally. In principle, these isomers could tilt about the axis connecting their two adsorbed thiolate moieties, out of the plane normal to the gold substrate, resulting in a portion of their dipole moments orienting parallel to the surface. Nevertheless, we observe the same trend in 5CB alignment induced by carboranedithiol isomers as in the cases of monothiol isomers, dependent upon the polarity of the normal dipole. As such, we conclude that the net in-plane dipole of a SAM is either compensated through one or more of the mechanisms mentioned above, or is a less significant contributor than the normal dipole when determining LC alignment.

In addition to the factors discussed above, other surface anisotropies may contribute to the existence of an easy alignment axis. One such contribution originates from an anisotropic electric susceptibility of the alignment surface. Obliquely deposited films are expected to have an anisotropic response to electric stimuli (e.g., from mesogen dipoles) due to their dune-like or columnar surface textures.[85,86] Molecular monolayers can modify this anisotropy, dependent on the adsorbate polarizabilities and orientations on the surface. To examine this effect, molecular

polarizability tensors (α) were calculated using density functional theory for each of the six carboranethiol and -dithiol isomers considered here (see Section 2.5.8). To facilitate comparison, Cartesian coordinate bases were chosen for each molecule such that the bond(s) connecting the sulfur atom(s) to the carborane cage moiety coincided with (or symmetrically straddled) the *z*-axis. Additionally, one or both of the carbon atoms within the isomers were designated to lie along the *x*-axis, in the cases of M1, O9, O1, 9O12, and 1O2, and symmetrically about the *x*-axis in the case of M9. These coordinate bases closely coincided with the molecules' principal polarizability axes, such that the off-diagonal polarizability tensor elements ($\alpha_{ij}, i \neq j$) were negligible (<1%) by comparison to the diagonal elements (α_{ii}). Considering upright adsorption, we found that the molecular polarizabilities of carboranethiols were nearly symmetric in the plane of the substrate ($\alpha_{xx} \approx \alpha_{yy}$), with variations of <2%. Larger in-plane variations in molecular polarizability were found for 9O12 and 1O2 (~10%), in part due to the lower (two-fold) rotational symmetry of carboranedithiols compared with monothiol isomers (five-fold). Symmetric adsorbate polarizabilities reduce the likelihood of anisotropic in-plane polarizations of a SAM inducing LC alignment on flat, isotropic surfaces. On textured surfaces, however, the local (microscopic) surface normal generally deviates from that of the average (macroscopic) plane of the substrate, effectively varying the orientations of molecules within the assembly. As a result, the in-plane electric susceptibility of a SAM depends, in part, on the polarizability of carboranethiols along their *z*-axes (α_{zz}), which is ~20% greater than along orthogonal directions. Therefore, geometric surface anisotropies present in obliquely deposited films, generate additional anisotropies in a monolayer without requiring, *a priori*, long-range azimuthal alignment of carboranethiols. However, we do not find any consistent correlation between the observed LC alignment and all six of the carboranethiol molecular polarizabilities considered here.

Comparing the alignments of mesogens with oppositely signed dielectric anisotropies provides insight into the role of the dipolar field on LC anchoring by functionalized surfaces. Assuming direct coupling between the mesogens and the field, 5CB and MBBA LCs were expected to align along orthogonal directions, relative to each other, at the SAM-LC interface. Instead, both mesogens adopted the same planar orientation, dependent on the polarity of the monolayer's constituent molecular dipoles normal to the surface, as detailed previously. However, in the case of MBBA alignment, M9 and 1O2 carboranethiol monolayers were found to be exceptions to this trend. Alignment layers functionalized with M9 induced alignment of MBBA parallel to $\overrightarrow{\text{Au}}$, whereas 1O2 monolayers resulted in more heterogeneous and less reproducible anchoring of MBBA than observed on surfaces treated with other isomers under the same conditions. To understand these anomalies, we reemphasize that the monolayer's constituent dipoles are not the sole factor affecting LC alignment, despite being the focus of these studies. Other influences, including surface topography, molecular geometry, tilt, and order are still present (albeit consistent) in each cell, while the contribution from carboranethiol dipoles varies between isomers. Out of the three isomers with dipoles directed away from the underlying gold surface tested here, M9 possesses the weakest moment and is the only one to induce LC alignment counter to the prevailing trend (and only with MBBA). Previously, we noted that the anchoring strength of 5CB on carborane-functionalized surfaces did not depend on the magnitude of the molecular dipoles of a SAM. This unexpected alignment of MBBA may indicate a minimum, threshold, strength of molecular dipoles required to orient LCs along a particular direction on these surfaces. Alternatively, we propose that the properties of MBBA itself may instead be responsible. Relative to 5CB, MBBA has a weaker internal dipole moment and smaller dielectric anisotropy (see Section 2.5.1). As a result, the coupling strength of MBBA to external electric fields is weaker

than that of 5CB, with which no alignment anomalies were observed. Future experiments using a LC with a more negative dielectric anisotropy could test this hypothesis and distinguish whether or not the observed alignment is indicative of the carboranethiol monolayer or a property of the mesogen itself. In the case of the heterogeneous alignment of MBBA on 1O2 monolayers, we note the potential for dithiol isomers to chemisorb to the gold surface in either singly or doubly bound states. Here, we used ethanolic solutions of each of the carboranedithiols with added base (sodium hydroxide) to promote dual binding via both thiol moieties on each molecule. However, even under these circumstances, not every adsorbed molecule binds to the gold with both thiol moieties. We have observed elsewhere[64] that the 1O2 isomer is more likely to adsorb in mixed states (both singly and doubly bound) compared to the 9O12 isomer under alkaline conditions, resulting in a less uniform SAM. This molecular-scale heterogeneity may, in turn, produce more heterogeneous LC arrangements than those observed on alignment layers treated with other carboranethiol isomers.

2.3 Conclusion & Prospects

Here, LCs serve as advantageous probes of the nanoscale intermolecular forces between SAMs and their environment. These combinations of forces result from several factors, including surface topography, molecular orientation, and chemical functionality, which modulate the properties of the underlying substrate and mediate the assembly of adsorbates. We report on the uniaxial, planar alignment of 5CB and MBBA LCs on obliquely deposited gold films functionalized with carboranethiol and -dithiol SAMs. Carboranethiol monolayers enable direct comparisons of LC alignment modulated by differences in the magnitudes and orientations of assembled molecular dipoles on a surface. Carboranethiol monolayers hold *constant* other factors that influence LC alignment, such as molecular geometry, tilt, and order, which have confounded previous studies. Furthermore, comparing LC alignment on monolayers composed of monothiol

isomers (M9, M1, O9, and O1) to those composed of carboranedithiols (9O12 and 1O2) enabled inference of the roles of the normal and lateral surface dipoles. We observed that the in-plane, azimuthal, orientation of mesogens on anisotropic gold films were modulated predominantly by the carboranethiol dipole component normal to the surface. Monolayers composed of carboranethiols with dipoles oriented toward (away) from the underlying gold surface induced planar alignment of 5CB parallel (perpendicular) to the gold deposition direction. A similar trend was observed in the case of alignment of MBBA, which possesses an oppositely signed dielectric anisotropy. Since LCs with oppositely signed dielectric anisotropies align similarly, dependent on the monolayer's normal dipole polarity, we conclude that it is not a direct result of dipolar field coupling between SAMs and mesogens. Therefore, we attribute the observed alignment to more complicated mechanisms involving intermolecular dispersion forces. To quantify SAM-LC interaction strength, we measured the azimuthal anchoring energies of 5CB on alignment layers treated with M1, O9, O1, and 9O12 monolayers. A nearly bimodal distribution of anchoring energies was measured, dependent on the polarity of the carboranethiol isomer dipole moment component normal to the surface. Monolayers composed of carboranethiol isomers with dipoles oriented away from (O9 and 9O12) and toward (M1 and O1) the substrate were measured to anchor 5CB with strengths of ~7 and ~14 $\mu J \cdot m^{-2}$, respectively. Additionally, comparing the anchoring energies of pairs of isomers with the same polarity normal to the surface, we found no difference in anchoring strengths between monothiol species (M1 and O1). However, we observed that the anchoring energies measured on surfaces treated with 9O12 (dithiol) were about 10% lower than that of O9 (monothiol), coinciding with the decrease in areal density of carboranethiols within the close-packed monolayers. This result indicates that not only the polarities of the molecular dipoles affect LC anchoring, but also their densities on the surfaces. We also considered other sources of

surface anisotropy arising from the molecular polarizabilities of the carboranethiols used in this work that may affect LC anchoring direction and strength. We do not expect that long-range molecular alignment of carboranethiol adsorbates within SAMs at room temperature is likely.[14] However, others have previously observed azimuthal ordering of exposed methyl moieties in alkanethiol monolayers prepared on anisotropic gold films.[41] Complementary techniques, such as sum-frequency generation spectroscopy, may be used in future studies to test this possibility in the case of carboranethiol SAMs.[87] This work builds upon past studies of the alignment of LCs on functionalized, anisotropic surfaces in order to elucidate the role of molecular dipole moments of the monolayers on the subsequent adsorption and assembly of other molecular species. Extending this knowledge to other molecular systems will enhance the predictive capabilities of nanoscale engineering and enable rational design of structures extended to macroscopic scales on complex surfaces.

2.4 Experimental Section

Materials

Positional isomers of dicarba-*closo*-dodecaboranethiol and -dithiol O1, O9, 1O2, and 9O12 were synthesized using previously reported methods;[88–90] M1 and M9 isomers were purchased from Sigma-Aldrich (St. Louis, MO). Mesogens 5CB and MBBA, as well as sodium hydroxide, and alkanethiols 1-undecanethiol (C11) and 1-octadecanethiol (C18) were also obtained from Sigma-Aldrich. Ethanol (200 proof) was purchased from Goldshield Chemical Company (Hayward, CA), while potassium hydroxide and hydrogen peroxide (30%) were acquired from Fisher Scientific (Pittsburgh, PA). Sulfuric acid (98%) was purchased from EMD Chemicals (Gibbstown, NJ). All commercial chemicals were used as received. Deionized (DI) water (18.2 MΩ·cm) was dispensed from a Milli-Q water purifier (EMD Millipore, Billerica, MA).

Polymeric Stamp Preparation

Polymeric stamps were produced using a Sylgard 184 silicone elastomer kit (Dow Corning, Midland, MI) following a previously reported procedure.[91] Flat, featureless stamps were obtained and cut into strips approximately 8 mm wide, 76 mm long, and 4 mm thick.

Polarizing Microscopy & Image Analysis

An Olympus BX51-P Polarizing Microscope and CCD camera (Center Valley, PA) were used throughout this work to record the transmittances and optical textures of LC cells as 8-bit grayscale images. The transmittance of a LC cell was computed using the average intensity of all pixels within an image (1600 × 1200 pixels). Variations in the transmittance within the microscope field of view were quantified using the standard deviation of pixel intensities. Reported transmittance values reflect aggregated analyses of multiple cells and multiple locations within each cell. Automated routines facilitated image processing.

Alignment Layer Preparation

Eagle XG glass (Corning Display Technologies, Corning, NY), 1.1 mm thick, was used throughout this work. Glass used in anchoring energy measurements had lateral dimensions of 76 mm × 25 mm, while pieces intended for transmittance measurements were cut to approximately 19 mm × 25 mm.

Substrate Cleaning. Glass substrates were cleaned through sequential rinsing and ultrasonication steps (>20 min) in ethanol, DI water, and concentrated potassium hydroxide solution. Afterward, the glass was rinsed in DI water and then immersed in piranha solution (3:1 H_2SO_4/H_2O_2) for ~1 h before a final rinse in DI water and being blown dry with nitrogen gas.

Oblique Metal Deposition. Cleaned glass substrates were loaded into the vacuum chamber of an electron beam metal evaporator (Kurt J. Lesker Company, Jefferson Hills, PA) immediately after drying and held at a base pressure of ~1×10^{-7} Torr. The substrates were mounted with fixed positions and orientations within the chamber such that their surface normal was inclined at an angle of 50° away from the metal source. Semitransparent gold films (10 nm) were deposited on top of chromium adhesion layers (2 nm) at rates of ~0.5 Å/s. Nominal film thicknesses were measured using a quartz crystal microbalance orientated toward the metal source, thus overestimating the amount of metal adsorbed on the glass by a factor of $\sec(50°) \approx 1.6$. Due to the finite sizes of the glass substrates and their positions relative to the metal source, a deviation of <6° from the intended deposition angle is expected for gold films deposited in the same batch.

Self-Assembled Monolayer Preparation. Self-assembled monolayers were formed on obliquely deposited Au/glass substrates from 1 mM ethanolic solutions of the desired adsorbate: O1, O9, M1, M9, 1O2, 9O12, C11, or C18. In the cases of 1O2 and 9O12, 1:2 carboranedithiol/NaOH equivalent solutions in ethanol were used to promote divalent adsorption on the gold surface.[64] Immediately prior to SAM deposition, Au/glass substrates were exposed to an oxygen plasma (Harrick Plasma, Ithaca, NY) for 40 s in order to remove adventitious organic adsorbates. Substrates intended for use in transmittance measurements were immersed in solutions of the desired carboranethiol or -dithiol isomer for 12–18 h. Afterward, the uniformly functionalized surfaces were rinsed in copious amounts of ethanol and then blown dry with nitrogen gas. By contrast, soft lithography was employed to create two adjacent, spatially separated, SAMs on substrates used in anchoring energy measurements. A polymeric stamp was soaked in a solution of either C11 or C18 ‘ink’ for at least 20 min, then rinsed with ethanol and blown dry with nitrogen gas. The inked stamp was placed into conformal contact with a clean

Au/glass surface for 10 min. This stamping resulted in the formation of an alkanethiol SAM over about one-third of the alignment surface (conformal contact area). The surface was then immersed into a solution of the carboranethiol or -dithiol under investigation for 60 min in order to functionalize the remaining bare surface. Finally, the surface was rinsed with ethanol and blown dry with nitrogen gas. Observing the distinct wetting behavior of ethanol over the two SAM regions, possessing either non-polar (aliphatic) or polar (carborane) moieties, confirmed the bifunctional character of the surface.

Liquid Crystal Cell Assembly

All LC cells were assembled (*vide infra*) immediately following alignment layer preparation and their cavities filled with either 5CB or MBBA via capillary action. To prevent flow-induced LC alignment, the alignment layers and mesogens were heated to 5–10 °C above the mesogen's clearing temperature during filling. Afterward, the cells were allowed to cool to room temperature (~20 °C) and permanently sealed using cyanoacrylate adhesive (Henkel, Westlake, OH).

Transmittance Cells. Transmittance cells were assembled using plastic spacers (30 μm thick) to separate the matching functionalized-gold surfaces of two alignment layers. Alignment layers were paired such that their gold deposition axes were either parallel or crossed at angles of ~90°, producing cells with untwisted or twisted nematic structures, respectively. Copper wires were affixed to the outermost edges of both gold surfaces using conductive carbon glue (Ted Pella, Redding, CA), enabling manipulation of LC orientations by applied electric fields (potentials).

Anchoring Orientation Cells. The alignment layers of cells used to determine the in-plane LC anchoring orientations were prepared identically to those used in transmittance measurements. However, in contrast to transmittance cells, anchoring orientation cells were constructed as wedges

with a spacer separating the alignment layers at only one end. In this configuration, the thickness of the cavity between the alignment layers varied linearly along the cell's longitudinal axis, independent of the transverse position. Only untwisted nematic cells, with parallel anisotropy axes, were used to determine anchoring orientations.

Anchoring Energy Cells. Adopting the design described by Abbott and coworkers,[77,78] anchoring energy cells were constructed with the wedge cell geometry described previously and engineered to contain three nematic regions. Alignment layers were arranged with crossed gold deposition axes, oriented along the longitudinal and transverse cell axes, and with matched and mismatched overlapping SAM regions, as illustrated in Figure 2.2D. As such, the azimuthal director orientation was induced to twist by ~90° in the central region, whereas the regions on either side exhibited untwisted, uniaxial LC alignment (90° apart) through the bulk of the cell. To prevent flexing of the alignment layers during assembly, custom-built jigs were used to ensure uniform compression. Flexing was not observed to pose a problem when constructing other, comparatively shorter, types of LC cells.

Transmittance Measurements

Transmittance cells were examined between the crossed polarizers of a polarizing optical microscope while illuminated with white light. The optical axes of the cells were aligned initially with either of the microscope's polarizing axes, thus minimizing (maximizing) the relative intensity of light transmitted through cells constructed with no twist (90° twist) in their nematic directors. The transmittance was measured at 5° intervals over one complete rotation of a cell. This process was repeated three times, in different regions (1.2 mm × 0.9 mm field of view), for each cell measured. Afterward, the orientation of the cell was fixed and its transmittance measured as a

sinusoidally varying voltage was applied between the alignment layers (3.0 mm × 2.2 mm field of view).

Anchoring Orientation Determination

Anchoring orientation cells were illuminated with monochromatic light polarized 45° from their optical axes. When viewed through an analyzer crossed 90° from the polarization of the incoming light, a series of bright and dark fringes were observed, as illustrated in Figure 2.5. These fringes were a consequence of differences in the optical retardation of light transmitted through the birefringent, LC, wedges. Wave plates (RealD, Beverly Hills, CA and Edmund Optics, Barrington, NJ) were inserted between the polarizers, in series with the cells, to alter this retardation by fixed amounts. Changes in the fringe positions due to the wave plates were tracked within viewing areas of about 6.0 mm × 4.5 mm.

Anchoring Energy Measurements

Azimuthal anchoring energies were measured using a similar procedure to that reported by Abbott and coworkers.[78] The LC alignment directions and twist angles were determined using automated routines to fit the observed rotation–transmittance spectra in each of the cells' three nematic regions (590 µm × 440 µm field of view) to their expected trigonometric responses. Estimates of local wedge cavity thicknesses were made by comparing the observed color of cells illuminated with white light to a Michel-Lévy interference color chart.[79] These estimates were refined using the positions of the transmission fringes made visible by illuminating the cells with monochromatic light. Transmittance minima and maxima bands acted as internal graduations corresponding to known cavity thicknesses. Reported anchoring energies represent an average of all measurements weighted by their respective measurement uncertainties (see Section 2.5.6).

Density Functional Theory Calculations

The six carboranethiol isomers used in this work were analyzed using density functional theory. Optimized molecular structures, dipole moments, and polarizabilities were computed at the M062X level of theory using the 6-311G** basis set with the Gaussian 09 software package (Gaussian, Wallingford, CT).[92,93]

2.5 Associated Content

Physical Properties of Liquid Crystals

Relevant physical properties of the liquid crystals (LCs) used in this work, 4-cyano-4′-pentylbiphenyl (5CB) and *N*-(4-methoxybenzylidene)-4-butylaniline (MBBA), are summarized in Table 2.2.

Table 2.2: Physical properties of 5CB[a] and MBBA[b] liquid crystals.

Property[c]	**Liquid Crystals**	
	5CB[d]	**MBBA**[e]
Δn[f]	0.1873	0.184
$\Delta\varepsilon$[g]	+11.5	-0.5
K_{22} (pN)[h]	4.22	4.0
T_{NI} (°C)[i]	35	47
μ (D)[j]	5.1	2.2

[a]4-cyano-4′-pentylbiphenyl (5CB). [b]*N*-(4-methoxybenzylidene)-4-butylaniline (MBBA). [c]The values of these properties depend on the specific measurement conditions (e.g., temperature, optical wavelength, and chemical purity). Here, we report values applicable to this work. [d]See Refs. 78,94–96. [e]See Refs. 55,76,97. [f]Birefringence (Δn), calculated as the difference in the indices of refraction of light polarized along the mesogen's extraordinary and ordinary axes. [g]Dielectric

anisotropy (Δε), calculated as the difference in the mesogen's dielectric constant parallel and perpendicular to the director. [h]Mesogen twist elastic constant (K_{22}). [i]Transition temperature (T_{NI}) between the nematic and isotropic phases. [j]Permanent molecular dipole moment (μ) of the mesogen. The dipole moment of 5CB lies along its molecular axis, whereas the dipole moment of MBBA is directed primarily perpendicular to its long axis.

MBBA Cell Rotation–Transmittance Spectra

Figure 2.7 shows the modulation in the intensity of the light transmitted through MBBA cells as they were rotated between crossed polarizers (Figure 2.2B). Alignment layers treated with *m*-9-carboranethiol (M9), *m*-1-carboranethiol (M1), *o*-9-carboranethiol (O9), *o*-1-carboranethiol (O1), and *o*-9,12-carboranedithiol (9O12) SAMs induced uniaxial planar alignment in MBBA cells, as indicated by the four-fold symmetry of their transmittance spectra. Cells constructed without a twist in their nematic directors vary from nearly extinguishing all transmitted light to transmitting ~50%. By contrast, cells that possess a 90° twist in their directors have transmittances varying from ~50% to nearly 100%, due to the rotation of the polarization of the transmitted light as it traverses the cell.

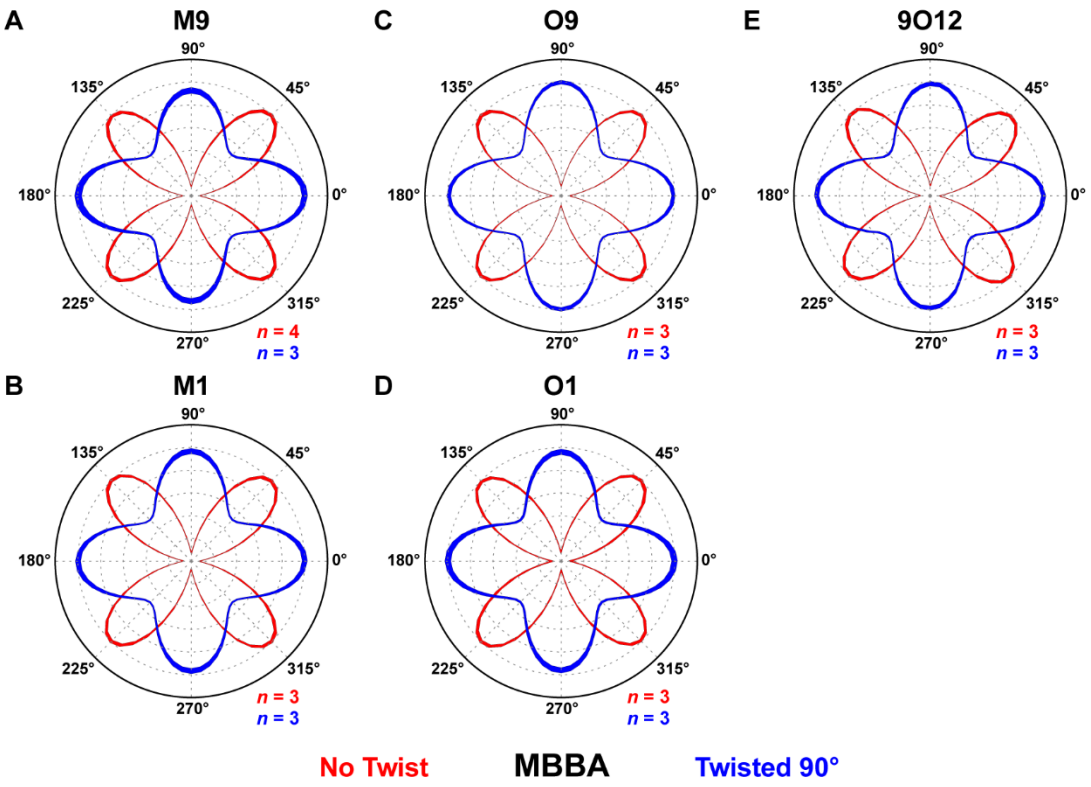

Figure 2.7: Optical transmittances (indicated by the radial distance from the origin, in arbitrary units) of liquid crystal (LC) cells rotated between crossed polarizers. Alignment layers were prepared with matching self-assembled monolayers of *m*-9-carboranethiol (M9), *m*-1-carboranethiol (M1), *o*-9-carboranethiol (O9), *o*-1-carboranethiol (O1), and *o*-9,12-carboranedithiol (9O12), as indicated. At these surfaces, uniaxial, planar alignment was manifest in *N*-(4-methoxybenzylidene)-4-butylaniline (MBBA) LCs, as evidenced by the variations in optical transmittance possessing four-fold rotational symmetry. Cells were constructed with 0° or 90° angles between their alignment layers' gold deposition axes, producing untwisted (red) or twisted (blue) nematic structures, respectively. Initially, one or both of a cell's gold deposition axes were aligned with the polarizer axis, defined to be at 0°. Rotation angles were measured with respect to this reference orientation, incremented in 5° steps. Reported spectra are averages of analyses performed on n separate LC cells, each consisting of three measured regions,

where the radial line widths indicate the data's standard deviation. Spectra are scaled such that their respective transmittance maxima are equal; in actuality, the maximum transmittance of an untwisted nematic cell nearly equals the minimum transmittance of a cell with a 90° twist in its director.

MBBA Cell Voltage–Transmittance Spectra

Applying a potential difference between the alignment layers generates an electric field that can distort the LC alignment. Mesogens with negative dielectric anisotropies ($\Delta\varepsilon < 0$) adopt an orientation perpendicular to the applied field. In the case of MBBA, such fields would induce (or reinforce) planar alignment, parallel to the surface. Any reorientation of the mesogens upon the application of an electric potential ($V_{AC} \leq 7$ V) would alter the transmittances of LC cells viewed between crossed polarizers. As seen in Figure 2.8, transmittances of cells containing MBBA remain constant, indicating prior planar alignment of the mesogens and no subsequent reorientation.

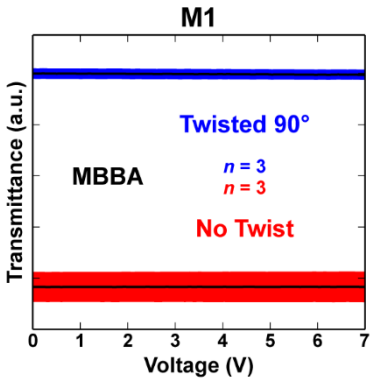

Figure 2.8: Normalized optical transmittances of electrically modulated liquid crystal (LC) cells viewed between crossed polarizers. Alignment layers were prepared with matching self-assembled monolayers of *m*-1-carboranethiol (M1), which induced uniaxial planar alignment in *N*-(4-methoxybenzylidene)-4-butylaniline (MBBA) LCs. Cells were constructed with 0° or 90°

angles between their alignment layers' gold deposition axes, producing untwisted (red) or twisted (blue) nematic structures, respectively. Cells were positioned between crossed polarizers such that their zero-voltage optical transmittance was maximized (minimized) for twisted (untwisted) nematic structures. Subsequently, a sinusoidally varying (1 kHz) voltage was applied between the alignment layers. Root-mean-square voltages, varied in 0.1 V steps, are indicated along the horizontal axes. Reported spectra are averages (black lines) of analyses performed on $n = 3$ separate LC cells, of each type, where the vertical widths of the surrounding blue outlines indicate the data's standard deviation. No changes in the transmittance spectra were observed with increasing voltage, indicating that the MBBA mesogens did not reorient as a result of the applied electric field.

MBBA Anchoring Orientation Cells

Anchoring orientation wedge cells were used to determine the in-plane orientation of MBBA LCs relative to the oblique gold deposition direction ($\overrightarrow{\text{Au}}$): parallel or perpendicular. As shown in Figure 2.9, the fringes observed in cells made using M1, M9, and O1 shift toward the thinner ends of the wedges with increased optical retardation along the gold deposition axis, indicating that the MBBA nematic director is aligned parallel to $\overrightarrow{\text{Au}}$. By contrast, cells made with O9 and 9O12 exhibited planar alignment of MBBA perpendicular to $\overrightarrow{\text{Au}}$, as evident from the observed fringe shifts toward the thicker ends of the wedges. As such, the orientations of the MBBA director match those of 5CB on alignment layers treated with M1, O1, O9, and 9O12 SAMs. However, in the case of M9 SAMs, 5CB and MBBA LCs were observed to align along opposite directions, planar alignment perpendicular and parallel to $\overrightarrow{\text{Au}}$, respectively. We attribute this discrepancy to relatively weak interactions of the M9 molecular dipole moment with MBBA

mesogens, in comparison to those of other carboranethiol isomers, and other factors contributing to LC alignment that are always present in each cell, though presumed consistent.

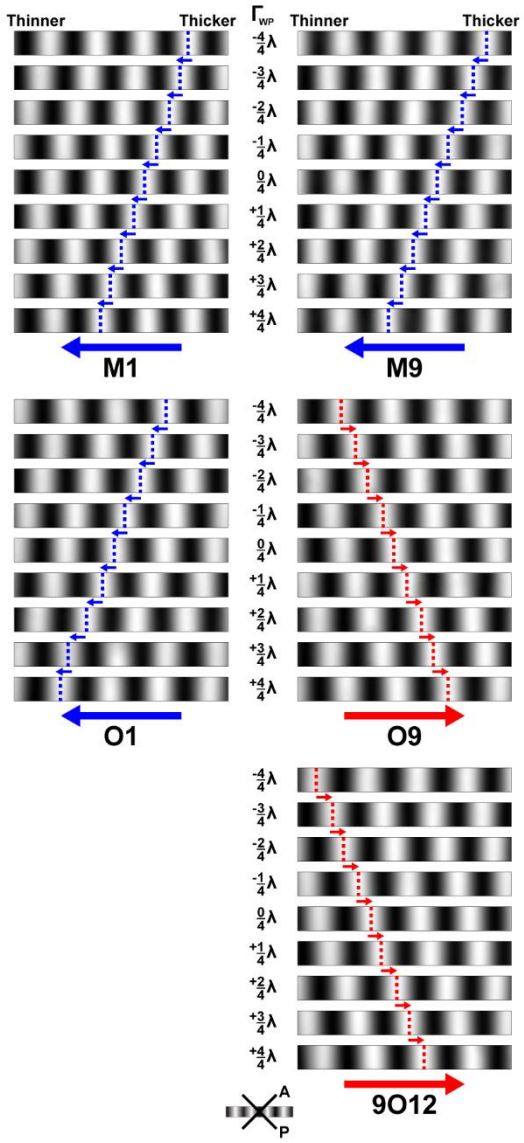

Figure 2.9: Transmission fringes observed in liquid crystal (LC) wedge cells viewed between crossed polarizers while illuminated with monochromatic light (wavelength $\lambda = 531$ nm). Alignment layers prepared with matching self-assembled monolayers of *m*-1-carboranethiol (M1), *m*-9-carboranethiol (M9), *o*-1-carboranethiol (O1), *o*-9-carboranethiol (O9), and *o*-9,12-carboranedithiol (9O12), as indicated, induced uniaxial planar alignment of

N-(4-methoxybenzylidene)-4-butylaniline (MBBA) LCs. Wave plates inserted between the polarizers modified the optical retardation of light transmitted through the cells by fixed amounts (Γ_{WP}). Here, positive (negative) values of Γ_{WP} signify that a wave plate's optically slow axis was aligned parallel (perpendicular) to a cell's gold evaporation direction ($\overrightarrow{\mathbf{Au}}$). Arrows and dashed lines track transmittance maxima of constant order within 4.8 mm × 0.5 mm fields of view. Fringes in cells containing M1, M9, and O1 monolayers were observed to shift toward the thinner ends of the wedges with increasing Γ_{WP} (blue), indicating that their nematic directors were oriented parallel to $\overrightarrow{\mathbf{Au}}$. By contrast, fringes shifted toward the thicker ends of wedges containing O9 and 9O12 monolayers (red), indicating director alignment perpendicular to $\overrightarrow{\mathbf{Au}}$.

5CB Cell Voltage–Transmittance Spectra

Figure 2.10 depicts the normalized optical transmittances of untwisted 5CB cells modulated by an electric field. The scaling applied to these spectra exaggerates the apparent variations in the measured transmittances. Comparing absolute transmittances, the change observed in untwisted 5CB cells is only about 10% of that seen in 5CB cells with 90° twists in their directors (Figure 2.4). The observed transmittance variations in these cells is similar to those expected from untwisted 5CB cells using other LC alignment techniques (e.g., rubbed polyimide).

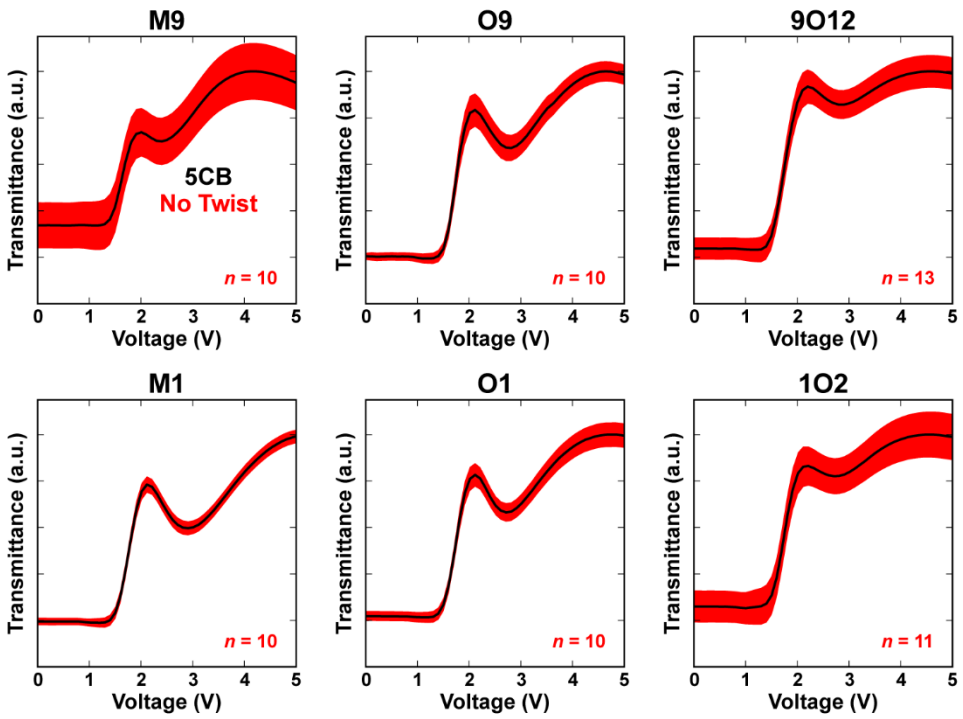

Figure 2.10: Normalized optical transmittances of electrically modulated liquid crystal (LC) cells viewed between crossed polarizers. Alignment layers were prepared with matching self-assembled monolayers of *m*-9-carboranethiol (M9), *m*-1-carboranethiol (M1), *o*-9-carboranethiol (O9), *o*-1-carboranethiol (O1), *o*-9,12-carboranedithiol (9O12), and *o*-1,2-carboranedithiol (1O2), as indicated. These surfaces induced uniaxial planar alignment in 4-cyano-4′-pentylbiphenyl (5CB) LCs. Cells were constructed with parallel gold deposition axes, producing untwisted nematic structures, and were positioned between crossed polarizers such that their zero-voltage optical transmittance was minimized. Subsequently, a sinusoidally varying (1 kHz) voltage was applied between the alignment layers in order to distort the LC director away from the surface. Root-mean-square voltages, varied in 0.1 V steps, are indicated along the horizontal axes. Reported spectra are averages (black lines) of analyses performed on n separate LC cells, where the vertical widths of the surrounding red outlines indicate the data's standard deviation.

Azimuthal Anchoring Energy

Azimuthal anchoring energies (W_{az}) of 5CB aligned by SAMs composed of M1, O9, O1, and 9O12 isomers were measured using the torque balanced method described by Abbott and coworkers.[78] Here, we summarize the methods used to determine the parameters d, φ, and Ψ in Eq. 2.2. All measurements were made on anchoring energy wedge cells (Figure 2.2D) viewed between crossed polarizers. Wedge thicknesses (d) were estimated by comparing the observed (transmitted) color of the cells, illuminated with white light polarized ±45° from their optical axes, to a Michel-Lévy interference color chart,[79] and then refined using Eq. 2.1 and the positions of the transmission fringes made visible using monochromatic light ($\lambda = 531$ nm).

We calculated φ and Ψ using the values of δ and γ (Figure 2.11), which were determined by monitoring the transmission of light through each of the three nematic regions within an anchoring energy cell. The easy alignment axis of the bottom carboranethiol alignment layer (η_0-bottom) was found by rotating the cell with respect to crossed polarizers while examining an untwisted nematic region. There, transmission minima occur when η_0-bottom coincides with either of the polarizer or analyzer axes. After aligning η_0-bottom with the polarizer, the easy axis of the top carboranethiol alignment layer (η_0-top) was identified by rotating the analyzer with respect the fixed cell until the intensity of light transmitted through the second untwisted nematic region was minimized. In doing so, the analyzer was aligned perpendicular to η_0-top. The relative angle formed between the polarizer and analyzer axes equaled δ. Finally, the optical transmittance in the central, twisted nematic, region was minimized by, again, rotating the analyzer while keeping the cell orientation fixed. In this configuration, the analyzer was orthogonal to the equilibrium orientation of the director anchored by the top alignment layer (η_d-top), and the angle formed between the analyzer and polarizer axes equaled γ.

Once δ and γ were determined, the angle (φ) by which the azimuthal orientation of the director departs from the easy alignment axes and the angular twist (Ψ) of the director through the cell's thickness were found using the equations:

$$\varphi = \delta - (\gamma - 90°)$$

$$\Psi = 2(\gamma - 90°) - \delta$$

The anchoring energies reported in Table 2.1 represent a weighted average of measurements made on multiple cells (at least four of a given isomer) and multiple areas within each cell (up to 10). We computed the uncertainties (σ) of d, φ, and Ψ using the following equations:

$$\sigma_d = \frac{\sigma_\Gamma}{\Delta n}$$

$$\sigma_\varphi = \sqrt{\sigma_\delta^2 + \sigma_\gamma^2}$$

$$\sigma_\Psi = \sqrt{\sigma_\delta^2 + (2\sigma_\gamma)^2}$$

The partial derivatives of W_{az} were found with respect to φ, Ψ, and d, as shown below:

$$\frac{\partial W_{az}}{\partial \Psi} = \frac{2K_{22}}{d \sin(2\varphi)}$$

$$\frac{\partial W_{az}}{\partial \varphi} = \frac{-4K_{22}\Psi}{d \tan(2\varphi) \sin(2\varphi)}$$

$$\frac{\partial W_{az}}{\partial d} = \frac{-2K_{22}\Psi}{d^2 \sin(2\varphi)}$$

These quantities, evaluated using the parameters of each measurement, were then used to compute the uncertainty in W_{az} ($\sigma_{W_{az}}$):

$$\sigma_{W_{az}} = \sqrt{\left(\frac{\partial W_{az}}{\partial \Psi}\sigma_{\Psi}\right)^2 + \left(\frac{\partial W_{az}}{\partial \varphi}\sigma_{\varphi}\right)^2 + \left(\frac{\partial W_{az}}{\partial d}\sigma_{d}\right)^2}$$

The weighted average of W_{az} and $\sigma_{W_{az}}$ were calculated for i independent measurements using:

$$\text{Weighted Average } W_{az} = \left.\sum_i \frac{W_{az\,i}}{\sigma^2_{W_{az}\,i}}\right/ \sum_i \frac{1}{\sigma^2_{W_{az}\,i}}$$

$$\text{Weighted Average } \sigma_{W_{az}} = \left. 1 \right/ \sqrt{\sum_i \frac{1}{\sigma^2_{W_{az}\,i}}}$$

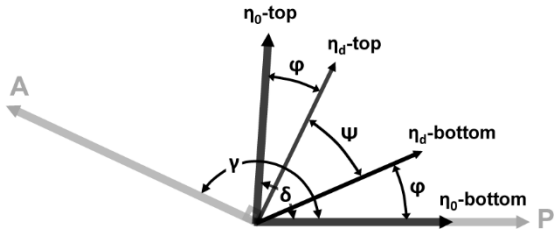

Figure 2.11: Schematic illustrating the angles used to compute the azimuthal anchoring energy. Orientations of the polarizer and analyzer are denoted by P and A, respectively. Easy alignment axes are indicated for the top (η_0-top) and bottom (η_0-bottom) alignment layers, while η_d-top and η_d-bottom indicate the equilibrium director orientations at the top and bottom alignment surfaces, respectively, as a result the opposing torques acting on the twisted nematic. The angle by which the azimuthal orientation of the director deviates from the easy axes is denoted by φ, whereas Ψ is the twist in the LC director between the top and bottom alignment surfaces. Figure adapted with permission from Ref. 78. Copyright 2006 American Chemical Society.

Table 2.3: Azimuthal anchoring energy (W_{az}) of 4-cyano-4′-pentylbiphenyl (5CB) liquid crystals in cells prepared with *m*-1-carboranethiol (M1) SAMs.

M1		**Γ (nm)**[a]	**δ (°)**[b]	**γ (°)**[c]	W_{az} **(μJ·m^{-2})**
Sample 1	Spot 1	1590	86.1	1.6	24 ± 3
	Spot 2	2120	86.2	0.8	21 ± 3
Sample 2	Spot 1	800	89.2	1.7	160 ± 30
	Spot 2	1060	89.0	1.2	90 ± 30
	Spot 3	1330	81.8	5.5	11 ± 1
	Spot 4	1590	88.6	1.3	49 ± 13
	Spot 5	1860	88.4	1.4	37 ± 9
	Spot 6	2120	88.5	0.9	41 ± 12
Sample 3	Spot 1	1860	88.0	1.3	35 ± 8
	Spot 2	2120	87.7	2.8	19 ± 3
Sample 4	Spot 1	800	89.1	1.5	110 ± 30
	Spot 2	1060	89.4	1.3	110 ± 40
	Spot 3	1330	89.6	1.0	120 ± 60
	Spot 4	1590	89.8	1.1	110 ± 60
	Spot 5	1860	89.8	0.6	150 ± 140
	Spot 6	2120	89.7	0.9	85 ± 51
	Spot 7	2390	89.9	0.4	180 ± 270
Sample 5	Spot 1	800	86.3	2.0	46 ± 6
	Spot 2	1060	85.0	3.3	24 ± 2
	Spot 3	1330	86.0	2.7	24 ± 3
	Spot 4	1590	85.6	2.9	18 ± 2
	Spot 5	1860	85.5	2.3	16 ± 2
	Spot 6	2120	85.5	3.0	13 ± 1
	Spot 7	2390	86.2	2.2	15 ± 2
	Spot 8	2660	85.7	2.6	11 ± 1
	Spot 9	2920	85.9	2.3	11 ± 1
	Spot 10	3190	86.3	1.9	12 ± 2
Sample 6	Spot 1	1330	88.9	0.8	85 ± 32
	Spot 2	1590	88.6	0.9	58 ± 18
	Spot 3	1860	88.6	0.4	65 ± 26
	Spot 4	2120	88.0	0.0	49 ± 17
	Spot 5	2390	88.0	0.7	32 ± 9
	Spot 6	2660	88.2	0.1	43 ± 17
	Spot 7	2920	88.5	0.1	45 ± 20
Sample 7	Spot 1	1330	86.7	2.7	26 ± 3
	Spot 2	1590	85.8	3.4	17 ± 2
Weighted Average (*n* = 36)					**14.3 ± 0.4**

[a]Retardation (Γ) between ordinary and extraordinary waves traversing the cell. All retardation values are assumed to have a measurement uncertainty of $\sigma_\Gamma = 50$ nm. [b]The angle (δ) formed between the alignment layers' easy axes. [c]The

angle (γ) formed between the polarizer and analyzer that minimizes transmittance through the twisted nematic region when the easy axis of the bottom alignment layer lies parallel to the polarizer axis. Uncertainties in the measured angles (δ and γ) are $\sigma_\delta = \sigma_\gamma = 0.5^\circ$.

Table 2.4: Azimuthal anchoring energy (W_{az}) of 4-cyano-4′-pentylbiphenyl (5CB) liquid crystals in cells prepared with *o*-1-carboranethiol (O1) SAMs.

O1		**Γ (nm)**[a]	**δ (°)**[b]	**γ (°)**[c]	**W_{az} (μJ·m^{-2})**
Sample 1	Spot 1	1060	84.7	3.5	22 ± 2
	Spot 2	1330	83.1	4.3	14 ± 1
	Spot 3	1590	84.8	2.9	16 ± 2
	Spot 4	1860	85.3	2.5	16 ± 2
	Spot 5	2120	85.4	2.2	14 ± 2
Sample 2	Spot 1	800	87.0	2.1	51 ± 8
	Spot 2	1060	86.7	3.4	29 ± 3
	Spot 3	1330	86.9	3.2	25 ± 3
	Spot 4	1590	86.9	2.5	24 ± 3
	Spot 5	1860	87.5	1.6	27 ± 5
	Spot 6	2120	87.2	0.1	35 ± 9
Sample 3	Spot 1	1330	88.3	3.5	30 ± 4
	Spot 2	1590	88.1	1.1	45 ± 11
	Spot 3	1860	88.7	2.4	30 ± 6
	Spot 4	2120	88.6	2.7	24 ± 4
	Spot 5	2390	89.4	2.3	30 ± 7
	Spot 6	2660	89.0	2.0	27 ± 6
Sample 4	Spot 1	2920	88.2	1.7	20 ± 4
	Spot 2	3190	88.0	1.4	19 ± 4
	Spot 3	3450	87.4	1.1	17 ± 3
Sample 5	Spot 1	530	81.9	0.5	46 ± 6
	Spot 2	800	85.3	4.8	27 ± 2
	Spot 3	1330	85.4	4.3	17 ± 2
	Spot 4	1590	85.4	2.3	19 ± 2
	Spot 5	1860	86.3	2.5	18 ± 2
	Spot 6	2120	85.7	3.7	12 ± 1
	Spot 7	2390	86.6	3.0	14 ± 2
	Spot 8	2660	86.8	2.6	13 ± 2
Sample 6	Spot 1	1060	85.7	3.7	24 ± 2
	Spot 2	1330	86.0	3.5	21 ± 2
	Spot 3	1590	86.0	2.8	19 ± 2
	Spot 4	1860	86.6	1.9	21 ± 3
	Spot 5	2120	86.4	2.9	15 ± 2
	Spot 6	2390	86.6	2.4	15 ± 2
	Spot 7	2660	86.6	2.4	14 ± 2
	Spot 8	2920	87.0	2.4	13 ± 2
	Spot 9	3190	87.2	1.9	14 ± 2
Weighted Average (*n* = 37)					**14.3 ± 0.4**

[a]Retardation (Γ) between ordinary and extraordinary waves traversing the cell. All retardation values are assumed to

have a measurement uncertainty of $\sigma_\Gamma = 50$ nm. [b]The angle (δ) formed between the alignment layers' easy axes. [c]The angle (γ) formed between the polarizer and analyzer that minimizes transmittance through the twisted nematic region when the easy axis of the bottom alignment layer lies parallel to the polarizer axis. Uncertainties in the measured angles (δ and γ) are $\sigma_\delta = \sigma_\gamma = 0.5^\circ$.

Table 2.5: Azimuthal anchoring energy (W_{az}) of 4-cyano-4′-pentylbiphenyl (5CB) liquid crystals in cells prepared with *o*-9-carboranethiol (O9) SAMs.

O9		**Γ (nm)**[a]	**δ (°)**[b]	**γ (°)**[c]	W_{az} **(μJ·m^{-2})**
Sample 1	Spot 1	1060	87.4	2.4	40 ± 6
	Spot 2	1590	87.5	2.3	27 ± 4
	Spot 3	3190	88.6	0.7	32 ± 11
Sample 2	Spot 1	1060	90.3	2.0	110 ± 50
	Spot 2	1330	90.0	1.6	96 ± 41
	Spot 3	1590	89.9	2.4	54 ± 16
	Spot 4	1860	89.4	0.8	83 ± 43
Sample 3	Spot 1	800	85.4	5.5	26 ± 2
	Spot 2	1060	83.4	7.6	14 ± 1
	Spot 3	1330	84.8	5.6	14 ± 1
	Spot 4	1590	84.9	7.0	11 ± 1
	Spot 5	1860	85.3	5.1	11 ± 1
	Spot 6	2120	84.3	6.5	7.9 ± 0.5
Sample 4	Spot 1	1060	84.4	4.3	20 ± 2
	Spot 2	1330	84.6	3.8	17 ± 1
	Spot 3	1590	84.7	4.0	14 ± 1
	Spot 4	1860	85.2	3.0	14 ± 1
	Spot 5	2120	85.7	3.3	13 ± 1
	Spot 6	2390	85.2	3.4	11 ± 1
Sample 5	Spot 1	1060	81.5	9.9	11 ± 1
	Spot 2	1330	83.4	7.4	11 ± 1
	Spot 3	1590	83.1	7.7	8.9 ± 0.5
	Spot 4	1860	83.5	6.7	8.4 ± 0.5
	Spot 5	2120	83.2	7.4	6.8 ± 0.4
	Spot 6	2390	83.7	6.4	6.8 ± 0.4
	Spot 7	2660	83.3	7.0	5.6 ± 0.3
	Spot 8	2920	83.7	6.5	5.5 ± 0.3
	Spot 9	3190	83.7	6.1	5.2 ± 0.3
Weighted Average (*n* = 28)					**7.5 ± 0.1**

[a]Retardation (Γ) between ordinary and extraordinary waves traversing the cell. All retardation values are assumed to have a measurement uncertainty of $\sigma_\Gamma = 50$ nm. [b]The angle (δ) formed between the alignment layers' easy axes. [c]The angle (γ) formed between the polarizer and analyzer that minimizes transmittance through the twisted nematic region when the easy axis of the bottom alignment layer lies parallel to the polarizer axis. Uncertainties in the measured angles (δ and γ) are $\sigma_\delta = \sigma_\gamma = 0.5°$.

Table 2.6: Azimuthal anchoring energy (W_{az}) of 4-cyano-4′-pentylbiphenyl (5CB) liquid crystals in cells prepared with *o*-9,12-carboranedithiol (9O12) SAMs.

9O12		**Γ (nm)**[a]	**δ (°)**[b]	**γ (°)**[c]	**W_{az} (μJ·m^{-2})**
Sample 1	Spot 1	800	86.2	4.6	31 ± 3
	Spot 2	1060	83.5	3.1	20 ± 2
	Spot 3	1330	84.7	0.3	28 ± 4
	Spot 4	1590	84.2	0.7	20 ± 2
	Spot 5	1860	85.5	2.0	17 ± 2
	Spot 6	2120	84.2	0.6	15 ± 2
	Spot 7	2390	85.9	0.8	18 ± 3
Sample 2	Spot 1	1590	89.9	3.4	38 ± 8
	Spot 2	1860	89.9	2.4	46 ± 13
	Spot 3	2120	88.7	2.2	29 ± 6
	Spot 4	2390	89.1	1.7	34 ± 9
	Spot 5	2660	89.9	2.4	32 ± 9
	Spot 6	2920	88.8	3.3	16 ± 3
Sample 3	Spot 1	1330	81.6	7.0	10 ± 1
	Spot 2	1590	80.9	7.5	7.8 ± 0.4
	Spot 3	1860	82.6	5.7	8.5 ± 0.5
	Spot 4	2120	81.9	6.5	6.6 ± 0.3
	Spot 5	2390	82.8	5.4	6.8 ± 0.4
	Spot 6	2660	81.8	5.8	5.6 ± 0.3
	Spot 7	2920	83.5	5.2	6.0 ± 0.4
	Spot 8	3190	81.5	6.4	4.3 ± 0.2
Sample 4	Spot 1	1330	85.8	5.8	16 ± 1
	Spot 2	1590	86.0	5.7	13 ± 1
	Spot 3	1860	85.8	3.8	14 ± 1
	Spot 4	2120	85.7	4.4	11 ± 1
	Spot 5	2390	86.0	2.9	13 ± 1
	Spot 6	2660	86.1	2.7	12 ± 1
	Spot 7	2920	85.9	2.4	11 ± 1
	Spot 8	3190	84.9	3.0	8.0 ± 0.7
Weighted Average (*n* = 29)					**6.7 ± 0.1**

[a]Retardation (Γ) between ordinary and extraordinary waves traversing the cell. All retardation values are assumed to have a measurement uncertainty of $\sigma_\Gamma = 50$ nm. [b]The angle (δ) formed between the alignment layers' easy axes. [c]The angle (γ) formed between the polarizer and analyzer that minimizes transmittance through the twisted nematic region when the easy axis of the bottom alignment layer lies parallel to the polarizer axis. Uncertainties in the measured angles (δ and γ) are $\sigma_\delta = \sigma_\gamma = 0.5°$.

Oblique Gold Deposition

Gold was deposited at an oblique angle (50° away from the normal) onto glass substrates, as shown in Figure 2.12. This angle describes the incidence angle of metal deposited in the center of the tilted substrate, located directly above the metal source. However, for extended substrates, this angle depends on the surface's distance away from the central deposition axis. Here, this deviation is no more than 6° from the intended deposition angle.

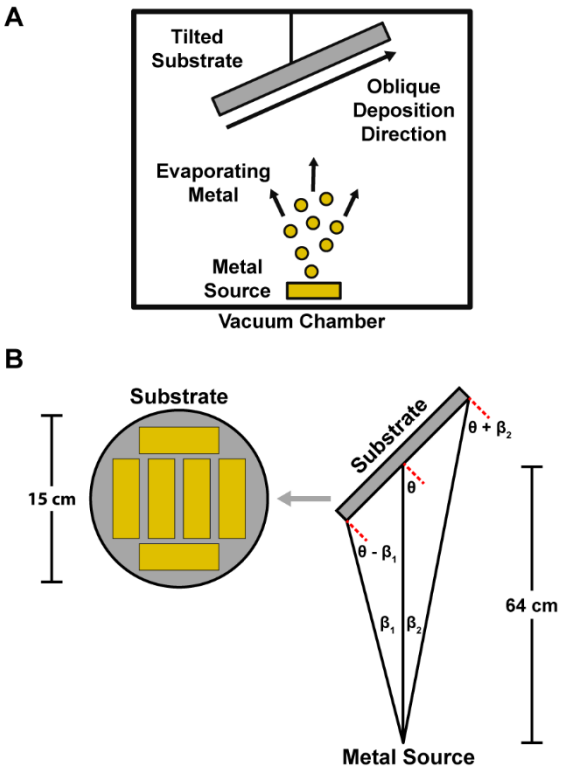

Figure 2.12: Schematic of oblique gold deposition. (A) Inside a vacuum chamber, gold is heated by an electron beam (not shown), causing it to evaporate from a source and deposit onto a tiled substrate located above. (B) Due to the non-zero widths and arrangement of glass, the deposition angle varies across the surface and between slides. Deviations from the intended angle ($\theta = 50°$) are expected to be, at most, $\beta_1 \approx \beta_2 \approx 6°$ for the dimensions and configuration used in this work.

Gaussian Calculations

Molecular Dipole Moments. Table 2.7 summarizes the molecular dipole moments of M9, M1, O9, O1, 9O12, and 1O2 calculated using density functional theory and the Gaussian 09 software package at the M062X level with the 6-311G** basis set. Dipole component vectors ($p_{||}$ and $p_{\perp}$) assume upright adsorption of the carboranethiol species on a gold surface.

Table 2.7: Molecular dipole moments (p) of carboranethiol and -dithiol isomers.

Isomer	Molecular Dipole Moment (D)		
	Magnitude	$\boldsymbol{p}_{\|\|}$ [a]	$\boldsymbol{p}_{\perp}$ [b]
M9[c]	3.94	1.38	3.70
M1[d]	2.20	2.13	-0.558
O9[e]	5.46	2.18	5.01
O1[f]	3.59	1.90	-3.05
9O12[g]	6.78	0.00	6.78
1O2[h]	3.20	0.00	-3.20

[a]In-plane dipole moment, parallel to the surface. [b]Out-of-plane dipole moment, normal to the surface. [c]*m*-9-carboranethiol (M9). [d]*m*-1-carboranethiol (M1). [e]*o*-9-carboranethiol (O9). [f]*o*-1-carboranethiol (O1). [g]*o*-9,12-carboranedithiol (9O12). [h]*o*-1,2-carboranedithiol (1O2).

Molecular Polarizability Tensor. The molecular polarizability tensors (α) of all six carboranethiols studied here were computed with the Gaussian 09 software package:

$$\alpha = \begin{bmatrix} \alpha_{xx} & \alpha_{xy} & \alpha_{xz} \\ \alpha_{xy} & \alpha_{yy} & \alpha_{yz} \\ \alpha_{xz} & \alpha_{yz} & \alpha_{zz} \end{bmatrix}$$

As described in the main text, Cartesian coordinate bases were chosen for each isomer based on its molecular symmetry and assumed upright adsorption onto underlying gold substrates. We found the polarizability tensors of each isomer to be *nearly* diagonalized in the chosen coordinate basis.

As such, we consider only the carboranethiol polarizabilities along each of the coordinate axes (α_{xx}, α_{yy}, and α_{zz}), as summarized in Table 2.8.

Table 2.8: Molecular polarizabilities ($\boldsymbol{\alpha_{ii}}$) of carboranethiol and -dithiol isomers.

Isomer	Principal Polarizabilities (Å^3)		
	$\boldsymbol{\alpha_{xx}}$	$\boldsymbol{\alpha_{yy}}$	$\boldsymbol{\alpha_{zz}}$
M9[a]	19.4	19.2	24.3
M1[b]	19.4	19.6	23.6
O9[c]	19.5	19.8	24.0
O1[d]	19.4	19.7	23.7
9O12[e]	24.0	21.3	26.3
1O2[f]	23.4	21.3	26.4

[a]*m*-9-carboranethiol (M9). [b]*m*-1-carboranethiol (M1). [c]*o*-9-carboranethiol (O9). [d]*o*-1-carboranethiol (O1). [e]*o*-9,12-carboranedithiol (9O12). [f]*o*-1,2-carboranedithiol (1O2).

Optimized Molecular Geometries and Dipoles. Computed values of the molecular dipole vectors and polarizability tensors depend on the optimized orientation of the thiol moiety (S–H bond) in each carboranethiol isomer. However, the hydrogen on the molecule's thiol functionality is lost during chemisoption onto the gold surface (becoming -thiol*ate*). As such, the dipoles and polarizabilities computed for these structures do not accurately reflect those of the actual *adsorbed* molecule. To account for this change in molecular structure upon chemisorption, we computed the molecular dipoles and polarizabilities of each isomer as the average of those values from multiple (nearly degenerate) conformations of each isomer. Each molecular conformation was distinguished by the initial value of the carborane–sulfur–hydrogen dihedral angle in the unoptimized structure, reflecting the rotational symmetry of the thiol moieties in each isomer (five-fold and two-fold symmetries in the cases of mono- and dithiol species, respectively). Averaging

effectively eliminates the thiol contributions to the in-plane molecular dipole and polarizability. The tables below present the atomic coordinates of each structure after optimization, labeled with the initial thiol dihedral angles. During optimization, atoms in each structure were allowed to relax into their lowest energy positions with the exceptions of dihedral angles denoted by "F." In these "frozen" structures, the value of the thiol dihedral angle was not optimized in order to maintain the desired molecular symmetry. These molecular conformations do not represent energetically optimized structures. If optimized without restrictions, an unfavorable interaction between the electron deficient carbon atoms in the carborane cage and the polar S–H bond would cause the thiol dihedral angle to deviate significantly from its initial value and disrupt the symmetry of the model. As such, these structures were used with only partial structural optimization. We reiterate, however, that the adsorbed molecule does not possess the carborane–sulfur–hydrogen dihedral angle left unoptimized here. In the cases of carboranedithiol isomers, the two conformations are distinguished by an "M" (or its absence) in the table heading. These conformations are mirror-symmetric versions of the fully optimized structures, reflecting the bilateral symmetry of the dithiol species.

M9 (0°) Energy: -730.121306 E_h

Atom	Position Coordinates (Å)		
	X	Y	Z
B	0.112328	-0.4994	-1.422584
B	-1.393971	-1.240065	-0.862785
B	0.131359	1.192437	-0.906861
B	1.065263	-0.016128	-0.000362
B	0.115184	-1.520253	0.025303
B	-1.360695	1.500783	-0.024783
B	0.132472	1.22187	0.865364
B	0.113277	-0.451841	1.437922
B	-1.393854	-1.210304	0.904755
C	-1.319917	0.443261	1.287942
H	0.545346	-0.778257	-2.48149
H	0.633748	-2.580157	0.042517
H	0.562947	2.034117	-1.609023
H	-1.965234	2.508414	-0.040872
H	0.54684	-0.695522	2.505253
H	0.564102	2.086491	1.539219
H	-1.978863	-1.950561	1.609212
H	-1.979496	-2.003201	-1.541961
B	-2.308671	-0.005531	0.000636
C	-1.321212	0.400457	-1.301621
H	-1.816124	0.69738	-2.21541
H	-3.478525	0.103897	-0.00055
H	-1.813884	0.770472	2.191888
S	2.927707	-0.084822	-0.000618
H	3.119158	1.243927	0.010164

M9 (72°, F) Energy: -730.121033 E_h

Atom	Position Coordinates (Å)		
	X	Y	Z
B	-0.107117	1.489342	-0.232513
B	1.407478	1.341038	0.681516
B	-0.124049	0.23107	-1.485054
B	-1.064653	0.023934	0.015641
B	-0.099851	0.71243	1.358978
B	1.361379	-0.70142	-1.331054
B	-0.144687	-1.331282	-0.667711
B	-0.12732	-1.032239	1.085953
B	1.396634	-0.222552	1.496113
C	1.298797	-1.351164	0.224497
H	-0.52408	2.559672	-0.494616
H	-0.619224	1.205486	2.295336
H	-0.556541	0.456686	-2.556171
H	1.961981	-1.17588	-2.222646
H	-0.567869	-1.855249	1.805434
H	-0.587619	-2.333491	-1.100653
H	1.982563	-0.502995	2.478173
H	2.004867	2.297188	1.021268
B	2.308309	-0.015211	0.004933
C	1.326391	0.944199	-0.974342
H	1.825069	1.607339	-1.666786
H	3.477842	-0.077383	-0.089676
H	1.778651	-2.3084	0.37096
S	-2.928377	0.083104	-0.008285
H	-3.103354	-1.236404	0.156996

M9 (144°) Energy: -730.121494 E_h

Atom	Position Coordinates (Å)		
	X	Y	Z
B	0.115038	-0.247782	1.486599
B	-1.389949	0.678357	1.355552
B	0.123054	-1.48438	0.211914
B	1.064465	0.002157	0.005351
B	0.124923	1.340214	0.714753
B	-1.376141	-1.318956	-0.701775
B	0.11839	-0.660627	-1.352864
B	0.124748	1.079833	-1.040262
B	-1.378709	1.50418	-0.204677
C	-1.321241	0.238252	-1.340791
H	0.547625	-0.521716	2.54693
H	0.654528	2.273163	1.206619
H	0.543676	-2.564026	0.422844
H	-1.989435	-2.205945	-1.168597
H	0.560845	1.805697	-1.859864
H	0.546522	-1.092243	-2.360608
H	-1.95537	2.496756	-0.466906
H	-1.972793	1.023154	2.318847
B	-2.308361	0.019761	0.005842
C	-1.322341	-0.970733	0.950342
H	-1.818246	-1.668702	1.609747
H	-3.479332	-0.064677	-0.041078
H	-1.815604	0.39646	-2.288699
S	2.927231	-0.080245	0.011026
H	3.116097	1.237102	-0.155119

M9 (216°) Energy: -730.121477 E_h

Atom	Position Coordinates (Å)		
	X	Y	Z
B	-0.124597	1.086609	-1.033387
B	1.379	1.505224	-0.195074
B	-0.118495	-0.651983	-1.35705
B	-1.06448	0.002546	0.005272
B	-0.124588	1.335919	0.723338
B	1.37587	-1.314633	-0.71017
B	-0.123365	-1.485513	0.202565
B	-0.115139	-0.256927	1.48488
B	1.390147	0.669584	1.359842
C	1.322024	-0.976836	0.944141
H	-0.560253	1.817911	-1.848367
H	-0.653903	2.265837	1.221148
H	-0.546574	-1.077265	-2.367499
H	1.988938	-2.198763	-1.182581
H	-0.548029	-0.537573	2.543311
H	-0.544392	-2.566275	0.40671
H	1.973231	1.007945	2.325235
H	1.955856	2.499308	-0.451081
B	2.308375	0.019311	0.005949
C	1.321141	0.246531	-1.339235
H	1.815492	0.410709	-2.286122
H	3.479296	-0.064984	-0.041786
H	1.817685	-1.679032	1.599219
S	-2.927112	-0.080227	0.011179
H	-3.116187	1.236947	-0.157323

M9 (288°, F) Energy: -730.121018 E_h

Atom	Position Coordinates (Å)		
	X	Y	Z
B	0.127109	-1.028763	1.089338
B	-1.396597	-0.217475	1.496728
B	0.144485	-1.33351	-0.663294
B	1.064659	0.023668	0.015675
B	0.099985	0.716784	1.356662
B	-1.361459	-0.705701	-1.328731
B	0.124055	0.226207	-1.485686
B	0.10728	1.488266	-0.237305
B	-1.407242	1.34333	0.677033
C	-1.326282	0.941081	-0.977404
H	0.567346	-1.849514	1.81159
H	0.619366	1.212841	2.291423
H	0.587356	-2.337148	-1.092998
H	-1.961899	-1.18308	-2.21888
H	0.524468	2.557678	-0.502845
H	0.556726	0.44801	-2.557526
H	-2.004556	2.300618	1.013718
H	-1.982526	-0.494497	2.479764
B	-2.308381	-0.014963	0.00492
C	-1.298953	-1.350281	0.228872
H	-1.778958	-2.306977	0.378352
H	-3.477942	-0.077368	-0.089287
H	-1.824922	1.602042	-1.671963
S	2.928368	0.083084	-0.008571
H	3.103583	-1.235965	0.160289

M1 (0°) Energy: -730.087128 E_h

Atom	Position Coordinates (Å)		
	X	Y	Z
B	-0.006375	-2.29319	0
B	-0.459726	-1.363726	1.437534
B	-0.459726	-1.363726	-1.437534
B	1.223728	-1.384639	-0.891013
B	1.223728	-1.384639	0.891013
B	-1.182181	0.149111	-0.892629
B	0.48693	0.123759	-1.444556
B	1.518888	0.119307	0
B	0.48693	0.123759	1.444556
B	0.024159	0.931496	0
S	0.083814	2.73539	0
H	-0.167801	-3.459906	0
H	2.067258	-1.914586	1.522554
H	2.067258	-1.914586	-1.522554
H	-0.921438	-1.89197	-2.383428
H	-2.065369	0.721566	-1.41736
H	-1.248119	2.907203	0
H	2.505108	0.764927	0
H	0.772391	0.773359	-2.38313
H	0.772391	0.773359	2.38313
H	-0.921438	-1.89197	2.383428
B	-1.182181	0.149111	0.892629
C	-1.363978	-1.267222	0
H	-2.347043	-1.716478	0
H	-2.065369	0.721566	1.41736

M1 (72°) Energy: -730.086719 E_h

Atom	Position Coordinates (Å)		
	X	Y	Z
B	-2.292922	0.008104	0.001202
B	-1.351529	1.477475	-0.319174
B	-1.366046	-1.382705	-0.59101
B	-1.384156	-0.997583	1.139364
B	-1.379755	0.774135	1.307899
B	0.135976	-0.774191	-1.272138
B	0.130363	-1.474634	0.347126
B	0.113794	-0.145286	1.521828
B	0.140591	1.378588	0.620809
C	0.931724	-0.00727	0.019786
S	2.734587	-0.082457	0.004335
H	-3.460917	0.028378	-0.149555
H	-1.904398	1.332514	2.204708
H	-1.913163	-1.710976	1.915695
H	-1.899745	-2.282461	-1.131451
H	0.704107	-1.213897	-2.20145
H	2.914123	1.246972	-0.047249
H	0.765394	-0.243144	2.497542
H	0.774677	-2.442482	0.538475
H	0.790995	2.289757	0.99037
H	-1.872732	2.469755	-0.681038
B	0.147192	0.989834	-1.103327
C	-1.281687	0.132558	-1.354182
H	-1.738415	0.228793	-2.329122
H	0.71892	1.595678	-1.932806

M1 (144°) Energy: -730.087017 E_h

Atom	Position Coordinates (Å)		
	X	Y	Z
B	-2.293109	0.017216	0.001486
B	-1.360217	0.669061	-1.354707
B	-1.373176	-1.313809	0.72623
B	-1.380499	0.282112	1.492663
B	-1.361946	1.51154	0.203894
B	0.134621	-1.474987	-0.174985
B	0.12058	-0.64859	1.381965
B	0.132345	1.09069	1.051876
B	0.143705	1.333847	-0.710188
C	0.932064	0.001243	0.013466
S	2.734744	-0.080646	-0.013276
H	-3.462148	-0.082814	-0.103683
H	-1.873994	2.567262	0.326204
H	-1.906431	0.46288	2.532934
H	-1.911767	-2.294378	1.094128
H	0.69376	-2.483458	-0.404766
H	2.912093	1.23049	0.212904
H	0.787364	1.799228	1.729461
H	0.766035	-1.098792	2.256971
H	0.799147	2.184055	-1.196109
H	-1.887121	0.999917	-2.354646
B	0.135456	-0.251719	-1.468886
C	-1.285171	-0.976151	-0.939641
H	-1.745808	-1.684442	-1.613714
H	0.7028	-0.536976	-2.456955

M1 (216°) Energy: -730.087017 E_h

Atom	Position Coordinates (Å)		
	X	Y	Z
B	2.293109	0.017216	0.001486
B	1.373176	-1.313809	0.72623
B	1.360217	0.669061	-1.354707
B	1.361946	1.51154	0.203894
B	1.380499	0.282112	1.492663
B	-0.135456	-0.251719	-1.468886
B	-0.143705	1.333847	-0.710188
B	-0.132345	1.09069	1.051876
B	-0.12058	-0.64859	1.381965
C	-0.932064	0.001243	0.013466
S	-2.734744	-0.080646	-0.013276
H	3.462148	-0.082814	-0.103683
H	1.906431	0.46288	2.532934
H	1.873994	2.567262	0.326204
H	1.887121	0.999917	-2.354646
H	-0.7028	-0.536976	-2.456955
H	-2.912093	1.23049	0.212904
H	-0.787364	1.799228	1.729461
H	-0.799147	2.184055	-1.196109
H	-0.766035	-1.098792	2.256971
H	1.911767	-2.294378	1.094128
B	-0.134621	-1.474987	-0.174985
C	1.285171	-0.976151	-0.939641
H	1.745808	-1.684442	-1.613714
H	-0.69376	-2.483458	-0.404766

M1 (288°) Energy: -730.086719 E_h

Atom	Position Coordinates (Å)		
	X	Y	Z
B	2.292922	0.008104	0.001202
B	1.366046	-1.382705	-0.59101
B	1.351529	1.477475	-0.319174
B	1.379755	0.774135	1.307899
B	1.384156	-0.997583	1.139364
B	-0.147192	0.989834	-1.103327
B	-0.140591	1.378588	0.620809
B	-0.113794	-0.145286	1.521828
B	-0.130363	-1.474634	0.347126
C	-0.931724	-0.00727	0.019786
S	-2.734587	-0.082457	0.004335
H	3.460917	0.028378	-0.149555
H	1.913163	-1.710976	1.915695
H	1.904398	1.332514	2.204708
H	1.872732	2.469755	-0.681038
H	-0.71892	1.595678	-1.932806
H	-2.914123	1.246972	-0.047249
H	-0.765394	-0.243144	2.497542
H	-0.790995	2.289757	0.99037
H	-0.774677	-2.442482	0.538475
H	1.899745	-2.282461	-1.131451
B	-0.135976	-0.774191	-1.272138
C	1.281687	0.132558	-1.354182
H	1.738415	0.228793	-2.329123
H	-0.704107	-1.213897	-2.20145

O9 (0°) Energy: -730.094599 E_h

Atom	Position Coordinates (Å)		
	X	Y	Z
B	0.542841	0.916284	0
B	1.083677	-0.516861	0.891108
B	1.083677	-0.516861	-0.891108
B	-0.350068	0.357946	-1.448694
B	-1.227917	0.912141	0
B	-0.350068	0.357946	1.448694
B	-0.350068	-1.400445	-1.44712
B	-1.778961	-0.51853	-0.88931
B	-1.778961	-0.51853	0.88931
B	-0.350068	-1.400445	1.44712
C	0.464261	-1.805781	0
C	-1.152496	-1.811643	0
H	-0.338989	0.957717	2.463669
H	-1.861642	1.90792	0
H	-0.338989	0.957717	-2.463669
H	2.096703	-0.672771	-1.472741
H	-0.344929	-2.189553	-2.319443
H	-2.788995	-0.685343	1.471825
H	-2.788995	-0.685343	-1.471825
H	-0.344929	-2.189553	2.319443
H	2.096703	-0.672771	1.472741
H	0.945015	-2.77296	0
H	-1.627003	-2.78164	0
S	1.505326	2.513933	0
H	2.719823	1.944986	0

O9 (72°) Energy: -730.0948 E_h

Atom	Position Coordinates (Å)		
	X	Y	Z
B	1.064565	-0.007598	0.027938
B	0.134338	-0.810727	-1.258873
B	0.143316	0.956589	-1.144262
B	0.12899	1.404468	0.576582
B	0.107352	-0.099379	1.526885
B	0.118428	-1.470079	0.38939
B	-1.357907	1.47662	-0.363681
B	-1.387357	0.81101	1.280286
B	-1.393438	-0.959102	1.166661
B	-1.371079	-1.41017	-0.549248
C	-1.287983	0.089642	-1.355432
C	-2.1468	0.007	0.006049
H	0.620355	-2.509586	0.634328
H	0.616099	-0.1701	2.588755
H	0.640394	2.4016	0.948246
H	0.552876	1.598589	-2.043203
H	-2.01611	2.381335	-0.726398
H	-2.075255	-1.594078	1.887139
H	-2.064889	1.354372	2.07603
H	-2.038895	-2.255197	-1.021612
H	0.540415	-1.333767	-2.232292
H	-1.853578	0.151736	-2.27357
H	-3.220411	0.019033	-0.108353
S	2.928301	-0.082815	0.011069
H	3.11884	1.243098	-0.068264

O9 (144°) Energy: -730.094923 E_h

Atom	Position Coordinates (Å)		
	X	Y	Z
B	1.065074	0.002122	0.023183
B	0.131243	-1.41369	-0.487481
B	0.136771	0.050894	-1.495056
B	0.133297	1.456604	-0.419792
B	0.121093	0.852553	1.261458
B	0.109025	-0.925264	1.219941
B	-1.363324	0.942262	-1.193502
B	-1.374003	1.431907	0.509057
B	-1.393051	-0.034717	1.511838
B	-1.37787	-1.444914	0.443129
C	-1.288402	-0.758845	-1.122134
C	-2.145982	0.016273	0.004706
H	0.614246	-1.594332	2.048968
H	0.631342	1.453155	2.140577
H	0.649726	2.46875	-0.739337
H	0.546208	-0.002402	-2.597481
H	-2.024455	1.432524	-2.033672
H	-2.075201	-0.078673	2.471003
H	-2.04357	2.353589	0.807858
H	-2.050969	-2.399175	0.583474
H	0.529885	-2.428919	-0.932385
H	-1.855808	-1.278364	-1.880146
H	-3.220111	-0.040784	-0.090707
S	2.927638	-0.075125	-0.021175
H	3.121548	1.183284	0.401344

O9 (216°) Energy: -730.094923 E_h

Atom	Position Coordinates (Å)		
	X	Y	Z
B	-1.065074	0.002122	0.023183
B	-0.136771	0.050906	-1.495056
B	-0.131243	-1.413686	-0.487492
B	-0.109025	-0.925274	1.219934
B	-0.121093	0.852544	1.261465
B	-0.133297	1.456607	-0.41978
B	1.37787	-1.444918	0.443117
B	1.393051	-0.034729	1.511837
B	1.374003	1.431903	0.509069
B	1.363324	0.942272	-1.193494
C	1.288402	-0.758837	-1.12214
C	2.145982	0.016273	0.004706
H	-0.649726	2.468756	-0.739317
H	-0.631342	1.453138	2.140589
H	-0.614246	-1.594348	2.048955
H	-0.529884	-2.428912	-0.932404
H	2.050969	-2.39918	0.583455
H	2.04357	2.353583	0.807876
H	2.075201	-0.078692	2.471003
H	2.024455	1.43254	-2.033661
H	-0.546207	-0.002381	-2.597482
H	1.855808	-1.278349	-1.880156
H	3.220111	-0.040784	-0.090707
S	-2.927638	-0.075125	-0.021175
H	-3.121547	1.183287	0.401335

O9 (288°) Energy: -730.094802 E_h

Atom	Position Coordinates (Å)		
	X	Y	Z
B	-1.064536	-0.007643	0.027622
B	-0.143157	0.954654	-1.145996
B	-0.134092	-0.812797	-1.257729
B	-0.11843	-1.469495	0.391623
B	-0.107604	-0.096901	1.526948
B	-0.129094	1.405411	0.574124
B	1.3712	-1.410938	-0.546798
B	1.393238	-0.957141	1.168435
B	1.387126	0.813125	1.279144
B	1.357892	1.475956	-0.36596
C	1.288246	0.087446	-1.355482
C	2.146739	0.007061	0.006297
H	-0.640899	2.402939	0.944164
H	-0.616934	-0.165838	2.588657
H	-0.620565	-2.508485	0.63831
H	-0.539891	-1.337663	-2.230285
H	2.039156	-2.25677	-1.017509
H	2.064568	1.358071	2.07388
H	2.075001	-1.591204	1.889772
H	2.016151	2.380114	-0.729966
H	-0.552612	1.595351	-2.045913
H	1.85402	0.148077	-2.273603
H	3.220378	0.018915	-0.107836
S	-2.928263	-0.082801	0.01103
H	-3.118797	1.243109	-0.068106

O1 (36°, F) Energy: -730.060377 E_h

Atom	Position Coordinates (Å)		
	X	Y	Z
B	-2.30685	0.033849	-0.027383
B	-1.328504	1.451868	-0.443923
B	-1.348304	0.036824	-1.512923
B	-1.395652	-1.419808	-0.50585
B	-1.421482	-0.895385	1.195554
B	-1.385301	0.882307	1.234811
B	0.121861	-0.902669	-1.218768
B	0.092666	-1.464022	0.464238
B	0.088928	-0.049452	1.542483
B	0.14777	1.401038	0.53479
C	0.094886	0.79469	-1.064737
C	0.919258	-0.049581	0.053283
S	2.718972	-0.073822	0.019126
H	-3.485049	0.078135	-0.074749
H	-1.884132	1.531127	2.084568
H	-1.955341	-1.531757	2.03398
H	-1.904568	-2.414726	-0.884153
H	-1.701203	0.148253	-2.631379
H	0.80432	-1.367142	-2.054957
H	2.852449	1.198599	-0.389503
H	0.749676	-0.06051	2.516726
H	0.743071	-2.408403	0.737016
H	0.836606	2.332059	0.745296
H	-1.669078	2.503683	-0.850972
H	0.699184	1.32844	-1.784302

O1 (108°) Energy: -730.064318 E_h

Atom	Position Coordinates (Å)		
	X	Y	Z
B	-2.306267	0.00202	-0.040636
B	-1.339281	0.75951	-1.314289
B	-1.341434	-1.003303	-1.132273
B	-1.38994	-1.384791	0.599931
B	-1.423673	0.156642	1.487431
B	-1.3781	1.484951	0.304025
B	0.139879	-1.475167	-0.273575
B	0.084712	-0.75728	1.347705
B	0.097254	1.006965	1.163099
B	0.143612	1.386444	-0.572655
C	0.086061	-0.135484	-1.328059
C	0.921732	0.001967	0.076731
S	2.710186	-0.082665	-0.015151
H	-3.48456	0.000161	-0.102136
H	-1.873222	2.53962	0.490543
H	-1.958579	0.268377	2.533586
H	-1.896601	-2.376141	0.990377
H	-1.693514	-1.691212	-2.021323
H	0.821799	-2.385723	-0.575103
H	2.902823	1.240347	0.102007
H	0.752809	1.668739	1.885281
H	0.738169	-1.2607	2.187737
H	0.829823	2.215287	-1.049843
H	-1.687246	1.253901	-2.325501
H	0.704755	-0.228859	-2.20906

O1 (180°) Energy: -730.060695 E_h

Atom	Position Coordinates (Å)		
	X	Y	Z
B	-0.027166	-2.3076	0
B	-1.220813	-1.348573	0.888096
B	-1.220813	-1.348573	-0.888096
B	0.460222	-1.389453	-1.442525
B	1.500646	-1.406745	0
B	0.460222	-1.389453	1.442525
B	-0.427438	0.12721	-1.45233
B	1.249234	0.101204	-0.890081
B	1.249234	0.101204	0.890081
B	-0.427438	0.12721	1.45233
C	-1.329101	0.090015	0
C	0.059761	0.918474	0
S	-0.089639	2.717101	0
H	-0.081066	-3.486251	0
H	0.759699	-1.890494	2.467891
H	2.560175	-1.927466	0
H	0.759699	-1.890494	-2.467891
H	-2.178727	-1.703393	-1.474799
H	-0.821022	0.810995	-2.323021
H	1.238015	2.913728	0
H	2.03239	0.761416	1.473893
H	2.03239	0.761416	-1.473893
H	-0.821022	0.810995	2.323021
H	-2.178727	-1.703393	1.474799
H	-2.230976	0.686226	0

O1 (252°) Energy: -730.064318 E_h

Atom	Position Coordinates (Å)		
	X	Y	Z
B	2.306267	0.00202	-0.040636
B	1.341434	-1.003303	-1.132273
B	1.339281	0.75951	-1.314289
B	1.3781	1.484951	0.304025
B	1.423673	0.156642	1.487431
B	1.38994	-1.384791	0.599931
B	-0.143612	1.386444	-0.572655
B	-0.097254	1.006965	1.163099
B	-0.084712	-0.75728	1.347705
B	-0.139879	-1.475167	-0.273575
C	-0.086061	-0.135484	-1.328059
C	-0.921732	0.001967	0.076731
S	-2.710186	-0.082665	-0.015151
H	3.48456	0.000161	-0.102136
H	1.896601	-2.376141	0.990377
H	1.958579	0.268377	2.533586
H	1.873222	2.53962	0.490543
H	1.687246	1.253901	-2.325501
H	-0.829823	2.215287	-1.049843
H	-2.902823	1.240347	0.102007
H	-0.738169	-1.2607	2.187737
H	-0.752809	1.668739	1.885281
H	-0.821799	-2.385723	-0.575103
H	1.693514	-1.691212	-2.021323
H	-0.704755	-0.228859	-2.20906

O1 (324°, F) Energy: -730.060377 E_h

Atom	Position Coordinates (Å)		
	X	Y	Z
B	2.30685	0.033849	-0.027383
B	1.348304	0.036824	-1.512923
B	1.328504	1.451868	-0.443923
B	1.385301	0.882307	1.234811
B	1.421482	-0.895385	1.195553
B	1.395652	-1.419808	-0.505851
B	-0.14777	1.401038	0.53479
B	-0.088928	-0.049452	1.542483
B	-0.092666	-1.464022	0.464238
B	-0.121862	-0.902669	-1.218768
C	-0.094886	0.79469	-1.064737
C	-0.919258	-0.049581	0.053283
S	-2.718972	-0.073822	0.019126
H	3.485049	0.078135	-0.074749
H	1.904568	-2.414726	-0.884153
H	1.955341	-1.531757	2.03398
H	1.884132	1.531127	2.084568
H	1.669078	2.503683	-0.850972
H	-0.836606	2.332059	0.745296
H	-2.852449	1.198599	-0.389503
H	-0.743071	-2.408403	0.737016
H	-0.749675	-0.060511	2.516726
H	-0.80432	-1.367142	-2.054957
H	1.701203	0.148253	-2.631379
H	-0.699184	1.32844	-1.784302

9O12 (±45°) Energy: -1128.303216 E_h

Atom	Position Coordinates (Å)		
	X	Y	Z
B	0.535882	0.897152	0.003172
B	-0.902604	1.433649	-0.889713
B	-0.902743	1.435681	0.882307
B	-0.015434	0.000035	1.441041
B	0.535975	-0.897034	0.003185
B	-0.014025	0.000031	-1.437214
B	-1.77226	-0.000068	1.446071
B	-0.902593	-1.435704	0.882248
B	-0.90249	-1.433668	-0.889672
B	-1.779833	-0.000048	-1.445936
C	-2.193546	0.806423	-0.003676
C	-2.193468	-0.806438	-0.003681
H	0.590193	0.000054	-2.450789
H	0.586889	0.000075	2.456094
H	-1.059389	2.445061	1.469722
H	-2.555257	-0.000124	2.323534
H	-1.054603	-2.441755	-1.477865
H	-1.059401	-2.444977	1.469814
H	-2.558908	-0.000119	-2.326608
H	-1.054576	2.441888	-1.477674
H	-3.16217	1.284042	0.000373
H	-3.161933	-1.284378	0.000376
S	2.111133	-1.884974	-0.066359
S	2.111078	1.885012	-0.066373
H	1.928085	-2.521092	1.101578
H	1.928399	2.520681	1.101867

9O12 (±45°, M) Energy: -1128.303216 E_h

Atom	Position Coordinates (Å)		
	X	Y	Z
B	-0.535882	0.897152	0.003172
B	0.902743	1.435681	0.882307
B	0.902604	1.433649	-0.889713
B	0.014025	0.000031	-1.437214
B	-0.535975	-0.897034	0.003185
B	0.015434	0.000035	1.441041
B	1.779833	-0.000048	-1.445936
B	0.90249	-1.433668	-0.889672
B	0.902593	-1.435704	0.882248
B	1.77226	-0.000068	1.446071
C	2.193546	0.806423	-0.003676
C	2.193468	-0.806438	-0.003682
H	-0.586889	0.000075	2.456094
H	-0.590193	0.000054	-2.450789
H	1.054576	2.441888	-1.477674
H	2.558908	-0.000119	-2.326608
H	1.059401	-2.444977	1.469814
H	1.054603	-2.441755	-1.477865
H	2.555257	-0.000124	2.323534
H	1.059389	2.445061	1.469722
H	3.16217	1.284042	0.000373
H	3.161933	-1.284378	0.000376
S	-2.111133	-1.884974	-0.066359
S	-2.111078	1.885012	-0.066373
H	-1.928085	-2.521092	1.101578
H	-1.928399	2.520681	1.101867

1O2 (±45°) Energy: -1128.239475 E_h

Atom	Position Coordinates (Å)		
	X	Y	Z
B	2.335055	0.883042	0.006139
B	0.913764	1.438384	-0.885606
B	0.904109	1.440401	0.884974
B	1.765084	-0.000011	1.443479
B	2.335052	-0.883037	0.006125
B	1.77926	0.000017	-1.434374
B	0.000667	0.000003	1.415744
B	0.904088	-1.440395	0.884941
B	0.91377	-1.438375	-0.885644
B	0.006779	0.00001	-1.418041
C	-0.409429	0.860743	-0.002616
C	-0.409434	-0.860747	-0.00264
H	2.354583	0.000047	-2.464216
H	2.330562	-0.000056	2.479187
H	0.734061	2.43911	1.487298
H	-0.78023	-0.000066	2.298465
H	0.746364	-2.436059	-1.487646
H	0.7341	-2.439103	1.487277
H	-0.771712	0.000081	-2.302012
H	0.746422	2.436074	-1.487613
H	3.322752	1.528521	0.012549
H	3.322727	-1.528551	0.012538
S	-1.969506	1.717671	-0.080274
S	-1.969479	-1.717719	-0.080256
H	-2.045457	-1.962396	1.23783
H	-2.045378	1.962987	1.237691

1O2 (±45°, M) Energy: -1128.239475 E_h

Atom	Position Coordinates (Å)		
	X	Y	Z
B	-2.335055	0.883042	0.006139
B	-0.904109	1.440401	0.884974
B	-0.913764	1.438384	-0.885606
B	-1.77926	0.000017	-1.434374
B	-2.335052	-0.883037	0.006125
B	-1.765084	-0.000011	1.443479
B	-0.006779	0.00001	-1.418041
B	-0.91377	-1.438375	-0.885644
B	-0.904088	-1.440395	0.884941
B	-0.000667	0.000003	1.415744
C	0.409429	0.860743	-0.002616
C	0.409434	-0.860747	-0.00264
H	-2.330562	-0.000056	2.479187
H	-2.354583	0.000047	-2.464216
H	-0.746422	2.436074	-1.487613
H	0.771712	0.000081	-2.302012
H	-0.7341	-2.439103	1.487277
H	-0.746364	-2.436059	-1.487646
H	0.78023	-0.000066	2.298465
H	-0.734061	2.43911	1.487298
H	-3.322752	1.528521	0.012549
H	-3.322727	-1.528551	0.012538
S	1.969506	1.717672	-0.080274
S	1.969479	-1.717719	-0.080256
H	2.045457	-1.962396	1.23783
H	2.045377	1.962988	1.237691

2.6 References and Notes

(1) Whitesides, G. M.; Grzybowski, B. Self-Assembly at All Scales. *Science* **2002**, *295*, 2418–2421.

(2) Smith, R. K.; Lewis, P. A.; Weiss, P. S. Patterning Self-Assembled Monolayers. *Prog. Surf. Sci.* **2004**, *75*, 1–68.

(3) Love, J. C.; Estroff, L. A.; Kriebel, J. K.; Nuzzo, R. G.; Whitesides, G. M. Self-Assembled Monolayers of Thiolates on Metals as a Form of Nanotechnology. *Chem. Rev.* **2005**, *105*, 1103–1170.

(4) Claridge, S. A.; Liao, W.-S.; Thomas, J. C.; Zhao, Y.; Cao, H. H.; Cheunkar, S.; Serino, A. C.; Andrews, A. M.; Weiss, P. S. From the Bottom up: Dimensional Control and Characterization in Molecular Monolayers. *Chem. Soc. Rev.* **2013**, *42*, 2725–2745.

(5) Fersht, A. R.; Matouschek, A.; Serrano, L. The Folding of an Enzyme: I. Theory of Protein Engineering Analysis of Stability and Pathway of Protein Folding. *J. Mol. Biol.* **1992**, *224*, 771–782.

(6) Kudernac, T.; Lei, S.; Elemans, J. A. A. W.; Feyter, S. D. Two-Dimensional Supramolecular Self-Assembly: Nanoporous Networks on Surfaces. *Chem. Soc. Rev.* **2009**, *38*, 402–421.

(7) Grzelczak, M.; Vermant, J.; Furst, E. M.; Liz-Marzán, L. M. Directed Self-Assembly of Nanoparticles. *ACS Nano* **2010**, *4*, 3591–3605.

(8) Israelachvili, J. N. *Intermolecular and Surface Forces*; Israelachvili, J. N., Ed.; Third Edition.; Academic Press: San Diego, 2011.

(9) Lee, H. J.; Jamison, A. C.; Lee, T. R. Surface Dipoles: A Growing Body of Evidence Supports Their Impact and Importance. *Acc. Chem. Res.* **2015**, *48*, 3007–3015.

(10) Paniagua, S. A.; Hotchkiss, P. J.; Jones, S. C.; Marder, S. R.; Mudalige, A.; Marrikar, F. S.; Pemberton, J. E.; Armstrong, N. R. Phosphonic Acid Modification of Indium−Tin Oxide Electrodes: Combined XPS/UPS/Contact Angle Studies. *J. Phys. Chem. C* **2008**, *112*, 7809–7817.

(11) Bishop, K. J. M.; Wilmer, C. E.; Soh, S.; Grzybowski, B. A. Nanoscale Forces and Their Uses in Self-Assembly. *Small* **2009**, *5*, 1600–1630.

(12) Liang, H.; Sun, W.; Jin, X.; Li, H.; Li, J.; Hu, X.; Teo, B. K.; Wu, K. Two-Dimensional Molecular Porous Networks Formed by Trimesic Acid and 4,4′-Bis(4-Pyridyl)biphenyl on Au(111) through Hierarchical Hydrogen Bonds: Structural Systematics and Control of Nanopore Size and Shape. *Angew. Chem. Int. Ed.* **2011**, *50*, 7562–7566.

(13) Kim, J.; Rim, Y. S.; Liu, Y.; Serino, A. C.; Thomas, J. C.; Chen, H.; Yang, Y.; Weiss, P. S. Interface Control in Organic Electronics Using Mixed Monolayers of Carboranethiol Isomers. *Nano Lett.* **2014**, *14*, 2946–2951.

(14) Thomas, J. C.; Schwartz, J. J.; Hohman, J. N.; Claridge, S. A.; Auluck, H. S.; Serino, A. C.; Spokoyny, A. M.; Tran, G.; Kelly, K. F.; Mirkin, C. A.; Gilles, J.; Osher, S. J.; Weiss, P. S. Defect-Tolerant Aligned Dipoles within Two-Dimensional Plastic Lattices. *ACS Nano* **2015**, *9*, 4734–4742.

(15) Kulkarni, C.; Bejagam, K. K.; Senanayak, S. P.; Narayan, K. S.; Balasubramanian, S.; George, S. J. Dipole-Moment-Driven Cooperative Supramolecular Polymerization. *J. Am. Chem. Soc.* **2015**, *137*, 3924–3932.

(16) Lewis, P. A.; Smith, R. K.; Kelly, K. F.; Bumm, L. A.; Reed, S. M.; Clegg, R. S.; Gunderson, J. D.; Hutchison, J. E.; Weiss, P. S. The Role of Buried Hydrogen Bonds in Self-Assembled Mixed Composition Thiols on Au{111}. *J. Phys. Chem. B* **2001**, *105*, 10630–10636.

(17) Zhang, S. Fabrication of Novel Biomaterials through Molecular Self-Assembly. *Nat. Biotechnol.* **2003**, *21*, 1171–1178.

(18) Dameron, A. A.; Charles, L. F.; Weiss, P. S. Structures and Displacement of 1-Adamantanethiol Self-Assembled Monolayers on Au{111}. *J. Am. Chem. Soc.* **2005**, *127*, 8697–8704.

(19) Barth, J. V.; Costantini, G.; Kern, K. Engineering Atomic and Molecular Nanostructures at Surfaces. *Nature* **2005**, *437*, 671–679.

(20) Aizenberg, J.; Black, A. J.; Whitesides, G. M. Oriented Growth of Calcite Controlled by Self-Assembled Monolayers of Functionalized Alkanethiols Supported on Gold and Silver. *J. Am. Chem. Soc.* **1999**, *121*, 4500–4509.

(21) Chen, S.; Liu, L.; Zhou, J.; Jiang, S. Controlling Antibody Orientation on Charged Self-Assembled Monolayers. *Langmuir* **2003**, *19*, 2859–2864.

(22) Briseno, A. L.; Aizenberg, J.; Han, Y.-J.; Penkala, R. A.; Moon, H.; Lovinger, A. J.; Kloc, C.; Bao, Z. Patterned Growth of Large Oriented Organic Semiconductor Single Crystals on Self-Assembled Monolayer Templates. *J. Am. Chem. Soc.* **2005**, *127*, 12164–12165.

(23) Hermes, S.; Schröder, F.; Chelmowski, R.; Wöll, C.; Fischer, R. A. Selective Nucleation and Growth of Metal−Organic Open Framework Thin Films on Patterned COOH/CF_3-Terminated Self-Assembled Monolayers on Au(111). *J. Am. Chem. Soc.* **2005**, *127*, 13744–13745.

(24) Lee, C.-Y.; Gong, P.; Harbers, G. M.; Grainger, D. W.; Castner, D. G.; Gamble, L. J. Surface Coverage and Structure of Mixed DNA/Alkylthiol Monolayers on Gold: Characterization by XPS, NEXAFS, and Fluorescence Intensity Measurements. *Anal. Chem.* **2006**, *78*, 3316–3325.

(25) Scherb, C.; Schödel, A.; Bein, T. Directing the Structure of Metal–Organic Frameworks by Oriented Surface Growth on an Organic Monolayer. *Angew. Chem.* **2008**, *120*, 5861–5863.

(26) Yao, Y.; Dong, H.; Hu, W. Ordering of Conjugated Polymer Molecules: Recent Advances and Perspectives. *Polym. Chem.* **2013**, *4*, 5197–5205.

(27) Palma, C.-A.; Cecchini, M.; Samorì, P. Predicting Self-Assembly: From Empirism to Determinism. *Chem. Soc. Rev.* **2012**, *41*, 3713–3730.

(28) Roussel, T. J.; Barrena, E.; Ocal, C.; Faraudo, J. Predicting Supramolecular Self-Assembly on Reconstructed Metal Surfaces. *Nanoscale* **2014**, *6*, 7991–8001.

(29) Meier, G.; Sackmann, E.; Grabmaier, J. G. *Applications of Liquid Crystals*; Springer-Verlag: Berlin, 1975.

(30) Gelbart, W. M. Molecular Theory of Nematic Liquid Crystals. *J. Phys. Chem.* **1982**, *86*, 4298–4307.

(31) Jerome, B. Surface Effects and Anchoring in Liquid Crystals. *Rep. Prog. Phys.* **1991**, *54*, 391.

(32) Lee, K.-W.; Paek, S.-H.; Lien, A.; Durning, C.; Fukuro, H. Microscopic Molecular Reorientation of Alignment Layer Polymer Surfaces Induced by Rubbing and Its Effects on LC Pretilt Angles. *Macromolecules* **1996**, *29*, 8894–8899.

(33) Stöhr, J.; Samant, M. G. Liquid Crystal Alignment by Rubbed Polymer Surfaces: A Microscopic Bond Orientation Model. *J. Electron Spectrosc. Relat. Phenom.* **1999**, *98–99*, 189–207.

(34) Janning, J. L. Thin Film Surface Orientation for Liquid Crystals. *Appl. Phys. Lett.* **1972**, *21*, 173–174.

(35) Ichimura, K. Photoalignment of Liquid-Crystal Systems. *Chem. Rev.* **2000**, *100*, 1847–1874.

(36) O'Neill, M.; Kelly, S. M. Photoinduced Surface Alignment for Liquid Crystal Displays. *J. Phys. D: Appl. Phys.* **2000**, *33*, R67–R84.

(37) Skaife, J. J.; Abbott, N. L. Quantitative Characterization of Obliquely Deposited Substrates of Gold by Atomic Force Microscopy: Influence of Substrate Topography on Anchoring of Liquid Crystals. *Chem. Mater.* **1999**, *11*, 612–623.

(38) Wilderbeek, H. T. A.; van der Meer, F. J. A.; Feldman, K.; D. J. Broer; Bastiaansen, C. W. M. Alignment of Liquid Crystals on Self-Assembled Monolayers Using Ultra-Thin Gold Films. *Adv. Mater.* **2002**, *14*, 655–658.

(39) Berreman, D. W. Solid Surface Shape and the Alignment of an Adjacent Nematic Liquid Crystal. *Phys. Rev. Lett.* **1972**, *28*, 1683–1686.

(40) Abelmann, L.; Lodder, C. Oblique Evaporation and Surface Diffusion. *Thin Solid Films* **1997**, *305*, 1–21.

(41) Follonier, S.; Miller, W. J. W.; Abbott, N. L.; Knoesen, A. Characterization of the Molecular Orientation of Self-Assembled Monolayers of Alkanethiols on Obliquely Deposited Gold Films by Using Infrared−Visible Sum-Frequency Spectroscopy. *Langmuir* **2003**, *19*, 10501–10509.

(42) Hoogboom, J.; Rasing, T.; Rowan, A. E.; Nolte, R. J. M. LCD Alignment Layers. Controlling Nematic Domain Properties. *J. Mater. Chem.* **2006**, *16*, 1305–1314.

(43) Drawhorn, R. A.; Abbott, N. L. Anchoring of Nematic Liquid Crystals on Self-Assembled Monolayers Formed from Alkanethiols on Semitransparent Films of Gold. *J. Phys. Chem.* **1995**, *99*, 16511–16515.

(44) Evans, S. D.; Allinson, H.; Boden, N.; Henderson, J. R. Surface-Field Induced Organisation at Solid/fluid Interfaces. *Faraday Discuss.* **1996**, *104*, 37–48.

(45) Gupta, V. K.; Abbott, N. L. Uniform Anchoring of Nematic Liquid Crystals on Self-Assembled Monolayers Formed from Alkanethiols on Obliquely Deposited Films of Gold. *Langmuir* **1996**, *12*, 2587–2593.

(46) Gupta, V. K.; Abbott, N. L. Azimuthal Anchoring Transition of Nematic Liquid Crystals on Self-Assembled Monolayers Formed from Odd and Even Alkanethiols. *Phys. Rev. E* **1996**, *54*, R4540–R4543.

(47) Gupta, V. K.; Abbott, N. L. Design of Surfaces for Patterned Alignment of Liquid Crystals on Planar and Curved Substrates. *Science* **1997**, *276*, 1533–1536.

(48) Alkhairalla, B.; Allinson, H.; Boden, N.; Evans, S. D.; Henderson, J. R. Anchoring and Orientational Wetting of Nematic Liquid Crystals on Self-Assembled Monolayer Substrates: An Evanescent Wave Ellipsometric Study. *Phys. Rev. E* **1999**, *59*, 3033–3039.

(49) Carlton, R. J.; Hunter, J. T.; Miller, D. S.; Abbasi, R.; Mushenheim, P. C.; Tan, L. N.; Abbott, N. L. Chemical and Biological Sensing Using Liquid Crystals. *Liq. Cryst. Rev.* **2013**, *1*, 29–51.

(50) Bramble, J. P.; Evans, S. D.; Henderson, J. R.; Anquetil, C.; Cleaver, D. J.; Smith, N. J. Nematic Liquid Crystal Alignment on Chemical Patterns. *Liq. Cryst.* **2007**, *34*, 1059–1069.

(51) Critchley, K.; Cheadle, E. M.; Zhang, H.-L.; Baldwin, K. J.; Liu, Q.; Cheng, Y.; Fukushima, H.; Tamaki, T.; Batchelder, D. N.; Bushby, R. J.; Evans, S. D. Surface Plasmon Raman Scattering Studies of Liquid Crystal Anchoring on Liquid-Crystal-Based Self-Assembled Monolayers. *J. Phys. Chem. B* **2009**, *113*, 15550–15557.

(52) Yoon, H.; Kang, S.-W.; Lehmann, M.; Park, J. O.; Srinivasarao, M.; Kumar, S. Homogeneous and Homeotropic Alignment of Bent-Core Uniaxial and Biaxial Nematic Liquid Crystals. *Soft Matter* **2011**, *7*, 8770–8775.

(53) Crawford, G. P.; Ondris-Crawford, R. J.; Doane, J. W.; Žumer, S. Systematic Study of Orientational Wetting and Anchoring at a Liquid-Crystal-Surfactant Interface. *Phys. Rev. E* **1996**, *53*, 3647–3661.

(54) Tao, F.; Bernasek, S. L. Understanding Odd−Even Effects in Organic Self-Assembled Monolayers. *Chem. Rev.* **2007**, *107*, 1408–1453.

(55) Nakata, M.; Zanchetta, G.; Buscaglia, M.; Bellini, T.; Clark, N. A. Liquid Crystal Alignment on a Chiral Surface: Interfacial Interaction with Sheared DNA Films. *Langmuir* **2008**, *24*, 10390–10394.

(56) Bai, Y.; Abbott, N. L. Enantiomeric Interactions between Liquid Crystals and Organized Monolayers of Tyrosine-Containing Dipeptides. *J. Am. Chem. Soc.* **2012**, *134*, 548–558.

(57) Bai, Y.; Abbasi, R.; Wang, C.; Abbott, N. L. Liquid Crystals Anchored on Mixed Monolayers of Chiral versus Achiral Molecules: Continuous Change in Orientation as a Function of Enantiomeric Excess. *Angew. Chem. Int. Ed.* **2014**, *53*, 8079–8083.

(58) Grimes, R. N. *Carboranes*; Second Edition.; Academic Press: Oxford, 2011.

(59) Kaszynski, P.; G. Douglass, A. Organic Derivatives of Closo-Boranes: A New Class of Liquid Crystal Materials. *J. Organomet. Chem.* **1999**, *581*, 28–38.

(60) Hohman, J. N.; Zhang, P.; Morin, E. I.; Han, P.; Kim, M.; Kurland, A. R.; McClanahan, P. D.; Balema, V. P.; Weiss, P. S. Self-Assembly of Carboranethiol Isomers on Au{111}: Intermolecular Interactions Determined by Molecular Dipole Orientations. *ACS Nano* **2009**, *3*, 527–536.

(61) Hohman, J. N.; Claridge, S. A.; Kim, M.; Weiss, P. S. Cage Molecules for Self-Assembly. *Mater. Sci. Eng., R* **2010**, *70*, 188–208.

(62) Cioran, A. M.; Musteti, A. D.; Teixidor, F.; Krpetić, Ž.; Prior, I. A.; He, Q.; Kiely, C. J.; Brust, M.; Viñas, C. Mercaptocarborane-Capped Gold Nanoparticles: Electron Pools and Ion Traps with Switchable Hydrophilicity. *J. Am. Chem. Soc.* **2012**, *134*, 212–221.

(63) Kabytaev, K. Z.; Everett, T. A.; Safronov, A. V.; Sevryugina, Y. V.; Jalisatgi, S. S.; Hawthorne, M. F. B-Mercaptocarboranes: A New Synthetic Route. *Eur. J. Inorg. Chem.* **2013**, *2013*, 2488–2491.

(64) Thomas, J. C.; Serino, A. C.; Goronzy, D. P.; Auluck, H. S.; Dadras, J.; Irving, O.; Deirmenjian, J. M.; Alexandrova, A.; Macháček, J.; Baše, T.; Weiss, P. S. Acid-Base Control of Valency within Carboranedithiol Self-Assembled Monolayers: Molecules Do the Can-Can.

(65) Kristiansen, K.; Stock, P.; Baimpos, T.; Raman, S.; Harada, J. K.; Israelachvili, J. N.; Valtiner, M. Influence of Molecular Dipole Orientations on Long-Range Exponential Interaction Forces at Hydrophobic Contacts in Aqueous Solutions. *ACS Nano* **2014**, *8*, 10870–10877.

(66) Dey, S.; Pal, A. J. Layer-by-Layer Electrostatic Assembly with a Control over Orientation of Molecules: Anisotropy of Electrical Conductivity and Dielectric Properties. *Langmuir* **2011**, *27*, 8687–8693.

(67) Brennan, T. P.; Tanskanen, J. T.; Bakke, J. R.; Nguyen, W. H.; Nordlund, D.; Toney, M. F.; McGehee, M. D.; Sellinger, A.; Bent, S. F. Dynamical Orientation of Large Molecules on Oxide Surfaces and Its Implications for Dye-Sensitized Solar Cells. *Chem. Mater.* **2013**, *25*, 4354–4363.

(68) Breuer, T.; Witte, G. Controlling Nanostructures by Templated Templates: Inheriting Molecular Orientation in Binary Heterostructures. *ACS Appl. Mater. Interfaces* **2015**.

(69) Pang, S. H.; Medlin, J. W. Controlling Catalytic Selectivity via Adsorbate Orientation on the Surface: From Furfural Deoxygenation to Reactions of Epoxides. *J. Phys. Chem. Lett.* **2015**, *6*, 1348–1356.

(70) Arrows illustrating dipole moments point from regions of relative negative to positive charge within the molecule.

(71) Baše, T.; Bastl, Z.; Šlouf, M.; Klementová, M.; Šubrt, J.; Vetushka, A.; Ledinský, M.; Fejfar, A.; Macháček, J.; Carr, M. J.; Londesborough, M. G. S. Gold Micrometer Crystals Modified with Carboranethiol Derivatives. *J. Phys. Chem. C* **2008**, *112*, 14446–14455.

(72) Lübben, J. F.; Baše, T.; Rupper, P.; Künniger, T.; Macháček, J.; Guimond, S. Tuning the Surface Potential of Ag Surfaces by Chemisorption of Oppositely-Oriented Thiolated Carborane Dipoles. *J. Colloid Interface Sci.* **2011**, *354*, 168–174.

(73) Kunkel, D. A.; Hooper, J.; Simpson, S.; Miller, D. P.; Routaboul, L.; Braunstein, P.; Doudin, B.; Beniwal, S.; Dowben, P.; Skomski, R.; Zurek, E.; Enders, A. Self-Assembly of Strongly Dipolar Molecules on Metal Surfaces. *J. Chem. Phys.* **2015**, *142*, 101921.

(74) Mauguin, C. Sur les cristaux liquides de Lehman. *Bull. Soc. Fr. Miner.* **1911**, *34*, 71–117.

(75) Fréedericksz, V.; Zolina, V. Forces Causing the Orientation of an Anisotropic Liquid. *Trans. Faraday Soc.* **1933**, *29*, 919–930.

(76) de Jeu, W. H. *Physical Properties of Liquid Crystalline Materials*; Gordon and Breach: New York, 1980.

(77) Fonseca, J. G.; Galerne, Y. Simple Method for Measuring the Azimuthal Anchoring Strength of Nematic Liquid Crystals. *Appl. Phys. Lett.* **2001**, *79*, 2910–2912.

(78) Clare, B. H.; Guzmán, O.; de Pablo, J. J.; Abbott, N. L. Measurement of the Azimuthal Anchoring Energy of Liquid Crystals in Contact with Oligo(Ethylene Glycol)-Terminated Self-Assembled Monolayers Supported on Obliquely Deposited Gold Films. *Langmuir* **2006**, *22*, 4654–4659.

(79) Sørensen, B. E. A Revised Michel-Lévy Interference Colour Chart Based on First-Principles Calculations. *Eur. J. Mineral.* **2013**, *25*, 5–10.

(80) Lowe, A. M.; Ozer, B. H.; Bai, Y.; Bertics, P. J.; Abbott, N. L. Design of Surfaces for Liquid Crystal-Based Bioanalytical Assays. *ACS Appl. Mater. Interfaces* **2010**, *2*, 722–731.

(81) Faetti, S.; Marianelli, P. Strong Azimuthal Anchoring Energy at a Nematic-Polyimide Interface. *Phys. Rev. E* **2005**, *72*, 051708.

(82) Anchoring energies depend on a variety of factors. When comparing values from such dissimilar surfaces, one should acknowledge the significant influence of textural and chemical differences in determining anchoring strengths.

(83) Skaife, J. J.; Brake, J. M.; Abbott, N. L. Influence of Nanometer-Scale Topography of Surfaces on the Orientational Response of Liquid Crystals to Proteins Specifically Bound to Surface-Immobilized Receptors. *Langmuir* **2001**, *17*, 5448–5457.

(84) Clare, B. H.; Guzmán, O.; de Pablo, J.; Abbott, N. L. Anchoring Energies of Liquid Crystals Measured on Surfaces Presenting Oligopeptides. *Langmuir* **2006**, *22*, 7776–7782.

(85) Otiti, T.; Niklasson, G. A.; Svedlindh, P.; Granqvist, C. G. Anisotropic Optical, Magnetic, and Electrical Properties of Obliquely Evaporated Ni Films. *Thin Solid Films* **1997**, *307*, 245–249.

(86) Everitt, D. L.; Miller, W. J. W.; Abbott, N. L.; Zhu, X. D. Evolution of a Preferred Orientation of Polycrystalline Grains in Obliquely Deposited Gold Films on an Amorphous Substrate. *Phys. Rev. B* **2000**, *62*, R4833–R4836.

(87) Jang, J. H.; Jacob, J.; Santos, G.; Lee, T. R.; Baldelli, S. Image Contrast in Sum Frequency Generation Microscopy Based on Monolayer Order and Coverage. *J. Phys. Chem. C* **2013**, *117*, 15192–15202.

(88) Smith, H. D.; Obenland, C. O.; Papetti, S. A New Series of Organoboranes. IX. The Preparation and Some Reactions of Sulfur-Carborane Derivatives. *Inorg. Chem.* **1966**, *5*, 1013–1015.

(89) Plešek, J.; Janoušek, Z.; Heřmánek, S. Synthesis and Properties of Some Icosahedral Carborane B,B'-Dithiols. *Collect. Czech. Chem. Commun.* **1980**, *45*, 1775–1779.

(90) Spokoyny, A. M.; Machan, C. W.; Clingerman, D. J.; Rosen, M. S.; Wiester, M. J.; Kennedy, R. D.; Stern, C. L.; Sarjeant, A. A.; Mirkin, C. A. A Coordination Chemistry Dichotomy for Icosahedral Carborane-Based Ligands. *Nat. Chem.* **2011**, *3*, 590–596.

(91) Schwartz, J. J.; Hohman, J. N.; Morin, E. I.; Weiss, P. S. Molecular Flux Dependence of Chemical Patterning by Microcontact Printing. *ACS Appl. Mater. Interfaces* **2013**, *5*, 10310–10316.

(92) Goerigk, L.; Grimme, S. A Thorough Benchmark of Density Functional Methods for General Main Group Thermochemistry, Kinetics, and Noncovalent Interactions. *Phys. Chem. Chem. Phys.* **2011**, *13*, 6670–6688.

(93) Hickey, A. L.; Rowley, C. N. Benchmarking Quantum Chemical Methods for the Calculation of Molecular Dipole Moments and Polarizabilities. *J. Phys. Chem. A* **2014**, *118*, 3678–3687.

(94) Toyooka, T.; Chen, G.; Takezoe, H.; Fukuda, A. Determination of Twist Elastic Constant K_{22} in 5CB by Four Independent Light-Scattering Techniques. *Jpn. J. Appl. Phys.* **1987**, *26*, 1959–1966.

(95) Belyaev, B. A.; Drokin, N. A.; Shabanov, V. F.; Shepov, V. N. Dielectric Anisotropy of 5CB Liquid Crystal in a Decimeter Wavelength Range. *Phys. Solid State* **2000**, *42*, 577–579.

(96) Li, J.; Wen, C.-H.; Gauza, S.; Lu, R.; Wu, S.-T. Refractive Indices of Liquid Crystals for Display Applications. *J. Disp. Technol.* **2005**, *1*, 51–61.

(97) Maurel, P.; Price, A. H. Dipole Moment of *N*-(*p*-Methoxybenzylidene)-*p*-Butylaniline. *J. Chem. Soc., Faraday Trans. 2* **1973**, *69*, 1486–1490.

CHAPTER 3

Towards Chemical Sensing and Atomic-Resolution Structural Determination via Nuclear Magnetic Resonance Scanning Tunneling Microscopy

3.1 Introduction

Uncovering the three-dimensional, atomic-scale structure of materials will transform our understanding of chemical and biological processes at the nanoscale. Many such processes involve a series of complex interactions between specific components and their surroundings.[1–5] Insight into the spatial distributions and chemical compositions of materials at the smallest scales will enable us to harness these processes and engineer new materials with tailored properties.[6] Techniques such as nuclear magnetic resonance (NMR) and X-ray diffraction reveal this information from certain classes of materials, but typically are limited to relatively simple structures or those that crystallize readily, and may require large quantities of pure analytes.[7,8] Expanding these capabilities to measure complex structures of single molecules represents one of

the great challenges faced by nanoscience today, and one that promises immense benefits when realized.

Here, we propose to determine the chemical compositions and three-dimensional structures of objects at the nanoscale. To accomplish this goal, we will monitor periodic fluctuations in the tunneling current of a STM corresponding to the precession of a sample's nuclear magnetic moments in an inhomogeneous magnetic field. Such measurements will enable nanoscale chemical identification of a sample's constituent nuclei with isotope selectivity. Molecular structure determination, in three dimensions, will be achieved by leveraging the sub-Ångström spatial precision of STM measurements[9] combined with high magnetic field gradients.[10] These capabilities will elucidate the buried structures of molecular monolayers and thin films that are not normally accessible to scanning probe measurements. Additionally, this technique may provide insight into the molecular structures of biomolecules,[11] and a means accessing long-lived nuclear spin states for spintronic applications.[12–14]

This project relies on the ability to detect magnetic dipole moments within an object related to its inherent, quantum-mechanical spin. A variety of sources may contribute to these magnetic moments, including unpaired electrons and certain atomic nuclei. These moments preferentially align parallel to applied magnetic fields, thereby magnetizing the object. If the total number (N) of dipole moments in the system is small, then the statistical fluctuations in dipole alignment (which scale as $\sqrt{N}$) dominate the instantaneous magnetization.[15–17] This "noise" signal[18] is the basis of two existing scanning probe techniques designed to measure nanoscale spins: electron spin noise STM (ESN-STM)[19,20] and magnetic resonance force microscopy (MRFM).[19,21] In the case of ESN-STM, the spin signal manifests itself as fluctuations in the tunneling current at the Larmor precession frequency of unpaired electrons within the sample. We hypothesize a similar

effect, modulated by nuclear spins, in the case of the proposed NMR-STM. Additionally, in the style of MRFM, we will employ a magnetic field gradient in order to determine the position of the spin within a molecular-scale measurement volume. Analogously to other magnetic resonance measurements, a magnetic field gradient will enable us to determine the spatial distribution of spins present within a measured region by virtue of variations in their Larmor frequencies.

Here, we outline the development of this project and a plan for its future with specific, carefully chosen, intermediate stages ("stepping stones") to assess its feasibility. The ultimate goal is to make nanoscale spin measurements with single-nucleus sensitivity and submolecular spatial resolution. We start by measuring an NMR style signals from individual magnetic nanoparticles. Following this experiment, we will scale down the target system to smaller particles and to molecules containing just a single nuclear dipole moment. Once proficient in detecting and localizing the nuclear spin signal in the plane of the substrate, we will add a strong magnetic field gradient to the measurement scheme. This known magnetic field gradient (see Section 3.8.3) will enable us to determine the position of the signal source(s) above/below the plane of the measurement (i.e., normal to the substrate surface), providing the third dimension of spatial localization (and resolution).

Systems targeted for investigation include: cobalt nanoparticles (Co-NPs),[22] organic molecules possessing a nuclear spin center (such as Co-phthalocyanine),[23,24] and linear, 'chain-like' molecules containing biologically relevant nuclei (such as molecules containing nitrogen,[25] phosphorus, and/or fluorine[26]). If the measurement technique proves successful, then the scope of target molecules will increase dramatically to include simple biological molecules, such as model peptides investigated elsewhere.[27,28]

3.2 Existing Nanoscale Spin Measurements

Spin spectroscopies, in the form of NMR and electron spin resonance (ESR),[29] have been integral to the understanding of molecular structure. Spin-flip resonance frequencies are exceedingly sensitive to the chemical environment of the sample due to coupling between a sample's electronic or nuclear spins to their surroundings. Differences in chemical bonding and nuclear (hyperfine) interactions modify the magnetic field sensed by the spin under investigation, thereby altering the splitting between accessible spin states. Typically, these techniques probe samples containing an ensemble of many, presumed identical, species targeted simultaneously. This ensemble-based measurement scheme is used, primary, due to insufficient detector sensitivities to the signal produced by only a few, or one, spin. In the case of magnetic resonance imaging (MRI), which also discerns spatial information in the measurement, the smallest probed volumes are on the order of cubic picometers,[30] far larger than the target systems (neurons) commonly examined, or the species targeted here. For these reasons, conventional NMR, MRI, and ESR spectroscopies are inadequate for nanoscale, single-molecule spin measurement and structural determinations. New measurement modalities for nanoscale spin detection have made remarkable progress: ESN-STM, MRFM, and nitrogen-vacancy spin-dependent fluorescence, each with their own advantages and disadvantages, as described below.

Electron Spin Noise Scanning Tunneling Microscopy

Electron spin noise STM (ESN-STM) utilizes similar principles to NMR and ESR to detect electronic spins within a single molecule. Conventional ESR techniques require the measurement of a minimum of $\sim 10^9 - 10^{10}$ spins in order to obtain a reliable signal.[31] By contrast, ESN-STM takes advantage of the inherently local nature of STM, as well as its sensitivity to the electronic properties of molecules in the tunneling junction, to probe individual spins on single molecules.

This technique was first discussed by Manassen and co-workers for single spins on partially oxidized silicon surfaces.[32,33] Durkan and Welland later demonstrated the ability to use ESN-STM to detect spin centers on individual α,γ-bisdiphenylene β-phenylallyl (BDPA) molecules.[34] More recently, others have collected ESN-STM spectra on other molecules containing free radicals;[35–37] such molecules are extensively studied using conventional ESR and thus make ideal candidates for preliminary ESN-STM measurements.

In ESN-STM, a static magnetic field (100−300 G) is applied normal to the sample surface, using a permanent magnet placed near the sample.[34] The magnetic field causes unpaired spins in the sample to align parallel (and antiparallel) to the axis of the field and to precess around this axis at a constant rate known as the Larmor frequency (for an electron, about 560 MHz at a field strength of 200 G). The precession of the electron spin dipole around the field manifests itself as a small time-varying (AC) current superimposed upon the constant (DC) tunneling current measured by STM, which is measured using a high-sensitivity spectrum analyzer. Signal-to-noise ratios can be improved by using phase-sensitive detection, which employs an additional, small (∼10 mG), time-varying magnetic field,[33,35] to modulate the AC resonance peak. Monitoring the shift in the resonance peak relative to the phase of the time-varying magnetic field improves the measurement sensitivity enabling real-time monitoring of the ESN-STM signal.

Magnetic Resonance Force Microscopy

At the nanoscale, a variation on atomic force microscopy (AFM) can detect electronic and nuclear spins through force-based measurements.[21] In magnetic resonance force microscopy (MRFM), samples are mounted on an ultrasensitive silicon cantilever and positioned about 25 nm from a magnetic nanoparticle. Due to the particle's shape and size, it produces a highly inhomogeneous magnetic field, with field gradients exceeding 10^6 T m^{-1} in the vicinity of the

sample.[38] The spatially dependent magnetic field from the nanoparticle, combined with an additional uniform field of around 2.8 T,[39] creates a small resonance region of aligned spins within the sample. The local magnetic field strength inside this resonance region is such that the Larmor precession frequency of the aligned spins matches the frequency of an applied radio frequency (RF) pulse. Measuring the resonant response of the cantilever to the RF pulse as it moves in a 3D raster pattern through the resonance region enables 3D mapping of spins within the sample.

Although conceptually similar to conventional magnetic resonance imaging (MRI), MRFM has important differences. In both techniques, the applied magnetic field polarizes the spins within the sample and induces a net magnetic dipole moment with a magnitude dependent on the Boltzmann distribution. In MFRM, however, the resonance region may contain as few as $\sim 10^3$ nuclear spins.[21,38,39] With such a small number of spins probed, the resulting Boltzmann polarization is relatively weak at commonly employed field strengths. Instead, the signal is derived from the larger "spin noise" ($\sqrt{N}$) statistical polarization, enabling measurements of about nine orders of magnitude fewer spins than required for MRI.[21] MRFM measures the force experienced by these polarized spins in the inhomogeneous magnetic field. This force (typically on the order of 10^{-17} N) generates sub-Ångström oscillations of the cantilever, detected via interferometry, as the spins are resonantly inverted by the RF pulse.[38]

Detecting such weak signals requires careful measurement techniques and instrument design. Maximizing the magnetic field gradient is critical to single-spin detection since larger gradients result in both higher forces acting on the magnetic moments (causing greater cantilever deflections) and smaller resonance regions (increasing spatial resolution and reducing the number of spins probed). To improve signal-to-noise ratios, relatively long averaging times (1−10 min per

pixel) are used. This necessitates an extremely stable environment, achieved by operating in high or ultrahigh vacuum and at low temperatures ($\sim 10^{-1}$ K).[21]

Rugar, Mamin, and co-workers have already demonstrated the ability to detect single electron spins with a spatial resolution of 25 nm in one dimension using MRFM.[40] Nuclear spin detection poses a greater challenge due to the much smaller magnitudes of nuclear magnetic moments ($\mu_{electron} \approx 650\ \mu_{proton}$). Currently, detection limits are still two to three orders of magnitude above those required for the detection of a single nuclear spin. However, spatial resolutions of <10 nm have been achieved, enabling imaging of large biological macromolecules such as tobacco mosaic virus.[38]

Nitrogen-Vacancy Spin Detection

Certain types of single spins can be detected optically, a property that may ultimately be used to understand single-molecule structures. Early optical single-spin detection was performed at cryogenic temperatures using single pentacene molecules embedded in *p*-terphenyl host crystals.[41,42] More recently, nitrogen-vacancy (NV) defects in diamond have enabled optical single-spin detection at room temperature,[43] which is being investigated both for quantum computing and as a detection method for single-molecule structure determination.

Nitrogen-vacancy defects in diamond have photon scattering cross sections that differ by approximately 30% based on their spin state.[43] A confocal microscope can be used to locate a single defect in either bulk diamond or a diamond nanocrystal and track its photon scattering over time, providing a readout of the spin state. Such systems are good quantum computing candidates since it is possible to pump spins to a known state optically and because the spins can be manipulated quickly (~10 ns) and have relatively long coherence times (up to 0.3 ms), making it possible to perform relatively large numbers of operations ($\sim 10^4$).[44]

As with NMR, the NV spin can couple with local magnetic fields from surrounding ^{13}C nuclei,[13] which split its degenerate spin states $m_s = \pm 1$, decreasing spin coherence times. However, such coupling can also be used to advantage since nuclear spins have longer coherence times. For instance, coupling with nuclear spins has been used both to allow multiple reads of the electron spin state[45] and to read out nuclear spins.[46]

More broadly, the ability of the nitrogen electron spin to make sensitive measurements of local magnetic fields opens the possibility of performing single-molecule structure measurements similar to NMR.[47,48] Fields as small as 3 nT can be detected in this way by using long averaging times (100 s) and spin echo pulsing tailored to decouple the NV spin from nearby ^{13}C nuclei;[47] this is roughly equivalent to the field produced by a nuclear spin at a distance of 10 nm. Magnetic scanning probes can also be incorporated to localize the single spin in space with nanometer-scale resolution.[48] More recently, NVs have been used to image the presence of multiple nuclear species (^{1}H, ^{19}F, ^{31}P) in nm-thick films of adsorbed water and hydrocarbons on a diamond surface, under ambient conditions.[49]

3.3 Experimental Plan & Reasoning

In the following sections, we detail the proposed measurement scheme, giving particular focus to Co-NPs as an ensemble nuclear spin system. We also summarize other, promising, target systems and their relative merits and challenges. Many design choices were made throughout this project to preserve biologically relevant measurement conditions: near room temperature (T ~300 K) and pressure (P ~760 Torr). By forgoing more controlled environments (cryogenic temperatures, $\lesssim$4 K, and ultrahigh vacuum, $<10^{-10}$ Torr), we enhance the chance that this technique may be used to determine the structures of biologically relevant molecules. Outside of their native environments, proteins and other bio-molecules may undergo significant conformational changes,

denaturation, or other changes to their structure that impact the applicability and relevance of the measurements. Nevertheless, many (non-biological) systems would be unaffected by these extreme environments – inorganic systems, such as Co-NPs, and alkanethiol self-assembled monolayers or their analogs. As such, we retain this option if our initial attempts are unsuccessful.

Ensemble Measurements

We expect the nuclear spin signal under investigation to be incredibly weak and challenging to detect based on the reported signal strengths and measurement capabilities of two analogous spin-measurement techniques, namely ESN-STM and MRFM. Although ESN-STM is reported to detect single-electron spins at room temperature,[32–35,37,50,36,51] it suffers from poor signal-to-noise ratio (SNR), with an estimated signal strength less than -120 dBm.[52,35] Similarly, MRFM[21,38–40,53,54] also suffers from poor SNR that is compensated using long signal-averaging times, at low temperature and under ultrahigh vacuum (though not always[55,56]), giving it the ability to detect ensembles of nuclear spins.[39] These difficulties are expected to be especially significant for measurements of just a few (or one) nuclear spins under ambient conditions due to the indirect coupling of the nuclear spins with tunneling electrons.[16,57–60] As such, first measuring an ensemble of numerous, identical, spins is expected to increase the overall signal strength proportional to the number of species probed. Thus, we start with what we hypothesize to be an easier goal: detecting the ensemble signal of many nuclei in a relatively large system (Co-NPs).

Choice of Cobalt Nanoparticles

There are a number of advantages to the choice of Co-NPs as the first measurement target. Cobalt exhibits room-temperature ferromagnetism, meaning that its nuclei will experience a high magnetic field inside the particles due to the spontaneous magnetization of its electron magnetic dipoles.[61] Additionally, the small size[62,63] and spherical shape[64] Co-NPs ensures that their internal

field will be nearly uniform and directed along a single-domain's magnetization for sufficiently small particles. Although the orientation of the magnetic dipoles of the particles will likely depend on a number of factors, evidence[65] suggests that they will adopt an out-of-plane orientation when deposited on Au{111} surfaces, matching the magnetizations used in ESN-STM. Cobalt's ferromagnetism will also enable greater coupling of the nuclear spin signal to the environment, enhancing its detectability compared to that of diamagnetic or paramagnetic materials.[66] Spherical cobalt particles, with diameters of 15 nm, contain approximately 10^5 cobalt atoms.[67] We hypothesize that this large collection of nuclear spins, precessing around a strong, nearly uniform magnetic field will increase the magnitude of the spin signal, making it easier to detect.

Cobalt is isotopically pure in its natural state; ^{59}Co has a 100% natural abundance and possesses a relatively large nuclear dipole moment ($\mu = 4.63\ \mu_N$, spin = $\frac{7}{2}\hbar$), [67] which may enhance the spin signal's magnitude. Its isotopic purity means that each Co nucleus will contribute to a single resonance, unlike other elements that may exhibit multiple resonances (due to differing isotopic dipoles), or reduced peaks (due to only a fraction of their isotopes possessing a nuclear dipole). Various isotopes commonly studied via NMR are shown in Table 3.1, along with their natural abundances, dipole moments, and precession frequencies. Several of these nuclei represent other potential targets for future studies, in particular ^{14}N and ^{39}F. However, we specifically avoid the most common NMR-studied isotope, ^{1}H, in these experiments due to its ubiquity in the measurement environment. Adsorbed water or advantageous organic contamination (–CH_2– or –CH_3 moieties) may make signal discrimination and interpretation extremely challenging in the case of ^{1}H.

Table 3.1: A partial list of isotopes possessing nuclear magnetic dipole moments, adapted from Reference 67.

Isotope	Spin (ħ)	Dipole Moment (μ_N)	Larmor Frequency (MHz T^{-1})	Natural Abundance (%)
^{1}H	$^{1}/_{2}$	2.79285	42.58	99.9885
^{2}H	1	0.85744	6.54	0.0115
^{13}C	$^{1}/_{2}$	0.70241	10.71	1.07
^{14}N	1	0.40376	3.08	99.636
^{15}N	$^{1}/_{2}$	0.28319	4.32	0.364
^{17}O	$^{5}/_{2}$	1.8938	5.77	0.038
^{19}F	$^{1}/_{2}$	2.62887	40.08	100
^{29}Si	$^{1}/_{2}$	0.5553	8.47	4.685
^{31}P	$^{1}/_{2}$	1.13160	17.25	100
^{33}S	$^{3}/_{2}$	0.64382	3.27	0.76
^{59}Co	$^{7}/_{2}$	4.63	10.1	100

Additionally, Co-NPs have already been shown to exhibit a nuclear resonance signal. Studies of bulk single- and multi-domain cobalt nanoparticles inside a cavity spectrometer show an electromagnetic absorption peak that is attributed to the ^{59}Co nuclear dipole resonance.[66,68,69] These earlier measurements on bulk cobalt power provide encouraging evidence supporting NMR-signal detection from isolated, single particles via STM. As such, in our first proof-of-concept experiments, we consider Co-NPs to be the target most likely to produce a detectable signal.

Cobalt Nanoparticle Characteristics

For the purposes of these experiments, we desire single-magnetic-domain particles in order to reduce uncertainty in their magnetization orientation. Additionally, single-domain structures preclude cross-domain coupling of magnetic dipoles, and could result in a stronger resonance signal since the spins will have only a single preferred alignment axis. By contrast, multi-domain particles will have at least two different internal field directions (and thus nuclear alignment directions), increasing uncertainty of the orientation of the nuclear moments probed. Additionally, nuclei in domain walls will experience different field strengths than those completely inside the domain, and thus will resonate at different frequencies, acting to broaden resonance peaks. Based on past NMR studies of cobalt powders, single-domain particles show greater variation in their resonance frequencies as a function of applied magnetic field, compared with multi-domain particles.[68] We will exploit this frequency shift to verify the origin of the detected signal by modulating the magnetic field strength with a small-amplitude AC field and a phase-sensitive detection scheme. This scheme is complicated in the case of multi-domain particles, with less well-defined magnetization directions and the potential for domain wall motion, which alters the magnetization with in less controlled ways (magnetic hysteresis), with applied fields.

To ensure that the Co-NPs exhibit ferromagnetism at the desired measurement temperatures, one must consider the blocking temperature (T_{blocking}) of the particles. This temperature is the maximum temperature at which the magnetization of single-domain particles is stable on the time scale of the measurement. Above T_{blocking}, the particles will respond superparamagnetically to applied fields and do not retain a permanent magnetization. This temperature is distinct from the Curie temperature (T_{Curie}) of the material; typically $T_{\text{blocking}} < T_{\text{Curie}}$. Modeling the variations of a particle's total magnetic dipole as a stochastic switching process, the

average time (τ_N) for its magnetization to 'relax' into a new, random orientation depends on several factors, including the particle size (volume, *V*) and anisotropy (*K*), as well as the absolute temperature (*T*), as described by the Néel-Arrhenius equation:[70,71]

$$\tau_N = \tau_0 \exp\left(\frac{KV}{k_B T}\right). \qquad \textbf{Eq. 3.1}$$

The coefficient τ_0 may be thought of as an 'attempt period,' characteristic of the material, which is typically in the range of nano- to picoseconds.[72,73] The exponential dependence on the effective energy barrier for dipole switching (*KV*) makes the relaxation times extremely sensitive to particle size since a particle's volume is proportional to the cube of its radius.[70,74]

As such, the size of the Co-NPs is an important characteristic to consider since it plays a critical role in determining their magnetic response. As discussed previously, we desire ferromagnetic, single-domain cobalt particles at room temperature. Particles below a certain threshold size will behave superparamagnetically (the superparamagnetic limit). Although the particles will possess only a single domain, below this limit, they suffer from diminished strengths of their net magnetic moment due to random (thermal) fluctuations in their dipole orientation. Such behavior may reduce, or prevent, NMR signal detection.[68] Conversely, particles that are too large may possess multiple magnetic domains. Large particles will also increase the difficulty of measuring surface topography, as STM is best suited to imaging very flat surfaces, ideally with only atomic or molecular scale changes in topography. Nanoparticles are obstacles that the STM tip must avoid while scanning the surface. For these reasons, particles with diameters of around 15 nm are chosen to be large enough to ensure room-temperature ferromagnetism (as explained below),[75,76] but small enough to contain only a single magnetic domain[70,75] without causing undue difficulty to imaging surface topography.[77–79]

Additionally, magnetic systems do not always respond in an isotropic manner to applied magnetic fields. The magnetic anisotropy parameters are a way to quantify this asymmetry and more accurately predict a system's magnetization. Magnetic anisotropy arises from a variety of sources, the more significant sources of which are the crystal structure of the material (crystalline anisotropy) and the material's geometry (shape anisotropy).[80] Additionally, the local environments of atoms on the surface also affects their magnetic behavior, an effect that becomes more pronounced for smaller systems with larger surface area to volume ratios.[81] Due to the system's magnetic anisotropy, dipoles within a material are predisposed to orient along certain crystallographic and geometric directions ("easy axes"), even in the absence of applied fields. As such, the system may be magnetized more easily along one direction compared to another. In large (macroscopic) objects, these influences may be negligible. However, in small systems, like nanoparticles, the magnetic anisotropy can play a significant role in determining their overall properties.[80]

The crystal structure of the nanoparticles will influence their magnetic anisotropy, which is also critical to ensuring their ferromagnetism. At room temperature, metallic cobalt is known to exist in three possible crystal phases: α-Co (hcp), β-Co (fcc), and ϵ-Co[82,83] (a cubic structure, similar to β-Mn), as illustrated in Figure 3.1.[84] Of these, α-Co is the most thermodynamically stable phase for bulk cobalt under standard conditions. Due to the small difference in crystal packing energy, however, β-Co is often found to coexist with α-Co, and may even be preferred in some cases for small particles.[85] While ϵ-Co nanoparticles are metastable at room temperature, they transform into the more-stable α-phase when annealed.[83] Nanoparticles of all three phases are strongly magnetic, but possess slightly different properties. Each phase possesses a characteristic magnetic anisotropy, which are reported to be 4.2×10^6, 2.7×10^6, and 1.5×10^6 erg cm^{-3} for α-Co,

β-Co, and ϵ-Co, respectively.[59] Here, anisotropies are specified in the centimeter-gram-second system of units commonly used for magnetic systems, but we specifically note the conversion to the meter-kilogram-second unit system (1 erg cm^{-3} = 0.1 J m^{-3}). Compare these with the magnetocrystalline anisotropy of bulk hcp (α-phase) cobalt of about 4.5×10^6 erg cm^{-3}.[86,87] Therefore, α-Co is the most desirable crystal phase for this experiment since its high magnetic anisotropy will help stabilize the orientation of a single-domain's magnetic moment. This stabilization enables the use of smaller diameter particles than those afforded by less-anisotropic crystal phases (see Eq. 3.1). By extension, ϵ-Co is the least desirable in this respect, as it possess the lowest crystalline anisotropy of the three phases. The ϵ-phase does possess one notable advantage over other crystal phases in that the nanoparticles tend to be more spherically shaped.[88] Nanoparticles synthesized in the α-phase tend to be less uniform and more irregularly ("potato") shaped compared to those synthesized in the ϵ-phase.[75,82,89] A uniform, nearly spherical, shape is desired for this experiment since the resulting magnetic field will be the simplest to predict and model and will produce a consistent NMR signal from each nanoparticle measured.

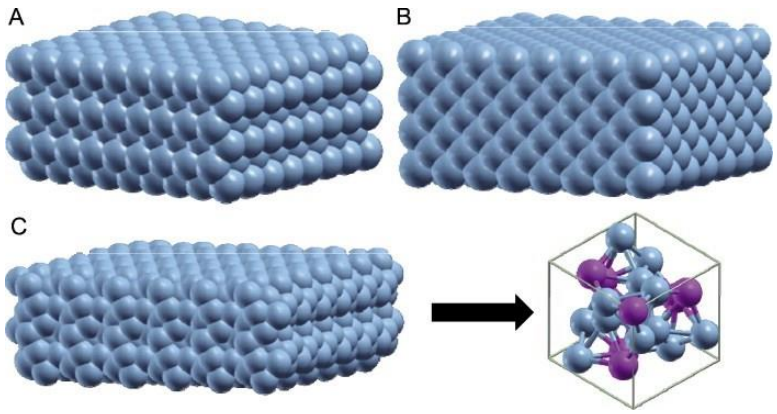

Figure 3.1: Schematic showing the different crystal structures of metallic cobalt: (A) α-Co, hcp; (B) β-Co, fcc; ϵ-Co. This figure is adapted with permission from Reference 84.

Uniaxial anisotropy of the Co-NPs is desired to ensure a known easy-axis of magnetization. Assuming spherically symmetric particles, the crystal structure will be the main contributor to their magnetic anisotropy, which predisposes the magnetization of the nanoparticle to lie along a particular crystallographic direction. In this respect, single-crystal α-Co nanoparticles are preferred as they exhibit strong uniaxial anisotropy along the *c*-axis of their hcp lattice.[86] However, even slight irregularities in the particle shape can be enough to cause uniaxial behavior in all phases of Co-NPs.[88,90]

Nanoparticle Surface Coverage

The Co-NPs must be deposited onto a smooth, conductive surface suitable for STM measurements. The diamagnetism, electrical conductivity, and well-studied chemistry make gold the most desirable substrate for use in this experiment. Alternatively, highly ordered pyrolytic graphite (HOPG), another common substrate for STM, may also be used, though it lacks the versatility of gold's surface functionalization chemistry and possesses a much greater diamagnetic susceptibility that can affect the magnetic field strength near the surface.

Ideally, Co-NPs should be dispersed uniformly over the entire sample surface such that isolated particles may be located readily. Practical STM scan areas are around 1 μm × 1 μm, though typically far less (smaller than 100 nm × 100 nm) in order to achieve molecular or atomic resolution of surface features. The areal density of Co-NPs on the surface should be sufficiently high such that, in a given (random) scan area near the sample's center, one is able to find at least one isolated nanoparticle without extensive searching. Nanoparticle densities that are too high may result in undesirable side-effects, such as nanoparticle aggregation and an effective increase in surface roughness that can hinder STM scanning. Additionally, the potential for magnetic dipole-dipole interactions between particles will increase with higher nanoparticle densities, which may

affect the NMR measurement. Minimizing this interparticle coupling simplifies the experiment, conceptually, and brings it closer to the goal of measuring the nuclear magnetic moment of individual nanoparticles. As such, areal densities of about 100 particles per μm^2 (1 particle per 100 nm × 100 nm scan area) are thought desirable. Section 3.3.5, below, provides an in-depth discussion of the strengths of interparticle interactions and their role in determining desired areal densities.

Magnetic Dipole-Dipole Interactions

Ferromagnetic dipole-dipole interactions can cause nanoparticle aggregation in solution and on surfaces, and may lead to rough, heterogeneous samples with perturbed nuclear resonant frequencies. Estimating the strengths of these interparticle interactions will assist in predicting their effects and planning this experiment. In this section, we describe a model of these interactions between neighboring magnetic nanoparticles and use it to estimate desired areal densities of deposited Co-NPs. This model accounts for the magnetic dipole-dipole interactions that exist between magnetically-hard particles possessing uniaxial anisotropy. The nanoparticles are assumed to have a spherical core-shell structure, as shown in Figure 3.2, where a "non-magnetic" shell (radius, R_{shell}), with a magnetic permeability equal to that of free space, surrounds a single-domain, ferromagnetic core (radius, R_{core}). We use the macrospin approximation to describe the magnetic moment of the nanoparticles as a single magnetic dipole located at the center of a nanoparticle. The results of this analysis are compared to previously published work that studied the formation of chain and ring structures of Co-NPs in solution using dynamics simulations based on a similar model to that used here.[91,92]

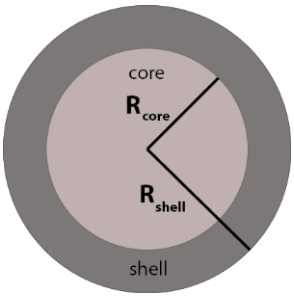

Figure 3.2: Schematic of a core-shell nanoparticle with a non-magnetic shell of radius R_{shell} (dark gray) surrounding a single-domain, ferromagnetic core with radius R_{core} (light gray); $R_{shell} \geq R_{core}$.

Due to the spherical shape of the nanoparticles, and the macrospin approximation, the magnetic induction ($\vec{B}$) produced by a single particle's dipole moment ($\vec{m}$) is estimated to be:

$$\vec{B}(\vec{r}) = \frac{\mu_0}{4\pi}\left[\frac{3(\vec{m}\cdot\hat{r})\hat{r} - \vec{m}}{r^3}\right], \qquad \textbf{Eq. 3.2}$$

where μ_0 is the permeability of free space and $\vec{r}$ is the position vector measured from the particle's center. The magnetization ($\vec{M}$) of an object is defined as its dipole moment per unit volume. We assume that the core of the nanoparticle is uniformly magnetized, therefore its total magnetic dipole moment may be calculated as:

$$\vec{m} = V_{\text{core}}\vec{M}_s = \frac{4}{3}\pi R_{\text{core}}^3\vec{M}_s, \qquad \textbf{Eq. 3.3}$$

where V_{core} is the volume of the spherical, single-domain nanoparticle with saturated magnetization $\vec{M}_s$. The potential energy of a magnetic dipole in an external field is given by:

$$E = -\vec{m}\cdot\vec{B}. \qquad \textbf{Eq. 3.4}$$

Combining these equations, the energy of one magnetic nanoparticle in the field produced by a neighboring nanoparticle is:

$$E = -V_{\text{core}}\vec{M}_{\text{s}} \cdot \frac{\mu_0}{4\pi}\left[\frac{3(\vec{m}\cdot\hat{r})\hat{r} - \vec{m}}{r^3}\right]. \qquad \textbf{Eq. 3.5}$$

This energy will be minimized when both dipoles are aligned along the same direction, denoted as $\hat{z}$, and arranged in a "head-to-tail" configuration, as illustrated in Figure 3.3, with particle core-core separation z. Thus, the interaction energy becomes:

$$E = -\frac{\mu_0 m V_{\text{core}} M_{\text{s}}}{2\pi}\frac{1}{z^3}. \qquad \textbf{Eq. 3.6}$$

The interaction energy is reduced further when the separation between the particles (z) is minimized, as a result of the attractive force experienced by the magnetic particles in this configuration. Due to their finite size, the shortest possible separation distance between the nanoparticles is twice the radius of their outer shells, $z \geq 2R_{\text{shell}}$. Thus, the minimum energy is:

$$E_{\text{min}} = -\frac{\mu_0\left(\frac{4}{3}\pi R_{\text{core}}^3 M_{\text{s}}\right)\left(\frac{4}{3}\pi R_{\text{core}}^3\right)M_{\text{s}}}{2\pi}\frac{1}{8R_{\text{shell}}^3}, \qquad \textbf{Eq. 3.7}$$

which further simplifies to:

$$E_{\text{min}} = -\frac{\mu_0 \pi M_s^2}{9}\frac{R_{\text{core}}^6}{R_{\text{shell}}^3} = -\eta\frac{R_{\text{core}}^6}{R_{\text{shell}}^3}, \qquad \textbf{Eq. 3.8}$$

Note that the interaction energy decreases (becomes more negative) as the cube of the particle radius. Thus, larger particles bind to each other more strongly than smaller particles. The saturation magnetization of bulk cobalt is $M_{\text{s}} = 1.44 \times 10^6$ A m^{-1} $=$ 162 emu g^{-1}.[93] With this parameter, the value of η in the above Eq. 3.8 is calculated to be $\eta = 9.10 \times 10^5$ J m^{-3}.

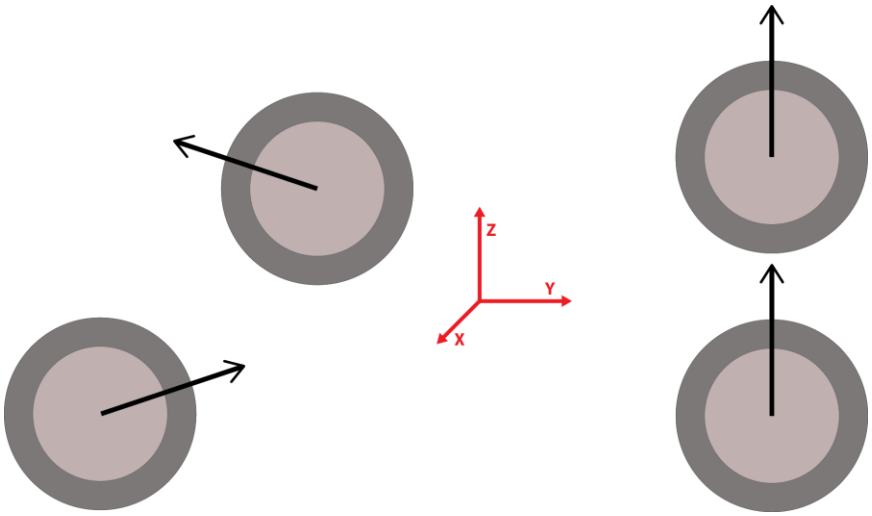

Figure 3.3: Two possible configurations of magnetic nanoparticles: particles with misaligned dipoles pointed in different directions (left) and particles with dipoles aligned along the same direction ($\hat{\boldsymbol{z}}$) in a head-to-tail configuration (right). Dipole moments shown as black arrows.

In order for the nanoparticles to aggregate, the binding energy must be comparable to, or larger than, the ambient thermal energy they possess. The average thermal energy of the particles may be estimated using the equipartition theorem, where

$$E_{\text{ave}} = \frac{f}{2} k_{\text{B}} T = \frac{5}{2} k_B (300 \text{ Kelvin}) = 1.04 \times 10^{-20} \text{ J} = 0.065 \text{ eV}, \qquad \textbf{Eq. 3.9}$$

where k_{B} is the Boltzmann constant, T is the absolute temperature of the system, and f is the number of degrees of freedom that the particles possess. In the situation modeled here, there are $f = 5$ degrees of freedom: 3 translational degrees of freedom (motion along the *x*-, *y*-, *z*-axes) and 2 rotational degrees of freedom (rotations about the *x*- and *y*-axes). Rotation about the z-axis, along which the magnetic moment of the particles aligns, does not produce a distinguishable change in the system and does not alter the magnetic energy, and should not be considered.

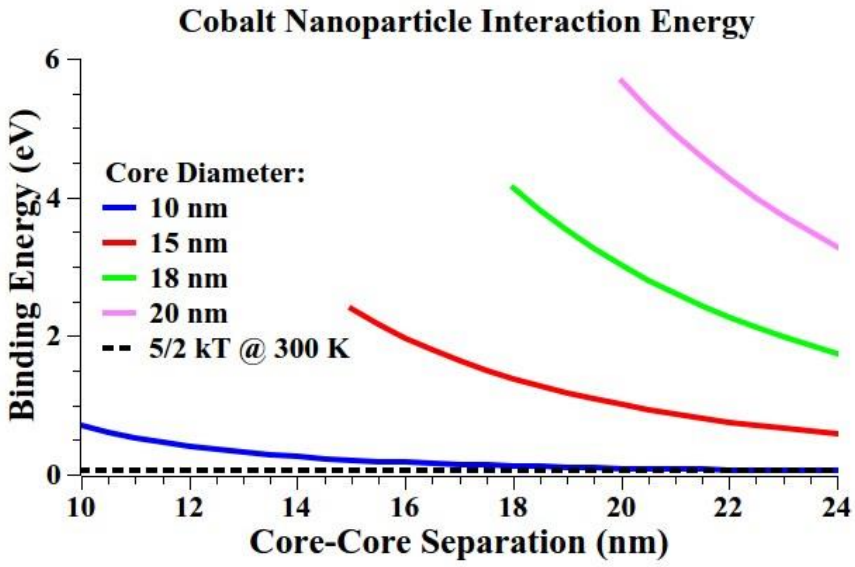

Figure 3.4: Head-to-tail magnetic dipole interaction energy of two ferromagnetic cobalt nanoparticles. In such a configuration, the particles experience an attractive force and are bound within a potential well, the depth of which is plotted above as a function of core-core separation distance. Here, greater binding energies represent more-strongly interacting particles. For comparison, the average (thermal) kinetic energy of the particles at 300 K is also plotted (dashed, black line).

Figure 3.4 shows the interaction energy of Co-NPs of various radii as a function of their core-core separation distance, where the thicknesses of their outer shells determines the minimum separation for each pair of particles. Reasonable values for R_{core} range from ~5 nm (below the superparamagnetic limit for cobalt, at room temperature), to 15 nm (approaching the large-diameter limit for use in this project). Table 3.2 lists the interaction energies of Co-NPs with a core diameter of 20 nm, larger and more interacting than particles used in these experiments. The interaction energy is less than the average thermal kinetic energy at room temperature for separation distances greater than 90 nm, and less than 10% of the thermal energy at 200 nm. As

such, interparticle coupling between Co-NPs on a surface separated by >100 nm is not expected to be significant. For Co-NPs with diameters smaller than 20 nm, the interaction energy will be less than the listed value due to the weaker dipole moment possessed by smaller particles.

Table 3.2: Interaction energies of cobalt nanoparticles with core diameters of 20 nm, separated by 25, 50, 75, 100, and 200 nm.

Core-Core Separation (nm)	Interaction Energy (eV)
25	2.9
50	0.36
75	0.11
100	0.045
200	0.0057

The favorable interaction energy and attractive force between the particles implies that they will aggregate in solution. However, the above analysis fails to account for other effects that disrupt nanoparticle aggregation, such as turbulence in solution or weakened magnetic moments due to the quenching of surface spins.[91,94] The size and crystal phase of the Co-NPs can significantly affect their saturation magnetization, which can be as low as 40% of the bulk value in the case of ϵ-Co.[95] Others have observed chain and ring-like structures to form spontaneously in solutions of Co-NPs with diameters larger than about 20–25 nm.[91,96,97] Dynamics simulations also predict the formation of nanoparticle structures for critical diameters around 9–12 nm.[91] In the present experiment, significant nanoparticle aggregation is not observed to occur. Therefore, disruptive effects of ultrasonication of the solution and ligand-induced solubility prevent

nanoparticle aggregation or the particles are below the superparamagnetic limit and therefore do not possess the permanent dipole moment needed for aggregation.

3.4 Cobalt Nanoparticles

We pursued multiple strategies of acquiring and depositing cobalt nanostructures onto a surface for subsequent STM studies. Below, we present the results of our efforts to synthesize and tailor the ligands of colloidal Co-NPs. However, we also discuss an alternative strategy of depositing cobalt metal via metal evaporation onto masked substrates.

Nanoparticle Synthesis

We synthesized Co-NPs using established procedures, as shown in Figure 3.5.[75,89] Particles prepared in this way are approximately the size (~15 nm), shape (semi-spherical), and crystal phase (α-Co) desired for our experiment. We can optimize the particles to our precise specifications through subtle tuning of the synthetic procedure. As noted in Section 3.3.3, Co-NPs synthesized in the α-phase tend to be less uniform and symmetric in shape than other crystal phases, most notably ϵ-Co. Thermal annealing, however, changes ϵ-Co nanoparticles (possessing the more-desirable shape) into α-Co nanoparticles (that have more desirable magnetic properties).[84] As such, post-synthesis annealing of ϵ-Co-NP may be used to obtain a more desirable product in the future.

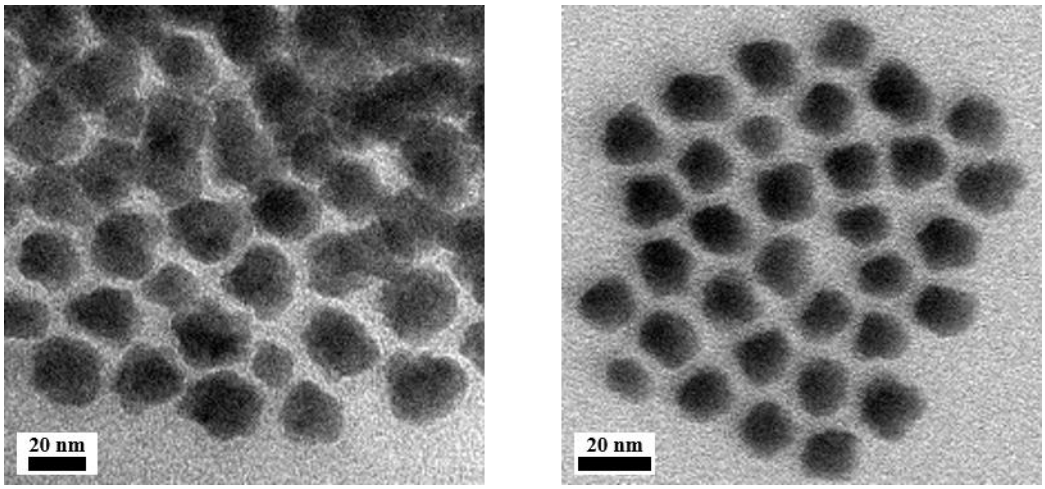

Figure 3.5: Transmission electron micrographs of synthesized cobalt nanoparticles. Particles exhibit a semi-spherical ("potato") shape with diameters of about 15–20 nm

Oxidation of the Co-NPs is a concern during synthesis and storage. Unprotected Co-NPs oxidize rapidly in air, and form a thin (~1 nm), passivating oxide layer in the presence of dissolved oxygen in solution.[82,83,98] A variety of ligands may be used to protect the nanoparticles and inhibit their oxidation, making them air-stable for many weeks or months.[82,99,100] The cobalt oxide that forms is a semiconductor that exhibits anti-ferromagnetic ordering[101] just below room temperature ($T_{\text{Néel}}$ = 291 K).[102–105] The oxide's band structure may complicate STM data collection,[106] and the differences in magnetic ordering and crystal structure between the oxide and metallic cobalt will alter the magnetic field at the nucleus.[107,108] The thin cobalt oxide layer is known to increase[109–112] the effective magnetic anisotropy of the nanoparticles through exchange bias pinning.[113,114] The antiferromagnetic layer helps to 'pin' (fix) the alignment direction of the ferromagnetic core.[115] However, any desirable effect is negated above the Néel temperature of the material, thus it is not expected to play a significant role in room temperature experiments. A small amount of oxidation is likely unavoidable, but care should be taken during the synthesis and storage of the nanoparticles to minimize its presence.

Commercial Cobalt Nanoparticles

We also used commercial Co-NPs (Strem Chemicals, Newburyport, MA, USA) that nearly meet our specifications, eliminating the challenge of fine-tuning the synthesis process but at the expense of losing precise control over their size, shape, and crystal structure. Additionally, these nanoparticles are supplied without a capping agent, making them vulnerable to oxidation. To rectify this deficiency, we attach oxalic acid ligands, thereby protecting them from oxidation and stabilizing them in solutions with organic solvents for timespans of months to years if properly stored. As shown in Figure 3.6 the commercial Co-NPs possess a semi-spherical, irregular shape, with diameters of about 12 nm.

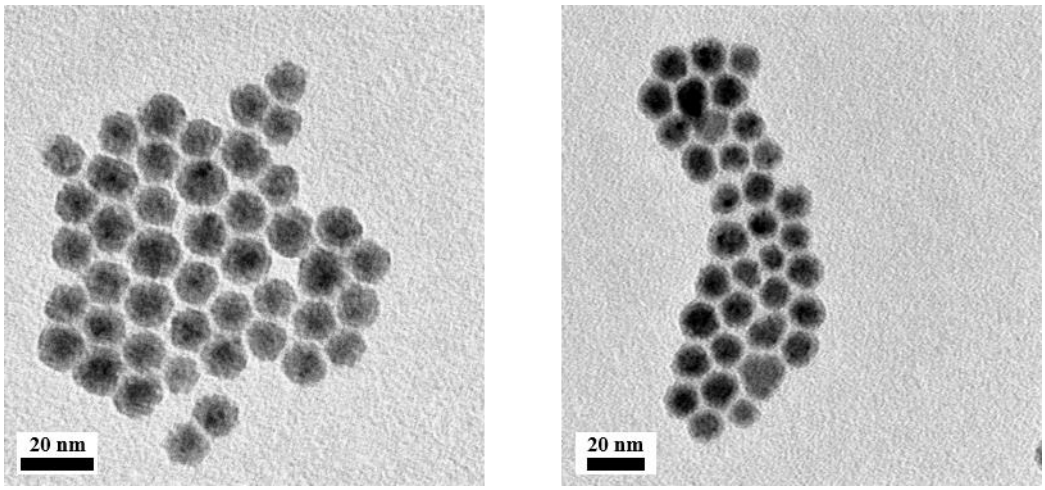

Figure 3.6: Transmission electron micrographs of commercial cobalt nanoparticles. Particles possess a semi-spherical shape with diameters with a core-shell structure, with inner (outer) radii of ~8 nm (~12 nm). The scale bars in both images show 20 nm.

Nanosphere Lithography

Nanosphere lithography[116,117] offers an alternative means of creating cobalt nanostructures on a surface, as depicted in Figure 3.7. In this technique, nanospheres, typically made of polystyrene or silica, self-assemble to form a close-packed monolayer that is weakly bound

(physisorbed) to the underlying surface. Despite the close-packing, gaps exist in the monolayer between assembled particles. These gaps enable other materials to reach the surface (e.g., during evaporative metal deposition), with the nanospheres acting as a mask. Following metal deposition, the nanosphere mask is removed using a combination of physical agitation (ultrasonication) and solvents. After removal of the mask, a hexagonal array of metal particles remains on the surface. The size and periodicity of these metal features is determined by the size of the nanospheres originally composing the mask. We prepared several surfaces in this way (see Figure 3.8) before ultimately abandoning the technique in favor of colloidal Co-NP deposition (Section 3.5), which proved more fruitful.

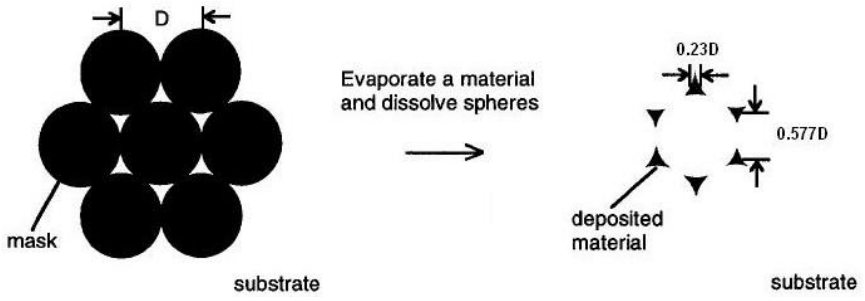

Figure 3.7: (Left) Schematically, hexagonal close-packed arrangement of black nanospheres, of diameter D, form a mask on a white substrate. (Right) Black deposited material, with a roughly triangular shape. The deposited material fills the gaps once present in the nanosphere mask, since removed. The size and spacing of the deposited material depends on the diameter of the nanospheres that composed the original mask. Figure adapted with permission from References 118 and 119.

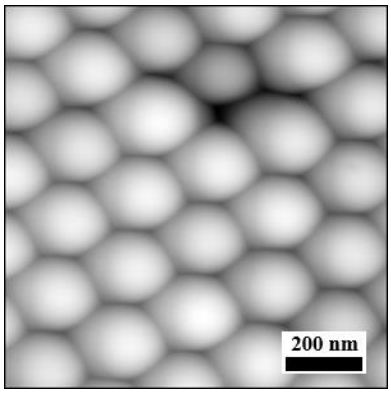

Figure 3.8: Atomic force topograph of self-assembled polystyrene nanospheres with diameters of 200 nm. Nanospheres form a close-packed monolayer on a gold/silicon surface, leaving a hexagonal array of gaps between spheres, enabling evaporated material (cobalt) to reach the surface.

3.5 Surface Deposition of Nanoparticles

Numerous strategies exist for depositing nanoparticles onto surfaces, employing physi-[79,120] and/or chemisorption[121] processes. Physisorption relies on van der Waals forces[122] between the particles (ligands) and their surroundings to attach the particles to the surface. Drop casting a nanoparticle suspension as a thin film and allowing the solvent to evaporate distributes nanoparticles on the surface in a way that depends on the nanoparticle concentration and choice of solvent, amongst other factors. Self-assembled monolayers enable one to tune the interactions of the surface with the nanoparticles and the solvent.[22,120] In this method, alkyl chains from ligand molecules surrounding the nanoparticles interdigitate with those of alkanethiols forming the SAM. The intermolecular forces experienced by the interdigitated molecules act to immobilize the nanoparticles on the surface. This method offers stronger particle-surface adhesion than that of physisorption onto unfunctionalized gold, but requires the use of molecules possessing (electrically insulating) alkyl moieties, where longer chains result in stronger attachment. These

techniques were used with some encouraging results, initially (Figure 3.9, but was ultimately found to produce inconsistent films that suffered from nanoparticle aggregation and surface contamination.

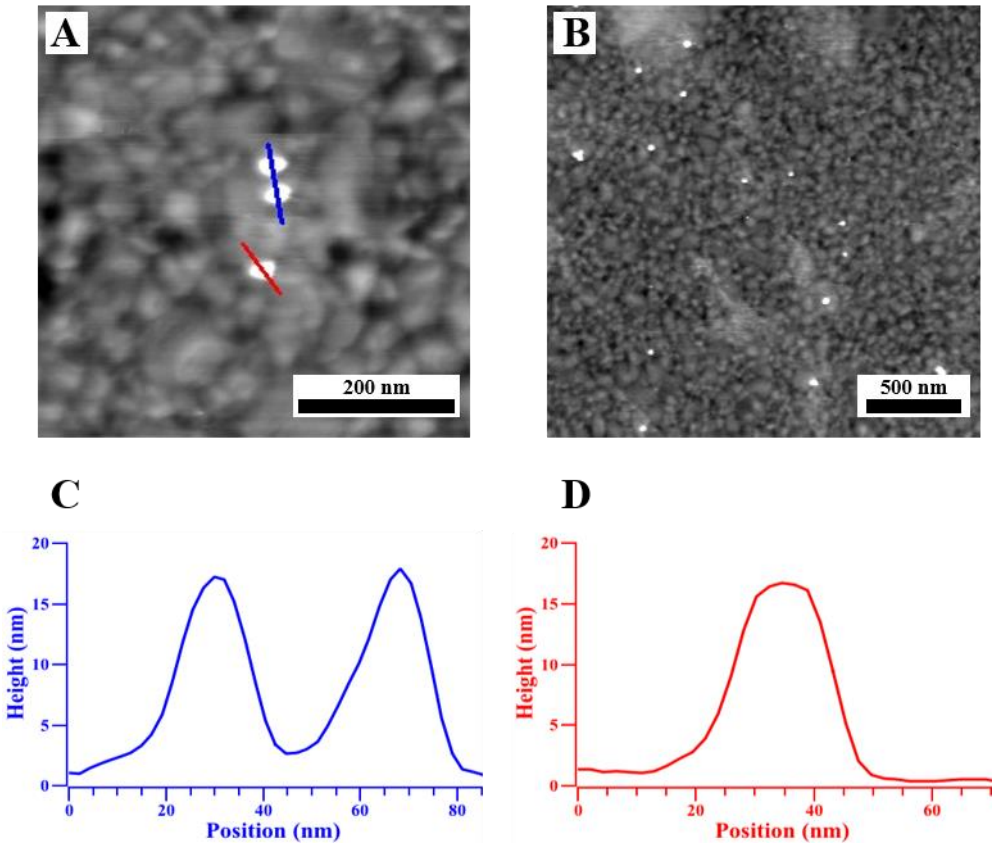

Figure 3.9: (A) 550 nm × 550 nm and (B) 2.27 µm × 2.27 µm atomic force topographs of cobalt nanoparticles deposited on a bare Au/Si surface by drop-casting. The rough texture of underlying evaporated-gold surface is evident in these images; the deposited nanoparticles appear as protrusions. Isolated particles were found tens or hundreds of nanometers away from neighboring particles, as well as clusters of several particles together. Topographic profiles were measured along the red and blue lines, as indicated in (A), and displayed in (C) and (D), respectively. The profiles indicate that the particles have diameters of about 15 nm, which agrees with transmission electron micrographs.

Chemisorption offers the advantage of a stronger link between the nanoparticle and the surface than that provided by physisorption. For example, intermolecular forces between neighboring alkanethiol molecules in a SAM provide a stabilizing (physisorption) interaction energy of about 65 meV per methylene (CH_2) group, or about 0.8 eV for 12-carbon alkyl chains (e.g., dodecanethiol molecules).[123] By contrast, gold–sulfur (Au–S) bonds, a model surface-molecule attachment present in alkanethiol SAMs, have a (chemisorption) bond energy of about 2.2 eV that anchors a thiol functional group to a gold surface.[123] Similar metal–thiol bonds are possible on other surfaces, including cobalt, providing a stronger and more robust tether between a nanoparticle and the surface than physisorption provides.[124]

Therefore, an alternative strategy for attaching Co-NPs to metal surfaces involves the use of bifunctional (dithiol) tethers. Here, dithiols, such as decanedithiol (C10DT) or biphenyldithiol (BPDT), are used to bridge gold surfaces and Co-NPs by chemisorption to opposite ends of the molecule. Using molecular tethers also adds the capability of site- and chemical-specific surface attachment though the tailoring of ligand and SAM functional groups. Insertion of bifunctinoal tether molecules into SAM defect sites enables specific chemisorption in those regions of the surface, over the nonspecific adsorption present elsewhere on the SAM matrix. In this way, the areal density of chemisorbed Co-NPs on a surface may be adjusted through controlled insertion of these molecular tethers.

We investigated several types of tethers for use in attaching Co-NPs to gold surfaces, most notably aliphatic (such octanedithiol) and aromatic (such BPDT) dithiols.[121] Mono-component SAMs made of aromatic dithiols have been found to immobilize Co-NPs with areal densities of up to 2800 particles per μm^2.[121] By contrast, aliphatic dithiols do not capture Co-NPs with as high areal densities as their aromatic counterparts, thought to be due to their lower molecular packing

densities and ordering when adsorbed onto the surface.[121] Molecular geometry and orientation must also be considered if these molecules are to be inserted into SAM defect sites. The length of an inserted molecule must be such that its exposed, terminal functional group protrudes from the surrounding matrix in order to access, and bind to, Co-NPs adsorbed on the SAM. Alkanethiols are known to tilt away from the surface normal by angle of 30° when assembled on Au{111} surfaces due to the stabilizing influence of increased intermolecular interactions.[123] Aromatic thiols, such as BDPT, exhibit smaller tilt angles of ≤20°.[123,125–128] The differences in tilt angle change the effective height of the terminal functionality of the molecule above the gold surface, since tilted molecules of a given length are effectively shorter than those oriented normal to the surface. The molecular structures and approximate lengths of various molecules considered in this experiment for use in nanoparticle chemisorption and to form surrounding SAM matrices are show in Figure 3.10. Considering these factors, insertion of BPDT or terphenyldithiol (TPDT) molecules into an octanethiol (or, shorter, hexanethiol[129,130]) matrix is expected to be a viable strategy for attaching Co-NPs to a gold surface, as illustrated in Figure 3.11, with the ability to tune nanoparticle density by controlling the SAM defect density.

Past spectroscopic studies of Au_{11} clusters have revealed the variability of the tunneling conductance of nanoparticles adsorbed on alkanethiol SAMs and their sensitivity to the local, microscopic environmental.[131] There, identical gold clusters were tethered to a surface using α,ω-alkanedithiol molecules inserted into an alkanethiol SAM, similar to the route proposed here to immobilize Co-NPs. Despite the controlled conditions (4.2 K, ultrahigh vacuum), tunneling conductance spectra measured with an STM tip positioned over isolated gold clusters showed remarkable variability between measurements. These results illustrate the significant affect that the nanoparticle's local, microscopic environment (electrostatic charge, ligand mobility,

compression of the underlying SAM) has on the tunneling current. Precise control of these environmental influences remains a challenge to spectroscopic studies of tethered nanoparticles, both gold clusters as well as Co-NPs. As such, added care is warranted when collecting and analyzing tunneling spectra, including time variations in that current.

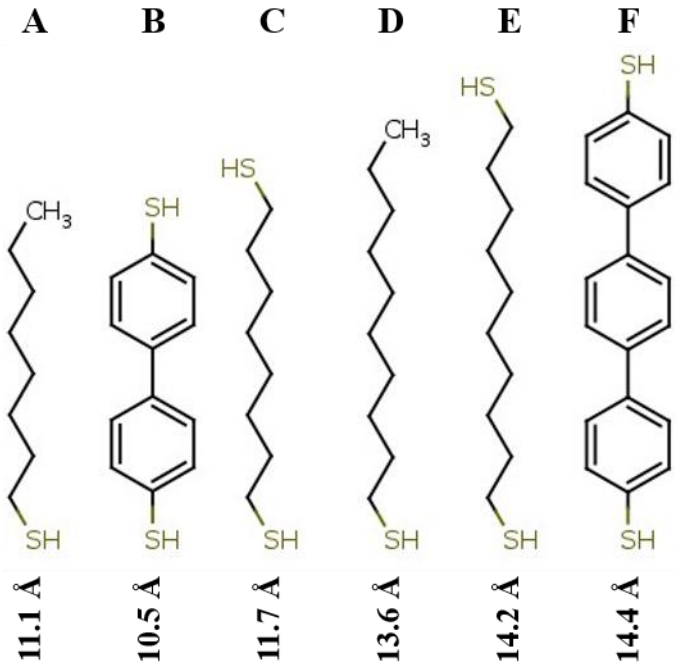

Figure 3.10: Structures of molecules considered for use in the deposition of cobalt nanoparticles: (A) 1-octanethiol, C8, (B) biphenyl-4,4′-dithiol, BPDT, (C) 1,8-octanedithiol, C8DT, (D) 1-decanethiol, C10, (E) 1,10-decanedithiol, C10DT, (F) *p*-terphenyl-4,4″-dithiol, TPDT. Molecular lengths, shown below the structures, were estimated using molecular modeling software (ChemDraw), measuring he distance from the bottom sulfur atom to the top-most hydrogen atom (in the case of thiols), or the top sulfur atom (for dithiols).

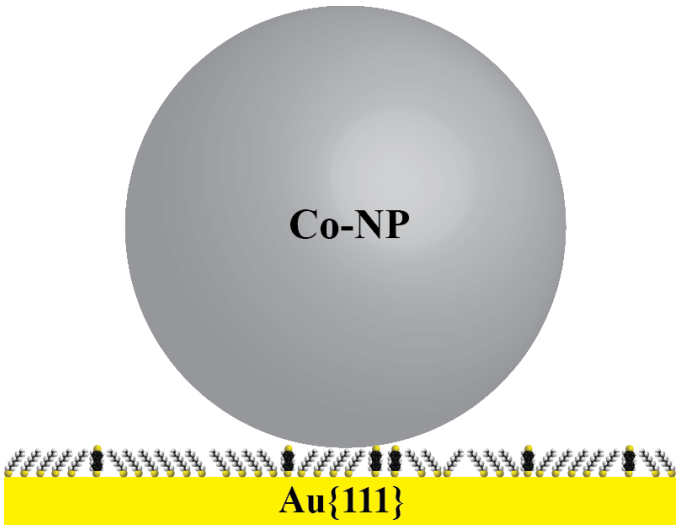

Figure 3.11: Cobalt nanoparticles (Co-NPs) chemisorb to the terminal thiol group of biphenyldithiol (BPDT) molecules inserted into an octanethiol (C8) matrix. Insertion of BPDT molecules occurs predominantly at defects in the C8 self-assembled monolayer (SAM), such as tilt domain boundaries, as shown in above. Controlling the areal density of SAM defects, by tuning sample preparation technique, enables one to adjust the availability of binding locations for Co-NPs. The nanoparticle's ligand coating has been omitted in the figure, but approximate relative sizes of the SAM molecules and nanoparticle have been preserved.

An electrically insulating layer of organic ligands surrounds the Co-NPs, preventing their aggregation in solution and protecting them from oxidation. These ligands remain after depositing the nanoparticles on the surface and, thus, insulate physisorbed Co-NPs from the conductive substrate. Additionally, as mentioned in Section 3.4.1, Co-NPs may possess a thin insulating oxide layer. The tunnel barrier presented by the insulating ligands and oxide layer presents a challenge to imaging Co-NPs with an STM. The feedback loop of the STM attempts to maintain a constant tunneling current between the probe tip and the surface (or objects adsorbed on the surface). Ordinarily, changes in surface topography result in changes in the magnitude of the tunneling

current, which the feedback loop compensates by adjusting the position of the probe tip relative to the surface. However, if an object (nanoparticle) is insulated from the surface, and the barrier for electron transport between it and the surface is sufficiently high, then the tunneling current may not change as the probe tip approaches. As such, the STM may not sense the nanoparticle's presence and, instead of the feedback loop adjusting the tip position to follow its topography, the tip may push the object laterally across the surface.[131] In which case, the nanoparticle would be 'invisible' to the tip and not appear in the image as well as interfere with the tip's ability to resolve other surface features. In the case of nanoparticles chemisorbed via conductive tethers, such as BPDT,[132,133] the barrier to electron transport between the nanoparticle and the surface is reduced greatly, increasing the likelihood of the tip following the topography of the surface and adsorbed Co-NPs. Nevertheless, the long, insulating ligand molecules may still interfere with the tip's ability to resolve fine features on or near adsorbed nanoparticles.

Several practical challenges exist when preparing dithiol SAMs. In order to attach Co-NPs to a surface, it is desired that α,ω-dithiol molecules adsorb upright, with one thiol group attached to the substrate while the other is oriented away from the surface, exposed to its surroundings. This orientation, however, is not guaranteed as both thiol groups have the potential to bind to the surface. Molecules possessing flexible, single-bonded alkyl chains may bend and form loops, thereby enabling both terminal groups attach to the surface with their flexible backbones protruding outward.[134–136] The likelihood of upright, singly-bound, dithiol adsorption may be increased with short-chain ($n \leq 8$) alkanedithiols ($HS(CH_2)_nSH$), elevating the temperature of SAM formation, or inserting the molecules into an existing SAM matrix.[129,137,138] Aromatic dithiols, such as BPDT and TPDT, are more rigid and less prone to looping and dual-thiol attachment than their alkyl counterparts, but difficulties still exist in imaging these SAMs via

STM.[121,139,140] Unbound thiol groups interact strongly with the STM tip and typically prevent molecular resolution imaging.[129] Additionally, exposed thiol groups may undergo oxidative S–S coupling, either with adjacent molecules in the SAM or with unbound molecules in solution, leading to multilayer formation and disordering of the monolayer surface.[139,141] Aromatic dithiols are particularly prone to dimerization in this way.[141] Working in reduced oxygen environments (e.g., inside a glovebox) with degassed solvents, and in the presence of antioxidants can help mediate this difficulty but not alleviate it entirely.[125] Another strategy involves the adsorption of protected dithiol analogs, which are subsequently deprotected after the SAM forms.[133,141] This method, however, complicates sample preparation and may act to disorder the SAM due to the chemical reactions that occur at the its surface.[142]

Patterning of Co-NPs on the surface was used to aid image interpretation. Successful deposition of Co-NPs in a particular region of the surface may be assessed by the observed pattern fidelity. Regions without the expected pattern may be excluded from further analysis, quickly, sparing the need for a tedious search for deposited particles or attempts to distinguish suspected Co-NPs from other advantageous particles present on the surface. Additionally, in the case of STM imaging, with limited scan ranges, patterns help one determine relative positions and distance scales where deposited Co-NPs are likely to be found. As such, many of the surfaces presented here were prepared with tether molecules and/or Co-NPs arranged on a gold surface in a periodic (patterned) manner. The lateral dimensions and pitches of these features were about 1–3 μm, prepared using microcontact printing (μCP), as shown in Figure 3.12. Unpatented samples were also prepared by inserting tether molecules into a SAM matrix (Figure 3.13), though less commonly used in the analysis presented here. In this case, tether molecules insert randomly over the entire surface, though are concentrated around defects in the surrounding molecular lattice.

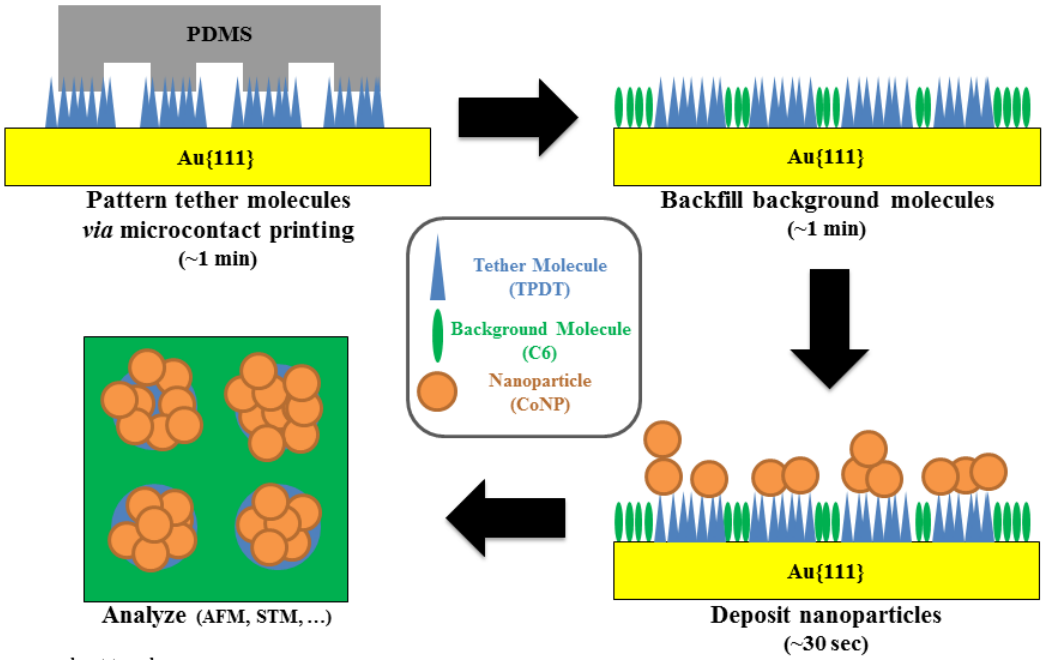

Figure 3.12: Schematics illustrating the patterning of gold surfaces with cobalt nanoparticles (Co-NPs) via microcontact printing of terphenyldithiol (TPDT) tethers and backfilling with hexanethiol (C6). Nanoparticles were deposited from a colloidal suspension in toluene and subsequently characterized using an atomic force microscope (AFM) and scanning tunneling microscope (STM). Co-NPs adsorbed predominantly in circular or square regions on the surface with characteristic lateral sizes and pitches determined by the polydimethylsiloxane (PDMS) stamp used.

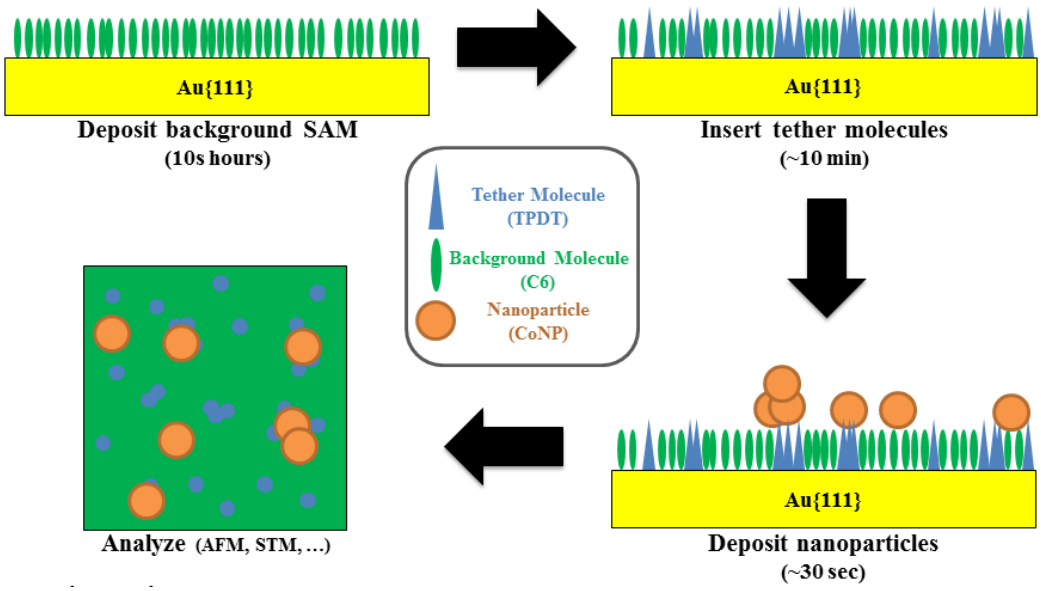

Figure 3.13: Schematic illustrating the deposition of cobalt nanoparticles (Co-NPs) onto gold surfaces with terphenyldithiol (TPDT) tether molecules inserted into a hexanethiol (C6) SAM. Nanoparticles were deposited from a colloidal suspension in toluene and subsequently characterized using an atomic force microscope (AFM) and scanning tunneling microscope (STM). Co-NPs adsorbed randomly over the surface, though tether molecules were concentrated near SAM defects due to increased surface accessibility at these sites.

3.6 Analysis of Nanoparticle Decorated Surfaces by Scanning Probe Microscopies

Two types of scanning probe microscopy were used to analyze surfaces decorated with Co-NPs: atomic force microscopy (AFM) and STM. Analysis via AFM provided the advantage of relatively fast (<10 minutes), large-area (up to 50 µm × 50 µm) topographic images, compared to those collected using an STM, which sometimes requires hours-long imaging times for areas less than 5 µm × 5 µm. In this way, samples could be screened quickly to assess the dispersion of Co-NPs on the surface prior to more thorough, but slower, analysis via STM. Additionally, AFM

provides a purely topographic image, as opposed to STM images that represent a convolution of topographic and electronic (conductivity) surface features, thereby simplifying interpretation of the images.

Surface-Deposited Cobalt Nanoparticles: Atomic Force Microscopy

Imaging Co-NP-decorated surfaces with an AFM reveals selective adsorption of nanoparticles in regions patterned with tether molecules (see Figure 3.14). In these regions, mono- and bilayers of particles are observed, as judged by topographic profiles showing feature heights approximately equal to that of the Co-NP diameter (or twice this value in the case of bilayers). The first layer of nanoparticles likely adsorbed due to chemical bonds between the terminal thiol functionality on the TPDT tethers and the cobalt surface of the nanoparticles. The second, less-prevalent, layer of nanoparticles likely forms as a result of weaker attractive forces between the particles, their ligands, and the SAM surface (physisorption). Nanoparticles adsorbed with greater areal surface densities near the edges of the TPDT regions than toward their interiors (see Figure 3.15). This difference in adsorption densities could result from differences in SAM order; TPDT molecules deposited by μCP will be least ordered at the edges of the transferred features due to adsorbate diffusion and exchange during SAM formation. A consequence of this relative disorder is that the nanoparticle ligands can more-easily penetrate (interdigitate with) the matrix, enabling the protruding thiol functionality on the TPDT to get closer to the particle's surface, increasing the likelihood of chemisorption.

Nanoparticle aggregates were observed on the hexanethiol (C6) matrix surrounding the tether molecules. In Figure 3.14, these aggregates appear as tentacle-like chains, multiple Co-NP diameters thick, oriented roughly along the same direction on the surface. These features likely form due to sudden aggregation during rinsing. The nanoparticles were deposited from a colloidal

suspension in toluene (non-polar solvent), but rinsed in ethanol (polar solvent). The sudden change in solvent polarity likely resulted in Co-NP precipitation onto the surface, with more nanoparticles (coated with non-polar, aliphatic ligands) accumulating on the non-polar (CH_3-terminated) C6 SAM, rather than the more-polar TPDT regions.

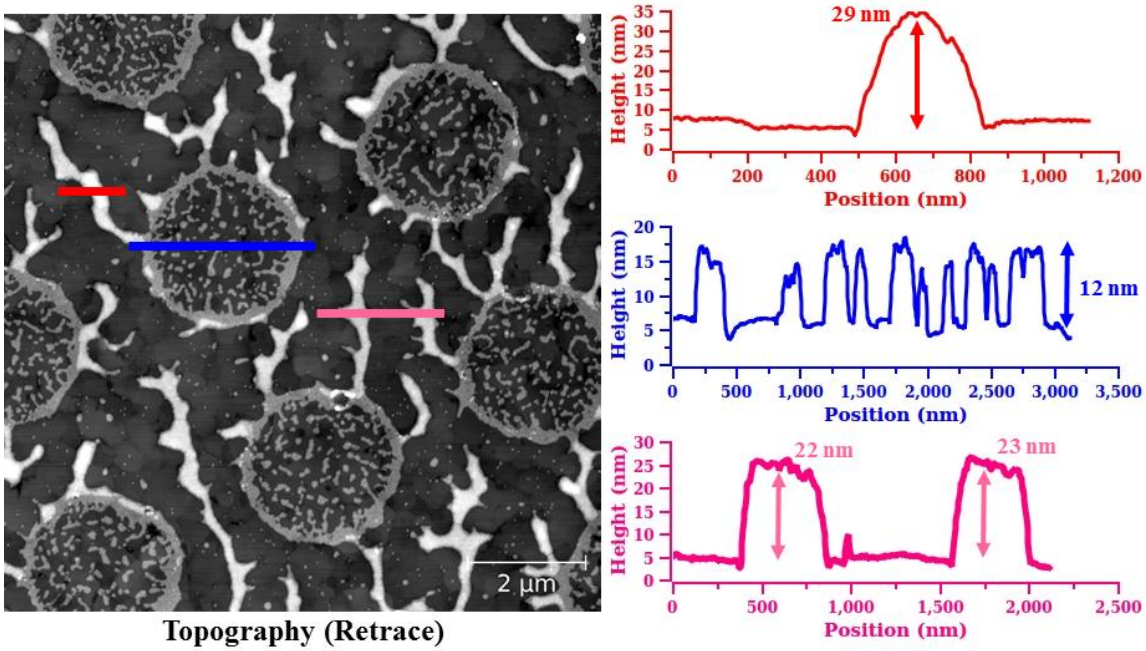

Figure 3.14: Cobalt nanoparticles (Co-NPs) deposited from a colloidal suspension onto a functionalized Au{111} surface. (Left) Atomic force topograph of patterned surface. Circular regions containing terphenyldithiol (TPDT) tethers specifically adsorb Co-NPs in preference of the background SAM matrix of hexanethiol (C6). (Right) Topographic profiles of adsorbed Co-NPs along red, blue, and pink lines indicated in left image. Profiles confirm that Co-NPs adsorb as single layers of particles on tether regions, and adsorb sporadically, in aggregates, on C6 matrix.

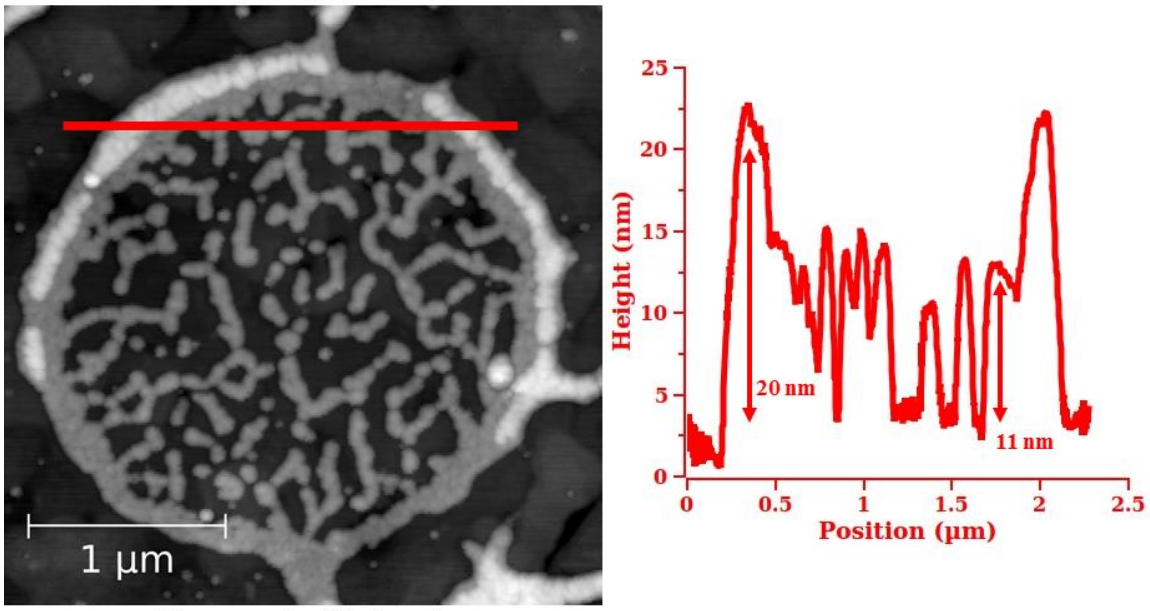

Figure 3.15: Cobalt nanoparticles (Co-NPs) deposited from a colloidal suspension onto a functionalized Au{111} surface. (Left) Atomic force topograph of patterned surface. Circular region containing terphenyldithiol (TPDT) tethers specifically adsorb Co-NPs in preference of the background SAM matrix of hexanethiol (C6). (Right) Topographic profile of adsorbed Co-NPs along red line indicated in left image. Adsorbed densities of Co-NPs on the TPDT region vary, with particles adsorbing more densely near the periphery of the patterned region compared to its interior.

Other adsorbates were tested, in place of C6, as constituents of the SAM matrix surrounding the TPDT tethers, including 1-decanethiol (C10) and 11-mercapto-1-undecanol (C11OH). Similar to the case of C6 SAMs, Co-NP aggregates were observed on C10 SAMs, which also possess a non-polar methyl ($–CH_3$) terminal group. By contrast, C11OH SAMs resisted Co-NP aggregation (see Figure 3.16), likely due to the hydrophilicity of the surface resulting the polarity of the molecule's terminal hydroxyl (–OH) group. Although C11OH reduced nanoparticle aggregation, such polar surfaces are undesirable for STM analysis due to their affinity for water

(adsorbed from the air) that can prevent molecular-scale resolution of features on the surface. For this reason, short-chain alkanethiols, such as C6, were used for the surrounding SAM matrix in further experiments.

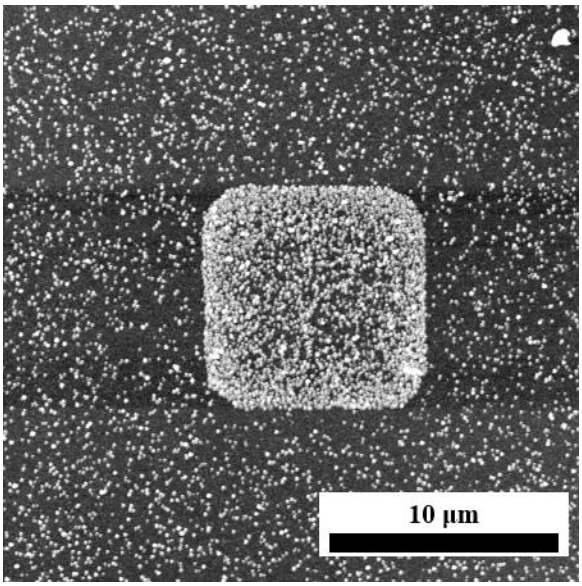

Figure 3.16: Atomic force topograph of cobalt nanoparticles (Co-NPs) deposited from a colloidal suspension onto a functionalized Au/Si surface. A single square region containing terphenyldithiol (TPDT) tethers is evident near the center of the image. Here, Co-NPs disproportionately adsorbed onto the TPDT region in preference of the background SAM matrix of 11-mercapto-1-undecanol (C11OH), without forming large aggregates or multilayers.

Surface-Deposited Cobalt Nanoparticles: Scanning Tunneling Microscopy

The presence of a well-ordered SAM around the deposited Co-NPs provides a convenient backdrop on which to calibrate the scanning of the instrument and test the quality of each STM tip before and between spin measurements. The Co-NPs appear as large, convex protrusions from the otherwise relatively featureless surface. The area surrounding the Co-NPs should be flat, unobstructed, and lacking an NMR signal in order to reduce the likelihood of fouling the STM tip

and to set a baseline for spin measurements. An alkanethiol SAM accomplishes these goals and may be used as a host matrix for tether molecules anchoring Co-NPs to the sample surface.

When analyzing STM topographs, the spatial derivatives (computed numerically from the topography signal) were also employed. Contrast in topography images is from differences in the apparent height of surface features. In the case of surfaces that possess large disparities in feature height (large changes in topography), as in the case of conductive molecular tethers and, especially, adsorbed nanoparticles, the contrast between features of comparable height is lost due to data scaling. For example, in images of Co-NPs adsorbed on an alkanethiol SAM, the difference in height between the apex of the nanoparticle and the top of the surrounding SAM can be so large (>10 nm) that the molecular-level changes in topography (~1 Å) are not evident when the image is *displayed*, despite the data being *measured* with sufficient precision. The topographic derivative image alleviates this display challenge by eliminating DC offsets in topography and emphasizing regions where the change in height between neighboring pixels is large (e.g., near edges). As such, topographic derivative images are useful in assessing surfaces with large variations in topography between regions, while relatively flat within the respective regions.

As an initial characterization step, we analyzed the insertion of BPDT and TPDT tether molecules into alkanethiol (C6 and C8) SAMs. As expected, tether molecules were observed to insert preferentially into defects sites in the SAM, particularly at tilt domain boundaries, as observed in Figures 3.17 and 3.18. Due to the longer, physical lengths of the tethers, as well as their higher conductivities compared to the surrounding alkanethiol SAM, the tethers appear as protrusions in the STM topography images. The number of inserted molecules depends on the number of defects in the surrounding SAM matrix as well as the time the surface was immersed in a solution containing tether molecules. By adjusting these parameters, immersion and annealing

times during and post-SAM deposition, we can tune the density of tethers and, by extension, the number of Co-NPs adsorbed to the surface.

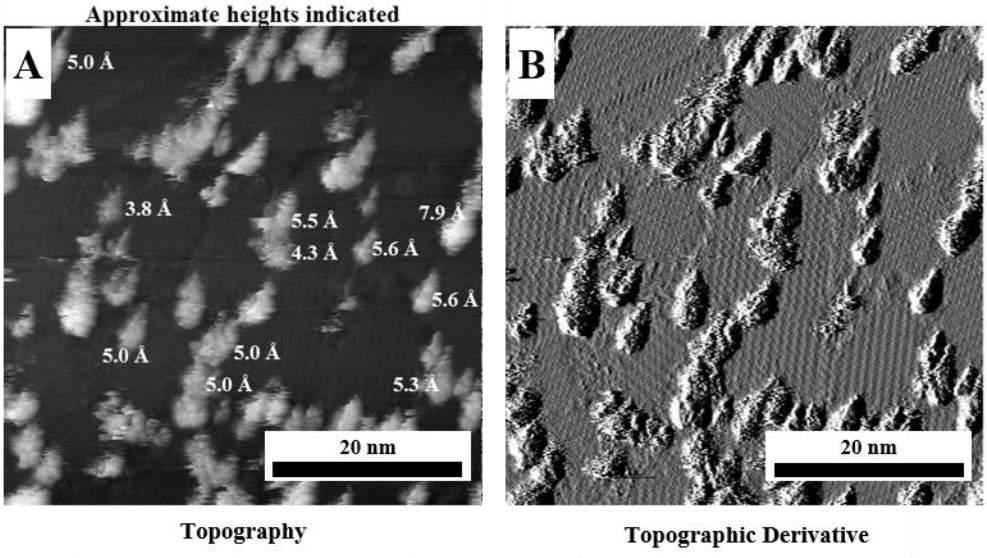

Figure 3.17: Scanning tunneling topograph (left) and topographic derivative (right) of terphenyldithiol (TPDT) molecules inserted into a hexanethiol (C6) matrix. Due to their greater electrical conductivity and longer physical length, TPDT molecules appear to protrude from top of the surrounding C6 matrix. Approximate protrusion heights are indicated next to select TPDT molecules. The molecular ordering of the C6 lattice is evident, particularly in the derivative image. Sample preparation: immersion of a clean Au{111} surface in 1 mM solution of C6 for 29 h at 60 °C; subsequent immersion into 0.2 mM solution of TPDT for 15 min. Imaging: $V_{tip} = +1$ V, $I_{set\ point} = 5$ pA.

Frequently, tether molecules were observed to exist as clusters, hosted within the alkanethiol SAM matrix. We lack the resolution to distinguish individual BPDT or TPDT tethers due to their greater conformational freedom of their termini (protruding from the well-packed matrix), resulting in molecular motion during imaging,[143] and interference of their exposed thiol

groups with the STM tip. However, we can surmise from the lateral sizes and groupings of protrusions in the alkanethiol matrix, which appear far larger than the known sizes of the molecules, that tethers accumulate in groups during or after insertion (Figure 3.18). Regions with larger groups of tethers, and more densely inserted, are more likely locations for Co-NPs to adsorb due to increased opportunity to form S–Co bonds, potentially more than one per nanoparticle.

We also analyzed patterned surfaces decorated with Co-NPs. The lateral dimensions and pitch of the features patterned via μCP posed a challenge to collecting data with an STM. Areas larger than about 1000 nm × 1000 nm necessitated multi-hour imaging times to reduce streak artifacts caused by the inability of the STM's feedback loop to respond promptly to changes in the tunneling current as the tip passed over the topographically varied surfaces. Additionally, even under relatively stable (ambient) scanning conditions, thermal drift of the tip toward or away from the surface limited our ability to image large areas over these time spans. Nevertheless, here we present STM images of assembled Co-NPs chemisorbed and physisorbed onto Au{111} surfaces functionalized with TPDT and C6 SAMs.

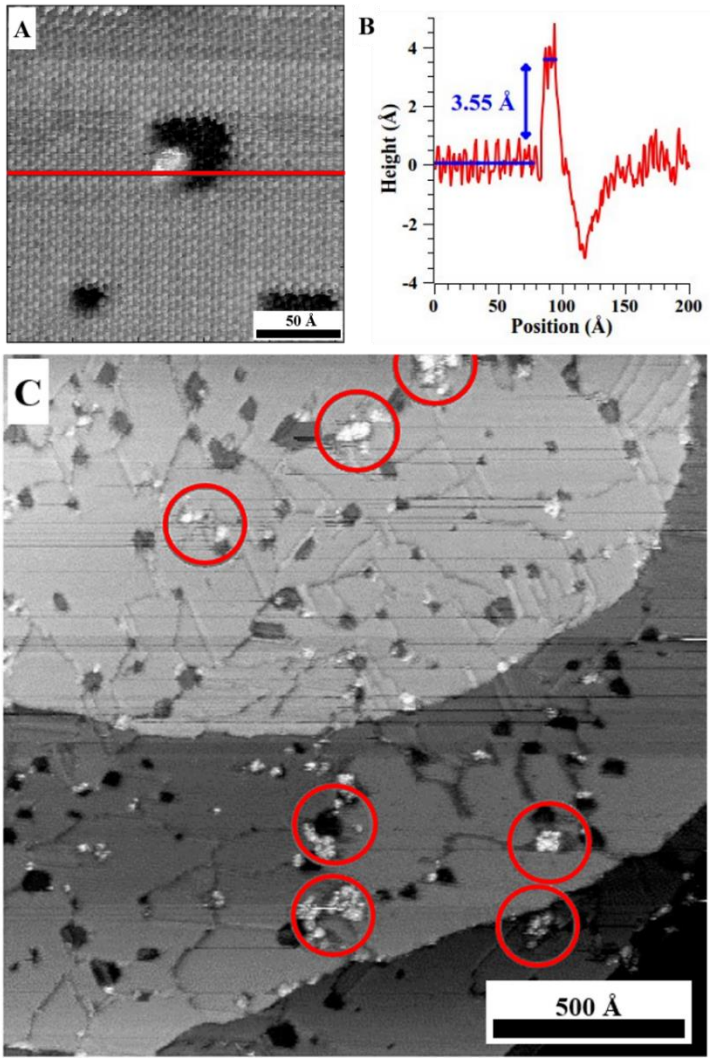

Figure 3.18: Scanning tunneling topographs of biphenyldithiol (BPDT) molecules inserted into an octanethiol (C8) matrix on Au{111}. Due to their greater electrical conductivity, BPDT molecules appear to protrude from top of the surrounding C8 monolayer. (Top-right) Topographic profile over a cluster of inserted BPDT molecules, along the red line indicated in the top-left image. (Bottom) An image of a representative area showing numerous clusters of inserted BPDT molecules located near surface defect sites. Red circles represent the cross-sectional projection of spherical, 20 nm particles overlaid onto the image on/near the larger clusters of BPDT tethers, which are likely chemisorption sites for cobalt nanoparticles. Imaging: V_{tip} = +1 V, $I_{set\ point}$ = 5 pA.

Figures 3.19 and 3.20 demonstrate our ability to image the microcontact printed patterns of TPDT tether molecules surrounded by a backfilled C6 matrix. In the STM topographic images presented, circular features are visible with diameters similar to those observed on similarly prepared samples imaged with an AFM (e.g., Figure 3.15). When imaging at this scale, molecular resolution is impossible (each pixel represents an area of ~10 nm^2, far larger than the sizes of these molecules), but we are able to assess the transferred pattern, identify the large-scale structure of the underlying gold surface (grains/facets), and Co-NPs. Unlike the AFM images, however, Co-NPs are not evident in these regions. The regions identified as containing TPDT appear to have a different surface texture than the surrounding C6 SAM, as seen in STM topographs. This difference in surface texture is particularly evident in the topographic derivative images, and results from the different chemical functionality of the TPDT tethers (and their interaction with the STM tip) compared to that of C6. Based on earlier AFM images of similar samples, we expect that Co-NPs were present on these surfaces prior to STM analysis, but the STM tip brushed the particles aside during imaging. The difficulty in detecting Co-NPs may indicate that, in this case, they were not strongly bound to the surface via the TPDT tether,[131] as expected, and were too insulated from the surface to affect the magnitude of the tunneling current. These results, however, likely depend on the cleanliness of the STM tip and the specific scanning conditions. If a nanoparticle adsorbs to the tip prior to collecting an image then it could interfere with other particles on the surface as the tip moves during imaging, with its ligand layer acting to insulate the particle.

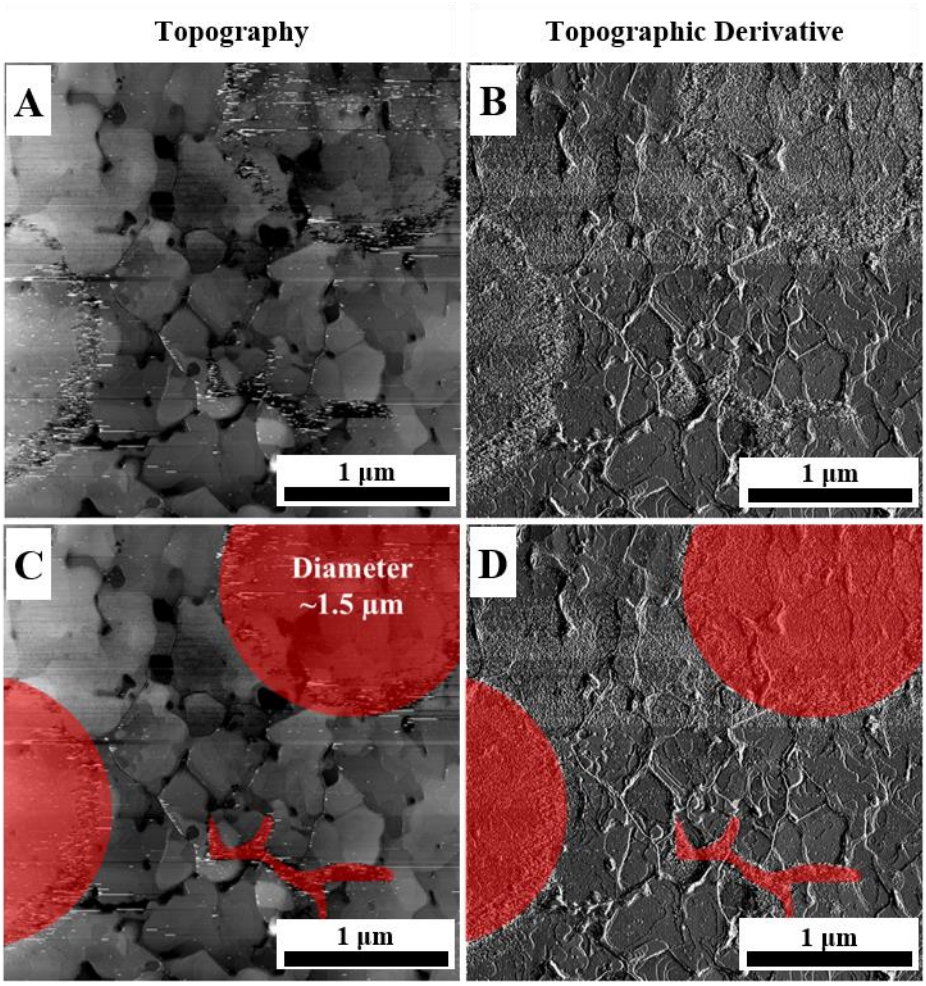

Figure 3.19: (A, C) Scanning tunneling topographs and (B, D) topographic derivative of surfaces patterned with terphenyldithiol (TPDT) molecules within a hexanethiol (C6) matrix with deposited cobalt nanoparticles (Co-NPs). (A, B) As-collected images. (C, D) The same images shown in (A) and (B), respectively, but with overlaid, red shapes to guide the eye in identifying surface features. Sample preparation: microcontact printing of TPDT onto a clean Au{111} surface for 1 min; subsequent immersion into 1 mM solution of C6 for 1 min, and then into a solution of Co-NPs for 15 s. Imaging: V_{tip} = +1 V, $I_{set\ point}$ = 5 pA, 700 × 700 pixels, 2500 nm × 2500 nm.

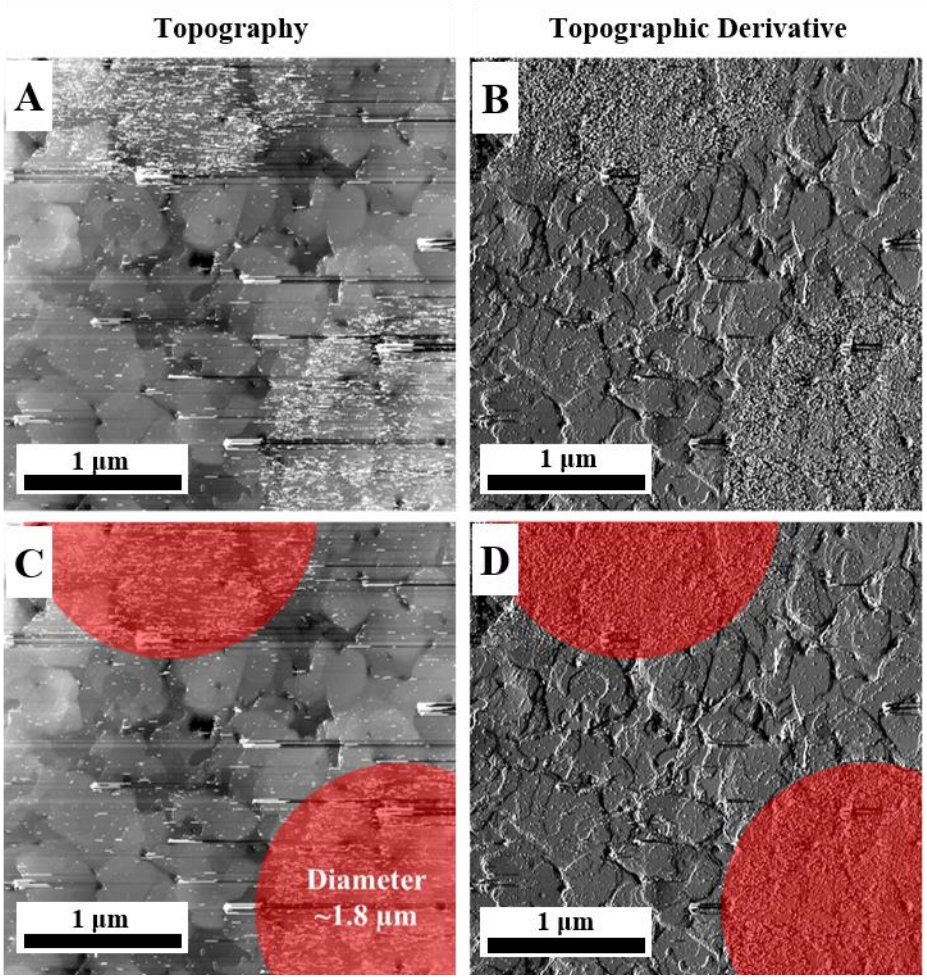

Figure 3.20: (A, C) Scanning tunneling topographs and (B, D) topographic derivative of surfaces patterned with terphenyldithiol (TPDT) molecules within a hexanethiol (C6) matrix with deposited cobalt nanoparticles (Co-NPs). (A, B) As-collected images. (C, D) The same images shown in (A) and (B), respectively, but with overlaid, red shapes to guide the eye in identifying surface features. Sample preparation: microcontact printing of TPDT onto a clean Au{111} surface for 1 min; subsequent immersion into 1 mM solution of C6 for 1 min, and then into a solution of Co-NPs for 15 s Imaging: V_{tip} = +1 V, $I_{set\ point}$ = 5 pA, 512 × 512 pixels, 2800 nm × 2800 nm.

In addition to the circular regions corresponding to patterned TPDT tethers, we also observe features resembling the aggregated chain of Co-NPs observed in AFM images. As

discussed previously, we observed aggregated Co-NPs on portions of the surface functionalized with C6 (Figure 3.14), noting their oriented, chain-like appearance. Similar features are observed in Figure 3.19 and, even more prominently, in Figure 3.21. In Figure 3.21, we measure features protruding from the surface by about 10 to 15 nm, corresponding to the expected diameters of the Co-NPs. These topographic profiles indicate a single-particle thick layer, in contrast to the multilayers indicated by AFM images. This discrepancy could, again, be a result of nanoparticle manipulation during scanning, caused by the tip (or adsorbed particles) pushing surface-bound particles away prior to their affecting the STM tunneling current. The lateral streaks visible in this image are indications that the tunneling junction may be affected by mobile species on the surface, such as nanoparticles being moving in/out of the tunneling junction as the tip moves across the surface.

Once we identified promising regions with large-area scans, specific surface features were analyzed. We rarely observed features that we could attribute to isolated Co-NPs. Instead, we observed aggregates with lateral and vertical dimensions several times that of the average diameter of the Co-NPs. This scarcity of isolated nanoparticles, as mentioned above, could be a result of tip manipulation during scanning, sweeping all but the largest clusters out of the scan area without affecting the tunneling current. Inspecting these clusters more closely, we identified features with lateral dimensions approximately equal to those of the deposited Co-NPs. As seen in Figure 3.22, dozens of round, convex features are evident within the imaged region with center-to-center distances of ~15 nm, as determined using topographic profiles. Additionally, a collection of round nanoparticle-like features of the correct lateral dimensions is also observed in Figure 3.23. There, the features near the center of the imaged area appear to form an ordered assembly, amongst other features protruding/receding much further from/into the surrounding surface. Large variations in

topography pose a continuous challenge to resolving the Co-NPs on surfaces, which is exacerbated by the formation of large aggregates of nanoparticles, as seen here.

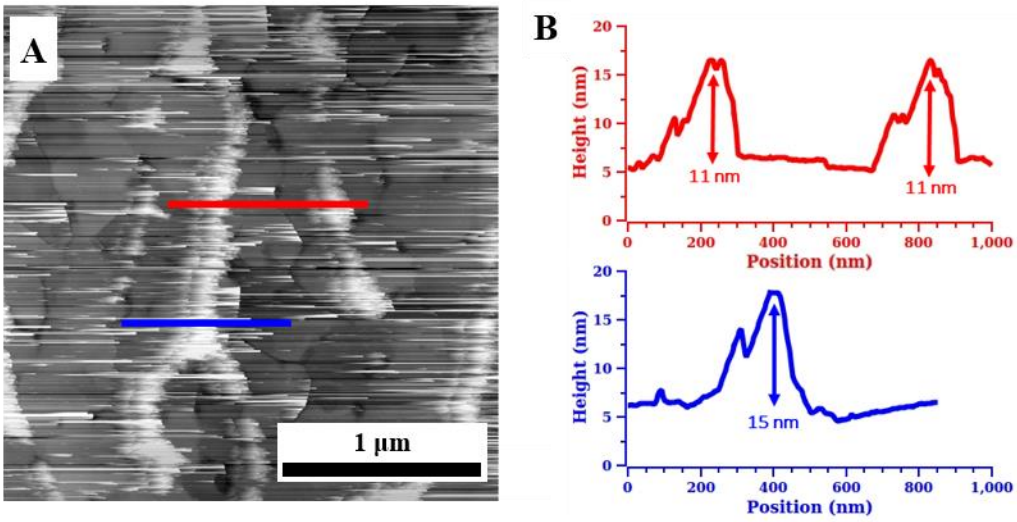

Figure 3.21: Scanning tunneling topograph (A) of Co-NPs deposited on a C6 SAM and (B) topographic profiles along red and blue lines indicated in the left image. Tentacle-like chains of aggregated Co-NPs are evident, with feature heights matching those of the nanoparticles. Sample preparation: microcontact printing of TPDT onto a clean Au{111} surface for 1 m; subsequent immersion into 1 mM solution of C6 for 1 min; and then into a solution of Co-NPs for 15 s. Imaging: V_{tip} = +1 V, $I_{set\ point}$ = 5 pA, 512 × 512 pixels, 2500 nm × 2500 nm.

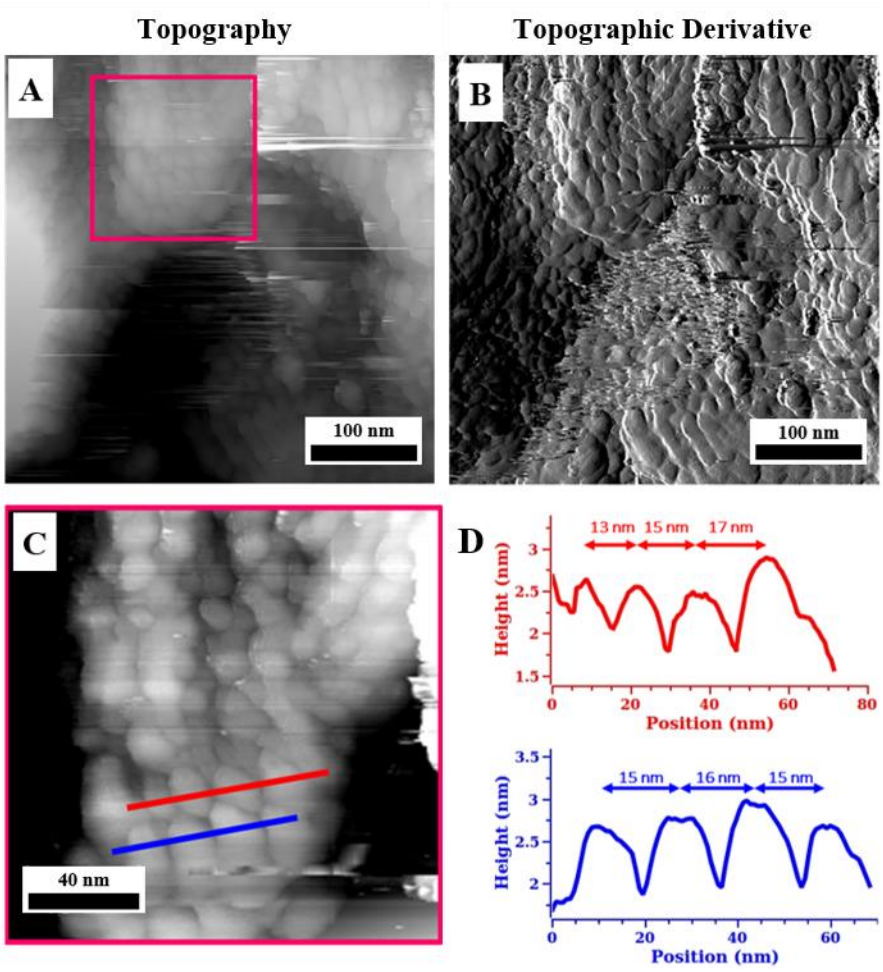

Figure 3.22: (A, C) Scanning tunneling topographs (B) and topographic derivative of Co-NPs deposited on a hexanethiol (C6) matrix. (D) Topographic profiles along red and blue lines indicated in (C). A cluster of Co-NPs is evident, with lateral feature spacing matching those of the nanoparticles. Sample preparation: microcontact printing of TPDT onto a clean Au{111} surface for 1 min; subsequent immersion into 1 mM solution of C6 for 1 m; and then into a solution of Co-NPs for 15 s. Imaging: V_{tip} = +1 V, $I_{set\ point}$ = 5 pA. (A, B): 512 × 512 pixels, 400 nm × 400 nm; (C) is cropped from (A, pink box): 193 × 193 pixels, 150 nm × 150 nm.

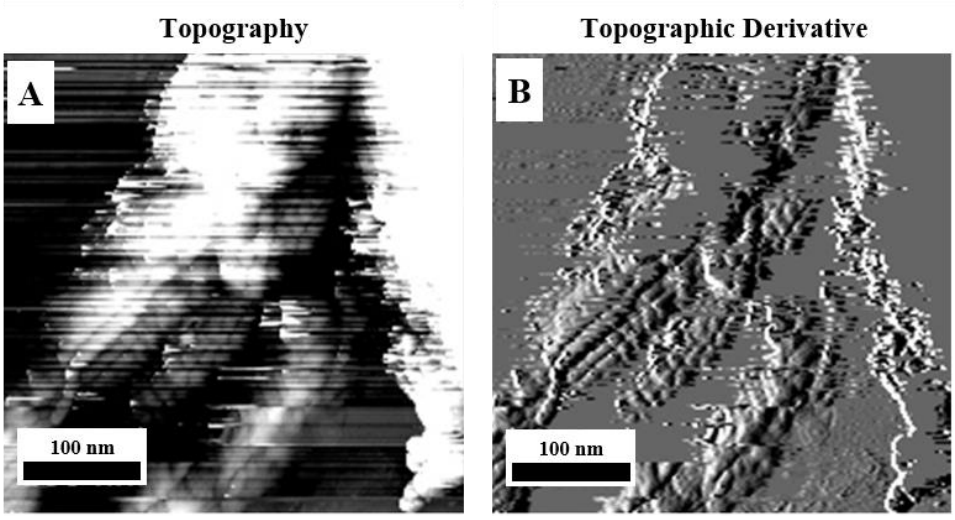

Figure 3.23: (A) Scanning tunneling topograph and (B) topographic derivative of Co-NPs deposited on a hexanethiol (C6) matrix. A multi-layer cluster of Co-NPs is evident. The vertical scaling (color) of these images, as displayed here, are saturated intentionally in order to enhance the visibility of the nanoparticles. Sample preparation: microcontact printing of TPDT onto a clean Au{111} surface for 1 min; subsequent immersion into 1 mM solution of C6 for 1 min; and then into a solution of Co-NPs for 15 s. Imaging: V_{tip} = +1 V, $I_{\text{set point}}$ = 5 pA, 200 × 200 pixels, 390 nm × 390 nm.

3.7 Spin Measurement Strategy

We will detect the nuclear spin signal by measuring the power spectrum of the time-varying tunneling current near the expected Larmor precession frequency of the spin. The high spatial confinement of the STM tunneling current enables sub-Ångström localization and resolution of spins in the plane of the surface. In this way, the spatial distribution of spins may be imaged in two dimensions.

Cobalt nanoparticles are a large, isotopically pure target spin system subject to a strong internal magnetic field due to their ferromagnetism. Surfaces will be decorated with isolated

Co-NPs in the manner described above (Section 3.5) and characterized using a combination of AFM and STM topographic imaging (Section 3.6). The STM tip will be positioned above an isolated nanoparticle and the tunneling impedance adjusted in order to minimize potential perturbations of the Co-NP, or its ligands, by the tip ($I_{\text{set point}}$ ~1 pA, V_{tip} ~1 V). The RF power spectrum of the tunneling current will be measured with a spectrum analyzer to determine the relative power of the signal as a function of frequency. In an analogous manner to that in ESN-STM, we expect to observe a peak in the power spectrum near the Larmor frequency (ω) of the nuclear magnetic moment (m) under investigation, which may be computed as:

$$\omega = \frac{mB}{I\hbar}, \qquad \textbf{Eq. 3.10}$$

This frequency depends linearly on the strength of the field (B) in which the spin precesses. As such, we may use a variable external field to modulate the precession frequency in order to confirm the source of the signal. We will use a permanent magnet placed near the sample to generate a strong field near the sample, though, in the case of ferromagnetic Co-NPs, this may not be necessary. Near room temperature, this field will not magnetize the small number of spins probed in this measurement to an appreciable degree. Rather, we rely on the statistical magnetization (spin noise) of the spins. This field is there to induce the precession of the spins at predictable frequencies around a common axis. In addition to this static field, we will apply a smaller, variable field to modulate the net field strength, causing the precession frequency to vary with time. Monitoring both the magnitude and phase of the variations in the precession frequency will enable us to ascribe more confidently the source of this signal to the precession of the nuclear magnetic moments in the sample, as detected by the STM. A schematic of the measurement scheme is shown in Figure 3.24.

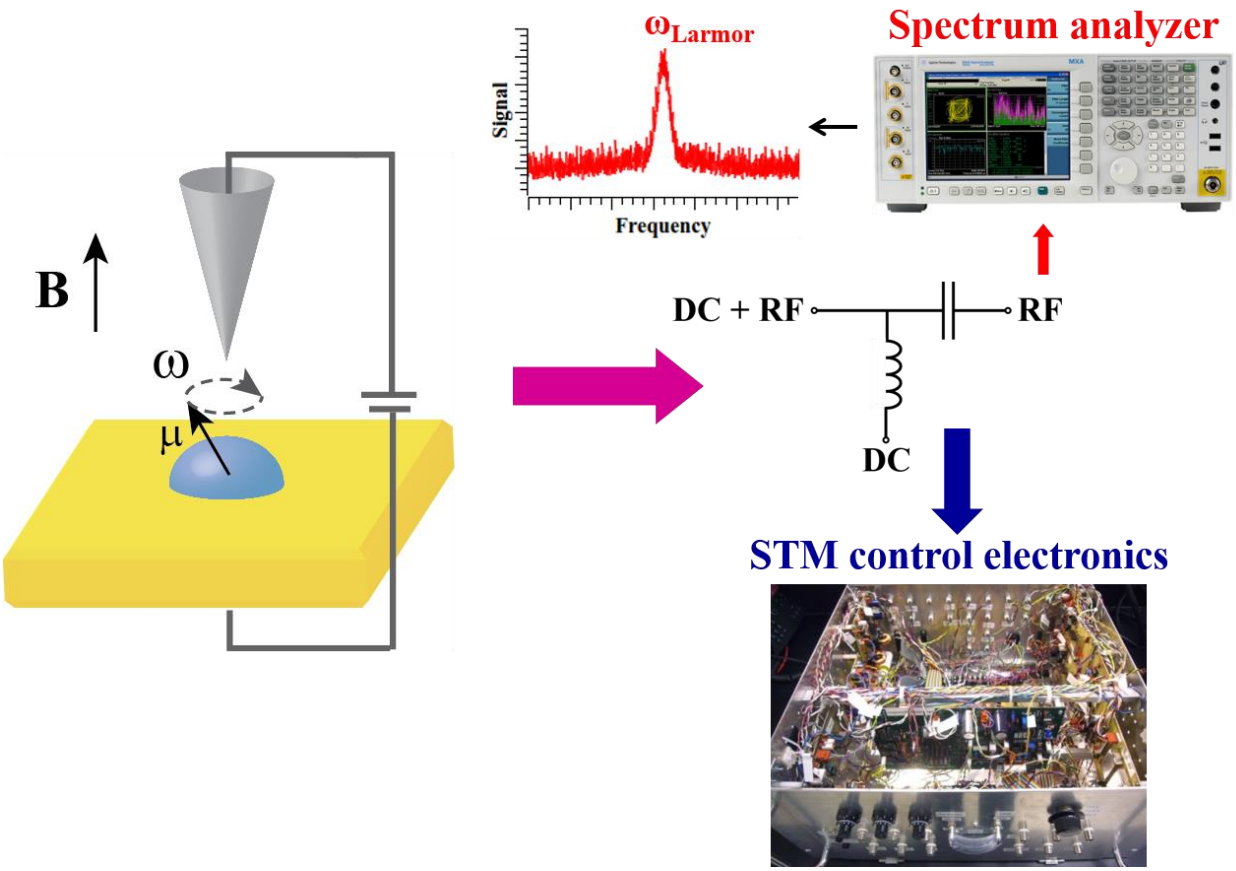

Figure 3.24: Nanoscale nuclear spin measurement scheme. The tip of a scanning tunneling microscope is positioned over a nuclear spin precessing at frequency ω in an external magnetic field (sum of B_{static} and $B_{solenoid}$). Here, a purple arrow depicts the measured tunneling current between the tip and the sample. A bias tee splits this current into two components: a time-varying (radio frequency, RF) component, and a time-independent (DC) component. The RF signal (red arrow) is sent to a spectrum analyzer capable of discerning extremely low-power signals with high frequency resolution. The STM control electronics (feedback loop) monitors the DC portion (blue arrow) of the tunneling current in order to maintain a constant tip-sample separation during the measurement.

Scanning Tunneling Microscope Construction

A new STM was constructed for use in this project, as shown in Figure 3.25, in order to facilitate instrument development while simultaneously optimizing sample preparation and imaging techniques. Aside from the custom-built control electronics and data acquisition system, this instrument features a spectrum analyzer to aid in the collection and analysis of low-power RF signals.

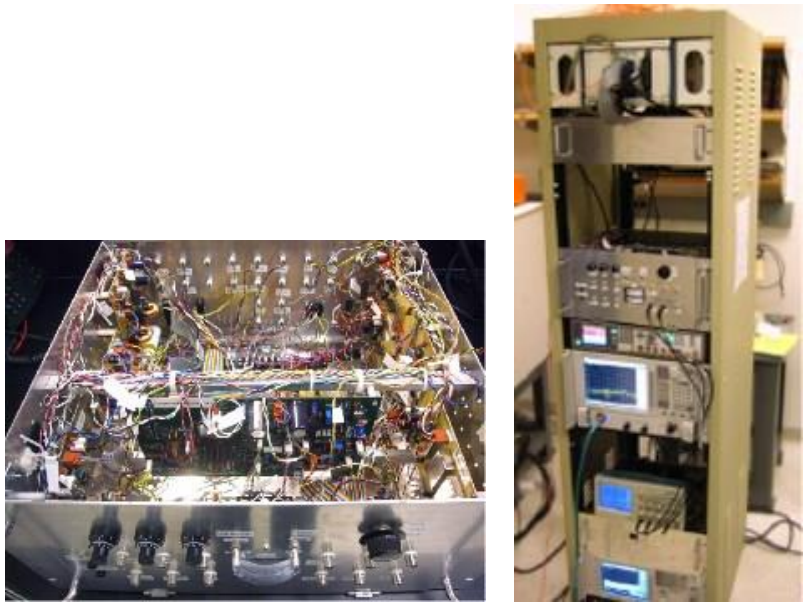

Figure 3.25: Scanning tunneling microscope control electronics (left) and data acquisition system (including control electronics, signal analyzer, and computer interface electronics), custom built for use in making single-molecule nuclear spin measurements.

We tested this STM by measuring the surface topographies of alkanethiol SAMs to demonstrate its ability to resolve molecular details (Figure 3.26) similar to those that will be studied later in these experiments. Additionally, we used these samples to calibrate the response of the STM against known surface features: intermolecular spacing in the assembled lattice and the heights of Au{111} step edge defects.

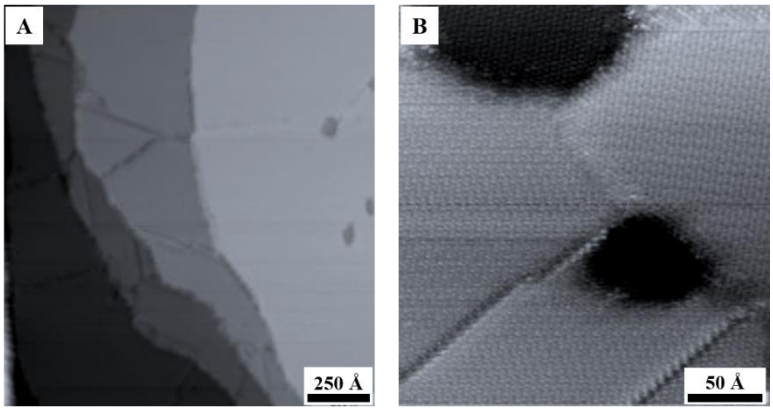

Figure 3.26: Scanning tunneling topographs of 1-decanethiol self-assembled monolayers on Au{111}; V_{tip} = +1 V, $I_{set\ point}$ = 3 pA. Common surface features, including gold step edges, vacancy islands, tilt domain boundaries, and close-packed molecular lattice may be seen clearly.

Scan Head & Amplifier Modifications

We use a Besocke, beetle-style STM scan head.[144,145] In this configuration, the sample rests on three, tripodal piezoelectric ("piezo") tubes. These tubes support the coarse approach of the sample toward the STM tip, which is located on a fourth, central, piezo tube. Once the surface is sufficiently close to the tip (<1 nm) such that the desired tunneling current (~1 pA) flows between the tip and sample, fine adjustment of tip position relative to the sample is controlled via the feedback electronics and the central piezo tube. However, in the case of this experiment and prospective spin measurements, we modified the design and construction of the scan head in order to incorporate other components not used in purely topographic imaging. Many of these changes and additions are visible in the photographs shown in Figure 3.27, and described below.

We incorporated high-frequency transmission lines in order to accommodate RF and microwave biases and tunneling currents with low attenuation compared to conventional thin-gauge, solid core copper cabling. In doing so, we enable high-frequency pump-probe measurements of molecules and nanoparticles in the tunneling junction. Additionally, in order to

incorporate variable magnetic fields in the tunneling junction, we built a solenoid that fits around the STM scan head during operation. Current flowing through the coils of the solenoid generates an axial magnetic field. The strength and spatial uniformity of this field depends on the size (length and radius) of the solenoid. As such, the design of the scan head was modified to be thinner and taller than heads typically used. This geometry was chosen so that the tip-sample junction is located at the center of the solenoid (at its midpoint along its central axis), where the field is strongest and most uniform.

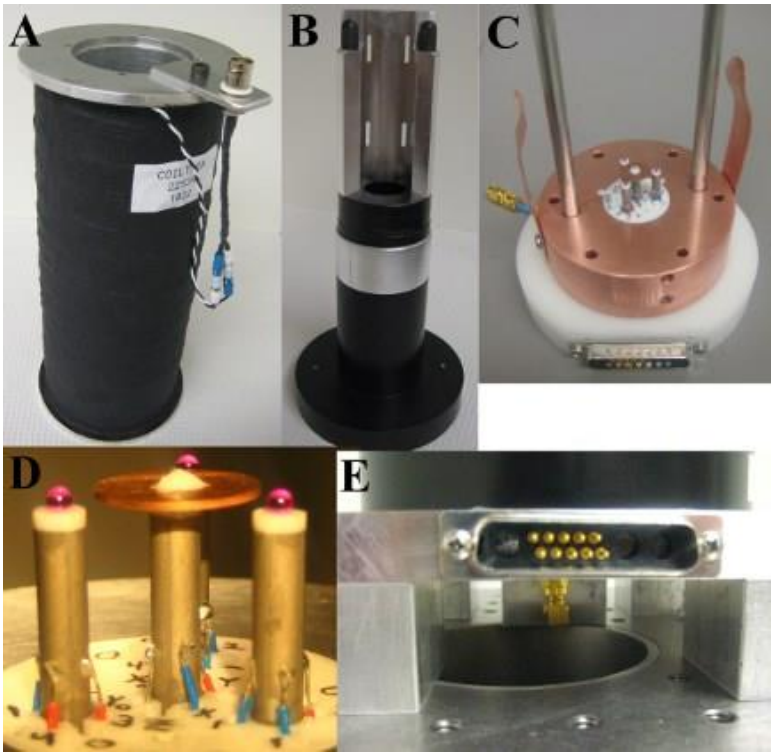

Figure 3.27: Besocke-style STM heads, and accessories, built for nuclear spin measurements. (A) Solenoid that fits around (B) the "solenoid head." (C) "Weiss-group-style" Besocke scan head, with a microwave-compatible bias cable. (D) Approach and scanning piezo tubes used in Besocke-style heads. (E) Side view of the platform that supports the solenoid head, providing a way for cables to access the underside of the head.

These changes in the design and construction of the STM head alter its behavior and response to external stimuli (e.g., vibration and electronic noise). The taller design of the scan head is undesirable since the added length makes the tip more susceptible to vibration. However, this susceptibility is compensated, in part, by the tight fit between the scan head and the inner bore of the solenoid, which stabilizes it with the aid of its much larger mass. One benefit of this solenoid design is that it acts as an excellent Faraday cage. Even when not using its magnetic field capabilities, the aluminum construction of the solenoid and its thick layers of coiled copper wires shields the tunneling junction from electromagnetic noise (e.g., 60 Hz from AC power lines).

Heat dissipation within the solenoid, while producing a magnetic field, was a specific challenge studied during the construction of the scan head. Current flowing through the (ohmic) wires within the solenoid dissipate heat, which act to raise its temperature. Over time, this heat will flow into the scan head, which can lead to thermal drift during imaging caused by asymmetric thermal expansion/contraction of the (different) materials used in its construction. Changes in temperature of the head are a source of instability for the STM over the extended measurement times used in these experiments. To understand the magnitude of this problem, we measured the temperature change of the solenoid as a function of time while the operating at its maximum power. The results of this experiment are shown in Figure 3.28. We measured an increase in the solenoid's temperature of about 5 °C over 8 h. The temperature changes most rapidly within the few hours after the current begins to flow (or ceases flowing). However, we reiterate that these changes were measured in the most extreme heating conditions (highest current operation) that the solenoid was designed experience. Furthermore, the solenoid is not intended to produce strong, constant, magnetic fields. As discussed previously, the solenoid is meant only to modify (and to modulate) the static field produced by a permanent magnet, which produces stronger fields without any

electric heating. As such, we do not expect this heating to preclude spin measurements. Nevertheless, we must acknowledge this source of instability in the STM head design.

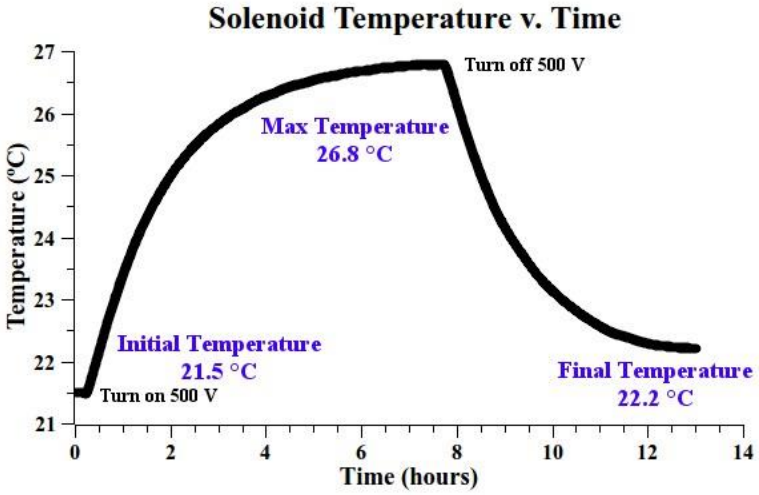

Figure 3.28: Temperature variation of the solenoid head over time. A constant potential of 500 V was applied across the input of the solenoid, causing a current of ~9 mA to flow (dissipating a power of 4.5 W). The solenoid operated in this condition for 7.5 h before abruptly stopping current from flowing by removing the applied voltage. The temperature of the solenoid was monitored continuously for a period of about 13 h, extending from 15 min before the voltage was applied, until 5.5 h after it was removed. The temperature data indicate that the Solenoid Head follows a Newton's law of cooling model, experiencing a temperature increase of around 5 °C at the tested power level.

Ultra-low noise, transimpedance amplifiers are required for these experiments and merited special attention when designing the STM. Amplifiers suffer from inherent limitations that necessitate making trade-offs between their noise level, gain, and bandwidth. As one of these characteristics improves, another suffers. Typically, STMs use transimpedance amplifiers with high gain (10^9 V A^{-1}) and low noise (~8 fA $Hz^{-½}$), but with relatively meager bandwidths (~1 kHz).

These specifications are sufficient for purely topographic imaging. We intend to use a similar amplifier in this experiment for the DC portion of the tunneling current, in order to maintain the desired tip-sample separation and for topographic imaging. However, this amplifier will be inadequate for the RF spin signal.

We will use an amplifier designed specifically for RF signals to detect the time-varying component of the tunneling current. This choice provides ample bandwidth with which to amplify the spin signal over a wide range of frequencies of interest, which depend on the specific spin under investigation and the local magnetic field it experiences. However, the gain of this amplifier will be substantially lower than that used to measure the DC tunneling current, only around 40 dB (10^2 current amplification) with a noise figure of 1 dB at 300 MHz. We intend to use a spectrum analyzer, which has a low noise floor (-166 dBm at 1 GHz bandwidth), to discern the weak spin signal. As such, the RF amplifier is not required to amplify the signal to the same degree as that used for the DC tunneling current. However, the weak signal will be attenuated as it passes through (imperfect) transmission cables prior to arriving at the spectrum analyzer and the maximum SNR will be degraded. As such, amplifying the RF spin signal, even by only a meager amount, close to the tunneling junction, serves to enhance the maximum SNR achievable in these measurements. A bias tee will be used to separate these two signals from the overall tunneling current flowing between the STM and sample. A bias tee acts as a combination of high- and low-pass filters, routing the AC and DC components of the input to different output terminals. Compact (surface-mount), wide bandwidth (15 GHz), low-noise (<0.2 dB) bias tees that can be incorporated into the design of the STM scan head, near the tunneling junction, have been used for this purpose when designing the amplification scheme for.

3.8 Single-Molecule Spin Measurements

Single-Molecule NMR

Following the detection of ^{59}Co nuclear spin ensembles, as described above, we will scale down the target system, both in physical size as well as in the number of spins probed. Smaller, superparamagnetic Co-NPs are one such system to study, building on the sample preparation and characterization techniques already developed. However, these would still represent a large collection of cobalt nuclei probed by the STM tip. Alternatively, phthalocyanine (Pc) molecules with a cobalt metal center offer another option. These molecules assemble into ordered monolayers on metal and graphite/graphene surfaces and are easily characterized using an STM, as shown in Figure 3.29. In the case of CoPc, each molecule contains only a single cobalt ion surrounded by a large, flat organic ligand. Electronically, the cobalt species differs significantly from that of Co-NPs, but possess identical nuclei. This system would enable us to test the effects of different chemical states and environments on the measured spin signal. Furthermore, chemical derivatives of Co-Pc that replace hydrogen with fluorine (F_{16}CoPc) offer the possibility to differentiate multiple nuclear spin species on the surface: ^{19}F and ^{59}Co. We would expect to measure the spin signal from ^{19}F around the periphery of the molecule at its distinctive Larmor frequency, compared to that of a ^{59}Co spin, localized near the molecule's center.

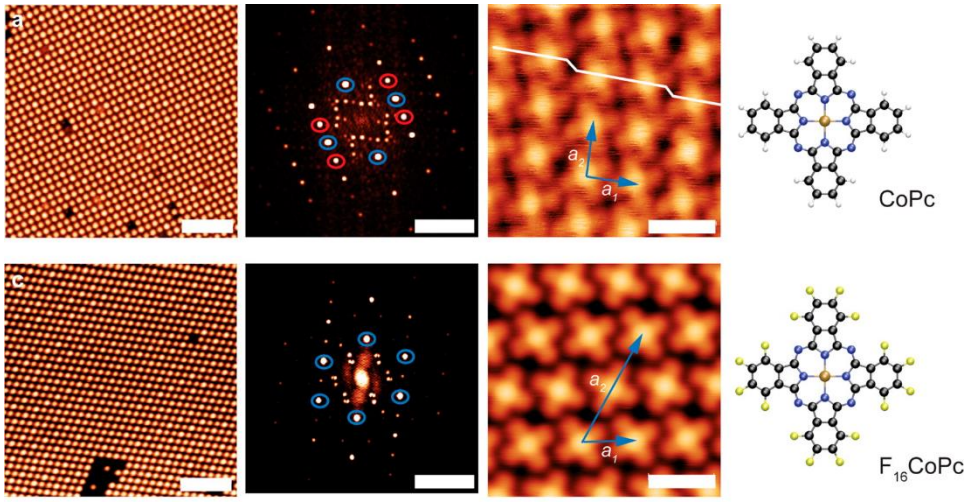

Figure 3.29: Scanning tunneling topographs, fast Fourier transforms of the two-dimensional topography, and molecular structures of cobalt phthalocyanine (CoPc) and fully fluorinated cobalt phthalocyanine (F_{16}CoPc). Self-assembled monolayers of CoPc (top row) and F_{16}CoPc (bottom row) on epitaxial graphene. From left to right, scale bars are 10 nm, 1 nm^{-1}, and 2 nm. Figure adapted with permission from Reference 146. Copyright 2014 American Chemical Society.

Single-Molecule Magnetic Resonance Imaging

Other promising systems to study include monolayers composed of nitrogen-containing molecules, such as 3-mercapto-*N*-nonylpropionamide (1ATC9) and nitro-functionalized oligo(phenylene ethynylene) molecules. Nitrogen-14 constitutes over 99.5% of natural nitrogen and possesses a nuclear spin of $I = 1$, though its NMR resonance is relatively broad due to quadrupole coupling with its environment.[147] Nevertheless, we may target nitrogen nuclei within 1ATC9 and 4-(2′-nitro-4′-phenylethynyl-phenylethynyl)-benzenethiol (NPPB) for NMR- and MRI-STM spin measurements. The molecules are known to assemble or insert into ordered monolayers on Au{111}, aided by the formation of hydrogen bonds between neighboring amide moieties within the assembled lattice.[148–150] This hydrogen-bonding network increases the stability of these monolayers and promotes phase separation when co-assembled with other types of

molecules (e.g., alkanethiols), as shown in Figure 3.30.[25] Such advantageous assembly makes this chemically heterogeneous system ideally suited for NMR- and MRI-STM studies.

We will use mixed monolayers of 1ATC9 and shorter-chain alkanethiols, such as C10 and C8, to prepare surfaces that possess domains of molecules with and without the ^{14}N spin under investigation. The spontaneous phase separation that occurs between 1ATC9 and alkanethiols, and the differences in their physical lengths enables us to distinguish the two species on the surface in STM images (Figure 3.30). Domains of the longer molecule, 1ATC9, will appear as more protruding regions on the surface, relative to domains of the shorter, less protruding alkanethiol species, providing an indirect means of chemical identification through topography. We expect to measure the ^{14}N nuclear spin signal by positioning the tip over 1ATC9 domains. When the tip is over alkanethiol domains, no spin signal is expected, serving as a spin-free control region that can be imaged *with the same STM tip* (controlling for spurious signals due to tip variations). This combination of measurements will serve to verify the origin of the spin signal and test the lateral range from which it may be measured by monitoring the signal intensity as the tip moves across 1ATC9/alkanethiol domain boundaries. We may further shrink the scale of the target system by making measurements on smaller domains or even single, inserted, 1ATC9 molecules located in alkanethiol SAM defects, enabling single-molecule NMR-STM measurements.

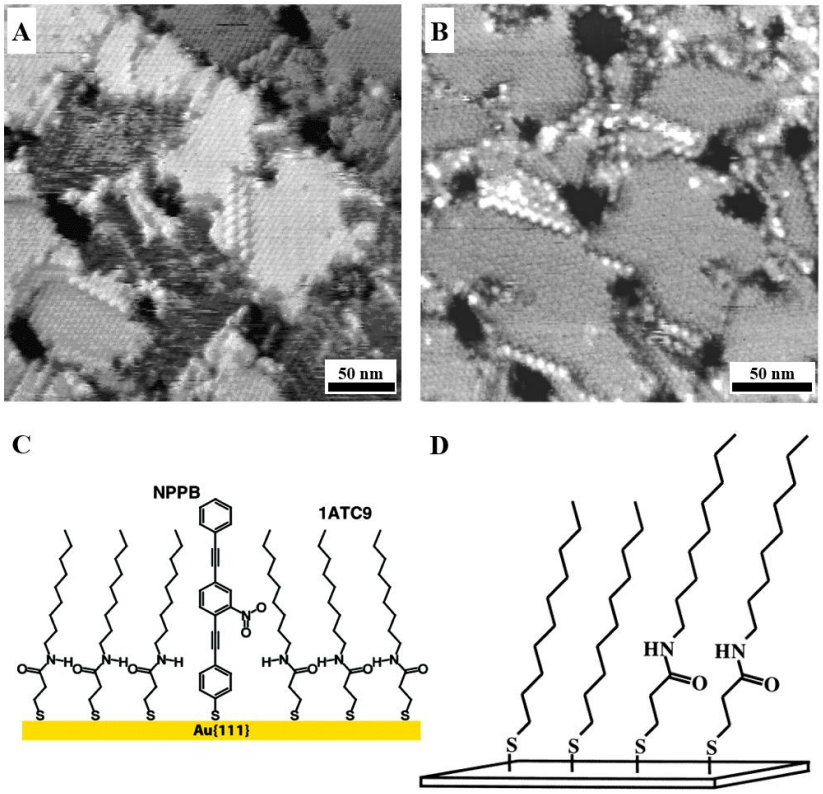

Figure 3.30: (A) Scanning tunneling topograph of mixed monolayer containing 3-mercapto-*N*-nonylpropionamide (1ATC9) and decanethiol (C10); V_{sample} = +1 V, $I_{set\ point}$ = 1 pA. (B) Scanning tunneling topograph of mixed monolayer containing 1ATC9 and C8; V_{sample} = +1 V, $I_{set\ point}$ = 2 pA. Phase segregation is observed between the alkanethiol and amide-containing molecules co-absorbed on Au{111}. The topographically higher regions in the images are the amide-containing molecules, which protrude further from the surface, while the topographically lower regions are the alkanethiol molecules. (C) Schematic of a 1ATC6 SAM matrix with an inserted 4-(2′-nitro-4′-phenylethynyl-phenylethynyl)-benzenethiol (NPPB) molecule. (D) Schematic of a mixed monolayer of C10 (left) and 1ATC9 (right) molecules. (A, D) Adapted with permission from Reference 148. Copyright 2001 American Chemical Society. (B) Adapted with permission from Reference 25. Copyright 2001 American Chemical Society. (C) Adapted with permission from Reference 149. Copyright 2004 American Chemical Society.

We will extend these nuclear spin measurements to include monolayers composed of inserted NPPB molecules, as shown schematically in Figure 3.30C. These molecules possess nitro moieties, the positions of which can reversibly switch between discrete locations within the assembled SAM using the probe tip of an STM. A strong magnetic field gradient in the proximity of the probed spins will split the resonance frequencies of spatially separated nuclei based on their positions. The detection of multiple resonance peaks enables us to infer the relative positions of spins within the probed region. Reconstructing the structure of the probed spins is contingent on a known magnetic field gradient within the measurement area, which we discuss in more detail in Section 3.8.3. Assemblies of 1ATC9 with inserted NPPB molecules would possess two different nitrogen-containing moieties, located at different positions above the underlying gold substrate, due to differences in molecules geometry. As such, an MRI-STM may be used to distinguish the relative positions of the probed nitrogen spins, buried within the SAM. Additionally, since NPPB may switch between two conductance states, which are distinguishable by STM topographic imaging,[149,150] we may also detect a more subtle shift in the ^{14}N spin signal due to the change in molecular conformation and chemical environment due to switching. As such, single-molecule MRI-STM measurements will aid our understanding of the buried structure of SAMs, and other materials, not normally accessible to scanning probe measurements.

Magnetic Field Gradients

The central principle of magnetic resonance imaging is that a spatially varying magnetic field, and the corresponding variations in Larmor precession frequency, enables one to determine the distribution of nuclear spins within an object.[10] Since the Larmor frequency depends on the local field strength (Eq. 3.10), knowledge of how the magnetic field varies in space enables one to determine the position of based on its this frequency. Increasingly precise position measurements

require the use of stronger magnetic field gradients in order to separate, spectrally, the resonances of two closely spaced nuclear moments.

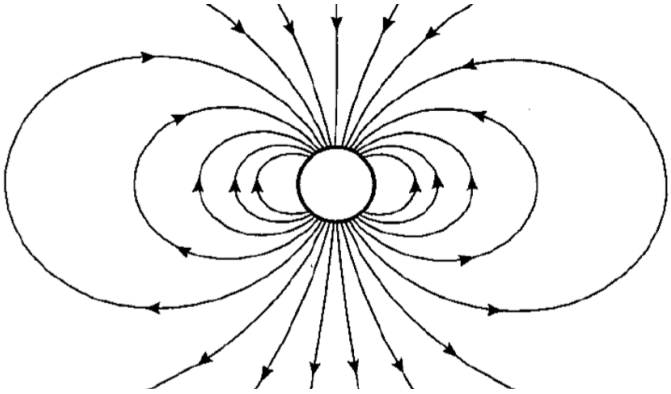

Figure 3.31: Schematic diagram of a sphere with uniform magnetization. Azimuthally symmetric magnetic field lines are depicted in the space outside the sphere. Figure adapted with permission from Reference 151.

We propose to leverage the techniques developed previously in these experiments and use Co-NPs as the source of a high magnetic field gradient for MRI-STM measurements. The field strength near single-domain ferromagnetic nanoparticles can be approach that of saturation field strength of the material (~1 T), since their internal electronic spins are aligned a long a common axis. Due to their size, this field decays rapidly with distance from the nanoparticle in a predictable manner (see Figure 3.31 and Eq. 3.2). As such, the magnetic field produced by Co-NPs has a high spatial gradient (~10^8 T m^{-1}), as plotted in Figure 3.32, as computed for nanoparticle with the magnetic properties of bulk cobalt. The actual magnetization and field from nanoparticles, however, is typically less than that of the bulk material; for example, ϵ-phase Co-NPs have been shown to have saturation magnetization of only ~40% of that of bulk cobalt.[95] Even accounting for these diminished field strengths, however, we expect that the magnetic field gradient in the

immediate vicinity of the nanoparticles (<10 nm) will be sufficient to split the resonance frequency of spatially separated ^{14}N nuclei by ~10 kHz, for Larmor frequencies of ~1 MHz.

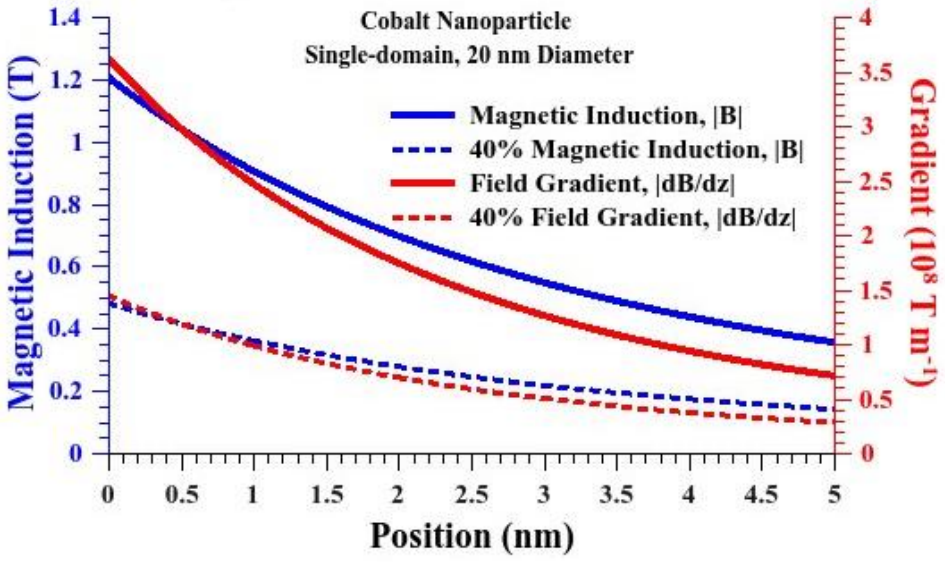

Figure 3.32: Variation in the magnetic induction field (*B*), and field gradient $\left(\boldsymbol{dB}/\boldsymbol{dz}\right)$ as a function of position away from the surface of a spherical cobalt nanoparticle, 20 nm in diameter. The fields and gradients depicted above assume saturation magnetization values of 100% (solid line) and 40% (dashed line)[95] that of bulk cobalt.

3.9 Recognizing the Challenges

The aims of this project are ambitious – to detect and to resolve single nuclear spins with sub-molecular resolution – and will undoubtedly be exceedingly challenging to accomplish. From an experimental standpoint, the inherently small signal expected, coupled with ambient measurement environment, makes the task a daunting one. From a theoretical point of view, the origin of the *electronic* spin signal monitored in analogous ESN-STM measurements is still not completely understood,[20,57,58,60,152] while the origin of a *nuclear* spin signal[59] seems less obvious. Additionally, existing MRFM and NV measurement techniques look to be a promising alternative

routes to fulfill this project's goals. Great progress has already been made with MRFM in detecting and distinguishing a variety of nuclear moments,[53,153,154] improving spatial resolution,[39,155] and performing three-dimensional, MRI-style measurements on biological systems.[38]

The success of these first measurements of cobalt nuclear spins will encourage the continuation and scaling-down the experiment to the single-molecule level. However, if no signal is detected, even in this large system, then a re-evaluation of the technique is warranted, considering the potential feasibility of the measurement itself.

3.10 Conclusions & Prospects

Measurement of ^{59}Co NMR Signal via Scanning Tunneling Microscopy

We will detect the NMR signal from isolated Co-NPs and study any effects that Co-NP size, shape, and interactions with neighboring Co-NPs have on the resonance signal. These secondary measurements will help us understand what factors affect the spin signal (in particular, its amplitude) while it is still relatively easy to measure, before progressing to the molecular scale.

Detection of ^{14}N Nuclear Spin in Mixed-Monolayers

We will measure the nuclear spin signal from 1ATC9 molecules in a mixed-monolayer SAM. Measurements on large 1ATC9 domains and isolated single-molecules within a NMR-signal-free matrix will be performed. We will establish the minimum domain size needed to detect a signal and understand effects of the local environment (defects, degree of ordering, and type of neighbor molecules) on the measurement. Understanding the influence of the environment on the NMR signal will be critical in the final stages of the development of MRI-style measurements that distinguish single-spins based on their positions.

Single-Molecule Magnetic Resonance Imaging

STM detection and resolution of multiple, spatially separated, spins within mixed SAMs (e.g., 1ATC9 and NPPB). A positive result here will demonstrate the feasibility of the MRI-STM design, opening the door to the measurement of more complex molecules. However, before we can sensibly use the data derived from complex molecules, we need to vet thoroughly and understand the spectra and spectral images of simple molecules, making these preliminary measurements significant.

3.11 References

(1) National Research Council (US) Committee on Research Opportunities in Biology. Molecular Structure and Function. In *Opportunities in Biology*; National Academies Press: Washington, D.C., 1989; pp. 33–76.

(2) Groll, M.; Ditzel, L.; Löwe, J.; Stock, D.; Bochtler, M.; Bartunik, H. D.; Huber, R. Structure of 20S Proteasome from Yeast at 2.4 Å Resolution. *Nature* **1997**, *386*, 463–471.

(3) Nissen, P.; Hansen, J.; Ban, N.; Moore, P. B.; Steitz, T. A. The Structural Basis of Ribosome Activity in Peptide Bond Synthesis. *Science* **2000**, *289*, 920–930.

(4) Alberts, B.; Johnson, A.; Lewis, J.; Raff, M.; Roberts, K.; Walter, P. Analyzing Protein Structure and Function. In *Molecular Biology of the Cell*; Garland Science: New York, 2002.

(5) Ferreira, K. N.; Iverson, T. M.; Maghlaoui, K.; Barber, J.; Iwata, S. Architecture of the Photosynthetic Oxygen-Evolving Center. *Science* **2004**, *303*, 1831–1838.

(6) *Structure-Based Drug Discovery*; Tari, L. W., Ed.; Humana Press: New York, 2012; Vol. 841.

(7) Feng, W.; Pan, L.; Zhang, M. Combination of NMR Spectroscopy and X-Ray Crystallography Offers Unique Advantages for Elucidation of the Structural Basis of Protein Complex Assembly. *Sci. China Life Sci.* **2011**, *54*, 101–111.

(8) Krishnan, V.; Rupp, B. Macromolecular Structure Determination: Comparison of X-Ray Crystallography and NMR Spectroscopy. *eLS*; John Wiley & Sons, Ltd, Chichester, 2012.

(9) Chen, C. J. *Introduction to Scanning Tunneling Microscopy*; 2nd ed.; Oxford University Press: New York, 2007.

(10) Lauterbur, P. C. Image Formation by Induced Local Interactions: Examples Employing Nuclear Magnetic Resonance. *Nature* **1973**, *242*, 190–191.

(11) Gross, L.; Mohn, F.; Moll, N.; Meyer, G.; Ebel, R.; Abdel-Mageed, W. M.; Jaspars, M. Organic Structure Determination Using Atomic-Resolution Scanning Probe Microscopy. *Nat. Chem.* **2010**, *2*, 821–825.

(12) Kane, B. E. A Silicon-Based Nuclear Spin Quantum Computer. *Nature* **1998**, *393*, 133–137.

(13) Childress, L.; Dutt, M. V. G.; Taylor, J. M.; Zibrov, A. S.; Jelezko, F.; Wrachtrup, J.; Hemmer, P. R.; Lukin, M. D. Coherent Dynamics of Coupled Electron and Nuclear Spin Qubits in Diamond. *Science* **2006**, *314*, 281–285.

(14) McCamey, D. R.; Tol, J. V.; Morley, G. W.; Boehme, C. Electronic Spin Storage in an Electrically Readable Nuclear Spin Memory with a Lifetime >100 Seconds. *Science* **2010**, *330*, 1652–1656.

(15) Bloch, F. Nuclear Induction. *Phys. Rev.* **1946**, *70*, 460–474.

(16) Sleator, T.; Hahn, E. L.; Hilbert, C.; Clarke, J. Nuclear-Spin Noise. *Phys. Rev. Lett.* **1985**, *55*, 1742–1745.

(17) Degen, C. L.; Poggio, M.; Mamin, H. J.; Rugar, D. Role of Spin Noise in the Detection of Nanoscale Ensembles of Nuclear Spins. *Phys. Rev. Lett.* **2007**, *99*, 250601.

(18) Crooker, S. A.; Rickel, D. G.; Balatsky, A. V.; Smith, D. L. Spectroscopy of Spontaneous Spin Noise as a Probe of Spin Dynamics and Magnetic Resonance. *Nature* **2004**, *431*, 49–52.

(19) Claridge, S. A.; Schwartz, J. J.; Weiss, P. S. Electrons, Photons, and Force: Quantitative Single-Molecule Measurements from Physics to Biology. *ACS Nano* **2011**, *5*, 693–729.

(20) Balatsky, A. V.; Nishijima, M.; Manassen, Y. Electron Spin Resonance-Scanning Tunneling Microscopy. *Adv. Phys.* **2012**, *61*, 117–152.

(21) Poggio, M.; Degen, C. L. Force-Detected Nuclear Magnetic Resonance: Recent Advances and Future Challenges. *Nanotechnology* **2010**, *21*, 342001.

(22) Petit, C.; Pileni, M. P. Physical Properties of Self-Assembled Nanosized Cobalt Particles. *Appl. Surf. Sci.* **2000**, *162–163*, 519–528.

(23) Yoshimoto, S.; Higa, N.; Itaya, K. Two-Dimensional Supramolecular Organization of Copper Octaethylporphyrin and Cobalt Phthalocyanine on Au(111): Molecular

Assembly Control at an Electrochemical Interface. *J. Am. Chem. Soc.* **2004**, *126*, 8540–8545.

(24) Iacovita, C.; Rastei, M. V.; Heinrich, B. W.; Brumme, T.; Kortus, J.; Limot, L.; Bucher, J. P. Visualizing the Spin of Individual Cobalt-Phthalocyanine Molecules. *Phys. Rev. Lett.* **2008**, *101*, 116602.

(25) Lewis, P. A.; Smith, R. K.; Kelly, K. F.; Bumm, L. A.; Reed, S. M.; Clegg, R. S.; Gunderson, J. D.; Hutchison, J. E.; Weiss, P. S. The Role of Buried Hydrogen Bonds in Self-Assembled Mixed Composition Thiols on Au{111}. *J. Phys. Chem. B* **2001**, *105*, 10630–10636.

(26) Lu, H.; Zeysing, D.; Kind, M.; Terfort, A.; Zharnikov, M. Structure of Self-Assembled Monolayers of Partially Fluorinated Alkanethiols with a Fluorocarbon Part of Variable Length on Gold Substrate. *J. Phys. Chem. C* **2013**, *117*, 18967–18979.

(27) Kalashnyk, N.; Nielsen, J. T.; Nielsen, E. H.; Skrydstrup, T.; Otzen, D. E.; Lægsgaard, E.; Wang, C.; Besenbacher, F.; Nielsen, N. C.; Linderoth, T. R. Scanning Tunneling Microscopy Reveals Single-Molecule Insights into the Self-Assembly of Amyloid Fibrils. *ACS Nano* **2012**, *6*, 6882–6889.

(28) Claridge, S. A.; Thomas, J. C.; Silverman, M. A.; Schwartz, J. J.; Yang, Y.; Wang, C.; Weiss, P. S. Differentiating Amino Acid Residues and Side Chain Orientations in Peptides Using Scanning Tunneling Microscopy. *J. Am. Chem. Soc.* **2013**, *135*, 18528–18535.

(29) Chiesa, M.; Giamello, E. Electron Spin Resonance Spectroscopy. *Encyclopedia of Analytical Chemistry*; John Wiley & Sons, Ltd, Chichester, 2014.

(30) Gray-Edwards, H. L.; Salibi, N.; Josephson, E. M.; Hudson, J. A.; Cox, N. R.; Randle, A. N.; McCurdy, V. J.; Bradbury, A. M.; Wilson, D. U.; Beyers, R. J.; Denney, T. S.; Martin, D. R. High Resolution MRI Anatomy of the Cat Brain at 3 Tesla. *J. Neurosci. Meth.* **2014**, *227*, 10–17.

(31) Hirai, M.; Yamanaka, C.; Ikeya, M. Some Trials on a New Method of ESR Detection Using Tunneling Current. *Appl. Radiat. Isot.* **1993**, *44*, 385–389.

(32) Manassen, Y.; Hamers, R. J.; Demuth, J. E.; Castellano, A. J., Jr. Direct Observation of the Precession of Individual Paramagnetic Spins on Oxidized Silicon Surfaces. *Phys. Rev. Lett.* **1989**, *62*, 2531–2534.

(33) Manassen, Y. Real-Time Response and Phase-Sensitive Detection to Demonstrate the Validity of ESR-STM Results. *J. Magn. Reson.* **1997**, *126*, 133–137.

(34) Durkan, C.; Welland, M. E. Electronic Spin Detection in Molecules Using Scanning-Tunneling- Microscopy-Assisted Electron-Spin Resonance. *Appl. Phys. Lett.* **2002**, *80*, 458–460.

(35) Messina, P.; Mannini, M.; Caneschi, A.; Gatteschi, D.; Sorace, L.; Sigalotti, P.; Sandrin, C.; Prato, S.; Pittana, P.; Manassen, Y. Spin Noise Fluctuations from Paramagnetic Molecular Adsorbates on Surfaces. *J. Appl. Phys.* **2007**, *101*, 053916.

(36) Mugnaini, V.; Fabrizioli, M.; Ratera, I.; Mannini, M.; Caneschi, A.; Gatteschi, D.; Manassen, Y.; Veciana, J. Towards the Detection of Single Polychlorotriphenylmethyl Radical Derivatives by Means of Electron Spin Noise STM. *Solid State Sci.* **2009**, *11*, 956–960.

(37) Gorini, L.; Fabrizioli, M.; Mannini, M.; Sorace, L.; Yakovenko, A. Addressing Single Molecules of a Thin Magnetic Film. *Inorg. Chim. Acta* **2008**, *361*, 4089–4093.

(38) Degen, C. L.; Poggio, M.; Mamin, H. J.; Rettner, C. T.; Rugar, D. Nanoscale Magnetic Resonance Imaging. *Proc. Natl. Acad. Sci. U.S.A.* **2009**, *106*, 1313–1317.

(39) Mamin, H. J.; Poggio, M.; Degen, C. L.; Rugar, D. Nuclear Magnetic Resonance Imaging with 90-nm Resolution. *Nat. Nanotechnol.* **2007**, *2*, 301–306.

(40) Rugar, D.; Budakian, R.; Mamin, H. J.; Chui, B. W. Single Spin Detection by Magnetic Resonance Force Microscopy. *Nature* **2004**, *430*, 329–332.

(41) Köhler, J.; Disselhorst, J. a. J. M.; Donckers, M. C. J. M.; Groenen, E. J. J.; Schmidt, J.; Moerner, W. E. Magnetic Resonance of a Single Molecular Spin. *Nature* **1993**, *363*, 242–244.

(42) Wrachtrup, J.; von Borczyskowski, C.; Bernard, J.; Orritt, M.; Brown, R. Optical Detection of Magnetic Resonance in a Single Molecule. *Nature* **1993**, *363*, 244–245.

(43) Gruber, A.; Dräbenstedt, A.; Tietz, C.; Fleury, L.; Wrachtrup, J.; Borczyskowski, C. von. Scanning Confocal Optical Microscopy and Magnetic Resonance on Single Defect Centers. *Science* **1997**, *276*, 2012–2014.

(44) Prawer, S.; Greentree, A. D. Applied Physics. Diamond for Quantum Computing. *Science* **2008**, *320*, 1601–1602.

(45) Jiang, L.; Hodges, J. S.; Maze, J. R.; Maurer, P.; Taylor, J. M.; Cory, D. G.; Hemmer, P. R.; Walsworth, R. L.; Yacoby, A.; Zibrov, A. S.; Lukin, M. D. Repetitive Readout of a Single Electronic Spin via Quantum Logic with Nuclear Spin Ancillae. *Science* **2009**, *326*, 267–272.

(46) Neumann, P.; Beck, J.; Steiner, M.; Rempp, F.; Fedder, H.; Hemmer, P. R.; Wrachtrup, J.; Jelezko, F. Single-Shot Readout of a Single Nuclear Spin. *Science* **2010**, *329*, 542–544.

(47) Maze, J. R.; Stanwix, P. L.; Hodges, J. S.; Hong, S.; Taylor, J. M.; Cappellaro, P.; Jiang, L.; Dutt, M. V. G.; Togan, E.; Zibrov, A. S.; Yacoby, A.; Walsworth, R. L.; Lukin, M. D. Nanoscale Magnetic Sensing with an Individual Electronic Spin in Diamond. *Nature* **2008**, *455*, 644–647.

(48) Balasubramanian, G.; Chan, I. Y.; Kolesov, R.; Al-Hmoud, M.; Tisler, J.; Shin, C.; Kim, C.; Wojcik, A.; Hemmer, P. R.; Krueger, A.; Hanke, T.; Leitenstorfer, A.; Bratschitsch, R.; Jelezko, F.; Wrachtrup, J. Nanoscale Imaging Magnetometry with Diamond Spins under Ambient Conditions. *Nature* **2008**, *455*, 648–651.

(49) DeVience, S. J.; Pham, L. M.; Lovchinsky, I.; Sushkov, A. O.; Bar-Gill, N.; Belthangady, C.; Casola, F.; Corbett, M.; Zhang, H.; Lukin, M.; Park, H.; Yacoby, A.; Walsworth, R. L. Nanoscale NMR Spectroscopy and Imaging of Multiple Nuclear Species. *Nature Nanotech.* **2015**, *10*, 129–134.

(50) Sainoo, Y.; Isshiki, H.; Shahed, S. M. F.; Takaoka, T.; Komeda, T. Atomically Resolved Larmor Frequency Detection on Si(111)-7×7 Oxide Surface. *Appl. Phys. Lett.* **2009**, *95*, 082504–082504 – 3.

(51) Krukowski, P.; Olejniczak, W.; Klusek, Z.; Pawlowski, S.; Kobierski, P.; Puchalski, M. An ESN-STM Spectrometer for Single Spin Detection. *Measurement* **2010**, *43*, 1495–1502.

(52) Messina, P.; Sigalotti, P.; Lenci, L.; Prato, S.; Gatteschi, D. Construction of an ESR-STM for Single Molecular Based Magnets Anchored at Surfaces. In *4th IEEE Conference on Nanotechnology*; Munich, Germany, 2004; pp. 642–644.

(53) Mamin, H. J.; Oosterkamp, T. H.; Poggio, M.; Degen, C. L.; Rettner, C. T.; Rugar, D. Isotope-Selective Detection and Imaging of Organic Nanolayers. *Nano Lett.* **2009**, *9*, 3020–3024.

(54) Xue, F.; Peddibhotla, P.; Montinaro, M.; Weber, D. P.; Poggio, M. A Geometry for Optimizing Nanoscale Magnetic Resonance Force Microscopy. *Appl. Phys. Lett.* **2011**, *98*, 163103.

(55) Schaff, A.; Veeman, W. S. Mechanically Detected Nuclear Magnetic Resonance Image of a Multilayer System at Normal Pressure. *Appl. Phys. Lett.* **1997**, *70*, 2598–2600.

(56) Verhagen, R.; Hilbers, C. W.; Kentgens, A. P. M.; Lenci, L.; Groeneveld, R.; Wittli, A.; van Kempen, H. Mechanical Detection of NMR. Advantages of a Digital Approach. *Phys. Chem. Chem. Phys.* **1999**, *1*, 4025–4031.

(57) Zhu, J.-X.; Balatsky, A. V. Quantum Electronic Transport through a Precessing Spin. *Phys. Rev. Lett.* **2002**, *89*, 286802.

(58) Nussinov, Z.; Crommie, M. F.; Balatsky, A. V. Noise Spectroscopy of a Single Spin with Spin-Polarized STM. *Phys. Rev. B* **2003**, *68*, 085402.

(59) Balatsky, A. V.; Fransson, J.; Mozyrsky, D.; Manassen, Y. STM NMR and Nuclear Spin Noise. *Phys. Rev. B* **2006**, *73*, 184429.

(60) Balatsky, A. V.; Martin, I. Theory of Single Spin Detection with STM. *Quantum Inf. Process.* **2002**, *1*, 355–364.

(61) Marshall, W. Orientation of Nuclei in Ferromagnets. *Phys. Rev.* **1958**, *110*, 1280–1285.

(62) Fernandez, A.; Bedrossian, P. J.; Baker, S. L.; Vernon, S. P.; Kania, D. R. Magnetic Force Microscopy of Single-Domain Cobalt Dots Patterned Using Interference Lithography. *IEEE Trans. Magn.* **1996**, *32*, 4472–4474.

(63) New, R. M. H.; Pease, R. F. W.; White, R. L. Lithographically Patterned Single-Domain Cobalt Islands for High-Density Magnetic Recording. *J. Magn. Magn. Mater.* **1996**, *155*, 140–145.

(64) Jackson, J. D. *Classical Electrodynamics*; 3rd ed.; Wiley: New York, 1998.

(65) Bansmann, J.; Kleibert, A.; Bulut, F.; Getzlaff, M.; Imperia, P.; Boeglin, C.; Meiwes-Broer, K.-H. Temperature Dependent Magnetic Spin and Orbital Moments of Mass-Filtered Cobalt Clusters on Au(111). *Eur. Phys. J. D* **2007**, *45*, 521–528.

(66) Gossard, A. C.; Portis, A. M. Observation of Nuclear Resonance in a Ferromagnet. *Phys. Rev. Lett.* **1959**, *3*, 164–166.

(67) *CRC Handbook Chemistry and Physics*; Lide, D. R., Ed.; 85th ed.; Boca Raton, FL, 2004.

(68) Gossard, A. C.; Portis, A. M.; Rubinstein, M.; Lindquist, R. H. Ferromagnetic Nuclear Resonance of Single-Domain Cobalt Particles. *Phys. Rev.* **1965**, *138*, A1415–A1421.

(69) Thomson, T.; Riedi, P. C.; Sankar, S.; Berkowitz, A. E. Nuclear Magnetic Resonance Investigations of Co Nanoclusters in a SiO_2 Thin Film Matrix. *J. Appl. Phys.* **1997**, *81*, 5549–5551.

(70) Leslie-Pelecky, D. L.; Rieke, R. D. Magnetic Properties of Nanostructured Materials. *Chem. Mater.* **1996**, *8*, 1770–1783.

(71) Néel, L. Théorie Du Traînage Magnétique des Ferromagnétiques en Grains Fins avec Applications aux Terres Cuites. *Ann. Géophys.* **1949**, *5*, 99–136.

(72) Respaud, M.; Goiran, M.; Broto, J. M.; Lionti, F.; Thomas, L.; Barbara, B.; Ely, T. O.; Amiens, C.; Chaudret, B. Dynamical Properties of Non-Interacting Co Nanoparticles. *Europhys. Lett.* **1999**, *47*, 122–127.

(73) Fannin, P. C.; Slawska-Waniewska, A.; Didukh, P.; Giannitsis, A. T.; Charles, S. W. Dynamic Properties of a System of Cobalt Nanoparticles. *Eur. Phys. J.: Appl. Phys.* **2002**, *17*, 3–9.

(74) Bean, C. P.; Livingston, J. D. Superparamagnetism. *J. Appl. Phys.* **1959**, *30*, S120–S129.

(75) Murray, C. b.; Sun, S.; Doyle, H.; Betley, T. Monodisperse 3d Transition-Metal (Co, Ni, Fe) Nanoparticles and Their Assembly into Nanoparticle Superlattices. *MRS Bull.* **2001**, *26*, 985–991.

(76) Su, Y. K.; Shen, C. M.; Yang, T. Z.; Yang, H. T.; Gao, H. J.; Li, H. L. The Dependence of Co Nanoparticle Sizes on the Ratio of Surfactants and the Influence of Different Crystal Sizes on Magnetic Properties. *Appl. Phys. A* **2005**, *81*, 569–572.

(77) Dahanayaka, D. H.; Wang, J. X.; Hossain, S.; Bumm, L. A. Optically Transparent Au{111} Substrates: Flat Gold Nanoparticle Platforms for High-Resolution Scanning Tunneling Microscopy. *J. Am. Chem. Soc.* **2006**, *128*, 6052–6053.

(78) Nielsen, R. M.; Murphy, S.; Strebel, C.; Johansson, M.; Nielsen, J. H.; Chorkendorff, I. A Comparative STM Study of Ru Nanoparticles Deposited on HOPG by Mass-Selected Gas Aggregation Versus Thermal Evaporation. *Surf. Sci.* **2009**, *603*, 3420–3430.

(79) Nielsen, R.; Murphy, S.; Strebel, C.; Johansson, M.; Chorkendorff, I.; Nielsen, J. The Morphology of Mass Selected Ruthenium Nanoparticles from a Magnetron-Sputter Gas-Aggregation Source. *J. Nanopart. Res.* **2010**, *12*, 1249–1262.

(80) Jun, Y. W.; Seo, J. W.; Cheon, J. Nanoscaling Laws of Magnetic Nanoparticles and Their Applicabilities in Biomedical Sciences. *Acc. Chem. Res.* **2008**, *41*, 179–189.

(81) Batlle, X.; Labarta, A. Finite-Size Effects in Fine Particles: Magnetic and Transport Properties. *J. Phys. D: Appl. Phys.* **2002**, *35*, R15–R42.

(82) Sun, S.; Murray, C. B. Synthesis of Monodisperse Cobalt Nanocrystals and Their Assembly into Magnetic Superlattices (Invited). *J. Appl. Phys.* **1999**, *85*, 4325–4330.

(83) Dinega, D. P.; Bawendi, M. G. A Solution-Phase Chemical Approach to a New Crystal Structure of Cobalt. *Angew. Chem., Int. Ed.* **1999**, *38*, 1788–1791.

(84) O'Shea, V. A. de la P.; Moreira, I. de P. R.; Roldán, A.; Illas, F. Electronic and Magnetic Structure of Bulk Cobalt: The α, β, and ε-Phases from Density Functional Theory Calculations. *J. Chem. Phys.* **2010**, *133*, 024701.

(85) Kitakami, O.; Sato, H.; Shimada, Y.; Sato, F.; Tanaka, M. Size Effect on the Crystal Phase of Cobalt Fine Particles. *Phys. Rev. B* **1997**, *56*, 13849–13854.

(86) Ferré, R.; Ounadjela, K.; George, J. M.; Piraux, L.; Dubois, S. Magnetization Processes in Nickel and Cobalt Electrodeposited Nanowires. *Phys. Rev. B* **1997**, *56*, 14066–14075.

(87) Cullity, B. D.; Graham, C. D. *Introduction to Magnetic Materials*; 2nd ed.; Wiley-IEEE Press: Hoboken, NJ, 2008.

(88) Gross, A. F.; Diehl, M. R.; Beverly, K. C.; Richman, E. K.; Tolbert, S. H. Controlling Magnetic Coupling between Cobalt Nanoparticles through Nanoscale Confinement in Hexagonal Mesoporous Silica. *J. Phys. Chem. B* **2003**, *107*, 5475–5482.

(89) Wu, N.; Fu, L.; Su, M.; Aslam, M.; Wong, K. C.; Dravid, V. P. Interaction of Fatty Acid Monolayers with Cobalt Nanoparticles. *Nano Lett.* **2004**, *4*, 383–386.

(90) Diehl, M. R.; Yu, J.-Y.; Heath, J. R.; Held, G. A.; Doyle, H.; Sun, S.; Murray, C. B. Crystalline, Shape, and Surface Anisotropy in Two Crystal Morphologies of Superparamagnetic Cobalt Nanoparticles by Ferromagnetic Resonance. *J. Phys. Chem. B* **2001**, *105*, 7913–7919.

(91) Salgueiriño-Maceira, V.; Correa-Duarte, M. A.; Hucht, A.; Farle, M. One-Dimensional Assemblies of Silica-Coated Cobalt Nanoparticles: Magnetic Pearl Necklaces. *Journal of Magnetism and Magnetic Materials* **2006**, *303*, 163–166.

(92) Hucht, A.; Buschmann, S.; Entel, P. Molecular Dynamics Simulations of the Dipolar-Induced Formation of Magnetic Nanochains and Nanorings. *Europhys. Lett.* **2007**, *77*, 57003.

(93) Russier, V.; Petit, C.; Legrand, J.; Pileni, M. P. Collective Magnetic Properties of Cobalt Nanocrystals Self-Assembled in a Hexagonal Network: Theoretical Model Supported by Experiments. *Phys. Rev. B* **2000**, *62*, 3910–3916.

(94) van Leeuwen, D. A.; van Ruitenbeek, J. M.; de Jongh, L. J.; Ceriotti, A.; Pacchioni, G.; Häberlen, O. D.; Rösch, N. Quenching of Magnetic Moments by Ligand-Metal Interactions in Nanosized Magnetic Metal Clusters. *Phys. Rev. Lett.* **1994**, *73*, 1432–1435.

(95) Yang, H. T.; Su, Y. K.; Shen, C. M.; Yang, T. Z.; Gao, H. J. Synthesis and Magnetic Properties of ε-Cobalt Nanoparticles. *Surf. Interface Anal.* **2004**, *36*, 155–160.

(96) Benkoski, J. J.; Breidenich, J. L.; Uy, O. M.; Hayes, A. T.; Deacon, R. M.; Land, H. B.; Spicer, J. M.; Keng, P. Y.; Pyun, J. Dipolar Organization and Magnetic Actuation of Flagella-like Nanoparticle Assemblies. *J. Mater. Chem.* **2011**, *21*, 7314–7325.

(97) Breidenich, J. L.; Wei, M. C.; Clatterbaugh, G. V.; Benkoski, J. J.; Keng, P. Y.; Pyun, J. Controlling Length and Areal Density of Artificial Cilia through the Dipolar Assembly of Ferromagnetic Nanoparticles. *Soft Matter* **2012**, *8*, 5334–5341.

(98) Doan, N.; Kontturi, K.; Johans, C. Directing Oxidation of Cobalt Nanoparticles with the Capping Ligand. *J. Colloid Interface Sci.* **2010**, *350*, 126–131.

(99) Petit, C.; Pileni, M. P. Cobalt Nanosized Particles Organized in a 2D Superlattice: Synthesis, Characterization, and Magnetic Properties. *J. Phys. Chem. B* **1999**, *103*, 1805–1810.

(100) Li, J.; Huang, J.; Qin, Y.; Ma, F. Magnetic and Microwave Properties of Cobalt Nanoplatelets. *Mater. Sci. Eng. B* **2007**, *138*, 199–204.

(101) Kittel, C. *Introduction to Solid State Physics*; 8th ed.; Wiley: New York, 2004.

(102) Zhang, L.; Xue, D.; Gao, C. Anomalous Magnetic Properties of Antiferromagnetic CoO Nanoparticles. *J. Magn. Magn. Mater.* **2003**, *267*, 111–114.

(103) Ghosh, M.; Sampathkumaran, E. V.; Rao, C. N. R. Synthesis and Magnetic Properties of CoO Nanoparticles. *Chem. Mater.* **2005**, *17*, 2348–2352.

(104) Rödl, C.; Fuchs, F.; Furthmüller, J.; Bechstedt, F. Quasiparticle Band Structures of the Antiferromagnetic Transition-Metal Oxides MnO, FeO, CoO, and NiO. *Phys. Rev. B* **2009**, *79*, 235114.

(105) Gupta, R.; Sinha, A.; Raja Sekhar, B.; Srivastava, A.; Singh, G.; Deb, S. Synthesis and Characterization of Various Phases of Cobalt Oxide Nanoparticles Using Inorganic Precursor. *Appl. Phys. A: Mater. Sci. Process.* **2011**, *103*, 13–19.

(106) Datar, S.; Kumar, P. M.; Sastry, M.; Dharmadhikari, C. V. Scanning Tunneling Microscopy/Spectroscopy of Titanium Dioxide Nanoparticulate Film on Au(111) Surface. *Colloids Surf., A* **2004**, *232*, 11–17.

(107) Watson, R. E.; Freeman, A. J. Origin of Effective Fields in Magnetic Materials. *Phys. Rev.* **1961**, *123*, 2027–2047.

(108) Wertheim, G. K. Hyperfine Structure of Divalent and Trivalent Fe^{57} in Cobalt Oxide. *Phys. Rev.* **1961**, *124*, 764–767.

(109) Peng, D. L.; Sumiyama, K.; Yamamuro, S.; Hihara, T.; Konno, T. J. Preparation and Magnetic Properties of Oxide-Coated Monodispersive Co Cluster Assembly. *Phys. Status Solidi A* **1999**, *172*, 209–216.

(110) Gangopadhyay, S.; Hadjipanayis, G. C.; Sorensen, C. M.; Klabunde, K. J. Exchange Anisotropy in Oxide Passivated Co Fine Particles. *J. Appl. Phys.* **1993**, *73*, 6964–6966.

(111) Tracy, J. B.; Weiss, D. N.; Dinega, D. P.; Bawendi, M. G. Exchange Biasing and Magnetic Properties of Partially and Fully Oxidized Colloidal Cobalt Nanoparticles. *Phys. Rev. B* **2005**, *72*, 064404.

(112) Lu, A.-H.; Salabas, E. L.; Schüth, F. Magnetic Nanoparticles: Synthesis, Protection, Functionalization, and Application. *Angew. Chem., Int. Ed.* **2007**, *46*, 1222–1244.

(113) Meiklejohn, W. H.; Bean, C. P. New Magnetic Anisotropy. *Phys. Rev.* **1956**, *102*, 1413–1414.

(114) Meiklejohn, W. H.; Bean, C. P. New Magnetic Anisotropy. *Phys. Rev.* **1957**, *105*, 904–913.

(115) Johnston-Peck, A. C.; Wang, J.; Tracy, J. B. Synthesis and Structural and Magnetic Characterization of Ni(Core)/NiO(Shell) Nanoparticles. *ACS Nano* **2009**, *3*, 1077–1084.

(116) Hulteen, J. C.; Van Duyne, R. P. Nanosphere Lithography: A Materials General Fabrication Process for Periodic Particle Array Surfaces. *J. Vac. Sci. Technol., A* **1995**, *13*, 1553–1558.

(117) Haynes, C. L.; Van Duyne, R. P. Nanosphere Lithography: A Versatile Nanofabrication Tool for Studies of Size-Dependent Nanoparticle Optics. *J. Phys. Chem. B* **2001**, *105*, 5599–5611.

(118) Xia, Y.; Gates, B.; Yin, Y.; Lu, Y. Monodispersed Colloidal Spheres: Old Materials with New Applications. *Adv. Mater.* **2000**, *12*, 693–713.

(119) Flavel, B. S.; Shapter, J. G.; Jiang, J. S. Nanosphere Lithography Using Thermal Evaporation of Gold. In *2006 International Conference on Nanoscience and Nanotechnology*; IEEE: Brisbane, Queensland, Australia, 2006.

(120) Petit, C.; Cren, T.; Roditchev, D.; Sacks, W.; Klein, J.; Pileni, M.-P. Single Electron Tunneling Through Nano-Sized Cobalt Particles. *Adv. Mater.* **1999**, *11*, 1198–1202.

(121) Zhao, J.; Spasova, M.; Li, Z.-A.; Zharnikov, M. Ferromagnetic Cobalt Nanoparticles and Their Immobilization on Monomolecular Films and Chemical Templates. *Adv. Funct. Mater.* **2011**, *21*, 4724–4735.

(122) Tadmor, R. The London-van der Waals Interaction Energy Between Objects of Various Geometries. *J. Phys.: Condens. Matter* **2001**, *13*, L195–L202.

(123) Love, J. C.; Estroff, L. A.; Kriebel, J. K.; Nuzzo, R. G.; Whitesides, G. M. Self-Assembled Monolayers of Thiolates on Metals as a Form of Nanotechnology. *Chem. Rev.* **2005**, *105*, 1103–1170.

(124) Devillers, S.; Hennart, A.; Delhalle, J.; Mekhalif, Z. 1-Dodecanethiol Self-Assembled Monolayers on Cobalt. *Langmuir* **2011**, *27*, 14849–14860.

(125) Liang, J.; Rosa, L. G.; Scoles, G. Nanostructuring, Imaging and Molecular Manipulation of Dithiol Monolayers on Au(111) Surfaces by Atomic Force Microscopy. *J. Phys. Chem. C* **2007**, *111*, 17275–17284.

(126) Kang, J. F.; Ulman, A.; Liao, S.; Jordan, R.; Yang, G.; Liu, G. Self-Assembled Rigid Monolayers of 4‘-Substituted-4-Mercaptobiphenyls on Gold and Silver Surfaces. *Langmuir* **2001**, *17*, 95–106.

(127) Tai, Y.; Shaporenko, A.; Rong, H.-T.; Buck, M.; Eck, W.; Grunze, M.; Zharnikov, M. Fabrication of Thiol-Terminated Surfaces Using Aromatic Self-Assembled Monolayers. *J. Phys. Chem. B* **2004**, *108*, 16806–16810.

(128) Leung, T. Y. .; Schwartz, P.; Scoles, G.; Schreiber, F.; Ulman, A. Structure and Growth of 4-Methyl-4′-Mercaptobiphenyl Monolayers on Au(111): A Surface Diffraction Study. *Surface Science* **2000**, *458*, 34–52.

(129) Qu, D.; Kim, B.-C.; Lee, C.-W. J.; Ito, M.; Noguchi, H.; Uosaki, K. 1,6-Hexanedithiol Self-Assembled Monolayers on Au(111) Investigated by Electrochemical, Spectroscopic, and Molecular Mechanics Methods. *J. Phys. Chem. C* **2010**, *114*, 497–505.

(130) Viana, A. S.; Leupold, S.; Montforts, F.-P.; Abrantes, L. M. Self-Assembled Monolayers of a Disulphide-Derivatised Cobalt-Porphyrin on Gold. *Electrochim. Acta* **2005**, *50*, 2807–2813.

(131) Smith, R. K.; Nanayakkara, S. U.; Woehrle, G. H.; Pearl, T. P.; Blake, M. M.; Hutchison, J. E.; Weiss, P. S. Spectral Diffusion in the Tunneling Spectra of Ligand-Stabilized Undecagold Clusters. *J. Am. Chem. Soc.* **2006**, *128*, 9266–9267.

(132) Haiss, W.; Wang, C.; Jitchati, R.; Grace, I.; Martín, S.; Batsanov, A. S.; Higgins, S. J.; Bryce, M. R.; Lambert, C. J.; Jensen, P. S.; Nichols, R. J. Variable Contact Gap Single-Molecule Conductance Determination for a Series of Conjugated Molecular Bridges. *J. Phys.: Condens. Matter* **2008**, *20*, 374119.

(133) Tivanski, A. V.; He, Y.; Borguet, E.; Liu, H.; Walker, G. C.; Waldeck, D. H. Conjugated Thiol Linker for Enhanced Electrical Conduction of Gold−Molecule Contacts. *J. Phys. Chem. B* **2005**, *109*, 5398–5402.

(134) Akkerman, H. B.; Kronemeijer, A. J.; van Hal, P. A.; de Leeuw, D. M.; Blom, P. W. M.; de Boer, B. Self-Assembled-Monolayer Formation of Long Alkanedithiols in Molecular Junctions. *Small* **2008**, *4*, 100–104.

(135) Kim, Y.-H.; Gorman, C. B. Standing Up versus Looping Over: Controlling the Geometry of Self-Assembled Monolayers of α,ω-Diynes on Gold. *Langmuir* **2011**, *27*, 6069–6075.

(136) Kind, M.; Wöll, C. Organic Surfaces Exposed by Self-Assembled Organothiol Monolayers: Preparation, Characterization, and Application. *Prog. Surf. Sci.* **2009**, *84*, 230–278.

(137) Fuchs, D. J.; Weiss, P. S. Insertion of 1,10-Decanedithiol in Decanethiolate Self-Assembled Monolayers on Au{111}. *Nanotechnology* **2007**, *18*, 044021.

(138) Ferreira, V. C.; Silva, F.; Abrantes, L. M. Electrochemical and STM Study of α,ω-Alkanedithiols Self-Assembled Monolayers. *Chem. Biochem. Eng. Q.* **2009**, *23*, 99–106.

(139) Azzam, W.; Wehner, B. I.; Fischer, R. A.; Terfort, A.; Wöll, C. Bonding and Orientation in Self-Assembled Monolayers of Oligophenyldithiols on Au Substrates. *Langmuir* **2002**, *18*, 7766–7769.

(140) Rieley, H.; Kendall, G. K.; Zemicael, F. W.; Smith, T. L.; Yang, S. X-Ray Studies of Self-Assembled Monolayers on Coinage Metals. 1. Alignment and Photooxidation in 1,8-Octanedithiol and 1-Octanethiol on Au. *Langmuir* **1998**, *14*, 5147–5153.

(141) Tour, J. M.; Jones, L.; Pearson, D. L.; Lamba, J. J. S.; Burgin, T. P.; Whitesides, G. M.; Allara, D. L.; Parikh, A. N.; Atre, S. Self-Assembled Monolayers and Multilayers of Conjugated Thiols, α,ω-Dithiols, and Thioacetyl-Containing Adsorbates. Understanding Attachments Between Potential Molecular Wires and Gold Surfaces. *J. Am. Chem. Soc.* **1995**, *117*, 9529–9534.

(142) Saavedra, H. M.; Thompson, C. M.; Hohman, J. N.; Crespi, V. H.; Weiss, P. S. Reversible Lability by in Situ Reaction of Self-Assembled Monolayers. *J. Am. Chem. Soc.* **2009**, *131*, 2252–2259.

(143) Cygan, M. T.; Dunbar, T. D.; Arnold, J. J.; Bumm, L. A.; Shedlock, N. F.; Burgin, T. P.; Jones, L.; Allara, D. L.; Tour, J. M.; Weiss, P. S. Insertion, Conductivity, and Structures of Conjugated Organic Oligomers in Self-Assembled Alkanethiol Monolayers on Au{111}. *J. Am. Chem. Soc.* **1998**, *120*, 2721–2732.

(144) Besocke, K. An Easily Operable Scanning Tunneling Microscope. *Surface Science* **1987**, *181*, 145–153.

(145) Frohn, J.; Wolf, J. F.; Besocke, K.; Teske, M. Coarse Tip Distance Adjustment and Positioner for a Scanning Tunneling Microscope. *Rev. Sci. Instrum.* **1989**, *60*, 1200.

(146) Järvinen, P.; Hämäläinen, S. K.; Ijäs, M.; Harju, A.; Liljeroth, P. Self-Assembly and Orbital Imaging of Metal Phthalocyanines on a Graphene Model Surface. *J. Phys. Chem. C* **2014**, *118*, 13320–13325.

(147) Lehn, J. M.; Kintzinger, J. P. Nitrogen-14 Nuclear Quadrupole Effects. In *Nitrogen NMR*; Witanowski, M.; Webb, G. A., Eds.; Springer US: New York, 1973; pp. 79–161.

(148) Smith, R. K.; Reed, S. M.; Lewis, P. A.; Monnell, J. D.; Clegg, R. S.; Kelly, K. F.; Bumm, L. A.; Hutchison, J. E.; Weiss, P. S. Phase Separation within a Binary Self-Assembled Monolayer on Au{111} Driven by an Amide-Containing Alkanethiol. *J. Phys. Chem. B* **2001**, *105*, 1119–1122.

(149) Lewis, P. A.; Inman, C. E.; Yao, Y.; Tour, J. M.; Hutchison, J. E.; Weiss, P. S. Mediating Stochastic Switching of Single Molecules Using Chemical Functionality. *J. Am. Chem. Soc.* **2004**, *126*, 12214–12215.

(150) Lewis, P. A.; Inman, C. E.; Maya, F.; Tour, J. M.; Hutchison, J. E.; Weiss, P. S. Molecular Engineering of the Polarity and Interactions of Molecular Electronic Switches. *J. Am. Chem. Soc.* **2005**, *127*, 17421–17426.

(151) Stern, D. P. A Millennium of Geomagnetism. *Rev. Geophys.* **2002**, *40*, 1007.

(152) Bulaevskii, L. N.; Hruška, M.; Ortiz, G. Tunneling Measurement of Quantum Spin Oscillations. *Phys. Rev. B* **2003**, *68*, 125415.

(153) Verhagen, R.; Wittlin, A.; Hilbers, C. W.; van Kempen, H.; Kentgens, A. P. M. Spatially Resolved Spectroscopy and Structurally Encoded Imaging by Magnetic Resonance Force Microscopy of Quadrupolar Spin Systems. *J. Am. Chem. Soc.* **2002**, *124*, 1588–1589.

(154) Thurber, K. R.; Harrell, L. E.; Smith, D. D. 170 Nm Nuclear Magnetic Resonance Imaging Using Magnetic Resonance Force Microscopy. *J. Magn. Reson.* **2003**, *162*, 336–340.

(155) Longenecker, J. G.; Mamin, H. J.; Senko, A. W.; Chen, L.; Rettner, C. T.; Rugar, D.; Marohn, J. A. High-Gradient Nanomagnets on Cantilevers for Sensitive Detection of Nuclear Magnetic Resonance. *ACS Nano* **2012**, *6*, 9637–9645.

CHAPTER 4

Molecular Flux Dependence of Chemical Patterning by Microcontact Printing

4.1 Introduction

Microcontact printing enables parallel soft-lithographic patterning of materials ranging from small-molecule inks to nanoparticles.[1–15] In its simplest form, an elastomeric stamp with a relief pattern is dosed with ink molecules (inked) and then is placed in conformal contact with a reactive surface.[16–25] Molecules, henceforth referred to simply as "ink," transfer from stamp to substrate and, in the cases of thiol inks on many metals, form self-assembled monolayers (SAMs), imbuing the contact sites with the chemical properties of the molecular assembly. The key advantages of μCP are its flexibility and intrinsic simplicity; the inking method, substrate, and stamp can be tailored to produce the desired results. For example, ink pads can be used to limit swelling of the elastomeric stamp by solvent absorption,[26] the stamp surface can be hydrophilized by UV/ozone or oxygen plasma treatment to modulate ink transfer between stamp and substrate,[27–30] or the stamp may be functionalized to catalyze reactions on the substrate.[31–35] Generally, μCP procedures for printing *n*-alkanethiol inks on noble metals call for short contact times; a bare gold surface is

sufficiently reactive to thiols that nearly full coverage films are produced after contact times on the millisecond scale.[36,37]

We have previously reported methods for controlling ink transfer by modulating the reactivity of substrates through the use of preformed SAMs.[38–41] Microdisplacement (μDP) printing utilizes the exchange of *n*-alkanethiols with a preformed 1AD SAM.[38,42–48] Time scales for μDP experiments are typically an order of magnitude longer than those for μCP experiments, ranging from 15 min to 24 h, depending on the ink employed and the desired coverage. Controlling the molecular flux (defined as the quantity of molecules delivered to the interface by diffusion per unit time) at the stamp/substrate interface becomes imperative when printing time scales are comparable to, or exceed, inking times.

4.2 Experimental

Materials and Methods

Undoped, single-side polished Si(100) wafers (<40 Ω cm resistivity, 350–400 μm thickness) were used as received from Silicon Quest International. Thiols (1-dodecanethiol, C12; 1-octadecanethiol, C18; and 1-adamantanethiol, 1AD), hexanes, and ethanol were all used as received from Sigma Aldrich. Deionized water (18.2 MΩ cm) was dispensed by a Milli-Q system purchased from Millipore (Billerica, MA, USA). Sylgard 184 Base and PDMS Sylgard 184 Cure were obtained from Dow Corning (Midland, MI, USA). Heptadecafluoro-1,1,2,2-tetra-hydrodecyl trichlorosilane was used as received from Gelest (Morrisville, PA, USA).

Preparation of Polymer Stamps

Patterned polydimethylsiloxane (PDMS) stamps were prepared from photolithographically defined features etched into a silicon wafer. An unpatterned wafer was used to prepare flat stamps.

Before the first use of the silicon masters, they were treated with (heptadecafluoro-1,1,2,2-tetra-hydrodecyl) trichlorosilane to prevent PDMS adhesion to the silicon. A small quantity (~0.1 mL) of the chemical was deposited on a glass coverslip in a vacuum desiccator, alongside the silicon masters, and a vacuum (1×10^{-2} Torr) was drawn until the chemical evaporated. Afterward, the wafers were rinsed serially with acetone and ethanol, and then dried with nitrogen gas.

The PDMS Sylgard 184 Base and PDMS Sylgard 184 Cure were combined in a 10:1 ratio (by weight) and stirred vigorously. The mixed prepolymer, in a disposable plastic container with tall sides, was placed in a vacuum desiccator and deaerated under vacuum (1×10^{-3} Torr) until no bubbles were visible (the mixed polymer expands substantially under reduced pressure as trapped gas bubbles expand in volume). The deaerated polymer was poured over the silicon masters in a foil-lined Petri dish. The dish is deaerated to remove any residual or introduced bubbles. Afterward, the PDMS was cured at 60 °C for 24 h. Stamps were then peeled from the silicon master and cut to the desired size with a razor blade.

Low molecular weight PDMS is removed by swelling cured stamps in hexanes for 6 h, replacing the hexanes every 2 h. Swelled stamps are heated at 40 °C for at least 24 h. As the hexane evaporates, the stamps shrink to their original size. Stamps can crack if they are laid flat on a surface, or if the temperature is too high, during baking. The stamp surface can be cleaned by sonication for 30 min in a 1:1 water/ethanol bath. Stamps are then dried with a stream of nitrogen and stored face up in a plastic Petri dish until needed.

Stamp Inking

The traditional wet-inking method, common among many variations of μCP experiments, involves pipetting an ethanolic solution of an alkanethiol ink onto the stamp surface, where it sits

for 10 to 60 s. After the desired inking time has elapsed (usually 60 s) the stamp is blown dry with a stream of nitrogen.

For saturation inking, a stamp is immersed in an ethanolic solution of the appropriate concentration for an order of magnitude longer than the printing time scale. Upon removal from solution, the stamp is briefly rinsed with neat ethanol and dried with nitrogen gas. Rinsing the stamp minimizes surface crystallization for high-molecular-weight inks. Thinner stamps (<5 mm) reach saturation more quickly than thicker stamps.

Printing

The PDMS stamps will generally adhere to flat surfaces, so it is convenient to center the stamp on a polished metal disk (here 60 g) to act as a weight, bringing the stamp/weight combination in contact with a surface in a single motion. Twisting or other motions result in smudged or doubled patterns. After the desired contact time, the weight and sample are removed together. The sample is rinsed with neat ethanol and dried with a stream of nitrogen.

For IR analysis, the substrate must be uniformly printed. To prepare these samples, an inked, featureless stamp is brought into contact with a substrate to form complete monolayers. It is most convenient to print with a stamp that is slightly larger than the sample.

Grazing Incidence IR Spectroscopy

Infrared spectra were collected using a Nicolet 6700 FTIR spectrometer (Thermo Electron Corp., Waltham, MA), equipped with a liquid-nitrogen-cooled mercury–cadmium-telluride detector and a Seagull variable-angle reflection accessory (Harrick Scientific, Inc., Ossining, NY). A FTIR Purge Gas Generator (Parker-Balston, Cleveland, OH) removed water and CO_2 from the gas stream used to purge the spectrometer and its accessory. The data were collected at grazing

incidence reflection (82° relative to the surface normal) with *p*-polarized light and a mirror speed of 1.27 cm s^{-1}, with a resolution of 2 cm^{-1}. All spectra were averaged over 1024 scans. Scans were normalized with spectra of perdeuterated *n*-dodecanethiolate monolayers on Au{111}.

Scanning Electron Microscopy

Scanning electron micrographs of patterned 1AD/C12 SAMs were collected using a Leo 1530 field-emission scanning electron microscope (SEM) at an accelerating voltage of 5 kV. We have previously shown that the SEM is sensitive to exposed chemical functionality and chemical patterns.[47]

4.3 Results & Discussion

Infrared Spectroscopy of Printed Films

Infrared reflectance adsorption spectroscopy (IRRAS) is an ensemble technique used to determine SAM structural and compositional details. Self-assembled monolayer order improves with increasing deposition time. A SAM formed only briefly is a kinetic product with a high defect density.[49,50] Exchange between molecules in solution and those on the surface tends to increase average domain size, resulting in SAMs with higher degrees of order.[42,51] Figure 4.1 shows four offset IR spectra for SAMs printed with varying contact times by a featureless slab of PDMS ("flat stamp"), saturation-inked for 24 h with 25 mM C12.

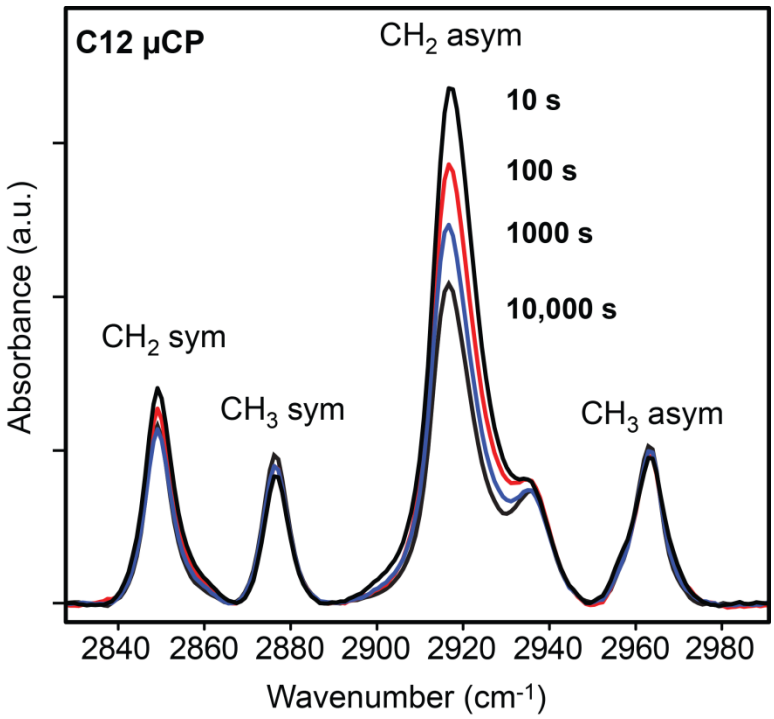

Figure 4.1: Infrared reflection absorbance spectra of the methyl (CH_3) and methylene (CH_2) stretches present in 1-dodecanethiol self-assembled monolayers (SAMs) on gold, prepared by microcontact printing with contact times varying by orders of magnitude. All four spectra are characteristic of full-coverage, crystalline SAMs, but the decrease in CH_2 asymmetric stretch intensity with printing time correlates to an improvement in overall order and uniformity of the film. The stamps are featureless PDMS slabs, saturation-inked in a 25 mM ethanolic solution of 1-dodecanethiol for 24 h prior to printing.

Infrared spectra of *n*-alkanethiolate SAMs show five characteristic peaks associated with hydrocarbon chains between 2800 and 3000 cm^{-1}, of which two are relevant diagnostically. The methylene (CH_2) asymmetric stretch is the dominant spectral feature and is found between 2918 and 2920 cm^{-1}. This stretch is highly sensitive to monolayer crystallinity. The peak shifts toward 2918 cm^{-1} for crystalline, solid-like films.[52] Disordered areas are more liquid-like, and the peak shifts to higher wavenumbers (higher energies).

Application of surface selection rules helps elucidate the structure and orientation of molecules at interfaces. Infrared radiation excites those vibrational modes that result in changes in the transition dipole moment; on conductive surfaces, absorption is maximized if the dipole is oriented normal to the surface and is attenuated if parallel to the surface.[53] Molecules in well-ordered domains are tilted uniformly from the surface normal by 30°, a configuration that tends to decrease infrared adsorption intensity of the CH_2 asymmetric stretch. Disordered molecules have more orientational degrees of freedom, resulting in an average increase in the absorption intensity of the methylene modes. This effect can be seen in Figure 4.1; as contact time increases logarithmically, CH_2 asymmetric intensity decreases linearly.[54]

The methyl (CH_3) symmetric stretch is an excellent indicator of absolute *n*-alkanethiolate coverage; IR adsorption is relatively insensitive to the orientation of the methyl group, compared to CH_2 orientation, once assembled into a SAM.[42,52] Printed SAMs can be expected to have >90% coverage within the first second of contact. The methyl symmetric stretch intensity increases by <8% during the 9000 s period that followed the first 1000 s of contact time. Other spectral features are the CH_2 symmetric, the CH_3 asymmetric, and the minor CH_3 Fermi resonance at 2850, 2990, and 2935 cm^{-1}, respectively.[52]

Monitoring and Controlling the Degree of Order of Printed Monolayers

Two series of samples were prepared and their IR spectra compared to test the reproducibility of conformational order in printed films. The first series was prepared using a stamp that was wet-inked for 1 min with 25 mM ethanolic C18 solution. The second series was prepared from a stamp that was saturation-inked by immersion in a 25 mM ethanolic C18 solution for 24 h. Both sets were prepared using virgin, featureless PDMS slabs that uniformly cover a

sample surface, with a printing contact time of 15 min for SAM formation. The stamps were reinked between each printing. The results of these experiments are shown in Figure 4.2.

The uniformity of printed SAMs is dependent on both the inking and the printing times. The wet-inked series (Figure 4.2A, red traces) show consistently higher methylene asymmetric stretch intensities, which correlate to lower conformational uniformity, than SAMs in the saturation-inked series (Figure 4.2A, black traces). The mean and standard deviation for each series are shown by the data points and error bars to the right of the spectra. Peaks from SAMs produced by saturation-inked stamps have a narrower standard deviation than the wet-inked films. In the case of saturation inking, the stamp is returned to the inking solution between printing experiments.

We note an additional trend in the methylene stretch intensity for the wet-inked series. Reinking the stamp between each printing procedure increases ink loading and, thus, maintains ink concentration at the stamp/sample interface with each subsequent print. This trend is apparent by tracking the observed 2919 cm^{-1} peak height versus the deposition sequence, as shown in Figure 4.2C, where each printed film shows higher conformational order than the preceding film.

In summary, saturation-inking improves the order and reproducibility of printed films over many samples and can be used to control their overall quality. This trend holds for all films printed with saturation-inked stamps; continuous control over absolute film quality can be obtained by the simple control of stamp interface concentration.

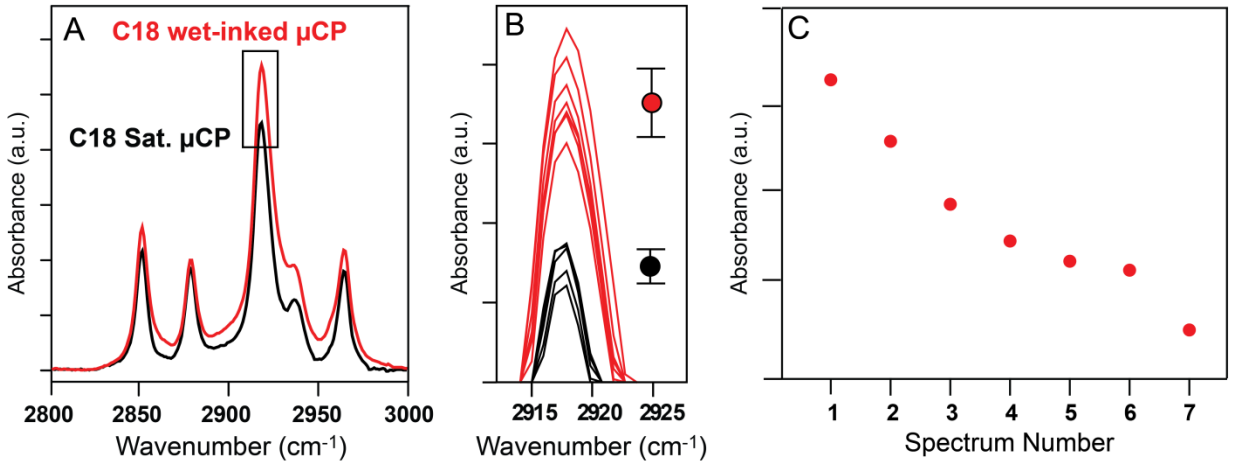

Figure 4.2: Increasing inking time results in a corresponding improvement in printed monolayer order and minimizes variability between experiments. (A) Representative infrared spectra for printed 1-octadecanethiol (C18) self-assembled monolayers (SAMs). Stamps were either sequentially wet-inked for 1 min (red trace) or saturation inked for 24 h (black trace). The methylene asymmetric stretch (2919 cm^{-1}) intensity correlates inversely to film quality; SAMs printed by saturation-inking show consistently higher conformational order than wet-inked films. (B) Expanded view of the boxed area in A, which shows an overlay of all spectra in the data set. The mean and standard deviation of each series are denoted by the black and red circles, which correspond to the saturation-inked and wet-inked series, respectively, and illustrate the superior control provided by the saturation-inking method. (C) Repeated wet-inking between prints increases the absolute ink loading of a stamp. Plotting the 2919 cm^{-1} peak height of the wet-inked series against the preparation sequence reveals consistent improvement in film quality. Each time the stamp is inked, the absolute ink loading increases, which in turn improves the conformational order of the printed SAMs.

Control of Microdisplacement Printed Film Coverage

The 1AD film is labile with respect to an *n*-alkanethiol ink with a chain length of at least eight carbon atoms. Alkanethiols are delivered by the stamp and insert into 1AD SAM defect sites, gradually displacing the film via perimeter-dependent island growth.[42] Microdisplacement printing has three main advantages over direct printing on gold: limited indirect ink transport (via edge spreading or gas-phase deposition), viability of low-molecular-weight inks, and nanoscale chemical patterning produced by the emergence of fractal-like structures of two-component, partially displaced films. Our early efforts focused on producing fully displaced *n*-alkanethiolate films at the contact sites, as controlling fractional coverage as a function of printing time was imprecise because of variability of the ink concentration at the stamp/substrate interface. Figure 4.3 depicts SEM images of chemical patterns produced by the microdisplacement printing of 25 mM C12 on a preformed 1AD monolayer at several contact time intervals. Without an internal standard, the contrast mechanism for the SEM is not quantitative and provides little information regarding the nanoscale composition of the patterned films.[47,55] In previous work, we have used scanning probe microscopy imaging of chemical patterns, which were observed to be consistent with the more efficiently recorded SEM data shown here.

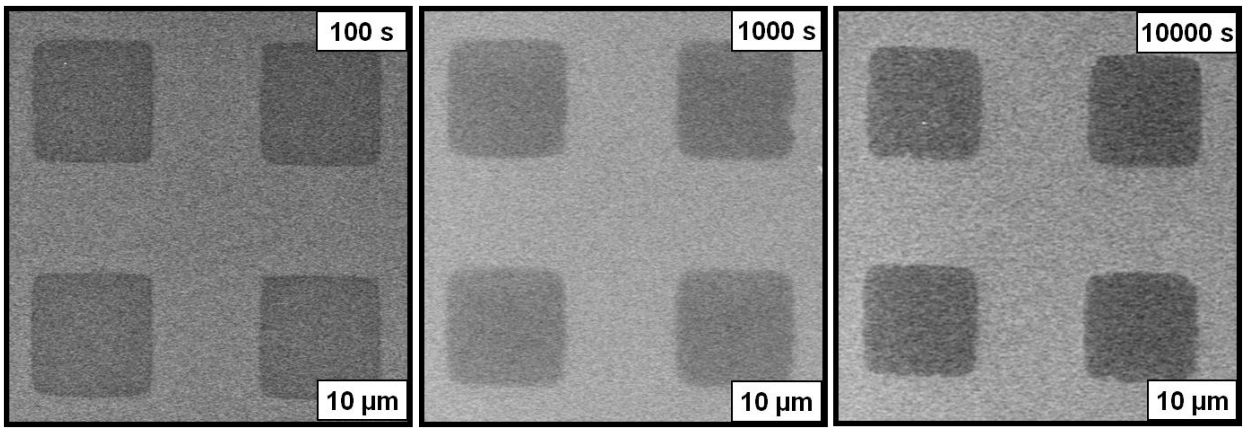

Figure 4.3: Scanning electron micrographs of chemical patterns produced by microdisplacement printing on a preformed 1-adamantanethiol self-assembled monolayer by contact with a stamp saturation-inked with 25 mM 1-dodecanethiol. Absolute coverage increases with contact time and the contrast between the pattern and background shifts (but cannot be estimated by scanning electron microscopy without an internal reference). Based on the observed patterns, we assign the higher intensity regions (shown as brighter) evident in each of the above images to be the 1-adamantanethiol preformed monolayer, while areas where 1-dodecanethiol (molecular ink deposited by the stamp) displaced 1-adamantanethiol molecules in the monolayer appear as lower intensity regions.

The initial displacement exchange rate is proportional to the square root of the *n*-alkanethiol concentration.[42] We use saturation-inking to maximize control over the displacement reaction and to monitor the kinetics of the process as well as relative coverage of mixed 1AD/C12 monolayer via IRRAS. The 1AD IR spectrum has two main peaks, the CH_2 symmetric and asymmetric stretches at 2850 and 2911 cm^{-1}, respectively.[42,56] We have previously tracked the relative fractional coverage of two-component 1AD/C12 SAMs by monitoring the orientation-insensitive CH_3 symmetric stretch of C12[42,45,46] (and have also successfully utilized the same strategy for other cage-molecule assemblies[57,58]). Figure 4.4 shows the spectral evolution of a 1AD

SAM (Figure 4.4A) gradually displaced by C12 delivered by a nonpatterned PDMS stamp (Figure 4.4B–E). The intensity of the adamantyl 2911 cm^{-1} stretch decreases concurrently with the emergence of the methyl symmetric and methylene asymmetric stretches, at 2877 and 2919 cm^{-1}, respectively. We use the methyl stretch to determine fractional coverage of mixed 1AD/C12 monolayers prepared with different stamp concentrations, the results of which are shown in Figure 4.5. The 25 mM ink concentration provided a good compromise of control and time at ~0.5% coverage per minute until >90% coverage. The higher and lower concentrations (50 and 10 mM, respectively) were inconvenient; displacement was too fast for fine control at high ink concentration, and lower concentrations did not provide sufficiently improved control over fine structure to justify the longer contact time.

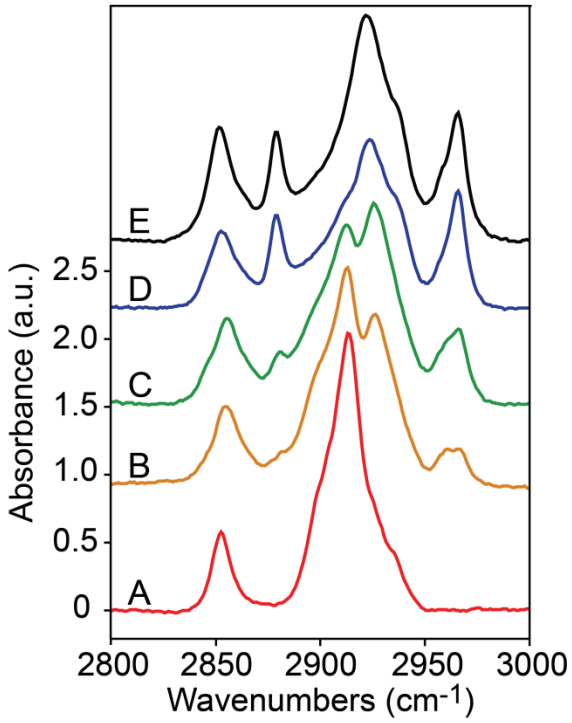

Figure 4.4: (A–E) Spectral evolution of 1-adamantanethiol (1AD) self-assembled monolayer (SAM) displacement. The preformed 1AD SAM is displaced gradually when held in contact with a PDMS stamp saturation-inked with 25 mM 1-dodecanethiol (C12). (A) Infrared spectrum of preformed 1AD SAM on Au. (B–E) Infrared spectra obtained after printing for 10, 100, 1000, and 10 000 s, respectively. (E) After 10 000 s of contact, the monolayer is a single-component C12 SAM.

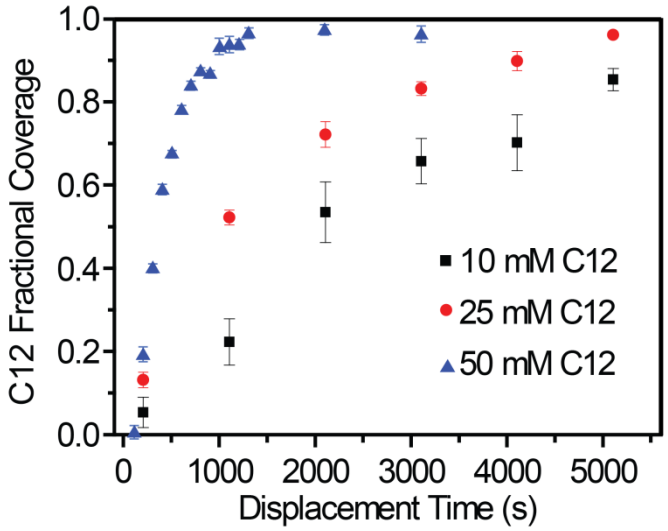

Figure 4.5: Fractional *n*-alkanethiolate self-assembled monolayer coverage by displacement printing at various ink concentrations. The 2877 cm^{-1} methyl symmetric stretch is analyzed to determine fractional 1-dodecanethiol coverage after partial displacement. At ~0.5% displacement per minute, the stamps that were saturation-inked with 25 mM 1-dodecanethiol proved the most convenient and reliable for fine control of fractional monolayer coverage by microdisplacement printing.

Modeling Diffusion of Molecular Ink at a Stamp Interface

In conventional μCP experiments, the stamp is placed in contact with a substrate for only a short printing time, usually about 30 s. Diffusion of ink into the stamp can be ignored as an important factor in these cases as the time required to obtain full monolayer coverage is short compared to the time scale for significant ink diffusion, and since increasing contact time tends to reduce pattern fidelity.[59–61] For experiments requiring longer contact times, however, ink diffusion into the stamp bulk becomes the determinant variable affecting performance and reliability of the technique.

A misconception regarding μCP ink transfer is that the polymeric stamp is coated only externally by ink. Although this is almost certainly the case for the transfer of nanomaterials, biomaterials, and polar molecular inks,[2,6,7,25,30,62,63] nonpolar *n*-alkanethiol inks dissolve readily in the PDMS, rather than pooling at the stamp surface.[64] The PDMS stamp medium can be thought of as a solvent of high viscosity.[65] Balmer and coworkers developed a model for the diffusion of *n*-alkanethiols in PDMS, and determined a diffusion coefficient of 5.0×10^{-7} cm^2 s^{-1} for 1-hexadecanethiol.[65] To illustrate the importance of effective flux at the stamp/substrate interface, we use their values, and a similar mathematical model, to approximate diffusion of *n*-alkanethiols of moderate length (C12 and C18) in PDMS stamps.

We consider the diffusion of ink molecules into and within a PDMS stamp by numerically solving Fick's second law:

$$\frac{\partial C}{\partial t} = D\frac{\partial^2 C}{\partial x^2} \qquad \textbf{Eq. 4.1}$$

using an iterative finite difference method. In the above equation, and in what follows, *C* represents the ink concentration, *t* is time, *x* is depth, *D* is the diffusion coefficient, and *L* is the thickness of the stamp. The stamp (as illustrated schematically in Figure 4.6D) is modeled as a semi-infinite medium that fills the space:

$$\text{stamp region} \begin{cases} 0 \leq x < L \\ -\infty < y < +\infty \\ -\infty < z < +\infty \end{cases}$$

Henceforth, we will neglect the *y*- and *z*-dimensions because of the effectively infinite nature and symmetry of the stamp and only consider the diffusion in one dimension (*x*).

During inking, the exterior of the stamp ($x < 0$) is assumed to be an inexhaustible ink reservoir, of known concentration (C_0), that diffuses into the stamp. After a set amount of time, T_{ink}, the concentration of molecules within the stamp, as a function of position, is approximately:

$$C(x, T_{ink}) = C_0 \operatorname{erfc}\left(\frac{x}{2\sqrt{DT_{ink}}}\right)$$

in the limit where $L \gg 2(DT_{ink})^{1/2}$, where erfc() represents the complementary error function.[66]

After inking, the reservoir is removed and the faces of the stamp ($x = 0$, $x = L$) become impenetrable barriers through which no molecules may enter or leave. In the time that follows, the ink continues to diffuse throughout the stamp, causing the concentration profile to change in time. Figure 4.6A depicts five concentration profiles of alkanethiols in PDMS after inking for the specified time. The time evolution of the concentration profile for a stamp inked for 10 min is illustrated in Figure 4.6B.

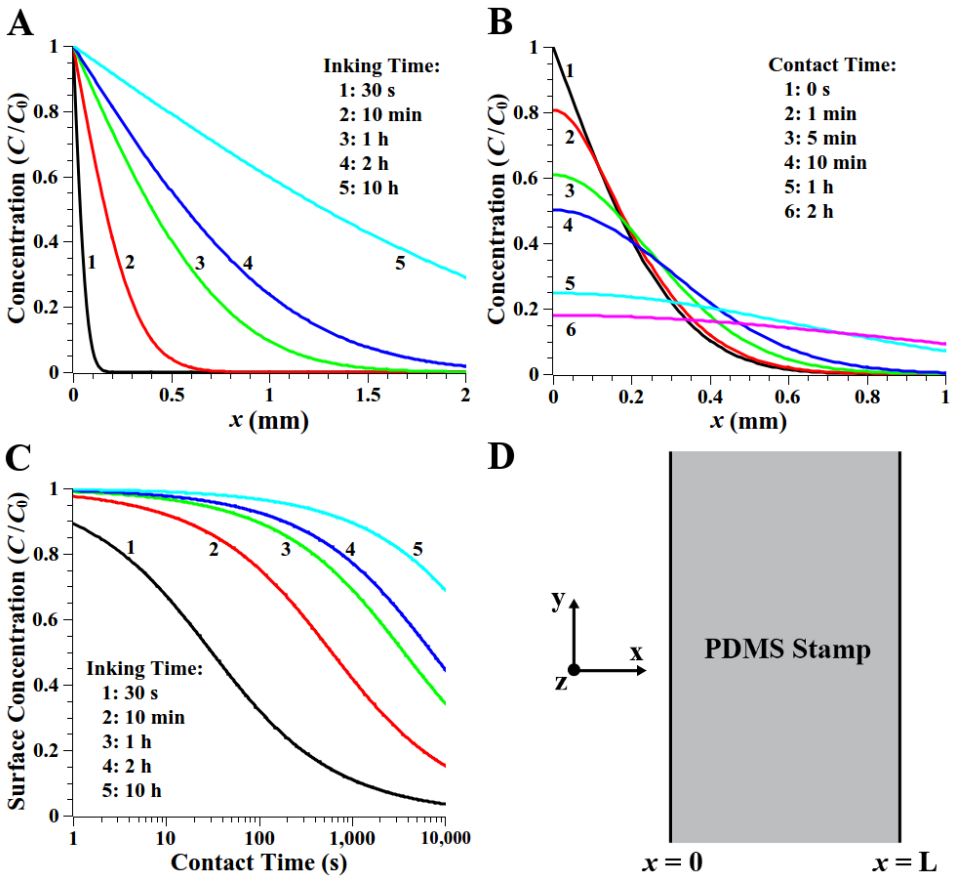

Figure 4.6: Model of linear one-dimensional diffusion of *n*-alkanethiol into a semi-infinite PDMS stamp. Plots depict concentration profiles of ink molecules within stamp as a function of position (depth beneath stamp surface) and time. (A) The ink reservoir maintains the stamp interface at a concentration of C_0 for all time $0 \leq t \leq T_{ink}$. The average diffusion length increases with the square root of inking time. (B) Concentration profile evolution (10 min inking time) after placing stamp in contact with an impermeable substrate. The interface concentration is no longer maintained at C_0, and the molecular ink diffuses further into the stamp. (C) Plot of ink concentration at the stamp/substrate interface as a function of contact time. Depletion by self-assembled monolayer deposition is neglected. Lower interface ink concentration corresponds to a lower effective flux, which in turn slows concentration dependent processes. Saturation-inking generates a concentration profile that varies less with position near the surface, and shows smaller changes in

surface concentration in time, than wet-inking provides. (D) Schematic of the PDMS stamp used in the numerical model.

A full-coverage *n*-alkanethiolate SAM on Au{111} is composed of approximately 4.6×10^{14} molecules per cm^2. Assuming a homogeneous, 25 mM ink distribution in a stamp, a full coverage monolayer may be formed from the molecules found within the first 0.31 μm beneath the stamp surface. For comparison, the *n*-alkanethiol diffusion length in PDMS is 14 μm after 1 s, and the short-term depletion by SAM deposition recovers in ~1 ms (*vide infra*). Therefore, ink depletion from deposition of a single SAM is negligible compared to that caused by diffusion over longer experimental time scales. However, if a stamp is to be used for multiple prints without reinking, ink depletion by SAM deposition becomes a more important variable with each print. Ink diffusion across the surface, away from the stamp-substrate contact region, occurs at a much slower rate ($D_{Surface} \approx 1 \times 10^{-11}$ cm^2 s^{-1})[67] than diffusion into the bulk of the stamp and is thus neglected in this model.

Dynamic, concentration-dependent processes (e.g., molecular exchange between deposited molecules and molecules in PDMS) rely only on the concentration at the stamp/substrate interface, so we focus our attention on the depletion of ink at this interface and its relationship to inking time. Interface concentrations as a function of contact time are shown in Figure 4.6C for stamps inked for a range of periods. The further the ink penetrates into the stamp, the slower the rate of change at the interface during stamping; longer inking times maintain the initial interface concentration over longer experimental time scales. We reiterate that there remains sufficient ink near the interface to deposit a full-coverage SAM after an hour of diffusion, even for stamps inked for only a few seconds. Ethanol is known to cause PDMS to swell, linearly, by about 4% when fully

saturated.[68] This swelling may subtly affect the final printed pattern; however, ethanol's swelling factor is relatively low compared to many other, less polar, solvents.

To summarize, ink concentration at the stamp/substrate interface depletes primarily by diffusion into the stamp interior. This becomes more significant as experimental time scales increase. For experiments involving stamping times over 1 h, ink concentration is best controlled by using a stamp of uniform concentration, although wet-inking methods can provide consistent results, provided long inking times. As a general rule, we immerse the stamp in an ink solution within a sealed vial for at least an order of magnitude longer than the planned contact time.

4.4 Conclusions and Prospects

Controlling transport phenomena is increasingly important for soft lithography. We have shown that by controlling the flux of ink at a stamp/sample interface, μCP and μDP can be used to produce films with control over composition, order, and reproducibility. We used a numerical model of one-dimensional ink diffusion into PDMS to illustrate the effect of ink depletion by diffusion into the stamp bulk as an important variable for long-duration patterning experiments. By saturation-inking, we can limit this variability and can prepare highly uniform SAMs with marked reproducibility and controllable crystallinity. These results are not limited to saturation-inking methodologies; any method of inking the stamp that can produce a near-uniform concentration profile over the experimental time scale can be used effectively. We have shown the precision with which μDP printing can be used for the control of monolayer composition, enabling finely tuned chemical and physical surface properties across the macro-, micro-, and nanolength scales.

4.5 References and Notes

(1) Tien, J.; Terfort, A.; Whitesides, G. M. Microfabrication through Electrostatic Self-Assembly. *Langmuir* **1997**, *13*, 5349–5355.

(2) Bernard, A.; Renault, J. P.; Michel, B.; Bosshard, H. R.; Delamarche, E. Microcontact Printing of Proteins. *Adv. Mater.* **2000**, *12*, 1067–1070.

(3) Fujihira, M.; Furugori, M.; Akiba, U.; Tani, Y. Study of Microcontact Printed Patterns by Chemical Force Microscopy. *Ultramicroscopy* **2001**, *86*, 75–83.

(4) Rogers, J. A.; Bao, Z.; Baldwin, K.; Dodabalapur, A.; Crone, B.; Raju, V. R.; Kuck, V.; Katz, H.; Amundson, K.; Ewing, J.; Drzaic, P. Paper-Like Electronic Displays: Large-Area Rubber-Stamped Plastic Sheets of Electronics and Microencapsulated Electrophoretic Inks. *Proc. Natl. Acad. Sci. U.S.A.* **2001**, *98*, 4835–4840.

(5) Jenkins, A. T. A.; Bushby, R. J.; Evans, S. D.; Knoll, W.; Offenhausser, A.; Ogier, S. D. Lipid Vesicle Fusion on μCP Patterned Self-Assembled Monolayers: Effect of Pattern Geometry on Bilayer Formation. *Langmuir* **2002**, *18*, 3176–3180.

(6) Porter, L. A.; Choi, H. C.; Schmeltzer, J. M.; Ribbe, A. E.; Elliott, L. C. C.; Buriak, J. M. Electroless Nanoparticle Film Deposition Compatible with Photolithography, Microcontact Printing, and Dip-Pen Nanolithography Patterning Technologies. *Nano Lett.* **2002**, *2*, 1369–1372.

(7) Santhanam, V.; Andres, R. P. Microcontact Printing of Uniform Nanoparticle Arrays. *Nano Lett.* **2003**, *4*, 41–44.

(8) Geissler, M.; Wolf, H.; Stutz, R.; Delamarche, E.; Grummt, U. W.; Michel, B.; Bietsch, A. Fabrication of Metal Nanowires Using Microcontact Printing. *Langmuir* **2003**, *19*, 6301–6311.

(9) Leufgen, M.; Lebib, A.; Muck, T.; Bass, U.; Wagner, V.; Borzenko, T.; Schmidt, G.; Geurts, J.; Molenkamp, L. W. Organic Thin-Film Transistors Fabricated by Microcontact Printing. *Appl. Phys. Lett.* **2004**, *84*, 1582–1584.

(10) Lange, S. A.; Benes, V.; Kern, D. P.; Horber, J. K. H.; Bernard, A. Microcontact Printing of DNA Molecules. *Anal. Chem.* **2004**, *76*, 1641–1647.

(11) Kraus, T.; Stutz, R.; Balmer, T. E.; Schmid, H.; Malaquin, L.; Spencer, N. D.; Wolf, H. Printing Chemical Gradients. *Langmuir* **2005**, *21*, 7796–7804.

(12) Azzaroni, O.; Moya, S. E.; Brown, A. A.; Zheng, Z.; Donath, E.; Huck, W. T. S. Polyelectrolyte Brushes as Ink Nanoreservoirs for Microcontact Printing of Ionic Species with Poly(dimethyl siloxane) Stamps. *Adv. Funct. Mater.* **2006**, *16*, 1037–1042.

(13) Sharpe, R. B. A.; Titulaer, B. J. F.; Peeters, E.; Burdinski, D.; Huskens, J.; Zandvliet, H. J. W.; Reinhoudt, D. N.; Poelsema, B. Edge Transfer Lithography Using Alkanethiol Inks. *Nano Lett.* **2006**, *6*, 1235–1239.

(14) Burdinski, D.; Blees, M. H. Thiosulfate- and Thiosulfonate-Based Etchants for the Patterning of Gold Using Microcontact Printing. *Chem. Mater.* **2007**, *19*, 3933–3944.

(15) Syms, R. R. A.; Zou, H.; Choonee, K.; Lawes, R. A. Silicon Microcontact Printing Engines. *J. Micromech. Microeng.* **2009**, *19*, 025027.

(16) Wilbur, J. L.; Kumar, A.; Kim, E.; Whitesides, G. M. Microfabrication by Microcontact Printing of Self-Assembled Monolayers. *Adv. Mater.* **1994**, *6*, 600–604.

(17) Biebuyck, H. A.; Whitesides, G. M. Autophobic Pinning of Drops of Alkanethiols on Gold. *Langmuir* **1994**, *10*, 4581–4587.

(18) Xia, Y. N.; Whitesides, G. M. Use of Controlled Reactive Spreading of Liquid Alkanethiol on the Surface of Gold to Modify the Size of Features Produced by Microcontact Printing. *J. Am. Chem. Soc.* **1995**, *117*, 3274–3275.

(19) Xia, Y. N.; Mrksich, M.; Kim, E.; Whitesides, G. M. Microcontact Printing of Octadecylsiloxane on the Surface of Silicon Dioxide and Its Application in Microfabrication. *J. Am. Chem. Soc.* **1995**, *117*, 9576–9577.

(20) Jeon, N. L.; Clem, P. G.; Nuzzo, R. G.; Payne, D. A. Patterning of Dielectric Oxide Thin-Layers by Microcontact Printing of Self-Assembled Monolayers. *J. Mater. Res.* **1995**, *10*, 2996–2999.

(21) Mrksich, M.; Whitesides, G. M. Patterning Self-Assembled Monolayers Using Microcontact Pringing - A New Technology for Biosensors. *Trends Biotechnol.* **1995**, *13*, 228–235.

(22) Jackman, R. J.; Wilbur, J. L.; Whitesides, G. M. Fabrication of Submicrometer Features on Curved Substrates by Microcontact Printing. *Science* **1995**, *269*, 664–666.

(23) Mrksich, M.; Chen, C. S.; Xia, Y. N.; Dike, L. E.; Ingber, D. E.; Whitesides, G. M. Controlling Cell Attachment on Contoured Surfaces with Self-Assembled Monolayers of Alkanethiolates on Gold. *Proc. Natl. Acad. Sci. U.S.A.* **1996**, *93*, 10775–10778.

(24) Smith, R. K.; Lewis, P. A.; Weiss, P. S. Patterning Self-Assembled Monolayers. *Prog. Surf. Sci.* **2004**, *75*, 1–68.

(25) Perl, A.; Reinhoudt, D. N.; Huskens, J. Microcontact Printing: Limitations and Achievements. *Adv. Mater.* **2009**, *21*, 2257–2268.

(26) Libioulle, L.; Bietsch, A.; Schmid, H.; Michel, B.; Delamarche, E. Contact-Inking Stamps for Microcontact Printing of Alkanethiols on Gold. *Langmuir* **1999**, *15*, 300–304.

(27) Lahiri, J.; Ostuni, E.; Whitesides, G. M. Patterning Ligands on Reactive SAMs by Microcontact Printing. *Langmuir* **1999**, *15*, 2055–2060.

(28) Donzel, C.; Geissler, M.; Bernard, A.; Wolf, H.; Michel, B.; Hilborn, J.; Delamarche, E. Hydrophilic Poly(dimethylsiloxane) Stamps for Microcontact Printing. *Adv. Mater.* **2001**, *13*, 1164–1167.

(29) Kaufmann, T.; Ravoo, B. J. Stamps, Inks and Substrates: Polymers in Microcontact Printing. *Polym. Chem.* **2010**, *1*, 371–387.

(30) Vaish, A.; Shuster, M. J.; Cheunkar, S.; Weiss, P. S.; Andrews, A. M. Tuning Stamp Surface Energy for Soft Lithography of Polar Molecules to Fabricate Bioactive Small-Molecule Microarrays. *Small* **2011**, *7*, 1471–1479.

(31) Li, X.-M.; Péter, M.; Huskens, J.; Reinhoudt, D. N. Catalytic Microcontact Printing Without Ink. *Nano Lett.* **2003**, *3*, 1449–1453.

(32) Scheres, L.; ter Maat, J.; Giesbers, M.; Zuilhof, H. Microcontact Printing onto Oxide-Free Silicon via Highly Reactive Acid Fluoride-Functionalized Monolayers. *Small* **2010**, *6*, 642–650.

(33) Wendeln, C.; Rinnen, S.; Schulz, C.; Arlinghaus, H. F.; Ravoo, B. J. Photochemical Microcontact Printing by Thiol-Ene and Thiol-Yne Click Chemistry. *Langmuir* **2010**, *26*, 15966–15971.

(34) Shestopalov, A. A.; Morris, C. J.; Vogen, B. N.; Hoertz, A.; Clark, R. L.; Toone, E. J. Soft-Lithographic Approach to Functionalization and Nanopatterning Oxide-Free Silicon. *Langmuir* **2011**, *27*, 6478–6485.

(35) Morris, C. J.; Shestopalov, A. A.; Gold, B. H.; Clark, R. L.; Toone, E. J. Patterning NHS-Terminated SAMs on Germanium. *Langmuir* **2011**, *27*, 6486–6489.

(36) Larsen, N. B.; Biebuyck, H.; Delamarche, E.; Michel, B. Order in Microcontact Printed Self-Assembled Monolayers. *J. Am. Chem. Soc.* **1997**, *119*, 3017–3026.

(37) Helmuth, J. A.; Schmid, H.; Stutz, R.; Stemmer, A.; Wolf, H. High-Speed Microcontact Printing. *J. Am. Chem. Soc.* **2006**, *128*, 9296–9297.

(38) Dameron, A. A.; Hampton, J. R.; Smith, R. K.; Mullen, T. J.; Gillmor, S. D.; Weiss, P. S. Microdisplacement Printing. *Nano Lett.* **2005**, *5*, 1834–1837.

(39) Mullen, T. J.; Srinivasan, C.; Hohman, J. N.; Gillmor, S. D.; Shuster, M. J.; Horn, M. W.; Andrews, A. M.; Weiss, P. S. Microcontact Insertion Printing. *Appl. Phys. Lett.* **2007**, *90*, 063114.

(40) Saavedra, H. M.; Thompson, C. M.; Hohman, J. N.; Crespi, V. H.; Weiss, P. S. Reversible Lability by in Situ Reaction of Self-Assembled Monolayers. *J. Am. Chem. Soc.* **2009**, *131*, 2252–2259.

(41) Liao, W.-S.; Cheunkar, S.; Cao, H. H.; Bednar, H. R.; Weiss, P. S.; Andrews, A. M. Subtractive Patterning via Chemical Lift-Off Lithography. *Science* **2012**, *337*, 1517–1521.

(42) Saavedra, H. M.; Barbu, C. M.; Dameron, A. A.; Mullen, T. J.; Crespi, V. H.; Weiss, P. S. 1-Adamantanethiolate Monolayer Displacement Kinetics Follow a Universal Form. *J. Am. Chem. Soc.* **2007**, *129*, 10741–10746.

(43) Dameron, A. A.; Charles, L. F.; Weiss, P. S. Structures and Displacement of 1-Adamantanethiol Self-Assembled Monolayers on Au{111}. *J. Am. Chem. Soc.* **2005**, *127*, 8697–8704.

(44) Dameron, A. A.; Hampton, J. R.; Gillmor, S. D.; Hohman, J. N.; Weiss, P. S. Enhanced Molecular Patterning via Microdisplacement Printing. *J. Vac. Sci. Technol., B* **2005**, *23*, 2929–2932.

(45) Mullen, T. J.; Dameron, A. A.; Saavedra, H. M.; Williams, M. E.; Weiss, P. S. Dynamics of Solution Displacement in 1-Adamantanethiolate Self-Assembled Monolayers. *J. Phys. Chem. C* **2007**, *111*, 6740–6746.

(46) Dameron, A. A.; Mullen, T. J.; Hengstebeck, R. W.; Saavedra, H. M.; Weiss, P. S. Origins of Displacement in 1-Adamantanethiolate Self-Assembled Monolayers. *J. Phys. Chem. C* **2007**, *111*, 6747–6752.

(47) Srinivasan, C.; Mullen, T. J.; Hohman, J. N.; Anderson, M. E.; Dameron, A. A.; Andrews, A. M.; Dickey, E. C.; Horn, M. W.; Weiss, P. S. Scanning Electron Microscopy of Nanoscale Chemical Patterns. *ACS Nano* **2007**, *1*, 191–201.

(48) Hohman, J. N.; Claridge, S. A.; Kim, M.; Weiss, P. S. Cage Molecules for Self-Assembly. *Mater. Sci. Eng., R* **2010**, *70*, 188–208.

(49) Ulman, A. Formation and Structure of Self-Assembled Monolayers. *Chem. Rev.* **1996**, *96*, 1533–1554.

(50) Love, J. C.; Estroff, L. A.; Kriebel, J. K.; Nuzzo, R. G.; Whitesides, G. M. Self-Assembled Monolayers of Thiolates on Metals as a Form of Nanotechnology. *Chem. Rev.* **2005**, *105*, 1103–1170.

(51) Bumm, L. A.; Arnold, J. J.; Charles, L. F.; Dunbar, T. D.; Allara, D. L.; Weiss, P. S. Directed Self-Assembly to Create Molecular Terraces with Molecularly Sharp Boundaries in Organic Monolayers. *J. Am. Chem. Soc.* **1999**, *121*, 8017–8021.

(52) Nuzzo, R. G.; Dubois, L. H.; Allara, D. L. Fundamental-Studies of Microscopic Wetting on Organic-Surfaces. 1. Formation and Structural Characterization of a Self-Consistent Series of Polyfunctional Organic Monolayers. *J. Am. Chem. Soc.* **1990**, *112*, 558–569.

(53) Born, M.; Wolf, E. *Principles of Optics*; 2nd ed.; Cambridge University Press: Cambridge, 1999.

(54) Pan, S.; Belu, A. M.; Ratner, B. D. Self Assembly of 16-Mercapto-1-Hexadecanol on Gold: Surface Characterization and Kinetics. *Mater. Sci. Eng. C* **1999**, *7*, 51–58.

(55) Mack, N. H.; Dong, R.; Nuzzo, R. G. Quantitative Imaging of Protein Adsorption on Patterned Organic Thin-Film Arrays Using Secondary Electron Emission. *J. Am. Chem. Soc.* **2006**, *128*, 7871–7881.

(56) Jensen, J. O. Vibrational Frequencies and Structural Determination of Adamantane. *Spectrochim. Acta, Part A* **2004**, *60*, 1895–1905.

(57) Kim, M.; Hohman, J. N.; Morin, E. I.; Daniel, T. A.; Weiss, P. S. Self-Assembled Monolayers of 2-Adamantanethiol on Au{111}: Control of Structure and Displacement. *J. Phys. Chem. A* **2009**, *113*, 3895–3903.

(58) Hohman, J. N.; Zhang, P.; Morin, E. I.; Han, P.; Kim, M.; Kurland, A. R.; McClanahan, P. D.; Balema, V. P.; Weiss, P. S. Self-Assembly of Carboranethiol Isomers on Au{111}: Intermolecular Interactions Determined by Molecular Dipole Orientations. *ACS Nano* **2009**, *3*, 527–536.

(59) Eberhardt, A. S.; Nyquist, R. M.; Parikh, A. N.; Zawodzinski, T.; Swanson, B. I. Defects in Microcontact-Printed and Solution-Grown Self-Assembled Monolayers. *Langmuir* **1999**, *15*, 1595–1598.

(60) Gannon, G.; Larsson, J. A.; Greer, J. C.; Thompson, D. Quantification of Ink Diffusion in Microcontact Printing with Self-Assembled Monolayers. *Langmuir* **2008**, *25*, 242–247.

(61) Bergmair, I.; Mühlberger, M.; Lausecker, E.; Hingerl, K.; Schöftner, R. Diffusion of Thiols During Microcontact Printing with Rigid Stamps. *Microelectron. Eng.* **2010**, *87*, 848–850.

(62) Delamarche, E. Microcontact Processing for Microtechnology and Biology. *Chimia* **2007**, *61*, 126–132.

(63) Casero, E.; Petit-Dominguez, M. D.; Parra-Alfambra, A. M.; Gismera, M. J.; Pariente, F.; Lorenzo, E.; Vazquez, L. One-Step Covalent Microcontact Printing Approach to Produce Patterns of Lactate Oxidase. *Phys. Chem. Chem. Phys.* **2010**, *12*, 2830–2837.

(64) Delamarche, E.; Schmid, H.; Bietsch, A.; Larsen, N. B.; Rothuizen, H.; Michel, B.; Biebuyck, H. Transport Mechanisms of Alkanethiols During Microcontact Printing on Gold. *J. Phys. Chem. B* **1998**, *102*, 3324–3334.

(65) Balmer, T. E.; Schmid, H.; Stutz, R.; Delamarche, E.; Michel, B.; Spencer, N. D.; Wolf, H. Diffusion of Alkanethiols in PDMS and Its Implications on Microcontact Printing (μCP). *Langmuir* **2005**, *21*, 622–632.

(66) We assume the diffusion length during inking is much less than the stamp's thickness. The physical interpretation of this condition is that, in the time allotted, a negligible amount of ink has diffused far enough into the bulk of the stamp such that it interacts with the far boundary. As such, we solve Eq. 4.1 for a stamp of infinite thickness.

(67) Sheehan, P. E.; Whitman, L. J. Thiol Diffusion and the Role of Humidity in "Dip Pen Nanolithography." *Phys. Rev. Lett.* **2002**, *88*.

(68) Lee, J. N.; Park, C.; Whitesides, G. M. Solvent Compatibility of Poly(dimethylsiloxane)-Based Microfluidic Devices. *Anal. Chem.* **2003**, *75*, 6544–6554.

CHAPTER 5

Conclusions & Prospects

5.1 Summary

In the preceding four chapters, we described a series of measurements designed to probe nanoscale assemblies with single-molecule sensitivities and the capabilities to resolve atomic-scale features on surfaces. We elucidated the interactions between SAMs and their environments using liquid crystals to probe the effects of the dipolar fields produced by carboranethiol isomers assembled on a surface. As such, we determined the role of the dipole moment strength and orientation on the subsequent assembly of molecules on textured, anisotropic surfaces. The orientations and anchoring strengths of adsorbed mesogens were found to depend on the polarity of the dipoles normal to the surface and the areal densities of the adsorbed species. Additionally, we presented an experimental roadmap for the detection of nuclear spins on a surface via scanning tunneling microscopy and described the progress made towards this goal. Instrument construction and modifications, optimized sample preparation, overall experimental design choices, and preliminary results toward NMR- and MRI-style single-molecule STM measurements were discussed in detail. We also described the optimization of μCP and μDP surface patterning techniques via inking and stamping times, which were used to pattern surfaces with micro- and nanoscale features. In this case, the quality of the transferred pattern depends on the diffusion of ink within the stamp, which we modeled numerically. Optimized patterning of SAMs aids in the

use of this technique in numerous other studies that require high-fidelity, nanoscale features on a surface (e.g., sample preparation for the NMR-STM experiments). This chapter summarizes the conclusions presented in this dissertation, as well as briefly discuss prospects for future experiments and extensions of this work.

5.2 Liquid Crystals as Nanoscale Probes

In Chapter 2, we described a series of experiments using LCs to probe the nanoscale intermolecular interactions between a SAM and its environment (subsequent mesogen adsorbates). Beyond the immediate scope of these experiments, this technique represents a powerful and relatively non-invasive means to probe interactions at surfaces. Liquid crystals are incredibly sensitive to the precise surface treatments used to prepare a substrate. As probes, LCs can reveal, by way of their optical anisotropy, subtle differences in the properties of surfaces that affect LC alignment that are difficult to distinguish or quantify using scanning probes or electron microscopies. This capability is exemplified by the sensitivity of LC alignment to differences in the molecular geometry, symmetry, and tilt of the exposed moieties in a SAM,[1–6] to which techniques such as STM, AFM, and scanning electron microscopy are largely insensitive. However, this sensitivity comes at the cost of spatial resolution; LC orientation is influenced by long-range molecular order and interactions that extend over hundreds of nanometers. Additionally, determination of their orientations by optical microscopies is diffraction limited. Although scanning probes measurements readily achieve sub-nanometer resolutions, they are typically limited in their lateral measurement ranges to <100 μm. Optical microscopy, by contrast, is much more easily extended to lateral ranges of several millimeters, or larger. In some circumstances, liquid crystals can also be a means of measuring surface properties with relatively little perturbation of the underlying adsorbed molecules compared to scanning probe techniques.

We estimate the interaction strengths of LCs with functionalized gold surfaces using the anchoring energies measured in Chapter 2 (on the order of 10 μJ m^{-2}). Assuming a lattice constant of ~5 Å, consistent with close-packed arrangements of alkanethiols on Au{111},[7] we calculate an interaction of ~10^{-5} eV per molecule within the SAM. We note that on a *per molecule* basis, this interaction energy is much weaker than the energies associated with molecule bond vibrations (~10^{-1} eV) and the dispersive intermolecular interactions between neighboring molecules (between ~10^{-1} and ~10^{0} eV).[7] The scanning probe tips from an AFM can apply controlled, variable forces to the surface ranging from ~10 pN are larger.[8] The actual force, and interaction energy, acting on a single molecule depends in large part on the specific properties of the probe tip, substrate, and adsorbate. However, if the entirety of a 10 pN force is applied to a single molecule beneath the probe causes it to deform by 0.1 Å (about 10% of the length of a typical chemical bond), then this amounts to an interaction (mechanical work) of ~10^{-3} eV. Estimating the interaction of the probe tip of a STM with the surface is more difficult since tip–sample interactions are neither intended nor desired during conventional topographic measurements. Nevertheless, the STM probe tip is typically in much closer proximity to the molecular adsorbates under investigation than that of an AFM and, therefore, more strongly interacting. Additionally, molecules in a STM tunneling junction experience a strong electric field (~10^{9} V m^{-1}) that can perturb the sample. As such, by this simplified reasoning, liquid crystals represent an extremely weakly interacting probe of surface properties. For these reasons, LCs can complement other nanoscale measurements of adsorbed species and aid the quantification of the interactions between functionalized surfaces and their environments.

Another situation in which LCs may reveal nanoscale information that is not available through scanning probe techniques involves the molecular-scale mixing of adsorbed species on a

surface. Mixed monolayers composed of dissimilar species are known to form separate phases on surfaces, driven by intermolecular interactions between the adsorbed species. For example, mixed monolayers composed of alkanethiol and 1ATC9 (and multi-amide analogs) adsorbates phase separate on the surface due to the formation of a hydrogen-bonding network between neighboring amide groups within the monolayer.[9,10] By comparison to the phase-separated monolayer, a homogeneously mixed SAM of these two molecules is less favorable due to the disruption of the hydrogen-bonding network by the species (alkanethiol adsorbates) that are not prone to hydrogen bonding with their neighbors. These two molecules, and their respective phases, may be distinguished on a surface, topographically, due to differences in molecular height for an appropriate choice of alkyl backbone length (e.g., comparing C8 with 1ATC9). In other cases, however, when the monolayer is composed of molecules with similar characteristics (e.g., length or conductivity), the species cannot be resolved easily using a STM or an AFM. As such, the degree of mixing between adsorbate species cannot be probed directly through typical scanning probe techniques. Understanding the degree of mixing between multiple species on surfaces will enable greater control in the engineering of complex nanoscale assemblies composed of molecules with differing geometries and functionalities. We can extend the work presented in Chapter 2 using the alignment of LCs on SAMs in order to elucidate the degree of mixing between different carboranethiol isomers. Using scanning probe techniques, these monolayers composed of either a single or multiple carboranethiol species appear identical.[11] However, due to differences in their molecular dipole strengths and orientations with respect to the underlying surface, differences in monolayer stability[11] and molecular azimuthal orientation have been measured.[12] We have demonstrated that the alignment of LCs on carboranethiol-treated surfaces are sensitive to the polarity of dipole moment normal to the surface. As such, mixed monolayers composed of

carboranethiol isomers with normal dipoles of opposite polarity should induce alignment of LCs along either of its constituent molecules' easy alignment axes, or an intermediate direction, depending on the degree of molecular mixing. Abbott and coworkers have shown that mixed monolayers of chiral molecules induce either continuous or abrupt transitions in the LC easy alignment axis depending on the molecular-scale homogeneity of the monolayer.[6] We propose to use the easy alignment axes of LCs on surfaces functionalized with mixtures of carboranethiols to infer the existence, or lack thereof, phase-separated regions of the different species. This result will elucidate the degree to which intermolecular dipole-dipole interactions determine the assembly and orientation of surface adsorbates that lack molecular tilt defects and which possess higher rotational symmetry compared to (chain-like) alkanethiol monolayers.

5.3 Surface-Dipole-Induced Ferroelectric Crystal Polarization

Self-assembled monolayers are known to influence and to direct the nucleation and growth of both organic and inorganic crystals on surfaces.[13–16] As in the case of functionalized gold surfaces directing the alignment of mesogens, crystal growth is sensitive to the exposed molecular moieties within the SAM. Carboranethiol SAMs, with their variable dipole strengths and orientations offer another parameter with which to tune this growth. Ferroelectric crystals represent one system that may be especially sensitive to the influences of molecular dipole moments.[17–19] Close-packed assemblies of carboranethiol molecules on surfaces present a uniformly polarized interface on which crystals may nucleate. Dipolar field polarity may influence the preferred crystal facets, polarization, or switching characteristics of ferroelectric materials grown on these surfaces.[17–22] Tuning these properties via functionalization of the underlying substrate would have applications in data storage, sensing, and micromechanical systems, where ferroelectric (and multiferroic) materials are used.[23,24]

5.4 References

(1) Gupta, V. K.; Abbott, N. L. Azimuthal Anchoring Transition of Nematic Liquid Crystals on Self-Assembled Monolayers Formed from Odd and Even Alkanethiols. *Phys. Rev. E* **1996**, *54*, R4540–R4543.

(2) Gupta, V. K.; Abbott, N. L. Design of Surfaces for Patterned Alignment of Liquid Crystals on Planar and Curved Substrates. *Science* **1997**, *276*, 1533–1536.

(3) Tao, F.; Bernasek, S. L. Understanding Odd−Even Effects in Organic Self-Assembled Monolayers. *Chem. Rev.* **2007**, *107*, 1408–1453.

(4) Nakata, M.; Zanchetta, G.; Buscaglia, M.; Bellini, T.; Clark, N. A. Liquid Crystal Alignment on a Chiral Surface: Interfacial Interaction with Sheared DNA Films. *Langmuir* **2008**, *24*, 10390–10394.

(5) Bai, Y.; Abbott, N. L. Enantiomeric Interactions between Liquid Crystals and Organized Monolayers of Tyrosine-Containing Dipeptides. *J. Am. Chem. Soc.* **2012**, *134*, 548–558.

(6) Bai, Y.; Abbasi, R.; Wang, C.; Abbott, N. L. Liquid Crystals Anchored on Mixed Monolayers of Chiral versus Achiral Molecules: Continuous Change in Orientation as a Function of Enantiomeric Excess. *Angew. Chem. Int. Ed.* **2014**, *53*, 8079–8083.

(7) Love, J. C.; Estroff, L. A.; Kriebel, J. K.; Nuzzo, R. G.; Whitesides, G. M. Self-Assembled Monolayers of Thiolates on Metals as a Form of Nanotechnology. *Chem. Rev.* **2005**, *105*, 1103–1170.

(8) Lussis, P.; Svaldo-Lanero, T.; Bertocco, A.; Fustin, C.-A.; Leigh, D. A.; Duwez, A.-S. A Single Synthetic Small Molecule That Generates Force against a Load. *Nat. Nanotechnol.* **2011**, *6*, 553–557.

(9) Lewis, P. A.; Smith, R. K.; Kelly, K. F.; Bumm, L. A.; Reed, S. M.; Clegg, R. S.; Gunderson, J. D.; Hutchison, J. E.; Weiss, P. S. The Role of Buried Hydrogen Bonds in Self-Assembled Mixed Composition Thiols on Au{111}. *J. Phys. Chem. B* **2001**, *105*, 10630–10636.

(10) Smith, R. K.; Reed, S. M.; Lewis, P. A.; Monnell, J. D.; Clegg, R. S.; Kelly, K. F.; Bumm, L. A.; Hutchison, J. E.; Weiss, P. S. Phase Separation within a Binary Self-Assembled Monolayer on Au{111} Driven by an Amide-Containing Alkanethiol. *J. Phys. Chem. B* **2001**, *105*, 1119–1122.

(11) Hohman, J. N.; Zhang, P.; Morin, E. I.; Han, P.; Kim, M.; Kurland, A. R.; McClanahan, P. D.; Balema, V. P.; Weiss, P. S. Self-Assembly of Carboranethiol Isomers on Au{111}: Intermolecular Interactions Determined by Molecular Dipole Orientations. *ACS Nano* **2009**, *3*, 527–536.

(12) Thomas, J. C.; Schwartz, J. J.; Hohman, J. N.; Claridge, S. A.; Auluck, H. S.; Serino, A. C.; Spokoyny, A. M.; Tran, G.; Kelly, K. F.; Mirkin, C. A.; Gilles, J.; Osher, S. J.; Weiss, P. S. Defect-Tolerant Aligned Dipoles within Two-Dimensional Plastic Lattices. *ACS Nano* **2015**, *9*, 4734–4742.

(13) Aizenberg, J.; Black, A. J.; Whitesides, G. M. Oriented Growth of Calcite Controlled by Self-Assembled Monolayers of Functionalized Alkanethiols Supported on Gold and Silver. *J. Am. Chem. Soc.* **1999**, *121*, 4500–4509.

(14) Briseno, A. L.; Aizenberg, J.; Han, Y.-J.; Penkala, R. A.; Moon, H.; Lovinger, A. J.; Kloc, C.; Bao, Z. Patterned Growth of Large Oriented Organic Semiconductor Single Crystals on Self-Assembled Monolayer Templates. *J. Am. Chem. Soc.* **2005**, *127*, 12164–12165.

(15) Hiremath, R.; Basile, J. A.; Varney, S. W.; Swift, J. A. Controlling Molecular Crystal Polymorphism with Self-Assembled Monolayer Templates. *J. Am. Chem. Soc.* **2005**, *127*, 18321–18327.

(16) Hiremath, R.; Swift, J. A. Directed Nucleation of Molecular Crystals on Self-Assembled Monolayer Surfaces. *Mol. Cryst. Liq. Cryst.* **2006**, *456*, 95–106.

(17) Park, Y. J.; Kang, S. J.; Park, C.; Lotz, B.; Thierry, A.; Kim, K. J.; Huh, J. Molecular and Crystalline Microstructure of Ferroelectric Poly(vinylidene Fluoride-Co-Trifluoroethylene) Ultrathin Films on Bare and Self-Assembled Monolayer-Modified Au Substrates. *Macromolecules* **2008**, *41*, 109–119.

(18) Hahm, S.-W.; Khang, D.-Y. Crystallization and Microstructure-Dependent Elastic Moduli of Ferroelectric P(VDF–TrFE) Thin Films. *Soft Matter* **2010**, *6*, 5802–5806.

(19) Tsutsumi, N.; Kitano, T.; Kinashi, K.; Sakai, W. Ferroelectric Switching of Vinylidene and Trifluoroethylene Copolymer Thin Films on Au Electrodes Modified with Self-Assembled Monolayers. *Materials* **2014**, *7*, 6367–6376.

(20) Lukyanchuk, I.; Sharma, P.; Nakajima, T.; Okamura, S.; Scott, J. F.; Gruverman, A. High-Symmetry Polarization Domains in Low-Symmetry Ferroelectrics. *Nano Lett.* **2014**, *14*, 6931–6935.

(21) Sharma, P.; Reece, T.; Wu, D.; Fridkin, V. M.; Ducharme, S.; Gruverman, A. Nanoscale Domain Patterns in Ultrathin Polymer Ferroelectric Films. *J. Phys.: Condens. Matter* **2009**, *21*, 485902.

(22) Cai, L.; Qu, H.; Lu, C.; Ducharme, S.; Dowben, P. A.; Zhang, J. Surface Structure of Ultrathin Copolymer Films of Ferroelectric Vinylidene Fluoride (70%) with Trifluoroethylene (30%) on Graphite. *Phys. Rev. B* **2004**, *70*, 155411.

(23) Catalan, G.; Scott, J. F. Physics and Applications of Bismuth Ferrite. *Adv. Mater.* **2009**, *21*, 2463–2485.

(24) Setter, N.; Damjanovic, D.; Eng, L.; Fox, G.; Gevorgian, S.; Hong, S.; Kingon, A.; Kohlstedt, H.; Park, N. Y.; Stephenson, G. B.; Stolitchnov, I.; Taganstev, A. K.; Taylor, D. V.; Yamada, T.; Streiffer, S. Ferroelectric Thin Films: Review of Materials, Properties, and Applications. *J. Appl. Phys.* **2006**, *100*, 051606.

APPENDIX A

Modeling Diffusion of Molecular 'Ink' within Polymeric Stamps

Summary

Here, we present the code used to model one-dimensional diffusion of alkanethiol 'ink' into a polymeric (PDMS) stamp, as discussed in Chapter 4, by numerically solving Fick's second law:

$$\frac{d}{dt}C(x,t) = D\frac{d^2}{dx^2}C(x,t),$$

using an iterative finite difference method. Two scripts are included: StampDiffusion.m (MATLAB) and SparseFile.pl (Perl). The former script (StampDiffusion.m) models, numerically, ink diffusion into a semi-infinite slab of material and reports the ink concentration profiles after specified inking and diffusion times. The latter script (SparseFile.pl) is used to parse and to simplify the output of the former, which frequently amounted to hundreds or thousands of megabytes of plain text, numeric data. Such a verbose output enabled modeling of ink diffusion with high spatial (100 nm) and temporal (1 ms) resolution over time periods of ~10^4 s in systems with characteristic length scales of ~1 cm. These high resolutions minimized unavoidable numerical errors inherent in computational models. However, such high precisions are not required

for faithful display of the data due to the limited practical resolutions of graphical representations and, more importantly, the macroscopic (millimeter and minute) scales that were of interest in these experiments. As such, the latter script makes data processing, analysis, and display far easier, without sacrificing precision in the aforementioned calculations.

StampDiffusion.m

```
% This script is intended to model the diffusion of long-chain alkanethiol
% molecules into a PDMS stamp by numerically solving Fick's Second Law,
%             d                  d^2
%             -- C(x, t)  =  D * ---- C(x, t)
%             dt                 dx^2
% using an iterative finite difference method.
%
% During inking, the PDMS stamp is modeled as a
% semi-infinite medium that fills the space,
%          0    <= x <= +infinity,
%     -infinity <= y <= +infinity,
%     -infinity <= z <= +infinity,
%
%     (Henceforth, we will neglect the y, z dimensions due to the infinite
%     nature and symmetry of the stamp and only consider the problem
%     in one dimension.)
%
% Initially, the stamp is prepared by 'inking' with a solution of known
% concentration (C0).  During the inking process, the region to the 'left'
% of the stamp (x <= 0) is filled with an inexhaustible supply of solution
% that is allowed to diffuse into the stamp.
% After a set amount of time (T0), the concentration of molecules
% within the stamp, as a function of position (x), is known to be:
%   C(x, T0) = C0 * erfc(x/(2*sqrt(D*T0)))
% where D is the diffusion constant.
%
% The above description assumes that a stamp of infinite thickness.
% However, for numerical solving purposes, the stamp is modeled to have
% a "large" finite thickness, L.  Here, "large" is taken to mean:
% L >> 2*sqrt(D*T0) = Ld
% When this holds true, then the stamp may then be considered,
% to a decent approximation, infinite.  Physically, this corresponds to
% the condition that molecules never 'see' the boundary at x = L because
% no significant number of them diffuse that far in the allotted time.

% Assumed Units: Position and Length --> millimeters, Time --> seconds

% To get a sense of scale,
%     for D = 5E-7 cm^2/s = 5E-5 mm^2/s,
%         T0 = 1 hours   --> Ld = 0.85 mm              erfc(L/Ld) = 10E-62
```

```
%         T0 = 10 hours  --> Ld = 2.7  mm              erfc(L/Ld) = 10E-7
%         T0 = 100 hours --> Ld = 8.5  mm              erfc(L/Ld) = 10E-1
% Therefore, we will model L = 10 mm, and feel confident that our model
% works in the inking time regime of <= ~10 hours.
%
% After inking, the ink solution is instantly removed and the interface of
% the stamp at x = 0 becomes an impenetrable barriers through which no
% molecules may enter or leave the stamp.  Actually, in this model both
% ends of the stamp (at x = 0, and x = L) are impenetrable barriers.
% In the time that follows, from T0 to T1, the molecules that are already
% within the stamp continue diffusing throughout the stamp, causing the
% concentration profile (C as a function of x) to change in time.
% The main purpose of this program is to determine the concentration at a
% certain position of the stamp, most-importantly the stamping surface
% at x = 0, as a function of time after inking (T1).

% A note on numerical error:
% One source of error in this program is mass loss / gain over the course
% of repeated iterations.  This problem is most significant when there
% are high concentration gradients at the boundaries, such as when the
% inking time of the stamp is very short --> very little mass has diffused
% into the stamp, and most of it is accumulated in a very narrow region
% along the interface.  This problem may be reduced by increasing the
% number of position grids used in the calculations; with more grids
% the contribution (error) of any one grid is reduced.  However, the
% trade-off of this solution is that the calculations take more time, and
% consume more memory, and runs the risk of destabilizing the solution if
% the position grid width is made too small, relative to the time spacing.

% This program will save portions of the data that it generated to an excel
% file named 'StampDiffusion.xls' in the current working directory.
% If such a file already exists, the program will delete it,
% and then save a new one, overwriting all old data in the process.

function StampDiffusion (iterations)
% The optional input parameter 'iterations' allows the program to be
% cycled the specified number of times to increase the total diffusion
% time.  For instance, if one sets T1 = 1 (hour), and specifies that the
% number of iterations should be 5, then the program will loop 5 times,
% calculating what the concentration will be within the stamp after 5
% consecutive hours.  The initial conditions for each subsequent hour are
% automatically set from the final conditions of the previous hour.

clc %clear screen

L = 10; % Thickness of stamp (mm)
numx = 1000;   %number of grid points in x (10000 needs a lot of RAM)
dx = L / numx; %width of each grid

% T0 = Inking time (s): pick one or set a custom value
 T0 = 30;      % 30 sec
% T0 = 600;    % 10 min
% T0 = 3600;   % 1 hour
```

```
% T0 = 7200;  % 2 hours
% T0 = 36000; % 10 hours
% T1 = Diffusion time (s): pick one or set a custom value
% T1 = 360;   % 6 minutes
 T1 = 3600;   % 1 hour
%T1 = 36000; %10 hours
% Remember, longer diffusion times encompass all shorter times, but they
% also consume a lot of memory when using trying to perform calculations
% with high spatial and temporal resolution.  Might need to lower the time
% resolution when doing calculations for longer than ~1 hour.
% (Keep in mind, plotting the end results also takes up a lot of memory.)

dt = 0.1;  % length of each time step (s), (0.01 needs a lot of RAM)
numt = T1 / dt; %number of time steps used in iteration

D = 5E-5; % Diffusion coefficient (mm^2 / s), from Balmer paper
C0 = 1;   % Concentration of ink solution,
          % currently normalized to 1, with arbitrary units

Ld = 2 * sqrt(D * T0); %Diffusion length

% Calculate the stability of our numerical solution,
% Von Neumann stability for diffusion equation:
%     Stable for: J = D * (dt) / (dx)^2 <= .5
% If this condition is not met then the numerical solution will
% experience oscillations due to numerical error, making it unreliable.
% Physically, this condition requires that the position grid width be
% greater than or equal to the diffusion length (Ld) divided by Sqrt(2).
% What this means is that the particles cannot diffuse 'too much' between
% time increments.  This is because this algorithm only takes into account
% diffusion across one position grid space at a time.  The larger the time
% increment, or the smaller the position grid width, the more significant
% the unaccounted for 'over-flow' is, which leads to larger and larger
% accumulated errors in the analysis.

% The J coefficient is also reused many times in the loop
J = D * dt / dx^2
if (J > .5)
    disp 'Warning, Stability Factor J > 0.5, Solution Is Unstable!'
    disp 'End Program'
    return;
    % Ends the program if J > 0.5 since the result that would be generated
    % is unstable and will be not be reliable (it will likely diverge)
else %else, continue running (rest of program is inside this else clause)

x = [-dx:dx:L+dx];            % Array of position elements
T = [0:dt:T1];                % Array of time elements
C = zeros(numx+1+2,numt+1);   %initialize everything to zero
% Notice that the position space is 2 extra units long, one on each side
% of the real domain that we are considering.

if (nargin ~= 1) % If no input parameter is specified, assume it to be = 1
    iterations = 1;
```

```
end

% Specify initial conditions, for no diffusion taken place since inking
InitialCondition = C0 * erfc(x / Ld);
    % Below: Two other initial conditions that are fun to play around with
    % to test the behavior of the program (linear and parabolic profiles).
        %InitialCondition = C0 * x;
        %InitialCondition = -C0 * (x - (L/2)) .* (x - (L/2)) + C0 *(L/2)^2;

for n=1:iterations % Loop through each of the iterations
      t = T + (n - 1) * T1; % Adjust the time values for subsequent iteration

      if (n ~= 1)
          % Re-sets the initial concentration profile for subsequent loops
          InitialCondition = C(:,numt+1);
          % Sets the initial conditions to that of the previous iterations'
          % final state
      end

      % Below: Set the values of the two 'extra' end points to the same
      % values as the real end points, ensuring zero-flux at the boundaries.
      C(:,1) = InitialCondition;
      C(1,1) = C(2,1);
      C(numx+3) = C(numx+2);

      if (n == 1) % Only calculate normalization factor using first iteration
          Mass = zeros(1,numt+1);
          %mass = trapz(C(2:(end-1), 1)); % Slow
          mass = 0.5 * (sum(C(2:(end-1)-1, 1)) + sum(C(2+1:(end-1), 1)));
      end
      % 'Mass' is the total amount of "stuff" inside the stamp at t = T0.
      % The above equation is merely an approximation of the integral of the
      % concentration over the length of the stamp.  There are scaling
      % factors missing, omitted for simplicity, since we are not really
      % interested in the actual number, but rather the fact that it is
      % conserved during the later diffusion.  This same technique is used
      % later to compare the mass at all other t <= T1 time steps.

      % Iterate difference equations
      disp(['Start Iterations ' num2str(n)]) % Just a flag for the user
      for j=1:numt+1 %loops through each time step
          for i=2:numx+2
                % Loop through each grid space, but not first and last
                % since those grid spaces are not really in our domain.
                % Concentration at a particular time =
                %                                 old concentration + change
                % where the change is found using a numerical approximation
                % of the second spatial derivative, times D, times dt.
                C(i,j+1) = C(i,j) + J * (C(i+1,j) - 2 * C(i,j) + C(i-1,j));
                % The error in the derivative is of the order dx^2, dt
          end
          C(1,j+1) = C(2,j+1);             % From no-flux condition
          C(numx+3,j+1) = C(numx+2,j+1);   % From no-flux condition
```

```
    % The above conditions force the gradient of the concentration
    % to be zero at the impenetrable interfaces, x = 0 and x = L,
    % thereby preventing mass flow out of the stamp.
end
disp 'Stop Iterations' % Lets the user knows what is happening

%% Plots the initial/final concentration profiles
% figure (1)
% plot (x(2:(end-1)), C(2:(end-1), 1)) % Initial
% hold on
% plot (x(2:(end-1)), C(2:(end-1), end)) % Final
% title('Initial Concentration Profile, t = T0 and t = T1')
% xlabel('0 \leq x \leq L, (mm)')
% ylabel('Concencentration (a.u.)')

% Check for conservation of mass:
%     This value should be constant due to the no-flux B.C.
%     (impenetrable barrier at both interfaces of the stamp).
%     Due to error in calculating integral, as well as in solving PDE,
%     there will be some deviation in the mass expected with time,
%     but, ideally, it should be small.
% Calculate mass sum and normalize to initial mass value
disp 'Calculating Mass' % Lets the user knows what is happening
Mass(1:numt+1) = 0.5 * (sum(C(2:(end-1)-1, 1:numt+1)) + ...
    sum(C(2+1:(end-1), 1:numt+1))) / mass;
%Mass(1:numt+1) = trapz(C(2:(end-1), 1:numt+1)) / mass;

% Plots the normalized mass in the stamp, as a function of time
% figure (2)
% plot(t, Mass)
% title('Mass v. Diffusion Time')
% xlabel('0 \leq t \leq T1, (s)')
% ylabel('Normalized Mass (a.u.)')

disp 'Saving Data' % Just a flag so that user knows what is happening

% Below: saving data to a Comma Separated Files (.CSV)

if (n == 1)
    % If first iteration, delete old files if any exist
    if (exist('ConcentrationProfiles.csv', 'file'))
        delete('ConcentrationProfiles.csv');
    end
    if (exist('SurfaceConcentration.csv', 'file'))
        delete('SurfaceConcentration.csv');
    end
    if (exist('IntegratedMass.csv', 'file'))
        delete('IntegratedMass.csv');
    end

    % Write position coordinates
    dlmwrite('ConcentrationProfiles.csv', ...
        [x(2:(end-1))'], 'precision', 14);
```

```
    % Write header labels
    dlmwrite('SurfaceConcentration.csv', ...
        ['Time (s), Concentration (x = 0)'], 'delimiter', '');
    dlmwrite('SurfaceConcentration.csv', ...
        ['t, C'], '-append', 'delimiter', '');

    % Write header labels
    dlmwrite('IntegratedMass.csv', ...
        ['Time (s), Integrated Mass (Normalized)'], 'delimiter', '');

    t_start = 1; % Start at the beginning on first iteration
else
    t_start = 2; % Start at 2nd spot,
                 % avoid overlap with previous iteration
end

% Time profiles to save:
% Put the time values (in seconds) to be saved into array
% (Also remember to update column labels too - must include commas)
TIMES = [0 30 600 3600 7200 36000]; %0 s, 30 s, 10 min, 1 h, 2 h, 10 h
TimeLabels = '0, 30, 600, 3600, 7200, 36000';

times = zeros(1); % Clear out previous values, if any

for k=1:length(TIMES) % Loop through array of times to save
    % Check to see if any of the times to save are in the current
    % domains, if yes then add it to the list to grab this time
    if ((TIMES(k) >= (n - 1) * T1) && (TIMES(k) <= n * T1))
        if ((((TIMES(k) - (n - 1) * T1) ./ dt)) ~= 0)
            % Do not double-count end points
            times(end+1) = ((TIMES(k) - (n - 1) * T1) ./ dt) + 1;
            % Adjust to find correct matrix element corresponding
            % to this time
        elseif (n == 1) % But the end point at n == 1 is alright
            times(end+1) = ((TIMES(k) - (n - 1) * T1) ./ dt) + 1;
        end
    end
end
if (length(times) > 1) % Are there any times to save on this iteration?
    % Below: read in all previous data in file
    data = dlmread('ConcentrationProfiles.csv', ',');
    for g=2:length(times) % for each time to save ...
        s = size (data);
        % Below: ... Add the time's data column to the array
        data(:, s(2) + 1) = C(2:(end-1), times(g));
    end
    % Below: Write the array back out to the file with the added data
    dlmwrite('ConcentrationProfiles.csv', data, 'precision', 14);
    % Append columns, and not rows
end
```

```
        if (n == iterations)
            % If this is the last iteration...
            % Then write the column labels at the top, then append on the data
            % below.  We must add these last since they are strings and are
            % difficult to read once they are in the file with this method.
            data = dlmread('ConcentrationProfiles.csv', ',');
            dlmwrite('ConcentrationProfiles.csv', ...
                ['Position (mm), Concentrations'], 'delimiter', '');
            dlmwrite('ConcentrationProfiles.csv', ...
                ['x, Times (s) T1 = ', TimeLabels] ,...
                 '-append', 'delimiter', '');
            dlmwrite('ConcentrationProfiles.csv', data, ...
                 '-append', 'precision', 14);
        end

        % Write concentration at surface as function of time
        dlmwrite('SurfaceConcentration.csv', ...
            [t(t_start:numt+1)' C(2, t_start:numt+1)'] , ...
                 '-append','precision', 14);

        % Write integrated mass as function of time
        dlmwrite('IntegratedMass.csv', ...
            [t(t_start:numt+1)' Mass(1, t_start:numt+1)'] , ...
                 '-append','precision', 14);

        disp(' ');
        end % End if statement

end % End iterations for loop

disp 'Done!'

clearvars %clear stored variables that might still exist

end % End function declaration
```

SparseFile.pl

```
# This script is intended to read in the contents of the three files
# generated by the StampDiffusion.m MATLAB program and then resave them in
# a more sparse form (saving only 1 in 10 or 100 lines from the original
# file).  The point of doing this is to make the files more usable since, in
# their original form, they can be several hundred MB (or even GB) large,
# making them impractical to open in standard graphing software packages, or
# even text editors.  By only re-saving 1/10 or 1/100 of the file, it
# reduces the file size considerably at the expense of losing most of the
# data points.  But this is alright because there are already ample data
# points to plot in the case of very large output files, since they were
# originally generated at very high spatial and / or temporal resolutions.
```

```
#!/usr/local/bin/perl

printf "\nOpening ConcentrationProfiles.csv\n";
open(MYFILE, "ConcentrationProfiles.csv") || die "$!";
        @contents = <MYFILE>;  # Reads in all contents of the file,
                               # line-by-line, into an array.
close(MYFILE);
$length = @contents; # Gets length of array
# Below two lines: puts the header lines (first two lines) into the new array
@newcontents = $contents[0];
push(@newcontents, $contents[1]);
for ($i = 2; $i <= $length; $i+=10)
{
        push(@newcontents, $contents[$i]);
        #Adds every 10th line to new array
}
printf "Saving Sparse-ConcentrationProfiles.csv\n";
#Below: open file for overwrite
open(MYFILE, ">Sparse-ConcentrationProfiles.csv") || die "$!";
        print MYFILE @newcontents;  # Writes out all lines of array into file
close(MYFILE);

printf "\n\nOpening SurfaceConcentration.csv\n";
open(MYFILE, "SurfaceConcentration.csv") || die "$!";
        @contents = <MYFILE>;  # Reads in all contents of the file,
                               # line-by-line, into an array.
close(MYFILE);
$length = @contents; # Gets length of array
# Below two lines: puts the header lines (first two lines) into the new array
@newcontents = $contents[0];
push(@newcontents, $contents[1]);
for ($i = 2; $i <= $length; $i+=100)
{
        push(@newcontents, $contents[$i]);
        #Adds every 100th line to new array
}
printf "Saving Sparse-SurfaceConcentration.csv\n";
#Below: open file for overwrite
open(MYFILE, ">Sparse-SurfaceConcentration.csv") || die "$!";
        print MYFILE @newcontents;  # Writes out all lines of array into file
close(MYFILE);


printf "\n\nOpening IntegratedMass.csv\n";
open(MYFILE, "IntegratedMass.csv") || die "$!";
        @contents = <MYFILE>;  # Reads in all contents of the file,
                               # line-by-line, into an array.
close(MYFILE);
$length = @contents; # Gets length of array
# Below line: puts the header lines (first line) into the new array
@newcontents = $contents[0];
```

```
for ($i = 1; $i <= $length; $i+=100)
{
        push(@newcontents, $contents[$i]);
        #Adds every 100th line to new array
}
printf "Saving Sparse-IntegratedMass.csv\n";
#Below: open file for overwrite
open(MYFILE, ">Sparse-IntegratedMass.csv") || die "$!";
        print MYFILE @newcontents;  # Writes out all lines of array into file
close(MYFILE);

printf "\n\nDone!\n";
```